Towards the development of one dimensional zinc oxide nanostructures as biosensor.

Tan, Michelle Tien Tien

Swansea University
Prifysgol Abertawe

Towards the Development of One Dimensional Zinc Oxide Nanostructures as Biosensor

By

Michelle Tien Tien Tan BEng (Hons)

Submitted to the University of Wales in fulfilment of the requirements for the Degree of Doctor of Philosophy

Swansea University

2009

Abstract

The ability to detect biomarkers at a molecular level is crucial to ensure high survival rates for patients with debilitating or life threatening diseases, for example cancer. The limitation associated with existing detection technologies call for more sensitive, selective, faster, cheaper and smaller biosensors for molecular analysis. Recent material advances made in One-dimensional (1-D) ZnO nanostructures hold great promise for fabricating the next generation of biosensors. Due to very high surface-to-volume ratios, they demonstrate high sensitivity to surface charge transfer and changes in the surrounding electrostatic environment, resulting in the significant modification of conductivity upon adsorption of certain molecules. By combining nature's bio-recognition functionalities with the nanostructure's novel electronic properties, an ultra-sensitive and selective biosensor can be developed. The first part of the work compares the electrical behaviour of 1-D ZnO nanostructures grown via hydrothermal and chemical vapour deposition (CVD) techniques, using the scanning conductance microscopy (SCM). For the first time, the polarisability of CVD grown 1-D ZnO nanostructures was observed. By using polarisability as a qualitative measure of the carriers' mobility, CVD nanostructures are shown to exhibit better carrier mobility and thus are more electrically active than hydrothermal ZnO nanorods. Hydrothermal synthesised ZnO nanostructures have higher defect density, generally oxygen vacancies, due to low oxygen concentration in the water and low temperature growth. The oxygen vacancies, known to be deep level traps, are believed to be the reason why the ZnO hydrothermal sample is less 'electrically active'. The successful implementation of biosensors is strongly related to the interface between the biological recognition system and the nanostructure. A surface plasmon resonance technique (Biacore X) is used to identify functional groups that show strong surface binding to ZnO. The respective binding of hexahistidine and zinc finger moieties to ZnO surface was investigated. For the first time, ZnO nanoparticles were discovered to bind directly to nitrilotriacetic acid (NTA), an aminotricarboxylic acid, pre-immobilised on a sensor chip. Subsequently, β-cyclodextrin (βCD) was modified with an NTA-like moiety to form a NTA-linked bioreceptor mimic. Analysis results revealed that NTA-like moiety significantly increased the ability of the native cyclodextrin to bind to the surface of ZnO nanoparticles. Following that, polyglutamic acid was shown to be an excellent intermediate between biological molecules (antibody) and ZnO surface. Employing polyglutamic acid as the intermediate linker between antibody and ZnO surface is novel and is recommended for the fabrication of future generation biosensor.

Declaration

This work has not previously been accepted in substance for any degree and is not being concurrently submitted in candidature for any degree.

Signed ..... (Candidate)

Date 25/01/2010

STATEMENT 1

This thesis is the result of my own investigation, except where otherwise stated. Other sources acknowledge, giving explicit references. A bibliography is appended.

Signed ... . (Candidate)

Date 25/01/2010

STATEMENT 2

I hereby give consent for my thesis, if accepted, to be available for photocopying and for inter-library loan, and for the title and summary to be made available outside organisations.

Signed ..... (Candidate)

Date 25/01/2010

Certificate of Originality

The thesis is submitted to the Swansea University, Swansea, under the supervision of Prof. S. P. Wilks in the Multidisciplinary Nanotechnology Center, School of Engineering, Swansea University, Swansea, in candidature for the degree of Philosophy Doctor. The material in this thesis is the original work of the author except where acknowledgement to other authors is expressly made.

Signed,

Michelle

.....

Michelle Tien Tien TAN

(Candidate)

Signed,

.....

Prof. S. P. Wilks

(Supervisor)

Date: .....

For the Glory of God

and

To my parents & my husband

Acknowledgement

I would like to express my gratitude to the supervisor of my studies, Professor Steve P. Wilks, for giving me the opportunity to perform research work within the Multidisciplinary Nanotechnology Centre at Swansea University. His advice and encouragement have been invaluable. I am also extremely grateful to Dr. Vincent Teng for his valuable advice, guidance and involvement throughout the entire research project. Many thanks go to Dr Steve Conlan and Dr Suzy D Kean for their advices and discussions of the results in Chapter 7. In addition, I would also like to thank Dr Thierry Maffies and Dr Mark W Penny for providing the chemical vapour deposition synthesised ZnO nanostructures samples and similar thanks to Professor Shu Ping Lau of Nanyang Technological University, Singapore for providing the hydrothermal grown ZnO nanorod. The discussion on the results obtained in Chapter 6 with Dr Thierry Maffies is also greatly appreciated. I would also like to extend my gratitude to Dr Shareen Doak and Sally James for the trainings on using the confocal and fluorescence microscope. Also, I would like to express my thanks to Dr Chris Wright for the trainings on the Dimension 3100 AFM system. In addition, I would also like to thank Dr Guy Own and Michal Lodzinski for growing the oxide layer on the silicon substrate. Many thanks also go to Deya Gonzalez for her advice and guidance in preparing biological samples. The financial supports given by Overseas Research Students Awards Scheme (ORSAS) and the School of Engineering are gratefully acknowledged. I am also very thankful to my friends; Brenda Lee, Chris Chan, Samson Chang,, Woan Yi, Jasmin Liu and Qun Ying for none of this would be possible without their constant support and encouragements. I would like to especially thank Chong, my husband for his love, care, patience, understanding, encouragement, food and for just being there throughout my PhD. Lastly, I would like to thank my parents for always believing in me and also for their constant love and support throughout my life.

Contents

Chapter 3: Scanning Probe Microscopy Technique

Chapter 6: Qualitative Conductance Studies of Zinc Oxide Nanostructures

Chapter 7: Surface Functionalisation of Zinc Oxide (ZnO)

List of Tables

List of Figures

Abbreviations

1-D	One dimensional
AFM	Atomic force microscope
Anti	Antibody
BA	Back angle
βCD	Beta-cyclodextrin
BSA	Bovine serum albumin
CNT	Carbon nanotube
COOH	Carboxylic acid
CVD	Chemical vapour deposition
Cy5	Cyanine dye
DAPI	4',6-diamidino-2-phenylindole
Dcbpy	2,2-bypyridine-4,4-dicarboxylate
DI	Deionised
DI 3100	Dimension 3100
EDC	1-ethyl-3-(3-dimethylaminopropyl)carbodiimide hydrochloride
EFM	Electrostatic force microscope
EtBr	Ethidium bromide
Et-NTA	Fluorescence tagged nitrilotriacetic acid
ER_{α}	Oestrogen receptor
FA	Front angle
FITC	Fluorescein isothiocyanate
FET	Field effect transistor
FM	Frequency modulation
GPC	Gel permeation chromatography
His_6	Hexahistidine
IFC	Integrated microfluidic cartridge
IgG	Immunoglobulin G
Ir	Iridium
KCl	Potassium chloride
MES	2-(N-morpholino)ethanesulfonic acid.

MFM	Magnetic force microscope
MWCO	Molecular weight cutoff
NaCl	Sodium chloride
$NaHPO_4$	Sodium phosphate
NH_2	Amine group
NaOH	Sodium hydroxide
NHS	N-hydroxysuccinimide
NTA	Nitrilotriacetic acid
P	Product
PEG	Polyethylene glycol
PEO	Polyethylene oxide
PEI	Polyethyleneimine
PGA	Polyglutamic acid
PGA-F	Fluorescence tagged polyglutamic acid
PSPD	Position-sensitive photodiode
PSAP	Polyaspartic acid
PSI	Polysuccinimide
Pt	Platinum
RMS	Root mean square
RU	Resonance unit
SA	Side angle
SCM	Scanning conductance microscope
Si	Silicon
SiO_2	Silicon dioxide
SiNW	Silicon nanowire
SnO_2	Tin dioxide
SP	Surface potential
SPM	Scanning probe microscopy
SPR	Surface plasmon resonance
SWNT	Single walled carbon nanotube
TIR	Total internal reflection
TiO_2	Titanium dioxide
TGA	Thermogravimetric analysis
TLC	Thin layer chromatography

TM-AFM	Tapping mode atomic force microscope
TR	Texas red
TRITC	Rhodamine
VdW	van der Waals
YFP	Yellow fluorescent protein
ZnO	Zinc Oxide
ZnO NPs	ZnO nanoparticles
ZrO2	Zirconium dioxide

Chapter 1

Introduction

1.1. General introduction

Early diagnosis of life-threatening diseases such as cancer, at easily-treatable and pre-symptomatic stage, is crucial in improving the survival rate of patients. Highly sensitive and selective techniques that are able to detect disease markers at ultra-low levels during early stages are urgently needed. Most existing diagnostic techniques are inefficient and often detect diseases in the deadly stages due to the insensitivity of the techniques. Moreover, current molecular diagnosis methods rely on well-resourced central laboratories, which are very expensive and time-consuming (e.g. ELISA). For a standard medical diagnostic of a certain disease, various types of samples and tests, such as blood tests, urine tests, X-rays, and etceteras, are needed. Besides that, current methods like the radioimmunoassay (RIA) require the usage of radioactive labels which has potential deleterious biological effects. The numerous complex tests will result in the delay of a patient's medical treatment. Therefore, in order to eliminate suffering and death due to life-threatening diseases, more sensitive, selective, faster and cheaper diagnostic methods are urgently needed.

Nanotechnology has become one of the most studied areas for the past quarter of a century. According to the National Nanotechnology Initiative (NNI), nanotechnology is defined as study and technology development at the atomic, molecular, or macromolecular scale, leading to the controlled creation and use of structures, devices, and systems with a length scale of 1-100 nanometres (nm). Materials in the nanoscale have excellent potential for designing powerful and remarkably sensitive bioanalytical protocols with multiplexing capability [1,2]. These nanomaterials exhibit novel properties and functions that are markedly different from those in bulk. Additionally, nanoscale materials are of similar size as many important biological entities, making nanotechnology a clear choice for creating powerful disease diagnostics tools. This similarity in size enables nanoscale devices to see and interact with biomolecules on the cell surface and within the cell, in avant-garde ways that do not alter the properties of those molecules [3]. There are a variety of nanoscale structures that are currently under development for biosensing applications [4]. Amongst these, the most promising nanomaterials for designing and manufacturing

future generation biosensor are the one-dimensional (1-D) nanostructures. The 1-D nanostructures such as nanowires [5], nanotubes [6], and nanobelts [7] are particularly attractive as biosensing platforms, due to their efficient transport of electrons. As a matter of fact, these 1-D systems are the smallest dimension structures available for the efficient transport of electrons and thus are crucial to the function and fabrication of nanoscale devices [8]. The 1-D nanostructures have high surface-to-volume ratio and novel tuneable electron transport properties due to quantum confinement, where their electrical properties are strongly influenced by minor surface perturbations. Any binding to the surface (i.e. binding of macromolecules) leads to the depletion or accumulation of charge carriers in the wire, resulting in significant changes to the entire cross-sectional conduction pathway of these nanostructures. The small scale of these 1-D nanostructures allows many sensing elements to be packed onto a small footprint for multiplexed bio-electronics. Therefore, 1-D nanostructures offer excellent prospects in the design and fabrication of novel nanoscale diagnostic devices, which combine the conductive or semiconductive properties of these nanomaterials with the recognition properties of biomaterials.

A biosensor (Figure 1.1) is defined as an analytical device, incorporating a biological detection or recognition system for a target molecule or macromolecule, intimately associated with a physiochemical transducer, which converts the biological recognition event into a useable output signal [9]. The 'holy grail' for medical biosensing is an implantable device which is able to produce highly accurate, specific and real time signals (either discrete or continuous digital electronic signals), which are proportional to the detection of a single analyte or a related group of analytes. However, there are several critical issues which needed to be addressed in fabricating such devices. To recap, the biosensor has three essential components: a biological recognition system which is usually made up of biological receptor that detect specific analyte, a physico-chemical transducer which converts biological signals into quantitative measurable signal, and an output system to present the measured signal into an appropriate format. The interfaces between each of these components should be given important consideration as they may constitute the major hurdle in the development of a practical device.

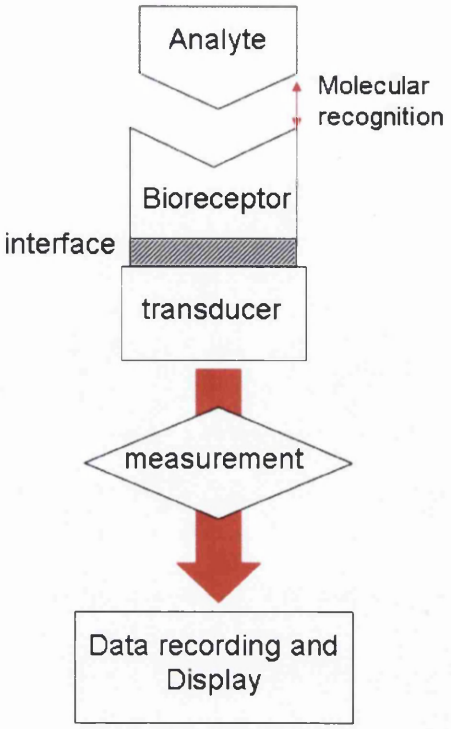

Figure 1.1 Schematic representation of a biosensor.

The key to success for a biosensor is selectivity, detecting only a specific target analyte and to maintain this selectivity in the presence of other species. This is inextricably related to the bio-recognition system (bioreceptor), in addition to its interface to the surface of the transducer. The utility of any biosensing platform is wholly dependent on the types and viability of the bioreceptors. There are many forms of bioreceptors and can be generally classified into five different major categories: 1) antigen-antibody, 2) enzymes, 3) nucleic acids/DNA, 4) cellular structures/cells and 5) biomimetic [10]. Amongst these, antibody as the recognition element is the most common, because of their high specificity, versatility and strong and stable affinity to a specific antigen. Furthermore, the breakthroughs in genomic and proteomic methods [11] in the last decades have enabled the identification and validation of certain diseases through the presence of associated biomarkers. These biomarkers are biological molecules that serve as indicators of the physiological state and also of the changes at different stages of the disease. Specific antibodies (bioreceptor) can be expressed against a single, well-characterized biomarker that can bind to it. The attachment of these bioreceptors to the surface of the transducer, or better termed as immobilisation, also play a crucial role to the effectiveness of the

biosensor. Such immobilisation should produce durable binding of the bioreceptor to the transducer and at the same time does not impair the activity or specificity of the bio-receptor to the target analyte. The transducer conveys signals to the output system via connected metal electrodes. To be able to deliver signals effectively to the integrated output system (i.e. current-voltage (I-V) probe station), the interface between the transducer and electrodes should be considered. An improper contact interface between these two elements will lead to major loss to the device performance, which is often caused by high resistance from thermal stress or contact failure.

ZnO nanowires, nanorods and nanobelts, are currently amongst the most researched 1-D nanostructures, due to their superior electrical, optical, mechanical and thermal properties. ZnO is a naturally n-type direct wide bandgap (3.37eV) semiconductor with a high exciton binding energy of 60 meV [12]. In addition, it has large piezoelectric and ferromagnetic coefficients. Its high isoelectric point of 9.5, biocompatibility and fast electron transfer kinetics make it a promising candidate for biosensing applications [12, 13, 14]. These diverse properties of ZnO and the ability to grow such nanomaterials, has fuelled the recent development of ZnO nanoelectronic devices, such as optoelectronics [15, 16], field effect transistors [17], Schottky diodes [18] and sensors [19, 20, 21, 22].

In the proposed work, the ZnO 1-D nanostructures will be used as the platform (transducer) for an ultrasensitive and ultraselective biosensing device. The detection mechanism of this 1-D nanostructure is based on the field-effect transistors (FET) operation. In the FET configuration, any variations in the electric field or potential at the surface of the 1-D nanostructure FET will result in changes to the electrical conductivity of the nanostructure [23]. Consider a standard FET device (Figure 1.2A), with a semiconductor connected to a metal source and drain electrode, through which current is injected and collected respectively. A third gate electrode which is capacitively coupled through a thin dielectric layer controls the conductance of the semiconductor between the source and drain [24]. In the case of a p-type semiconductor, an applied negative (positive) gate voltage leads to negative (positive) charges at the interface between the gate electrode and dielectric. This results in the accumulation (depletion) of positive holes carriers at the interface

leading to an increase (decrease) in the conductance of the semiconductor (Figure 1.2A). The dependence of the conductance on the gate voltage and corresponding charge at the gate electrode-dielectric interface is exploited for electrically based sensing, where the binding of a charged biological species to the gate is analogous to applying a voltage to the gate electrode (Figure 1.2B). Although this idea for sensing with FETs was introduced a few decades ago [25], it did not have a big impact as a biological or chemical sensor mainly due to the limited sensitivity of such a planar device.

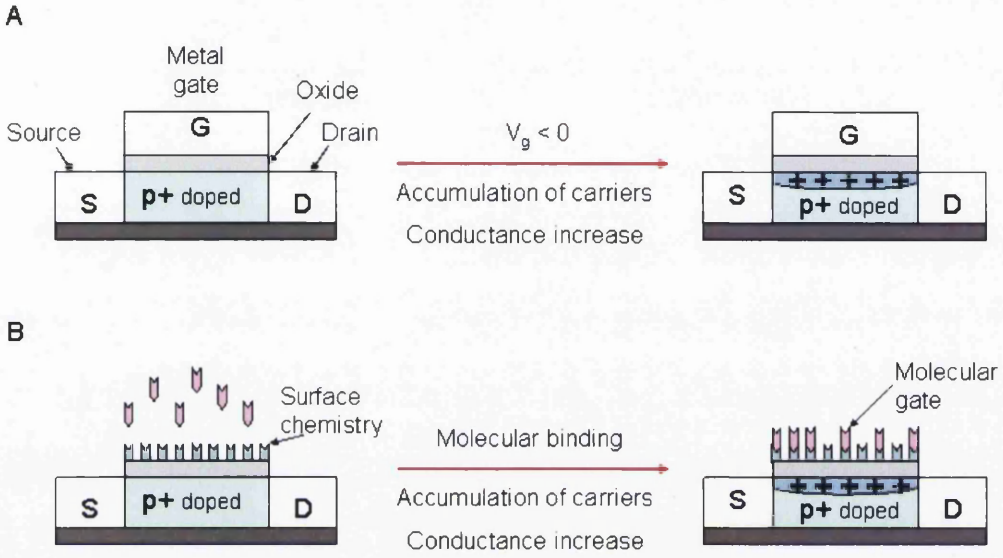

Figure 1.2 (A) Schematic of a conventional field-effect transistor (FET) device; S, D and G are the source, drain and metal gate electrodes respectively. (B) Schematic of an electrically based biosensor analogous to a FET device. The binding of a polar biological species to the modified gate is analogous to applying a voltage at the gate electrode [24].

The performance of the FET based nanobiosensor relies heavily on the electronic properties of the 1-D ZnO nanostructure. Therefore, to embark on development of a FET based biosensor, a study of the structural and electronic characteristics of the 1-D nanostructure is inevitable. The scanning conductance microscopy (SCM) technique was chosen for the study, as it provided an elegant route for characterising the electronic properties of nanomaterials without having to fabricate metal contacts to the nanostructures of interest. This 'electrode-less' measurement feature of SCM enables rapid qualitative characterisation of different samples without performing time-consuming electrode fabrication. Using the SCM, the qualitative difference in the conductance of ZnO 1-D nanostructures grown by two different methods; chemical vapour deposition (CVD) and the hydrothermal growth, will be presented.

This study aids in finding the most suitable nanostructure, in terms of the relative conductivity of the different samples as the platform for the biosensing device. Following that, suitable methods to attach a bioreceptor to the surface of the 1-D ZnO nanostructure are explored. The affinity of several bio-friendly functional moieties to the ZnO surface was investigated using the Biacore X, a real-time and label free detection technique that exploits the principle of surface plasmon resonance (SPR). Zinc fingers and hexahistidine (His_6), two small functional moieties that can be found tagged to certain proteins (antibodies) were evaluated due to their natural tendency to bind to zinc ions (Zn^{2+}). Subsequently, a bioreceptor mimic that incorporates a ZnO binding group was synthesised and its resultant affinity for ZnO was examined using thermogravimetric analysis. Following the findings, a polymer dense with the ZnO binding group was employed as the linker substitute. A confocal microscope and a fluorescence microscope were used to verify the feasibility of using the polymer as the intermediate linker between antibodies and ZnO nanostructures.

1.2. Thesis Organisation

Chapter 1 presents the problems associated with current diagnostics and how nanotechnology can be fused with life science to create novel and powerful methods that will open up new technology frontiers that could revolutionize many aspects of medicinal diagnosis. The objectives of this research and the methods used to achieve them are presented. The summary of a literature review discusses suitable conductive 1-D ZnO nanostructure as biosensing platforms and also determines methods to immobilise biomolecules on the surface of the ZnO.

Chapter 2 presents a brief literature review on the recent advances in FET based biosensor with emphasis on SiNWs and CNTs. The limitations of using SiNWs and CNTs for the fabrication implantable biosensor are also addressed. Following that, the structure, unique properties and applications of ZnO nanomaterials are discussed. The final part of this chapter presents the structures and properties of several functional moieties, namely the zinc fingers, the hexahistidine tag (His_6), the

nitrilotriacetic acid (NTA), the polyglutamic acid, the antibody molecule, which are relevant to the functionalisation methodologies attempted and reported in Chapter 7.

Chapter 3 addresses the principle of Atomic Force Microscopy (AFM). The theory of the scanning conductance microscopy (SCM), a secondary AFM technique, is also presented. A section on interpreting SCM measurements is also shown.

Chapter 4 describes the principles of surface plasmon resonance (SPR) and how it is exploited in the real-time Biacore system. The three essential components the SPR system; the optical detection unit, the micro-fluidics system (liquid flow channel) and the sensor chip are addressed.

Chapter 5 considers the various experimental techniques used in the research work. Details on the instrumentation of the AFM (Dimension 3100 AFM system) and the SPR technique (Biacore X) are given. Brief description of the theory of other techniques used; the thermogravimetric analysis, the thin layer chromatography method, and the fluorescence detection techniques are also described.

Chapter 6 presents the qualitative conductance studies of 1-D ZnO nanostructures grown from the chemical vapour deposition (CVD) and the hydrothermal methods using the scanning conductance microscopy technique. The obtained results are analysed and compared with SCM studies of other materials.

Chapter 7 presents the results of the affinity studies of zinc fingers and hexahistidine tag functional moieties to ZnO using the Biacore X. The synthesis step of a bioreceptor mimic is presented along with the results of the ZnO surface affinity analysis using thermogravimetric analysis. The last part of the chapter describes the steps to immobilised primary and secondary antibodies on the ZnO surface using polyamino acids as the mediator, along with the difficulties encountered. The imaging study of this immobilisation was investigated using fluorescence detection techniques (confocal and fluorescence microscopes).

Chapter 8 presents the conclusion and future work of the research. Results are discussed in terms of the overall findings of the work. As the research is still at its

preliminary stage, future challenges towards the development of a nanobiosensor are discussed.

1.3. References

[1] Jain K K 2004. Applications of biochips: from diagnostics to personalized medicine *Curr. Opin. Drug Discov. Dev.* 7 285–289

[2] Sun C P, Liao J C, Zhang Y H, Gau V, Mastali M, Babbitt J T, Grundfest W S, Churchill B M, McCabe E R B and Haake D A 2005 Rapid species-specific detection of uropathogen 16S rDNA and rRNA at ambient temperature by dot–blot hybridization and an electrochemical sensor array *Mol. Genet. Metab* **84** 90–99

[3] Bogunia-Kubik K and Suigisaka M 2002 From molecular biology to nanotechnology and nanomedicine *Biosystems* **65** 123-138

[4] Kelley S O 2006 Nanowires for Biomolecular Sensing *Nanotechnology in Biology and Medicine: methods, device and applications* (edited by: T. Vo-Dinh) CRC Press 6-1

[5](a) Morales A M and Lieber C M 1998 A laser ablation method for the synthesis of crystalline semiconductor nanowires *Science* **279** 208

(b) Hu J, Odom TW, and. Lieber CM 1999 Chemistry and physics in one dimension: synthesis and properties of nanowires and nanotubes *Acc. Chem. Res.* **32** 435

(c) Cui Y, Zhong Z, Wang D, Wang W U and Lieber C M 2003 High performance silicon nanowire field effect transistors *Nano Letters* **3** 149

(d) Wu Y, Xiang J, Yang C, Lu W and Lieber CM 2004 Single-crystal metallic nanowires and metal/semiconductor nanowire heterostructures *Nature* **430** 61

[6](a) Chen R J, Bangsaruntip S, Drouvalakis K A, Kam W S, Shim M, Li Y, Kim W, Utz P and Dai H J 2003 Noncovalent functionalization of carbon nanotubes for highly specific electronic biosensors *Proceedings of the National Academy of Sciences* 2003 **100** 4984

(b) Chen R J, Choi H C, Bangsaruntip S, Yenilmez E, Tang X T, Wang Q, Chang Y L and Dai H J 2004 An investigation of the mechanisms of electronic sensing of protein adsorption on carbon nanotube devices *J. Am. Chem. Soc.* **126** 1563

[7] Wang Y, Du G, Liu H, Liu D, Qin S, Wang N, Hu C, et al 2008 Nanostructured sheets of Ti_2O nanobelts for gas sensing and antibacterial applications *Adv. Funct. Mater.* **18** 1

[8] Wanekaya A K, Chen W, Myung N V and Mulchandani A 2006 Nanowire-based electrochemical biosensors *Electroanalysis* **18** 533

[9] Collings A F and Caruso F 1997 Biosensor: recent advances *Rep. Prog. Phys.* **60** 1397

[10] Vo-Dinh T and Cullum B 2000 Biosensors and biochips: advances in biological and medical diagnostics *Fresenius' J. Anal. Chem.* **366** 540

[11] (a) Srinivas P R, Kramer B S and Srivastava S 2001 Trends in biomarker research for cancer detection *Lancet Oncol.* **2** 698

(b) Srinivas P R, Srivastava S, Hanash S and Wright G L 2001 Proteomics in early detection of cancer *Clinical Chemistry* **47** 1901

[12] Özgür Ü, Alivov Y I, Liu C, Teke A, Reshchikov M A, Doan S, Avrutin V, Cho S J, and Morkoç H 2005 A comprehensive review of ZnO materials and devices *J. Appl. Phys.* **98** 041301

[13] Zhang C L, Liu M C, Li P, Xian Y Z, Cheng Y X, Zhang F F, Wang X L and Jin L T 2005 Fabrication of ZnO nanorod modified electrode and its application to the direct electrochemical determination of hemoglobin and Cytochrome c *Chin. J. Chem.* **23** 144

[14] Zhou J, Xu N S and Wang Z L 2006 Dissolving behaviour and stability of ZnO wires in biofluids: a study on biodegradability and biocompatibility of ZnO nanostructures *Adv.Mater.* **18** 2432

[15] Kind H, Yan H Q, Messer B, Law M and Yang P D 2002 Nanowire ultraviolet photodetectors and optical switches *Adv. Mater.* **14** 158

[16] Wang X D, Summers C J and Wang ZL 2004 Large-scale hexagonal patterned growth of aligned ZnO nanorods for nano-optoelectronics and nanosensors arrays *Nano Lett.* **4** 423

[17] Arnold M S, Avouris P, Pan Z W and Wang Z L 2003 Field-effect transistors based on single semiconducting oxide nanobelts *J. Phys. Chem.* B **107** 6594

[18] Park W I, Yi G C, Kim J W and Park S M 2003 Schottky nanocontacts on ZnO nanorod arrays *Appl. Phys. Lett.* **82** 4358

[19] Kumar N, Dorfman A and Hahm J 2006 Ultrasensitive DNA sequence detection using nanoscale ZnO sensor arrays *Nanotechnology* **17** 2875

[20] Wei A, Sun X W, Wang J X, Lei Y, Cai X P, Li C M, Dong Z L and Huang W 2006 Enzymatic glucose biosensor based on ZnO nanorod array grown by hydrothermal decomposition *Appl. Phys. Lett.* **89** 123902

[21] Wan Q, Li H, Chen Y J, Wang T H, He X L and Gao X G and Li J P L 2004 Positive temperature coefficient resistance and humidity sensing properties of Cd doped ZnO nanowires *Appl. Phys. Lett* **84** 3085

[22] Kim J S, Park W I, Lee C H and Yi G C 2006 ZnO nanorod biosensor for highly sensitive detection of specific protein binding *J. Kor. Phys. Soc.* **49** 4

[23](a) Lieber CM 2003 Nanoscale science and technology: building a big future from small things *MRS Bull* **28** 486

(b) Cui Y, Wei Q, Park H and Lieber CM 2001 Nanowire nanosensor for highly sensitive and selective detection of biological and chemical species *Science* **293** 1289

[24] Sze SM 1981 *Physics of Semiconductor Devices* Wiley New York USA 431

[25](a) Bergveld P 1972 Development, operation and application of ion-sensitive field effect transistor as a tool for electrophysiology *IEEE Trans. Biomed. Eng. BME* **19** 342

(b) Blackburn G F 1987 *In Biosensors: fundamentals and Applications* Turner APF, Karube I, Wilson GS (Eds), Oxford University Press, Oxford, UK, 481

Chapter 2

Literature Reviews of Different Material Properties

2.1. Introduction

The last three decades have witnessed an extraordinary growth in study of sensors, particularly biosensors, driven by the desires of many scientists to improve the quality of human life. The activities in the area of biosensors can be seen from the fact that, in 1985, there were 213 scientific publications and 119 patents on biosensors and some 3000 publications and 300 patents by the end of 1990. Another survey for the period 1990 to mid 1996 alone indicated a further 3300 articles and over 600 patents [1]. This intensively competitive area involves multi disciplines, ranging from physics, and life science to engineering. Therefore, the scientific challenges involved in this study are formidable! Nevertheless, the discovery of one-dimensional nanostructures has opened up a whole new frontier to biosensor research. Three of the most actively researched 1-D nanostructures are the carbon nanotubes (CNTs) [2], silicon nanowires (SiNWs) [3] and ZnO nanowire/nanobelts [4, 5]. Much research employing SiNW and CNT as a platform for biosensing application have been reported. Yet, not much has been reported on the use of 1-D ZnO nanostructures for the detection of biomolecules.

In this chapter, a brief review of SiNWs and CNTs based biosensors will be presented. This review is essential as the underlying detection mechanism of the SiNWs and CNTs based biosensor will be exploited in the fabrication of 1-D ZnO nanostructure based biosensor. The structure, properties, potential applications and biocompatibility of 1-D ZnO nanostructures; nanowires, nanorods and nanobelts, are addressed, which must be understood to employ them as potential building blocks for nanodevices. This chapter also presents the background into the structure and properties of several organic materials used in this research.

2.2. Recent advances in field effect transistor (FET) biosensor based on one dimensional (1-D) nanostructure

Conventional semiconductor field effect transistors (FETs) have been exploited as biosensing devices [6], though they exhibited limited sensitivity. On the other hand, FETs that incorporate 1-D nanostructures have been used for the detection of biochemical compounds such as proteins, DNA and viruses with markedly improved sensitivity. The electrical properties of nanostructures are highly influenced by minor surface perturbation due to their high surface-to-volume ratio. In the FET configuration, binding of biomolecules to the surface of 1-D nanostructure leads to the accumulation or depletion of carriers in the 'bulk' of the nanometre diameter, which in turn increase or decrease the conductance of the nanostructure. The selectivity of such device can be enhanced by immobilising recognition groups to the surface of the nanowire (Figure 2.1), for specific analyte detection.

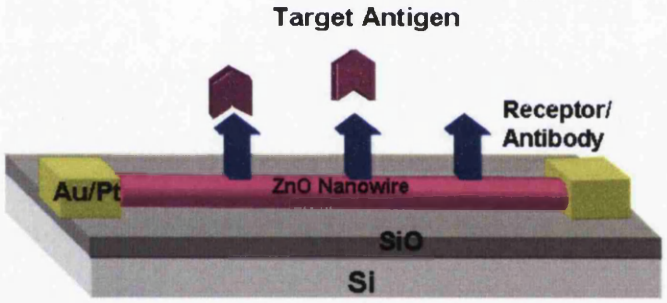

Figure 2.1 Schematic of a nanowire based FET with metal source and drain electrodes. Receptors are immobilised on the nanowire surface for the specific detection of target analyte. The detection of target analyte is analogous to applying a gate voltage to the FET biosensor.

Thus far, the most researched 1-D nanostructures as platform for biosensing devices are silicon nanowires (SiNWs) and carbon nanotubes (CNTs). In this section, literature reviews on recent advances in FET biosensing devices will be presented. In addition, issues on using these nanomaterials as implantable biosensors for in vivo detection of biomolecules will also be discussed.

2.2.1. Silicon nanowire (SiNW)

As conventional FETs consist of silicon materials, it is not surprising that silicon nanowires (SiNWs), which can be doped as p- and n-type, produce promising results as FET nanowire biosensor. In addition, existing data for chemical modifications of silicon oxide on planar chemical and biological arrays also encourage the fabrication of SiNWs biosensors. The performance of Si nanowire FETs are comparable to or even better than planar silicon devices [7]. In addition, the unique one-dimensional structure of Si nanowires exhibits far greater sensitivity than the conventional diagnostic techniques, enabling detection down to a single virus [8]. The pioneer in the research work of SiNW based biosensor is the *Lieber et. al*, who demonstrated the first label-free, highly sensitive electronic detection of biological species in solution using boron-doped (p-type) silicon nanowires (SiNW) [9]. In this work, SiNW was functionalised with biotins by depositing a drop of (20 μl) of phosphate-buffered solution (PBS) (250 μg/ml; pH5.6) of biotinamidocaproyl-labelled bovine serum albumin (Sigma) on the SiNW for 2 hours, followed by a five times rinse with buffer solution. Subsequently, changes in the conductance of the biotin-modified SiNW were monitored when streptavidin was introduced (Figure 2.2). On the exposure to a solution of streptavidin, the SiNW measured conductance increases, rapidly to a stable value (Figure 2.2B). They confirmed the specificity of this SiNW biosensor via several control experiments in which no changes in conductance were detected when streptavidin was introduced to un-modified SiNW (Figure 2.2C) and also when the biotin binding sites of the streptavidin were blocked (Figure 2.2D). The detection limit of this biotin-modified SiNW FET was reported to be down to the picomolar concentration range (< 10 pM) (Figure 2.2E). As an extension to this work, specific, real-time and reversible detection of monoclonal antibody (m-antibiotin) to the biotin modified SiNW FET as a function of m-antibiotin concentration was demonstrated. They reported that the measured conductance increased linearly as a function of the antibody concentration below ~10 nM and saturation was recorded at higher values [9].

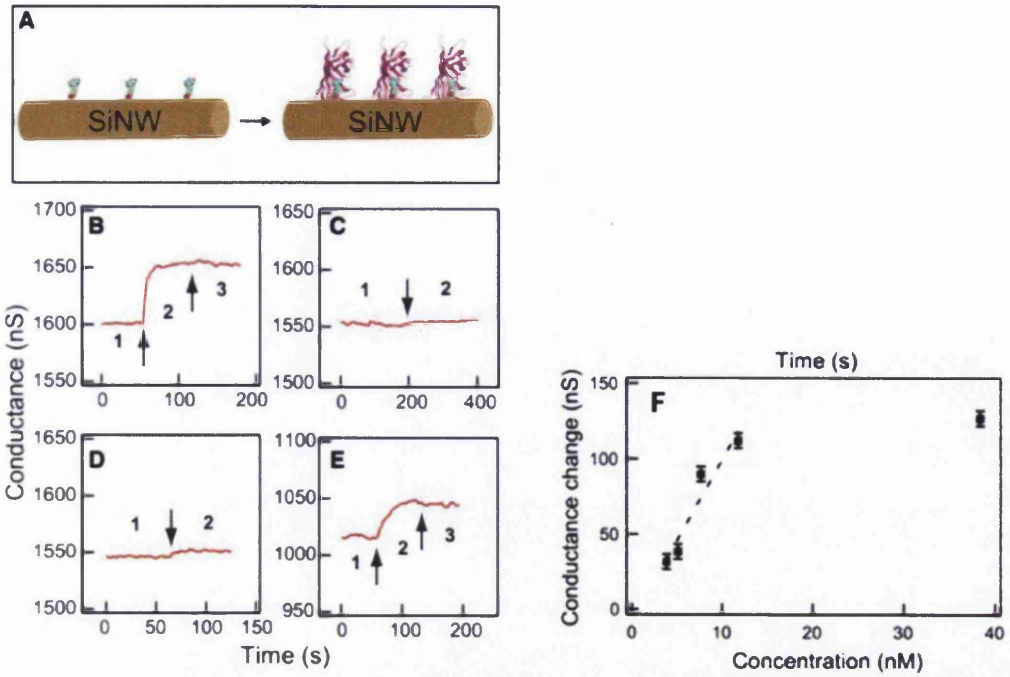

Figure 2.2 Real-time detection of protein binding. (A) Schematic illustrating a biotin- modified SiNW (left) and subsequent binding of streptavidin to the SiNW surface (right). The SiNW and streptavidin are drawn approximately to scale. (B) Plot of conductance versus time for a biotin-modified SiNW, where region 1 corresponds to buffer solution, region 2 corresponds to the addition of 250 nM streptavidin, and region 3 corresponds to pure buffer solution. (C) Conductance versus time for an unmodified SiNW; regions 1 and 2 are the same as in (B). (D) Conductance versus time for a biotin-modified SiNW, where region 1 corresponds to buffer solution and region 2 to the addition of a 250 nM streptavidin solution that was pre-incubated with 4 equivalents d-biotin. (E) Conductance versus time for a biotin- modified SiNW, where region 1 corresponds to buffer solution, region 2 corresponds to the addition of 25 pM streptavidin, and region 3 corresponds to pure buffer solution. Arrows mark the points when solutions were changed. Plot of the conductance change of a biotin-modified SiNW versus m-antibiotin concentration; the dashed line is a linear fit to the four low concentration data points. Error bars equal 6 1SD. [9].

Following this initial work, *Lieber et. al* reported an improved nanowires device able to detect multiple cancer marker proteins selectively and simultaneously with sensitivity down to the femtomolar concentrations [10]. Cancer markers are molecules found in blood or tissues and are very useful in disease diagnosis. In this study, a versatile detection platform was fabricated using spaced aligned SiNWs with metal deposition to define interconnects to the SiNWs arrays by photolithography This state-of-the art multiplexed sensor contains more than 100 independently addressable elements (Figure 2.3A).

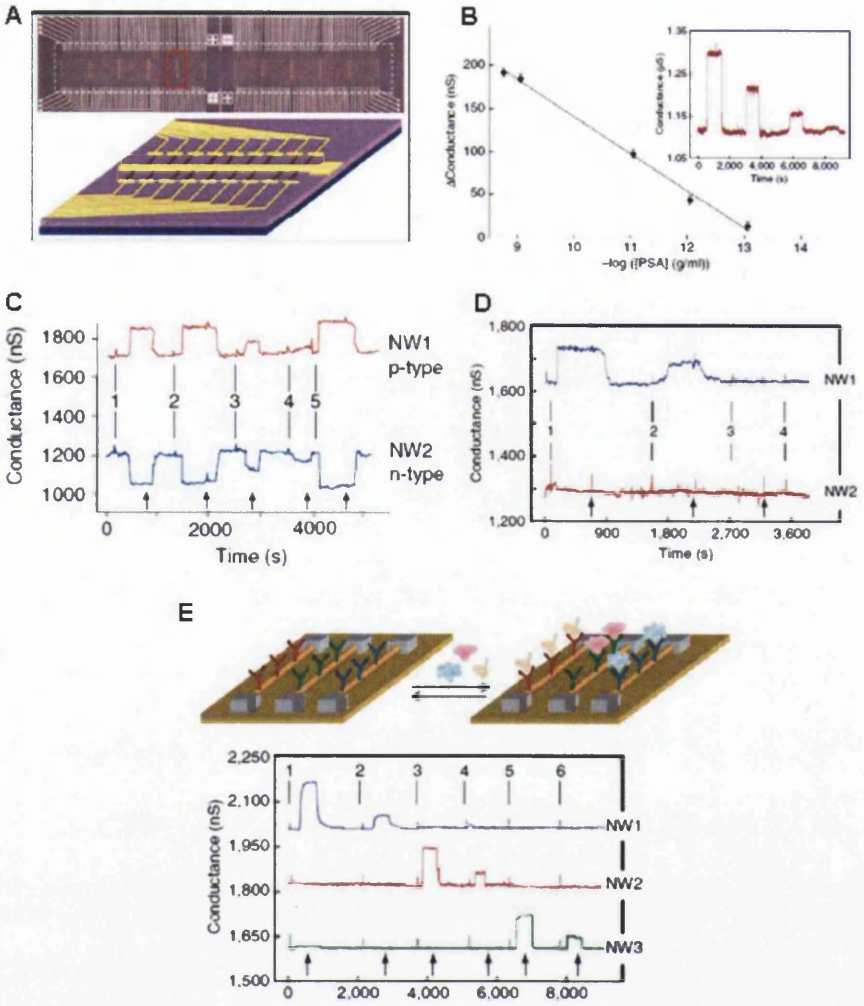

Figure 2.3 (A) Schematic of the nanowire array device. (B) The change in conductance versus concentration of PSA for a PSA-AB1 receptor modified p-type SiNW. Inset: conductance versus time recorded after alternate delivery of PSA and pure buffer solutions. The PSA concentrations used were 0.9ng/ml, 9pg/ml, 0.9pg/ml and 90fg/ml respectively. (C) Complementary sensing of PSA using p-type (NW1) and n-type (NW2) SiNW. The concentration of PSA solution delivered alternately were: (1,2) 0.9ng/ml, (3) 9pg/ml, (4) 0.9pg/ml and (5) 5 ng/ml. (D) The changes in conductance from two p-type SiNWs (NW1: functionalised with prostate specific antigen (PSA Ab1), NW2: functionalised with ethanolamine) were recorded when (1) 9pg/ml PSA (2) 1pg/ml PSA (3) 10 μg/ml BSA and (4) mixture of 1ng/ml PSA and 10μg/ml PSA Ab1 were delivered. (E) Schematic illustration of multiplexed protein detection using three SiNW in an array. The specificity of each nanowire is differentiated with functionalisation of distinct mAb receptors. The changes in conductance versus time of p-type SiNW functionalised with antibodies for PSA (NW1), CEA (NW2) and mucin-1(NW3) were recorded simultaneously when protein solutions of (1,2) PSA, (3,4) CEA and (5.6) mucin-1 were delivered sequentially to the device array [10].

In addition, different types of addressable nanowires (i.e. p-type and n-type doped SiNWs) functionalised with different receptors can be incorporated into the design. Selective binding of a protein with negative (positive) surface charge to the receptor will increase (decrease) the conductance of the p-type SiNW, whereas the opposite

response will be observed for an n-type SiNW (Figure 2.3C). To determine the sensitivity of this sensor device array, monoclonal antibodies for PSA (PSA-Ab1) were immobilised on the nanowire elements right after device fabrication. The changes in conductance of the PSA-Ab1 modified device were monitored as a function of PSA concentration. It was reported that the conductance change is directly proportional to the concentration of the PSA and the sensitivity of the device was down to femtomolar concentration (~2 fM) (Figure 2.3B). The authors have proven the reproducibility and selectivity of the sensor, by showing that there were no changes in conductance (no binding) when bovine serum albumin (BSA) solutions and PSA-Ab1 pre-blocked PSA solutions were delivered to the device (Figure 2.3D, point 3 and 4). The critical performance of the device was examined by functionalising each addressable SiNW with monoclonal antibody for PSA (NW1), carcinoembryonic antigen (CEA) (NW2) and mucin-1 (NW3) respectively. The changes in the conductance of each SiNW (NW1, NW2 and NW3) were monitored as different protein samples were sequentially introduced to the device array (Figure 2.3E). The reported results clearly demonstrated multiplexed real-time, label-free marker protein detection with essentially 100% selectivity.

To define the ultimate sensitivity of the SiNW FET device, *Lieber et. al* continued their studies with the detection of viruses (Figure 2.4A) [8]. In this study, two SiNWs in a device array were functionalised with monoclonal antibody receptors for influenza A (NW1) (red data) and adenovirus (NW2) (blue data) respectively (Figure 2.4B). Upon the introduction of ~ 100 virus particles per μl delivered, they observed real-time discrete changes in conductance of the nanowires. In addition, optical data of fluorescently labelled viruses clearly showed that the discrete conductance change of the device were solely due to a single virus binding to and unbinding from the silicon nanowires (Figure 2.4C).

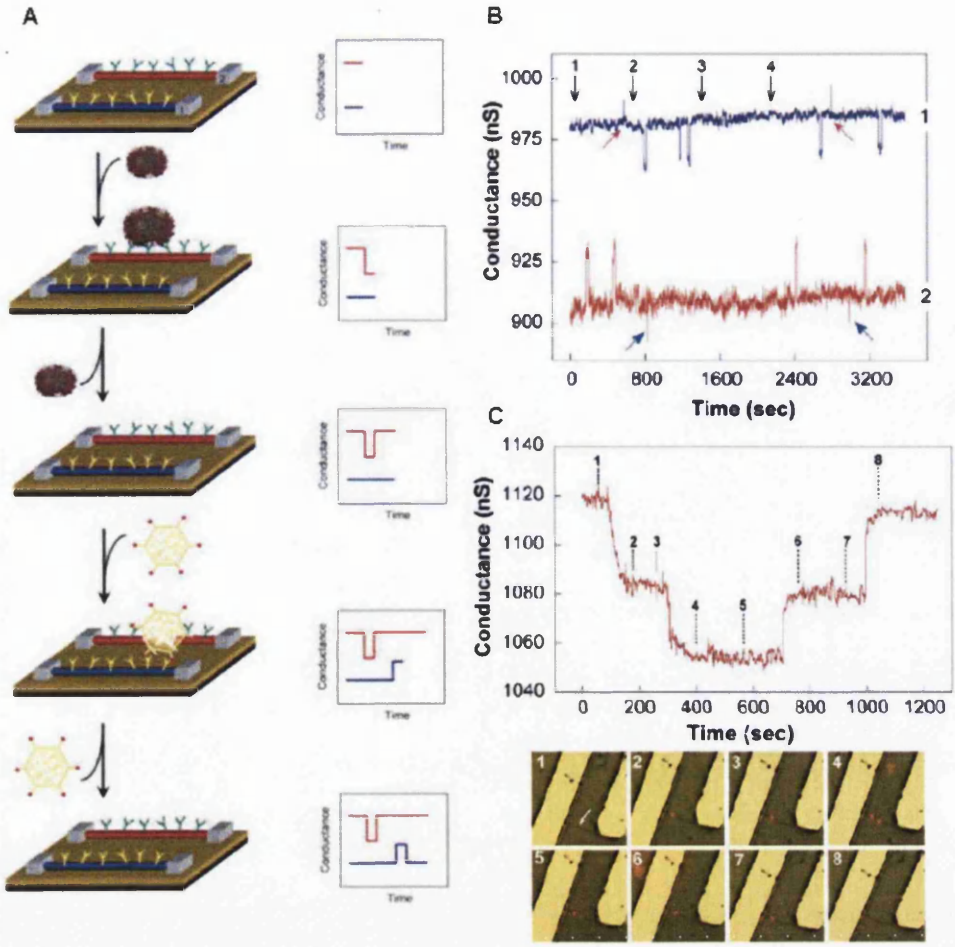

Figure 2.4 (A) Schematic of multiplexed single-virus detection using SiNW FET devices modified with antibody receptors for specific viruses. (B) The changes in conductance recorded simultaneously for two SiNWs with one SiNW functionalised with anti-influenza type A antibody (blue) and another with anti-adenovirus group III antibody (red). Small red and blue arrows in (B) highlight conductance changes corresponding to the diffusion of viral particles past the nanowire and non-specific binding. Black arrows 1-4 correspond to the introduction of adenovirus, influenza A, pure buffer, and a 1:1 mixture of adenovirus and influenza A. (C) The conductance and optical data recorded against time for a SiNW device, showing that the discrete change in conductance was due to the detection of a single virus entity.

2.2.2. Single walled carbon nanotube (SWNT)

Carbon nanotubes (CNTs), best described as a rolled-up sheet of graphite (a sheet formed of hexagons of carbon atoms), was first discovered by Iijima in 1991 [11]. It is another example of a superior nanomaterial that exhibits many novel properties and has great potential in applications such as nanoelectronics, biomedical engineering and biosensing/bioanalysis [12]. The CNTs have very simple chemical composition and are unique amongst solid-state material in that every atom is on the surface. Therefore, CNTs surface chemistry and electronic properties are highly

sensitive to its environment and vary significantly with changes in electrostatic charges and surface adsorption of various molecules [13, 14].

K Besteman et. al demonstrated the first enzymatic-activity sensors based on individual single walled CNTs (SWNT) (Figure 2.5A) [15].

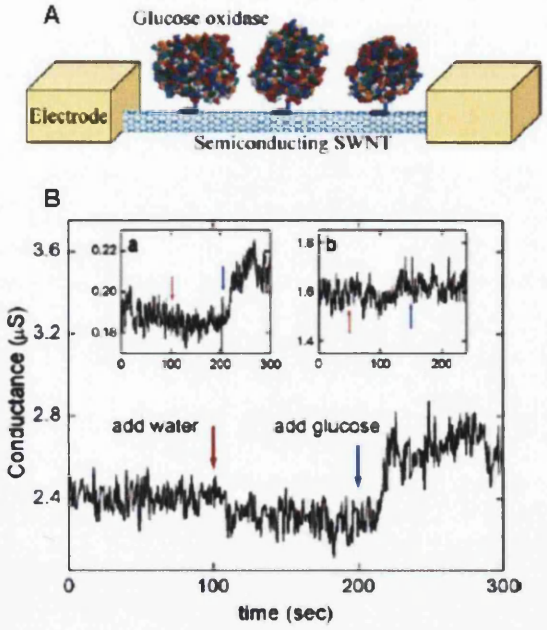

Figure 2.5 (A) Schematic illustration of the GOx enzymes coated SWNT biosensor. (B) Conductance change vs. time recorded when water (red arrow) and glucose solution (blue arrow) are introduced to the SWNT FET biosensor. Inset (a) is the measurement on a second device showing conductance change upon addition of glucose. Inset (b) is the same measurement done on a bare SWNT where no changes were observed upon addition of glucose [15].

In their study, a bi-functional molecule called 1-pyrenebutanoic acid, a succinimidyl ester, was used for the attachment of the enzyme on the SWNTs surfaces. The pyrenyl group, known to interact strongly with the basal plane of graphite via π-stacking, was coupled to the nanotubes via van der Waals force, with the succinimidyl ester groups at the other end, interacting with the enzyme through an amide bond [16]. They demonstrated changes in conductance of the enzyme glucose oxidase (GO_x) modified SWNT FET upon specific detection of glucose (Figure 2.5B).

Since CNTs are naturally hydrophobic, insoluble in most solutions, many studies have been looking for novel functionalisation techniques, which render the surface of

CNTs hydrophilic [17 , 18]. A hydrophilic surface will improve the CNTs' biocompatibility and at the same time eliminate non-specific protein binding. One group, *A Star et. al* explored this by using a polymer coated nanotube FET [17], for the specific detection of biotin to streptavidin [19]. In their work, the CNT were polymer coated by submerging them in a mixture of poly(ethylene imine) (PEI) and poly(ethylene glycol) (PEG) in water overnight. Specificity of this sensor was then enhanced by attaching biotins to the primary amines in PEI (Figure 2.6A).

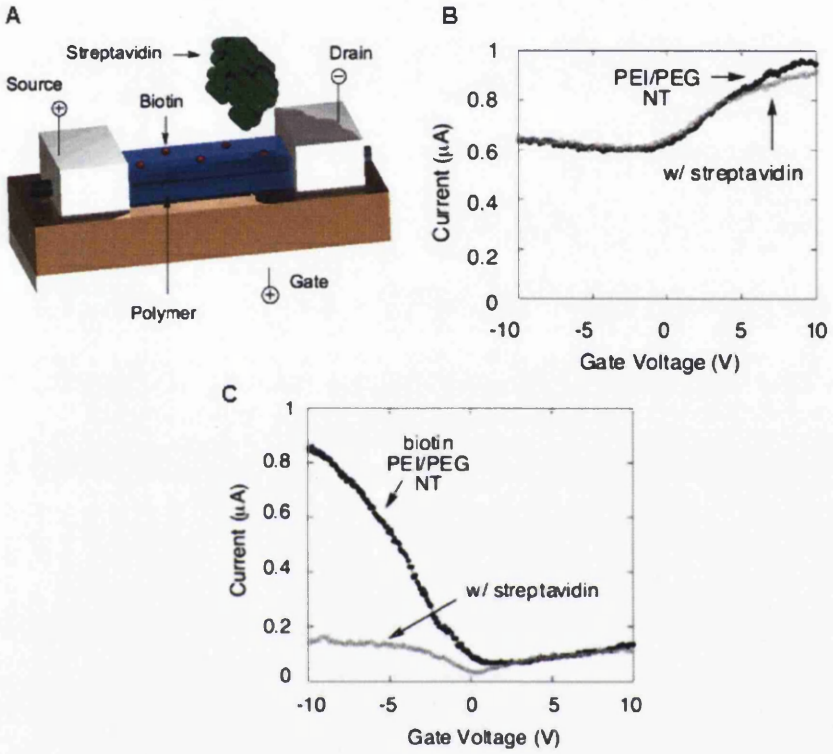

Figure 2.6 (A) Schematic illustration of a SWNT based FET device. Current-voltage dependence of $I_{sd}(V_g)$ of (B) a polymer (PEI/PEG) coated FET device and (C) a biotinylated polymer (PEI/PEG) coated FET device upon exposure to streptavidin.

A Star et. al demonstrated a change in the device characteristic from p-type, before chemical modification to n-type after polymer (PEI/PEG) coating. They postulated that this device characteristic change is due to the electron donating property of the amine (NH_2) groups of the polymer [19]. In addition, no conductance change was detected for the polymer coated CNT device upon exposure to streptavidin. This suggested that the polymer has successfully prevented direct and unspecific protein absorption (Figure 2.6B). Finally, they demonstrated the distinct loss of source-drain

current for negative voltages after exposure to streptavidin and the detection level was estimated to be of the order of 10 streptavidin molecules (Figure 2.6C).

The use of polymer coated SWNTs as highly specific electronic biosensor was further confirmed by *RJ Chen et. al* [18]. Instead of using non-medical related biomolecules (i.e. biotin-streptavidin), *RJ Chen et. al* had immobilised monoclonal antibodies for the specific detection of human autoantigen U1A, a marker for systemic lupus erythematosus and mixed connective tissue disease (Figure 2.7A). Upon exposure to 10EA, an antibody that specifically binds to U1A, changes in conductance of the CNT was detected (Figure 2.7B).

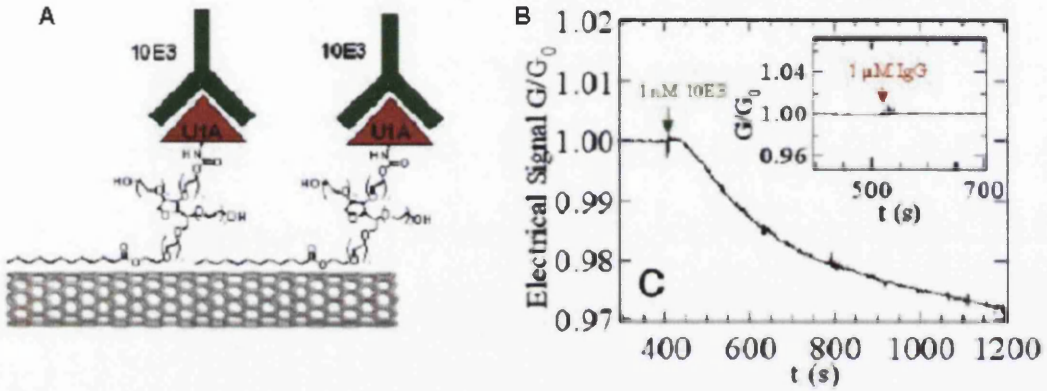

Figure 2.7 (A) Schematic illustration showing the scheme for functionalisation of CNT surface with U1A antigen-Tween conjugate for the specific detection of 10EA antibody. (B) Conductance vs. time curve of a device shows specific response to less than 1 nM 10EA while rejecting polyclonal IgG at a much greater concentration of 1μM (Inset) [18].

2.2.3. Issues concerning SiNWs and CNTs for in vivo sensing

The semiconducting nature of SiNWs and its compatibility with conventional Si-based technology has rendered its success as an FET-based biosensor. Both the SiNWs and CNTs are robust materials with high tensile strength. As discussed in the previous sections, the success of functionalized SiNWs and CNTs for the detection of various molecules such as proteins [7], viruses [8] and cancer markers [10] were unquestionable. However, the biocompatibility and biodegradability of both nanomaterials remain unclear. For example, there have been reports on the toxic effects of carbon nanotubes, when administered in sufficient amounts [20]. It was reported that all-carbon molecules with chemical formula C60- are powerful electron

sponges, readily swiping loosely bound electrons from nearby molecules. When they penetrate into cells, this aptitude may convert oxygen and other molecules into reactive radicals that can tear apart cell components [21]. Recent reports on polymer coated CNTs to improve biocompatibility using poly (ethylene glycol) (PEG) also have flaws. Although proven to be more biocompatible and eliminate non-specific binding, (EG)nOH , a polyether, can easily oxidise in the presence of oxygen and transition metal ions, which are found in most biological fluids [22]. Consequently, the CNT will be exposed and render it toxic to its surrounding. Other reports on the toxicity of these nanomaterials can be found in [23,24]. Another disadvantage of carbon nanotubes is that existing fabrication methods produce a mixture of metallic and semiconducting nanotubes [25]. Due to this extreme diversity in structure-dependent properties, characteristic studies of such devices are inaccurate, since metallic 'devices' will function differently. Furthermore, complicated purification steps are needed to separate impurities, such as catalyst particles, amorphous carbon and non-tubular fullerenes.

A better alternative to the SiNW and CNTs as platforms for implantable biosensing devices is the 1-D ZnO nanostructures. In addition to many novel properties, one of the main advantages of ZnO nanomaterials over SiNWs and CNTs is their biodegradability and biocompatibility. The properties of the 1-D ZnO nanomaterials will be discussed in the following section (Section 2.3).

2.3. ZnO one dimensional (1-D) nanostructures

2.3.1. Crystal and surface structure of ZnO

ZnO is a tetrahedrally coordinated wide bandgap (3.4 eV) II-VI compound semiconductor that has the stable wurtzite structure. The lattice parameters are a = 3.296 Å, c = 5.2065 Å and the ratio, $c/a \sim 1.60$, is close to the ideal hexagonal cell $c/a = 1.633$ [26]. As with the standard II-VI compound materials, the bonding within ZnO is largely ionic. The structure of ZnO is best described as a number of alternating planes composed of tetrahedrally coordinated oxygen anions (O^{2-}) and Zinc cations (Zn^{2+}), alternatively stacked along the c-axes (Figure 2.8) [5]. Due to

this Zn-O tetrahedral coordination, the entire ZnO structure lacks central symmetry, resulting in its piezoelectricity and pyroelectricity properties.

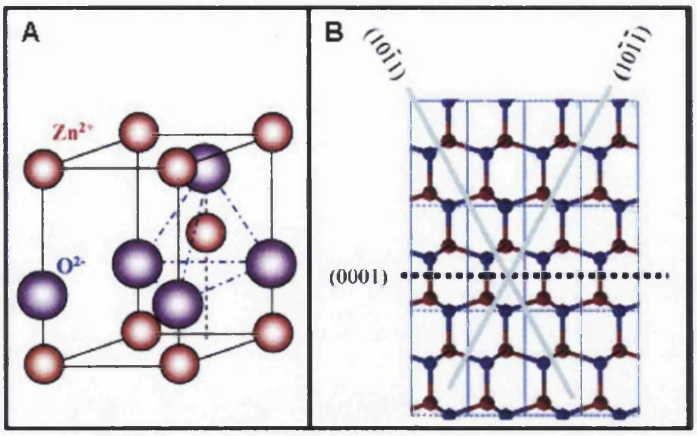

Figure 2.8 (A) The tetrahedral coordination of Zn-O is shown in the wurtzite structure model of ZnO. (B) The three types of facets of ZnO nanostructures [5].

In addition, certain configurations of the distribution of the cations and anions in the ZnO results in some surfaces that are terminated entirely with anions or cations. Hence, although the entire unit cell of the ZnO remains neutral, these surfaces will be positively or negatively charged surfaces, (i.e. polar surfaces). These surface charges are non-transferable and non-mobile ionic charges. As the distribution of charges influence the resultant interaction energy among the charges, the structure is arranged in such a configuration to minimize the electrostatic energy.

ZnO has three-types of fast growth directions: $\pm[0001]$, $\langle 2\bar{1}\bar{1}0\rangle$ ($\pm[2\bar{1}\bar{1}0]$, $\pm[\bar{1}2\bar{1}0]$, $\pm[\bar{1}\bar{1}20]$) and $\langle 01\bar{1}0\rangle$ ($\pm[01\bar{1}0]$, $\pm[10\bar{1}0]$, $\pm[1\bar{1}00]$). $\{0001\}$ is a common polar surface, known as the basal plane, where one end of the plane terminates with partially positive Zn lattice sites while the other end terminates in partially negative oxygen lattice sites. As a result, two oppositely charged surfaces exist at the basal plane, namely the positively charged Zn-$\{0001\}$ and negatively charged O-$\{000\bar{1}\}$ surfaces. These oppositely charged surfaces induce a normal dipole moment and spontaneous polarization along the c-axis as well as a variance in surface energy. In general, due to the variance in surface energy, polar surfaces normally have facets or exhibit massive surface reconstructions to maintain a stable structure. The basal planes are unique where they are atomically flat, stable and

exhibit no reconstruction [27, 28]. $\{2\bar{1}\,\bar{1}0\}$ and $\{01\,\bar{1}0\}$ are non polar surfaces and have lower energy than {0001} facets. By tuning the growth rate along these directions, combined with the polar surfaces, a wide range of novel ZnO structures that can be grown. Figure 2.9 shows the typical growth morphologies of 1-D ZnO nanostructure, where these structures tend to maximize the areas of $\{2\bar{1}\,\bar{1}0\}$ and $\{01\,\bar{1}0\}$ facets because of the lower energy [5]. The various existing ZnO nanostructures are shown in Figure 2.10.

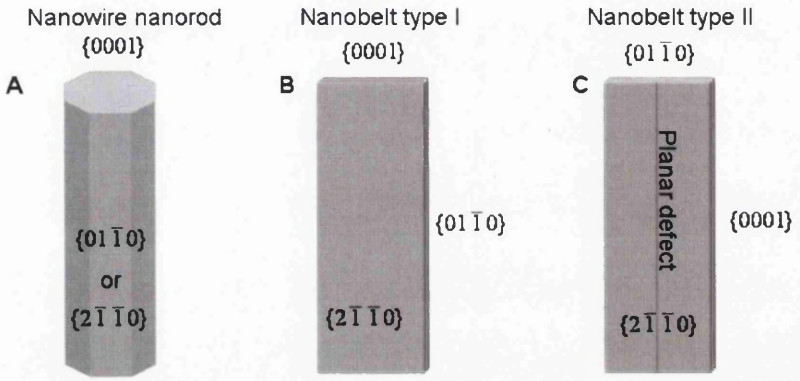

Figure 2.9 The typical growth morphologies of one-dimensional ZnO nanostructures and the corresponding facets [5].

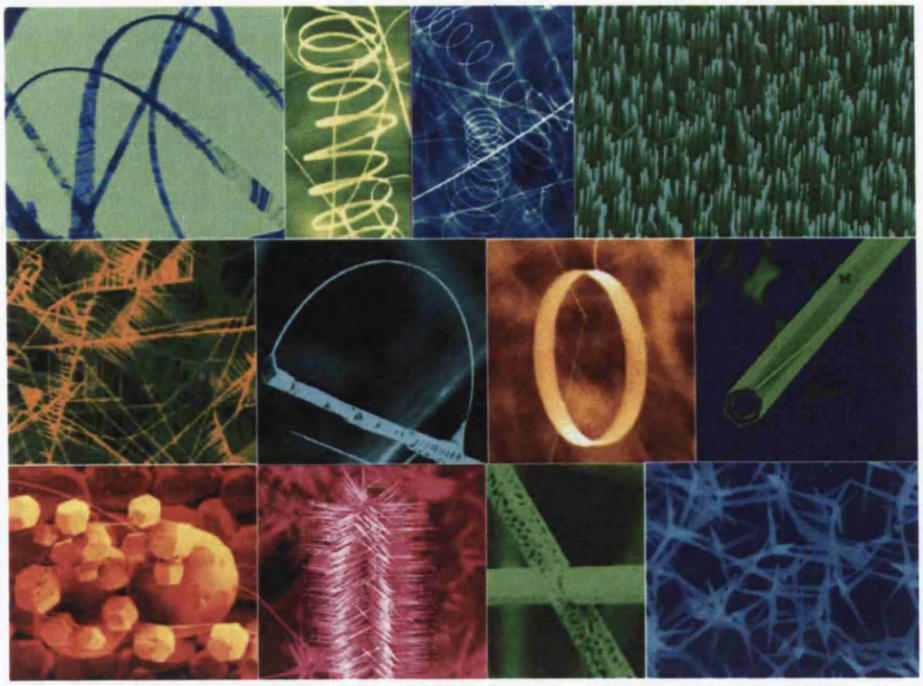

Figure 2.10 A collection of different types of ZnO nanostructures [29].

2.3.2. Common synthesis techniques

The growth of ZnO nanostructures generally follows two common routes: the vapour transport growth at relatively high temperature (gas phase synthesis) and the hydrothermal based chemical approach at low temperature (solution phase synthesis). The vapour transport approach (solid-vapour process) is one of the most common methods to synthesize ZnO nanostructures [30]. This synthesis is normally carried out in a gaseous environment in a closed chamber at high temperature from 500°C to 1500°C. In a typical solid-vapour process, decomposition of ZnO at high temperature produces Zn and oxygen vapours. The mixture vapours are transported and react with each other, and the resultant mixture is then condensed at specific conditions to form the desired ZnO nanostructures on a substrate surface. The specific growth condition is set by varying several processing parameters: temperature, pressure, carrier gas (the gas species and flow rate), substrate and evaporation time before and/or during the thermal vaporization [31]. The type and quality of the product are influence by the local temperature and the concentration of oxygen in the growth system [5].

The hydrothermal synthesis is another popular methodology for generating ZnO nanorods or nanowires [32, 33, 34, 35]. This simple growth process is carried out in aqueous solution under low temperature, usually less than the boiling point of water. Various additives are usually used in the aqueous medium for the successful synthesis of ZnO nanostructures of different morphologies. Amongst these, the mixture of zinc nitrate and hexamine are the most popular. The first successful fabrication of ZnO nanowires on glass and Si substrates was done by thermal decomposition of methenamine and zinc nitrate [36]. In the reported synthesis work, a thin layer of ZnO nanoparticles was first grown on the substrate. Thermal degradation of hexamethylenetetramine (HMT), a highly water soluble, non-ionic tetradentate cyclic tertiary amine, releases hydroxyl ions which react with Zn^{2+} ions to form ZnO [37]. The hydrothermal process to fabricate 1-D ZnO nanostructures has received much attention due to its simplicity, inexpensive and environmental friendly growth conditions.

2.3.3. Properties and potential applications of ZnO nanostructures

1-D ZnO nanostructures are among the few dominant nanomaterials in nanotechnology due to their unique properties and versatile applications in optics, optoelectronics, sensors, actuators, energy, biomedical sciences and spintronics [38]. The basic physical properties of bulk ZnO [39] are shown in Table 2.1.

Properties	Value
Lattice constants (T = 300 K)	a_o = 0.32469 nm c_o = 0.52069 nm
Density	5.606 g/cm^3
Melting point	2248 K
Relative dielectric constant	8.66
Gap energy	3.4 eV direct
Intrinsic carrier concentration	< 10^6 cm^{-3}
Exciton binding energy	60 meV
Electron effective mass	0.24
Electron mobility (T = 300 K)	200 cm^2/Vs
Hole effective mass	0.59
Hole mobility (T = 300 K)	5 – 50 cm^2 / Vs

Table 2.1 The physical properties of bulk ZnO [39].

As the dimension of the semiconductor materials decreases down to the nanometre size, the physical properties deviate substantially from those of the bulk due to 'quantum confinement effects'. Some examples are the increase of band gap energy of quasi 1-D ZnO nanostructures which was confirmed by the reported photoluminescence studies [40] and the enhancement of surface states observed from the downsizing of ZnO nanorods, detected by X-ray absorption spectroscopy and scanning photoelectron microscopy [41]. In regard to this, it is important to understand and investigate the fundamental physical properties of ZnO nanostructures for developing their potential as novel components for future nanoscale devices. In this section, the research progress on four important properties

of ZnO nanostructures such as the mechanical, piezoelectricity, electrical and sensing properties will be discussed.

2.3.3.1. Mechanical properties

The direct measurement of the mechanical properties of individual ZnO nanostructure is not as straight forward as traditional measurement method for bulk materials. The mechanical property measurement of ZnO nanobelts was performed based on an electric field induced resonant excitation using a transmission electron microscopy (TEM) [42]. In the experiment, a special TEM sample holder (Hitachi HF-2000 TEM (200 kV)) with two electrodes and a set of piezo-manipulation and translation devices was used. ZnO nanobelts were attached to one of the electrodes and an oscillating electric field was applied between the two electrodes. Mechanical resonance was induced when the frequency of the applied electric field matched the natural resonance frequency of the nanobelt (Figure 2.11).

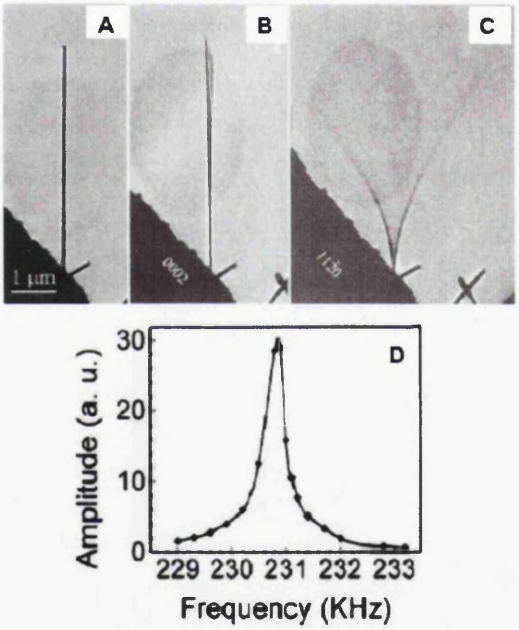

Figure 2.11 TEM images of a ZnO nanobelt at (A) stationary (B) the first harmonic resonance in x direction (V_x=622 kHz), (C) the first harmonic resonance in y direction (Vy=691 kHz) and (D) full width at half maximum (FWHM) of the resonance peak measured from another ZnO nanobelt [42].

Therefore, the bending modulus of the ZnO nanobelt can be quantified following the classical elasticity theory [43]. From this, ZnO nanobelts are promising materials as

nanoresonators, with potential applications as probes for SPM operated in tapping and scanning modes [44]. Besides that, *Hughes et. al* reported the manipulation of well aligned individual ZnO nanobelt with respect to the desired length and position [45]. The mechanical properties of ZnO nanobelt juxtaposed with its reduced dimension rendered it a promising highly sensitive cantilever for atomic force microscopy (AFM).

2.3.3.2. Piezoelectricity

Piezoelectricity, another important property of ZnO, is a crystal structure determined effect where the oxygen atoms and zinc atoms are tetrahedrally coordinated. The piezoelectric effect can convert mechanical vibration into electric signals (vice versa) which has been extensively studied for various applications [46]. Figure 2.12A illustrates piezoelectricity by considering the ZnO non-centrally symmetric structure with a positive charge centre which is surrounded tetrahedrally by anions.

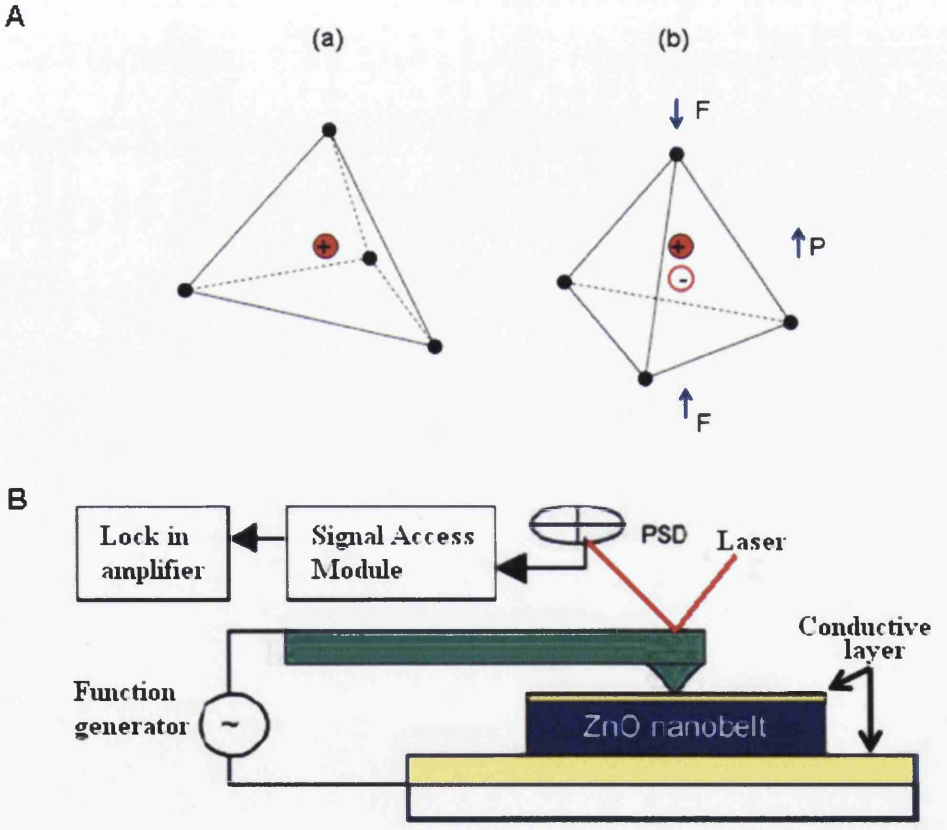

Figure 2.12 (A) The piezoelectric effect in a tetrahedrally coordinated cation-anion unit. (B) Schematic illustration of measuring the piezoelectric coefficient of ZnO nanobelts using conductive AFM [47].

External pressure exerted on the crystal induces lattice distortion where the centre of gravity of the negative charges no longer matches the position of the positive central atom. As a result, local dipole moment is generated ((b) in Figure 2.12). Therefore, with all the tetrahedral in the crystal experiencing the same orientation, the whole crystal will generate macroscopic dipole moments [44]. The piezoelectric coefficient of a ZnO nanobelt has been measured by the atomic force microscope (AFM) using a conductive tip [47] (Figure 2.12B). It was reported that the effective piezo coefficient of the measured nanobelt was frequency dependent and much larger than that of the bulk (0001) surface.

2.3.3.3. Electrical properties

Understanding the electrical properties of ZnO nanostructures is essential for developing their future applications in nanoelectronic devices. The electrical transport measurements on individual ZnO nanowires and nanorods have been performed by various groups [48]. Field effect transistors (FETs) have been fabricated using individual ZnO nanobelt [49] (inset in Figure 2.13).

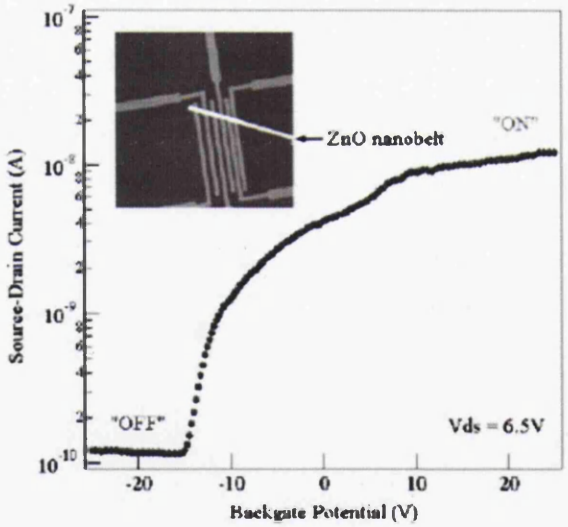

Figure 2.13 The source-drain current as a function of gate bias for a FET fabricated from ZnO nanobelt. Inset: The AFM image of the FET device.

Using a standard procedure, large bundle of ZnO nanobelts were dispersed in ethanol by ultrasonication and deposited on predefined gold electrode arrays on a SiO_2/Si (p^+) substrate. The SiO_2 gate dielectric thickness was 120 nm with a gold back gate

electrode on the Si (p^+) side of the substrate. It was observed that although the pre-fabricated gold electrodes led to very resistive contacts, the ZnO nanobelt FET performance is analogous to those of carbon nanotubes deposited on top of Au electrodes or covered by Ti electrodes. The reported threshold voltage was -15 V, a switching ratio of nearly 100 with a peak conductivity of 1.25 X 10^{-3} Ω/cm (Figure 2.13). Another group has fabricated high performance n-channel ZnO nanorod FETs with improved FET characteristics [50]. Single crystal ZnO nanorods were deposited on a 250-nm-thick-SiO_2 gate dielectric/Si (n^+) substrate. To achieve good ohmic contact for attaining high device performance, Au/Ti metal layers were coated on the nanorod ends and annealed at 300°C for 2 minutes [51]. The n-channel ZnO nanorod FET showed highly improved electron mobility with a maximum value of 1000-1200 cm^2/Vs, a high current on/off ratio of 10^5 and a transconductance of 1.8 μS. Recently, FETs based on high-crystalline ZnO nanowires displayed substantially higher electron mobility with the maximum value exceeding 4000 cm^2/Vs [52] (Figure 2.14). The ZnO nanowire was coated with SiO_2/Si_3N_4 passivation layers to reduce electron scattering and trapping due to surface defects and also to reduce the surface chemisorption processes at oxygen vacancy sites (Figure 2.14A). A comparative study on the device performance was carried out between 20 untreated surface devices (Figure 2.14B) and 20 devices coated with passivation layer (Figure 2.14C). Results showed that the drain-source (IDS) versus the gate voltage (VG) curves for the surface treated FET device exhibit clear saturation and a significantly enhanced on/off ratio on the order of 10^4 even at V_{DS} = 5 mV. The reported electron mobility of the ZnO nanowire FET was much higher than that of Si nanowire FET (1350 cm^2/Vs) [7] and the polymer coated ZnO nanorod FET (1200 cm^2/Vs) [50]. These single crystalline ZnO nanostructures show superior electrical properties compared to its polycrystalline thin film counterpart where an electron mobility of 7 cm^2/Vs is regarded quite high for ZnO thin film transistor [48]. Since the electron mobility indicates the carrier velocity and switching speed of FETs, these results demonstrate the promising potential of ZnO nanostructures, as building blocks for future applications of high frequency integrated electronics.

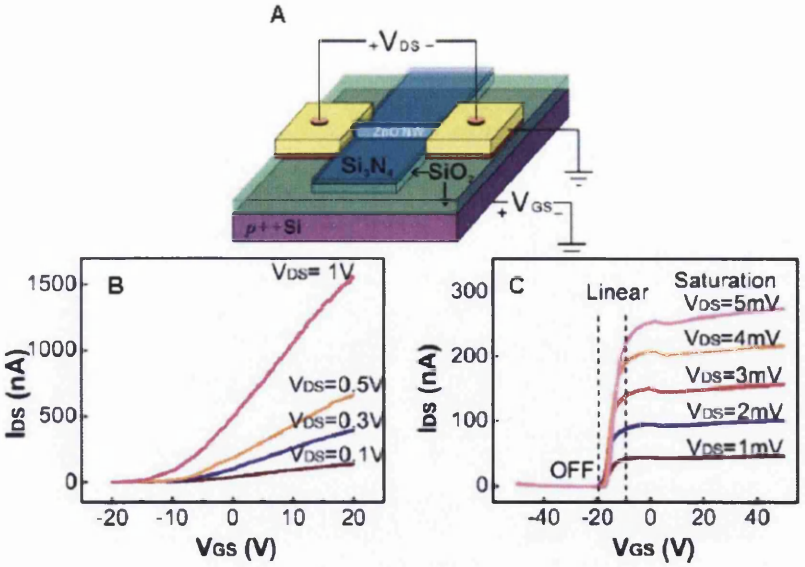

Figure 2.14 (A) Schematic of a ZnO nanowire FET with SiO_2/Si_3N_4 bilayer covering the nanowire channel. (B) The $I_{DS}V_{GS}$ curve of a ZnO nanowire FET without surface treatments. The results portray a typical n-type semiconducting characteristic. (C) The $I_{DS}V_{GS}$ curve of a ZnO nanowire FET with surface treatments showing significantly enhanced on/off ratio and transconductance [52].

2.3.3.4. Sensing properties

The basic principle of the sensing mechanism of a sensor (gas, chemical and biomolecules) depends on the detection of changes in electrical conductivity due to the interaction between the sensor surfaces with the molecules of interest [44]. In general, metal-oxide surfaces have oxygen vacancies that are electrically and chemically active. These vacancies function as n-type donors where adsorption of various molecules at the vacancy sites often changes the conductivity of the oxide. For example, adsorption of charge accepting molecules (e.g. NO_2 and O_2) at the vacancy sites leads to the depletion of electrons from the conduction band which results in the reduced electrical conductance of the n-type oxide. On the contrary, the adsorption of molecules such as CO and H_2 will remove surface adsorbed oxygen, resulting in the increase of the oxide conductivity [44]. Bulk and thin films of ZnO have been proposed as solid state gas sensor for CO [53], NH_3 [54], alcohol [55] and H_2 [56] sensing under elevated temperature (400°C). 1-D ZnO nanostructure based sensors are expected to be better than their film/bulk counterpart due to their high surface to volume ratio. The effect of oxygen adsorption on the electron transport of ZnO nanowire was investigated [57]. The FET device showed relatively good sensitivity to O_2 and this sensitivity was influenced by the diameter of the nanowire

as well as applied gate voltage. It was reported that the measured sensitivity was far better than the performance of the thin-film counterparts and also the metal oxide bulk material O_2 sensor at room temperature [57]. Unlike the SiNWs and CNTs counterparts, where their potential as a platform for the detection of biomolecules have been demonstrated [refer Section 2.2], work on exploiting 1-D ZnO nanostructure for biosensing is still relatively young. A paper on the fabrication of a ZnO nanorod based FET biosensor was reported by *JS Kim et. al* [58]. In this work, a ZnO nanorod was coated with biotin-PEG for the specific detection of streptavidin biomolecules. To reduce leakage current from the FET device, the source and drain contact electrodes are buried in 2μm copolymer/poly methyl methacrylate (PMMA) (Figure 2.15A). When the bare ZnO nanorod was functionalized with biotin, *JS Kim et. al* observed a small increase from 0.77 to 1.0 μS in conductance at source-drain voltage of 1V and gate voltage of 0 V (Figure 2.15B). Following the sequential addition of 0.025-, 0.25-, and 2.5-μM streptavidin, changes to the conductance of the device were observed. The detection limit of the ZnO nanorod FET device was down to 25 nM with conductance change as large as 1.8 μA, equivalent to an increase of 140% in conductance.

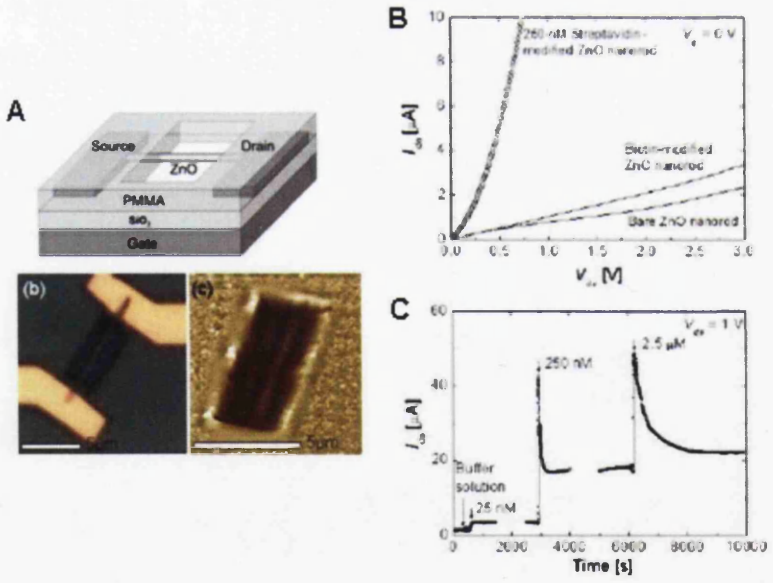

Figure 2.15 (A) Schematic illustration of a ZnO nanorod FET based biosensor. (B) source-drain current versus voltage of a bare, biotin-functionalised, and streptavidin-exposed ZnO nanorod FET. (B) Current monitored as a function of time for a biotin-modified ZnO nanorod FET device with the introduction of 0.025-, 0.25-, and 2.5-μM streptavidin respectively [58].

The potential application of ZnO 1-D nanostructures are varied due to their novel and unique properties. Other interesting properties which were not mentioned include their optical characteristics, magnetic doping, and polar surfaces [44]. As such, it will not be surprising if ZnO nanostructures become one of the most important nanomaterials in future research and applications.

2.3.4. Biodegradability and biosafety of ZnO nanostructures

In the quest to explore the potential of ZnO nanostructures as platforms for future in vivo electronic biosensing device, it is important to address their bio-safety and biocompatibility. Presently, ZnO nanoparticles are found to be nontoxic and biosafe, and have been used in various applications in our daily life, ranging from biomedical (drug carriers), cosmetics to industrial (dyes, plastics) applications. As a matter of fact, ZnO has been approved by the Food and Drug Administration (FDA) as sunscreen ingredients of the first category skin care products. Due to the silky and transparent appearance after being applied onto human skin, ZnO nanoparticles are also used in cosmetic products. Besides that, ZnO is also known to exhibit mild wound astringent, inflammation reduction/relief and anti-microbial functions. Therefore, it has been used as remedy for dermatitis and infection diseases, such as eczema, impetigo, ringworm, slack abscess, itch and psoriasis [59].

The first study on the biodegradability and biocompatibility of ZnO nanowire and nanobelts was performed by *ZL Wang et. al* [60]. Experiments were performed by etching and dissolving ZnO nanowires in various solutions with moderate pH values, including deionised water, ammonia, NaOH solution ((a) in Figure 2.16A), and pure horse blood serum ((b) in Figure 2.16A). The result showed that ZnO can be dissolved by deionized water (pH $\approx$ 4.5–5.0), ammonia (pH $\approx$ 8.7–9.0) and NaOH solution (pH $\approx$ 7.0–7.1) ((a), (b) and (c) respectively in Figure 2.16B). The study of the interaction of ZnO wires with pure horse blood serum (pH 8.5) showed that the ZnO wires can survive in the fluid for a few hours before they eventually degrade into mineral ions (Figure 2.16C).

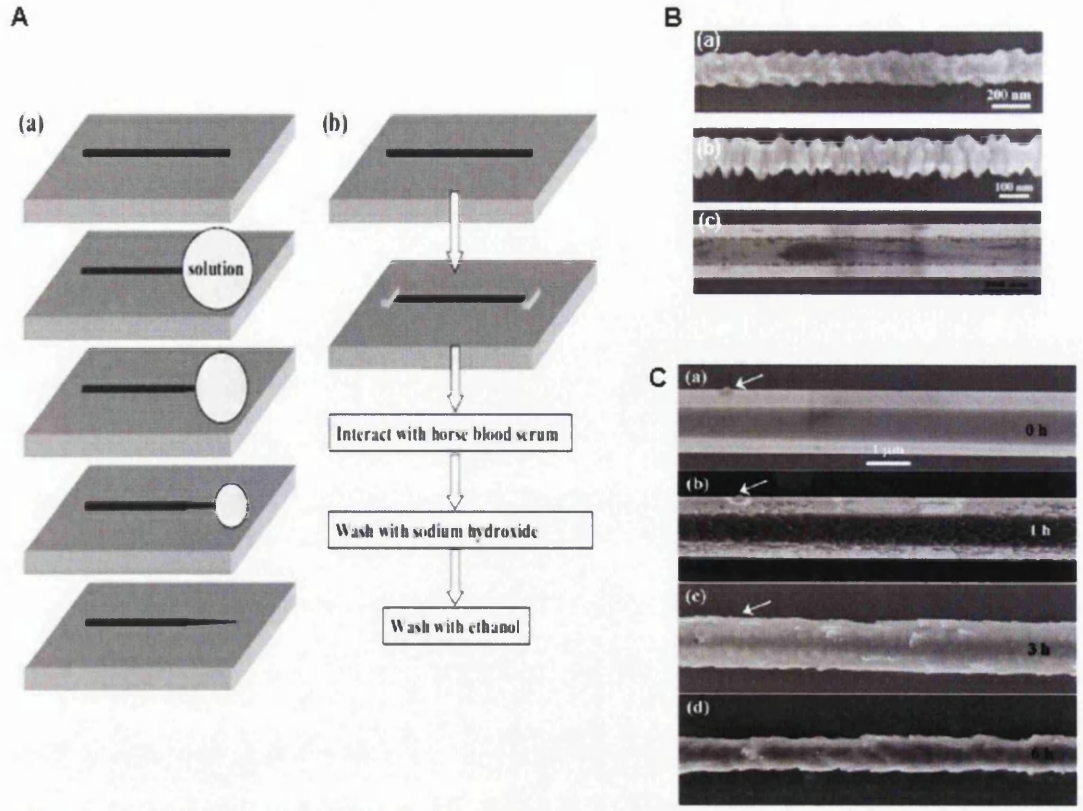

Figure 2.16 (A) The procedure for studying the interaction of ZnO wires for: (a) deionised water, ammonia, NaOH solution and (b) horse blood serum. (B) SEM images of ZnO wires after interactions with: (a) deionised water (pH 4.5-5.0), (b) ammonia (pH 8.7-9.0) and (c) NaOH solution (pH7.0-7.1). (C) SEM images of a ZnO wire that has interacted with pure horse blood serum (pH 8.5) after (a) 0 (b) 1 (c) 3 and (d) 6 hr [60].

ZL Wang et. al also performed the first cellular level study on the biocompatibility and biosafety of ZnO nanowires using Hela cells, a kind of epithelial cell. [61]. They observed that the presence of ZnO nanowires did not curb the growth and reproduction of Hela cells but were found to be degraded after a period of time (Figure 2.17(A)-(H)). *ZL Wang et. al* found that ZnO nanowires are biocompatible and biosafe for two different cell lines from different origins of tissues at normal concentration range (≤ 100 μg/ml).

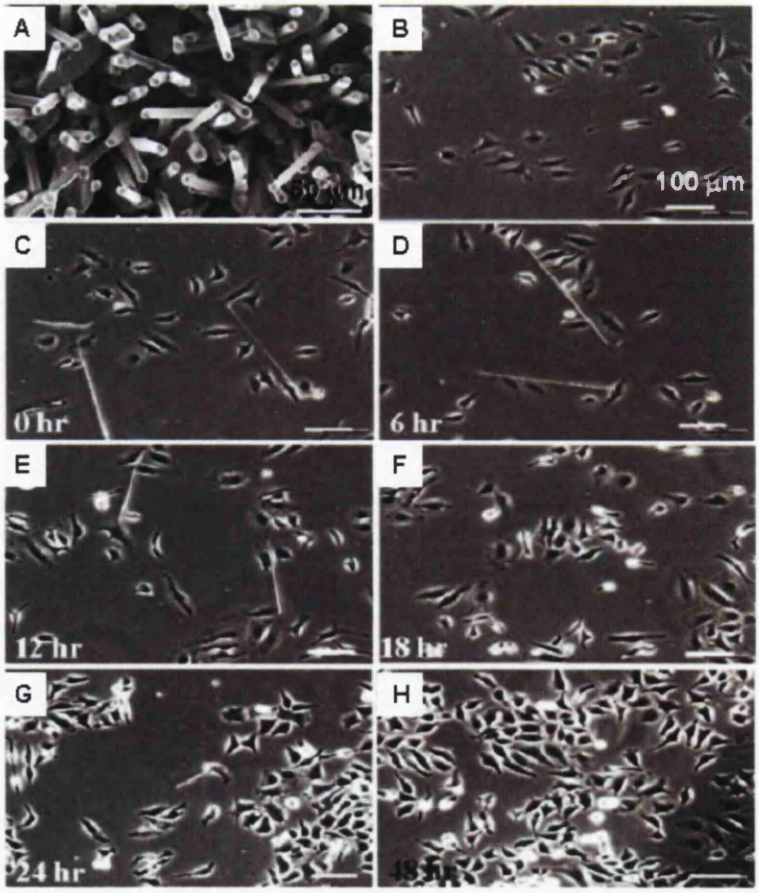

Figure 2.17 The effect of ZnO nanowires on the growth and reproduction of Hela cells monitored as a function of time. (A) As-grown ZnO nanowires on alumina substrate. (B) Hela cells, cultured for 4 hr. (C)-(H) Hela cells incubated with ZnO nanowires in solution at 0, 6, 12, 18, 24 and 48 hr respectively. The presence of ZnO nanowires did not affect the growth and reproduction of the Hela cells [61].

The demonstrated biodegradability, biosafety and biocompatibility of ZnO nanowires/nanorods and nanobelts show their potential use for in vivo biosensing and biodetection. These novel ZnO 1-D nanostructure sensors are implantable and will have a certain time to perform their functionality before being dissolved into ions that are then safely absorbed by the body.

2.4. Organic and inorganic functional moieties

The following are relevant to the functionalisation methodologies attempted and reported in Chapter 7.

2.4.1. Zinc fingers

Zinc finger proteins are any small, functional, independently folded domains that require coordination of one or more zinc ions to stabilize its structure. These fingers bind to a single zinc ion that is tetrahedrally coordinated between an α-sheet and two-stranded anti-parallel β-sheets (Figure 2.18) to form a compact ββα domain [62]. These extraordinary proteins have diverse functions which include DNA recognition, RNA packaging, transcriptional activation, regulation of apoptosis, lipid binding, protein folding and assembly. Therefore, it is not surprising that, they are among the most abundant proteins in eukaryotic genomes.

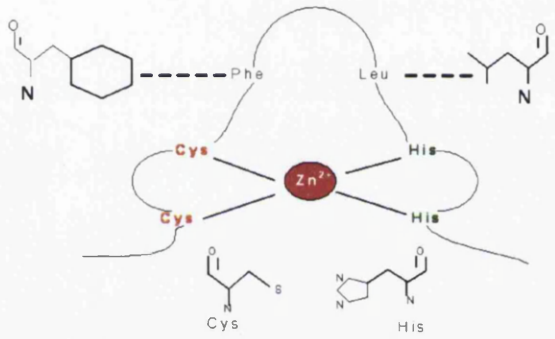

Figure 2.18 Zinc fingers interactions with zinc ions, Zn^{2+}.

2.4.1.1. The Oestrogen receptor (ERα)

In this study, Oestrogen receptor (ERα), a type of zinc finger protein from the nuclear hormone receptor family will be examined. ERα is classified as a class I members of the super-family of nuclear hormone receptors, defined as a ligand-inducible transcription factor. The ERα nuclear receptor has 6 functional domains as shown in Figure 2.19 and the functions of each domain are shown in Table 2.2. The C domain of the ERα receptor is the best characterized domain. The receptor binds as a homodimer (two receptors) to the Hormone Response Element (HRE) (specific sequences of DNA in nucleus). The residues located in the second zinc finger of the C domain are involved in the dimerisation of the receptor during HRE binding. It

was hoped that this C domain will interact with the zinc ions on the surface of ZnO nanostructures as part of the surface functionalisation strategy (see Chapter 7).

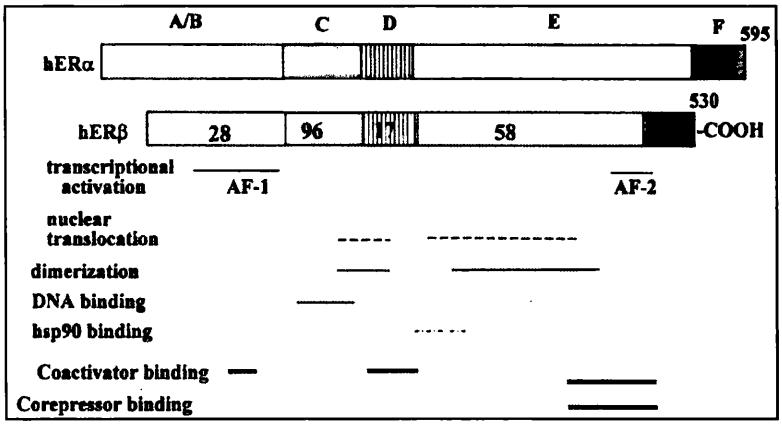

Figure 2.19 Schematic representation of the common structural and functional domains of ERα.

Domain	Functions
A/B	N'-terminal
C	Possesses 2 zinc fingers forming a helix-loop-helix motif and primarily functions in tightly binding the receptor to the DNA hormone element.
D	possesses signals for nuclear localization of the receptor
E	Ligand (hormones)-binding domain, confers ligand specificity to the receptor.
F	C'-terminal.

Table 2.2 Functions of the six domains in ERα.

2.4.2. Nitrilotriacetic acid (NTA)

Nitrilotriacetic acid (NTA), $C_6H_9NO_6$,, an aminotricarboxylic acid, is a well known chelating agent which binds to divalent metal ions such as Copper, Nickel, Magnesium and Zinc. The structure of NTA is shown in Figure 2.20. It is one of the most important complexones other than the ethylenediaminetetraacetic acid (EDTA), with over 100 publications dealing with its applications [63]. The applications of NTA and its metal complexes range from water and soil treatments, industrial applications (detergents, dyes, bleach) to biological and medical research [64]. This tetradentate chelating compound forms complexes with metal ions by forming bonds

with the oxygen from each ionized carboxylate group and the nitrogen atom. Its natural affinity towards zinc ions is examined as a functionalisation strategy on ZnO surfaces (refer Chapter 7).

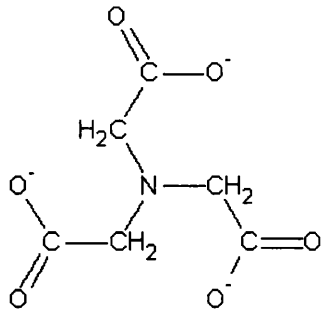

Figure 2.20 The chemical structure of the nitrilotriacetic acid (NTA). Di- or tri-valent metal ions bind to the compound via an oxygen atom from each carboxylated spacer arm and the nitrogen atom.

2.4.3. Beta-cyclodextrin (βCD)

Cyclodextrins, also known as cycloamyloses, cyclomaltoses and Schardinger dextrins, were first discovered by A.Villiers in 1891 [65,66]. They consists of a family of cyclic oligosaccharides, composed of six or more glucopyranose units linked by α-(1,4) bonds. They are produced as a result of intramolecular transglycosylation reaction from the degradation of starch by cyclodextrin glucanotransferase (CGTase) enzyme [67]. The three well known industrially produced major cyclic oligosaccharides are α–cyclodextrin, β–cyclodextrin and γ-cyclodextrin which have six, seven and eight glucopyranose respectively. Among these, β–cyclodextrin is generally the most useful in addition to being the most accessible and the lowest-priced. The unique structure of βCD is constituted by 6 glucopyranoside units, in a toroidal form with a larger and smaller opening at each end (Figure 2.21). The inner diameter is 0.62-0.78 nm, outer diameter is 1.53 nm, height is 0.79 nm and the cavity volume is 0.262 nm^3. X-ray crystallography reveals that the secondary hydroxyl groups (C_2 and C_3) in the cyclodextrins are located in the larger opening of the ring and the primary hydroxyl groups (C_6) are on the smaller opening, whereas the interior of the toroid comprise of apolar C_3 and C_5 hydrogen and ether-like oxygen [68]. This distinctive unique structural arrangement results in the amphipathic behaviour of βCD where the exterior of the toroidal molecule is

hydrophilic and its interior cavity is hydrophobic, described as a 'micro heterogeneous environment' [69].

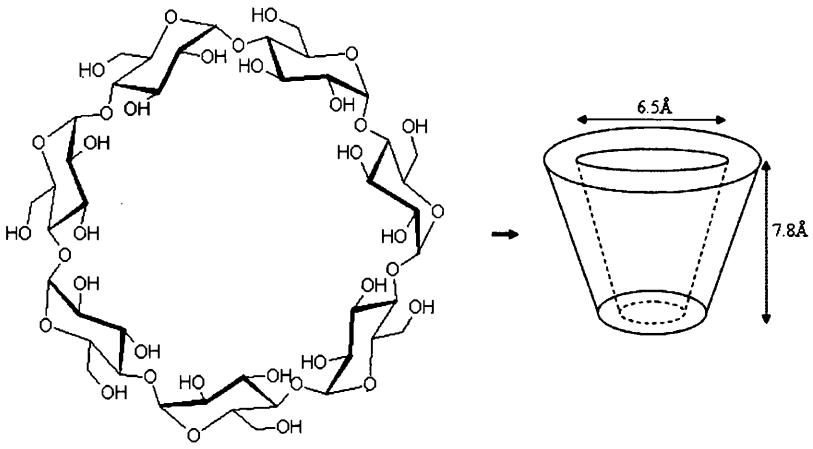

Figure 2.21 The structural representation of the Beta-cyclodextrin (βCD).

This notable feature of the cyclodextrins allows the formation of solid inclusion complexes (host–guest complexes) with a wide range of solid, liquid and gaseous compounds by a phenomenon of molecular complexation [70]. In other words, a guest molecule is allowed to 'dimensionally fit' within the cavity of the cyclodextrin host molecule [71] without breaking or forming any covalent bonds [72]. An appealing attribute of this host-guest complex is the beneficial modification to the physicochemical properties of the guest molecules [73]. Inclusion in cyclodextrins can enhance the solubility of highly insoluble guests, protect the guests from degradative effects (oxidation, heat, etc), modify taste by masking off flavours, physically isolate incompatible compounds and control the release of drugs. Therefore, the applications of βCD are wide, being used in the food [74], pharmaceuticals [75], cosmetics [76], environmental protection [77], bioconversion [78], packing and textile industry [79]. Besides that, the presence of multiple reactive hydroxyl groups on the primary and secondary groups on the cyclodextrins molecule enable chemical modification via various functional compounds substitution. As such, βCD can be modified with functional groups that have a molecular recognition feature, leading to their use as 'enzyme mimics' and for targeted drug delivery. These modified CDs were found to have improved enantio selectivity over native cyclodextrins [80].

2.4.4. Polyglutamic acid

2.4.4.1. Background

Polyamino acids are referred to polymers that are made up of numerous repeating units of amino acids. The repeating unit of amino acids can consist either of a single type of amino acid (homo polyamino acid) or of two or more different amino acids that repeat in random sequence. Polyglutamic acid (PGA) is an unusual anionic homo polyamino acid which contains only repeated glutamic acid units and is among the most extensively studied polyamino acids. The D- and L-glutamic acid units of the polymer are connected via amide linkages between α-amino and γ–carboxylic acid groups, as shown in Figure 2.22.

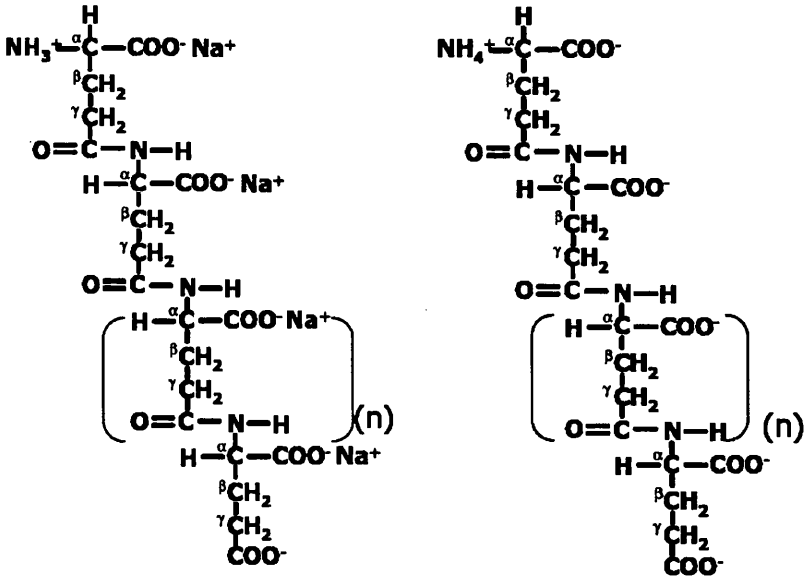

Figure 2.22 The structures of poly glutamic acid: Na salt form (left) and the acid form (right) [81].

PGA was first discovered as a capsule of *Bacillus anthracis* by Ivanovics and co-workers. It was isolated from the encapsulated *Bacillus anthracis* and released into the medium after autoclaving and autolysis of the cells [82]. This novel molecule was also known to be one of the components in the fermented soybeans mucilage (known as 'natto', a traditional food product in Japan), produced by the *Bacillus natto* [83]. In 1942, Bovarnick reported the freely discharge of γ-PGA into the growth medium from the outside of the cell walls of *Bacillus substilis* as the byproduct of fermentation. This led to the discovery of the production of γ-PGA

outside the cells by several other *Bacillus* species [84]. The PGA polyamino is a promising biopolymer known to be biodegradable, edible and nontoxic towards humans and the environment [85].

Each of the repeating unit of the naturally occurring L-glutamic acid comprises of a free γ-carboxyl group that is negatively charged at neutral pH, which explains its water solubility. The high proportion of this γ-carboxyl group was reported to provide functionality for novel binding properties for metal ions and also provide attachment points for the conjugation of certain molecules or substances (i.e. chemotherapeutic agents or drugs) via amide bonds. Therefore, potential applications of this unique biopolymer and their derivatives are varied in a broad range of industrial fields from food, cosmetics, medicine to water treatment [85]. In the following sections, the unique properties of the metal binding interactions and mechanism of PGA will be discussed. In addition, the applications of PGA in the environment, medicine, food and other areas will also be reviewed

2.4.4.2. Metal interactions and chelation mechanism

In general, PGA exists in three states: random coil, helix, and the helix coil transition region [86] and the conformational change between these states is mainly influenced by its pH environment. It was observed that with increasing pH at the midpoint of pH 5.5, PGA experiences transition in the α-helix state to the random coil structure [87]. This helix-coil transition is due to the deprotonation of the free carboxyl groups (COOH) on the biopolymer to COO^- as the pH environment changes [88]. Another factor that will cause significant changes in the helix-coil transitions is the binding interactions of PGA to metals. It was reported that for a homogeneous aqueous solution phase, the helical form of the biopolymer was found present at higher pH due to metal binding to the deprotonated carboxyl side chain (COO^-) [88].

It has been reported that PGA interacts with monovalent, divalent and trivalent metal ions in the aqueous phase. The specific metal-ligand interaction of this biopolymer has been investigated using NMR and polarography [89]. In each of these studies, it was found that the carboxylate side chain was responsible for the biopolymer main metal-binding functionality. As the isoelectric point (pK_a) of the carboxylate side

chain on PGA was found to be approximately 5.4, the maximum binding of PGA should occur at pH $\rangle\rangle$ pK_a when the side chain carboxylates are completely deprotonated and the chains are fully extended. Therefore, most metal-binding studies are performed at pH 7.0, which is significantly higher than the pKa value of the PGA carboxylate side chain. It was postulated that there are two possible mechanism of metal sorption onto polyelectrolytes, like the PGA. The first possibility is the direct interactions of metals with the free carboxylic sites and the second may be due to the electrostatic potential created by the COO^- groups which causes the retention of heavy metal counterions (in mobile form) [88]. Besides that, amide linkages of the biopolymer may also play a role by providing weak metal interaction sites. From NMR studies of the binding interactions of Cu^{2+} with PGA, in addition to the interactions with carboxylic groups, Cu^{2+} also formed short lived bonds with N of the amide linkages of the biopolymer. However, Mn^{2+} was discovered to only interact with the carboxylic acid groups [90].

An interesting property of the PGA was observed from its metal binding studies in a mixed metal solution [91]. It was shown that the total metal-binding capacity using the mixed metal solution was greater than the capacity for Cu^{2+} when run alone. It should be noted that Cu^{2+} exhibited the greatest individual capacity among the metals tested. Therefore, unlike nature's metal binding proteins or traditional metal chelators, such as EDTA or NTA, PGA does not have any fixed binding cavity. In fact, it was suggested that this homopolymer has the capability to adopt different tertiary structure in the presence of various metals. It was also suggested that different tertiary structure will be employed by the PGA, so that the formation of one metal-binding cavity may instill cooperative binding of another metal-binding cavity to maximize its total metal-binding capacity [91].

2.4.4.3. Applications

The potential applications of polyglutamic acid and its derivatives have been widely studied due to its multi-functionality, substantial biodegradability, edibility and non-toxicity towards human and environment. Due to its strong metal chelating capability, this novel extracellular polyamide is a potential biosorbent for the removal and recovery of heavy metals from industrial wastewater discharges [92]. PGA was

covalently incorporated into microfiltration membranes to produce extremely high heavy metal absorbing capacities [85]. It was reported that the PGA metal sorption mechanisms is different from conventional carboxylic ion-exchange resins, and thus has higher metal sorption capacities. This highly innovative and new approach to obtain high metal absorbing microfiltration membranes by using PGA was demonstrated to have a minimum of 380-fold volume reduction of lead in an aqueous waste [85].

As mentioned, polyglutamic acid is biocompatible, biodegradable, water soluble and non toxic. Its attribute of having multiple attachment sites for chemotherapeutic agent via its free carboxyl side chains render it a suitable drug delivery platform. Besides that, the biodegradability of the biopolymer allows the PGA-drug conjugate to enter the target sites and the drug will be released over time as the polymer degrades. Several drugs have been conjugated with PGA and their activity tested. One example is the Paclitaxel (Taxol, TXL), a chemotherapeutic agent against various human malignancies including breast and ovarian tumors [93, 94]. TXL was conjugated with PGA via covalent bonding to improve its solubility. It was reported that when high doses of PGA-TXL was administered, complete tumor regressions and cures were found in both ovarine and breast cancer animal models. In addition, it was found that the PGA modified TXL drugs has significantly better antitumor activity than pure TXL [95]. Other important anticancer agents are the Camptothecin (CPT) and its derivatives. The CPT solubility and biocompatibility were markedly improved when conjugated with PGA. In fact, enhanced anti-tumor activity of PGA-CPT in animal models of lung, colon and breast cancer, with up to 500% improvement over free drug was observed. Besides that, with the conjugated PGA, more drugs (up to 400%) could be administered without an increase in toxicity [96]. Other potential applications of PGA in medicine includes surgical adhesive and hemostatic agent that may replace blood-originated fibrin glue [97, 98].

In the food industry, PGA has been shown to be a bitterness-relieving agent, prevention of aging and the improvement of texture, ice-cream stabilizer and a thickener for fruit juice beverages [85]. This multifunctional biopolymer also has potential applications in cosmetics and skincare products [99].

2.4.5. The antibody molecule

Antibodies are gamma globulin proteins that are produced by B-lymphocytes (B-cells) cells of the immune system and can be found in blood or other bodily fluids of mammals. They form an important part of the body's natural defense system and help the body fight diseases by identifying and deactivating/removing foreign objects such as bacteria and viruses. In general, all antibodies have similar basic structural units consisting of four chains; two identical heavy chains (H) and two identical light chains (L) (Figure 2.23).

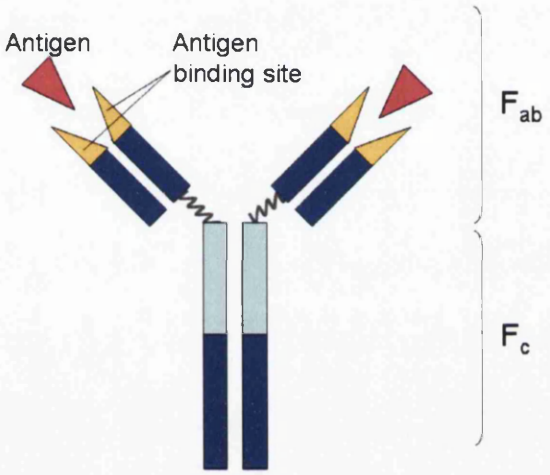

Figure 2.23 The schematic diagram of the basic antibody molecule.

All four chains (H and L) are held together by noncovalent interactions and disulfide bonds. The heavy chain varies between different classes and subclasses of antibody. There are 5 types of mammalian antibody heavy chains and each type defines the class of antibody with specialized roles in immunity. Each heavy chain has two regions, the *constant region*, which is the identical in all antibodies of the same class but is different for different classes, and the *variable region*, which is identical for antibodies produced from a single B cell but is different when produced by different B cells. There are two types of light chain in mammals and each light chain has two successive domains: a constant domain and a variable domain. Although these two types of light chain do not have different function, they serve to increase the diversity of immune recognition by antibodies. As shown in Figure 2.23, the Y shaped molecule can be categorized into two regions: F_{ab} (fragment, antigen binding) region and F_c (Fragment, crystallisable) region [100]. The F_{ab} is the important region of an

antibody that contains the antigen binding site. The F_{ab} regions consist of one constant and one variable domain from each of the heavy and light chain of the antibody [101]. The small region at the tip of the F_{ab}, known as the hypervariable region is responsible for the binding of different types of antigen. The F_c, the base of the Y shaped antibody is responsible for modulation of immune cell activity. It interacts with specific proteins and ensures that appropriate immune response for a given antigen is generated.

The interaction between antibody and antigen is very precise and involves non-covalent interactions such as ionic bonds, hydrogen bonds, van der Waal's forces and hydrophobic interactions [102]. The specific antibody-antigen interaction is analogous to the interaction between a lock and key, by which a specific geometrical configuration of a unique key enables it to open a lock [103]. By taking A as an antibody, B as the antigen and C as the complex of antibody and antigen, this reversible interaction can be represented equilibrium interactions:

$$A + B \Leftrightarrow C$$

Although a given type of B-cell can only produce one type of antibody, a human cells is made up of millions of different types of B-cells. As such, there are many different types of antibodies in a human body which can respond to the many thousands or even millions of different possible antigens that exist. The antigen-specific property of the antibodies is the key to their usefulness not only in the treatments of many types of disease but also in the diagnosis of different types of diseases. For diagnostic applications such as a biosensor, antibodies can be used as the bioreceptor for the detection of a specific antigen (i.e. tumour specific antigen).

2.4.5.1. Modification of an antibody

An important aspect in exploiting antibodies as the bioreceptor for the fabrication of a biosensor is the tethering or immobilisation of antibodies of interest to the transducer. One of the most commonly used methods for coupling antibodies to solid-phase affinity matrices or other appendages like biopolymers is via amine coupling. This is due to the abundance of surface exposed α- and ε-amino groups on a typical antibody molecule in its native state. These amino groups are in their un-protonated (non-ionised) form and are strong nucleophiles that react readily with

amine reactive reagents at near neutral pH, under mild, non-denaturing conditions. Random modifications of these amino groups are not likely to functionally inactivate more than a small fraction of the antibody as most of these modifiable amines are not near its antigen binding site [104].

2.5. Summary

This chapter has presented a brief review on the advances of SiNW and CNTs based FET biosensor and also their shortcomings as compared to ZnO nanomaterials. The biocompatibility and biodegradability of 1-D ZnO nanostructures, in addition to their novel properties render them a better alternative as a platform for biosensing devices. A comprehensive literature review related to 1-D ZnO nanostructures including the structure, common synthesis techniques, novel properties and potential applications was presented. Finally, the background into different types of organic molecules used in this research was discussed. Zinc fingers and NTA have naturally binding tendency toward divalent metal ion including zinc. The PGA is an interesting biopolymer with many useful potential applications. The abundance of carboxylate on the surface of this polymer was reported to be responsible for the chelation of various divalent metal ions. In addition, biomolecules such as antibodies can be conjugated to the PGA via the carboxylate group. The antibody molecule has many exposed α- and ε-amino groups allowing it to be attached to a solid surface or biopolymer via amine coupling. In general, such attachment is not likely to inactivate the antibody functionality.

2.6. References

[1] Collings A F and Caruso F 1997 Biosensor : recent advances *Rep. Prog. Phys.* **60** 1397

[2] (a) Lin N, Wang H, Dixit P, Xu T, Zhang S and Miaoa J 2009 Investigation of carbon nanotube growth on multi metal layers for advanced interconnect applications in microelectronic devices *J Electrochem Soc* **156** 3

(b) Collins P G, Arnold M S and Avouris P 2001 Engineering carbon nanotubes and nanotube circuits using electrical breakdown *Science* **292** 706.

(c) Lin Y, Taylor S, Li H, Fernando K A S, Qu L, Wang W et. al 2004 Advances toward bioapplications of carbon nanotubes *J. Mater. Chem.* **14** 527

[3] (a) Patolsky F, Zheng G and Lieber C M 2006 Nanowire sensors for medicine and life sciences Nanomedicine **1** 51

(b) Cui Y and Lieber C M 2001 Functional nanoscale electronic devices assembled using silicon nanowire building blocks *Science* **291** 851

[4] Dai Z R, Pan Z W and Wang Z L 2003 Novel nanostructures of functional oxides synthesized by thermal evaporation *Adv. Funct. Mater.* **13** 9

[5] Wang Z L 2009 ZnO nanowire and nanobelt platform for nanotechnology *Material Science and Engineering: R: Reports* **64** 33

[6] (a) Fritz J, Cooper E B, Gaudet S, Sorger P K and Manalis S R 2002 Electronic detection of DNA by its intrinsic molecular charge *Proc Natl Acad Sci USA* **99** 14142

(b) Zayats M, Raitman O A, Chegel V I, Kharitonov A B and Willner I 2002 Probing antigen-antibody binding processes by impedance measurements on ion-sensitive field-effect transistor devices and complementary surface plasmon resonance analyses: development of cholera toxin sensors *Anal Chem* **74** 4763

(c) Kharitonov A B, Zayats M, Lichtenstein A, Katz E and Willner I 2000 Enzyme monolayer-functionalized field-effect transistors for biosensor applications *Sens Actuat B Chem* **70** 222

(d) Pouthas F, Gentil C, Co^ te D and Bockelmann U 2004 DNA detection on transistor arrays following mutation-specific enzymatic amplification *Appl Phys Lett* **84** 1594

[7] Cui Y, Zhong Z, Wang D, Wang W U and Lieber C M 2003 High Performance Silicon Nanowire Field Effect Transistors *Nano Letters* **3** 149

[8] Patolsky F, Zheng G F, Hayden O, Lakadamyali M, Zhuang X W, Lieber C M 2004 Electrical detection of single viruses *Proc. Natl. Acad. Sci. USA* **101** 14017

[9] Cui Y, Wei Q, Park H and Lieber C M 2001 Nanowire nanosensors for highly sensitive and selective detection of biological and chemical species *Science* **293** 1289.

[10] Zheng G F, Patalsky F, Cui Y, Wang W U and Lieber C M 2005 Multiplexed electrical detection of cancer markers with nanowire sensor arrays *Nat. Biotechnol.* **23** 1294

[11] Gruner G 2006 Carbon nanotube transistors for biosensing applications *Anal. Bioanal chem.* **384** 322

[12](a) Cui D 2007 Advances and prospects on biomolecules functionalized carbon nanotubes. *J. Nanosci. Nanotechnol.* **7** 1298

(b) Pan B, Cui D, He R, Gao F and Zhang Y 2006 Covalent attachment of quantum dot on carbon nanotubes *Chem. Phys. Lett.* **417** 419

(c) Cui D, Tian F, Kong Y, Titushikin I and Gao H 2004 Effects of single-walled carbon nanotubes on the polymerase chain reaction *Nanotechnology* **15** 154

[13] Kong J, Franklin N R, Zhou C, Chapline M G, Peng S, Cho K and Dail H 2000 Nanotube molecular wires as chemical sensors *Science* **287** 622

[14] Collins P G, Bradley K, Ishigami and Zettl A 2000 Extreme Oxygen sensitivity of electronic properties of carbon nanotubes *Science* **287** 1801

[15] Besteman K, Lee J, Wiertz F G, Heering H A and Dekker C 2003 Enzyme-coated carbon nanotubes as single-molecule *Nano Letters* **3** 727

[16] Chen R J, Zhang Y, Wang D, and Dai H 2001 Noncovalent sidewall funtionalization of single-walled carbon nanotubes for protein immobilization *J. Am. Chem. Soc.* **123** 3838

[17] Star A, Stoddart J F, Steuerman D, Diehl M, Boukai A, Wong E W, Yang X, Chung S W, Choi H and Heath J R 2001 Preparation and properties of polymer wrapped single-walled carbon nanotubes *Angew. Chem. Int. Ed.* **40** 9

[18] Chen R J, Bangsaruntip S, Drouvalakis K A et. al 2003 Noncovalent functionalization of carbon nanotubes for highly specific electronic biosensors *Proc. Natl. Acad. Sci. USA* **100** 4984

[19] Star A, Christophe J, Bradley K and Grulner G 2003 Electronic detection of specific protein binding using nanotube FET devices *Nano Letters* **3** 459

[20] NCI Alliance for Nanotechnology in Cancer monthly report. January/ February 2006.

[21] Service R F 2004 Nanotechnology grows up *Science* **304** 1732

[22] Ostuni E, Chapman R G et. al 2001 Self-assembled monolayers that resist the adsorption of protein and the adhesion of bacterial and mammalian cells *Langmuir* **17** 6336

[23](a) Oberdorster G, Maynard A, Donaldson K, Castranova , Fitzpatrick J, Ausman K et. al. 2005 Principles for characterizing the potential human health effects from exposure to nanomaterials: Elements of a screening strategy *Part. Fibre Toxicol.* **2 8**

(b) Bottini M, Bruckner S, Nika K, Bottini N, Bellucci S, Magrini A, Bergamaschi A and Mustelin T 2006 Multi-walled carbon nanotubes induce T lymphocyte apoptosis *Toxicol. Lett.* **160** 121

(c) Donaldson K, Aitken R, Tran L, Stone V, Duffin R, Forrest G, and Alexander A 2006 Carbon Nanotubes: A Review of Their Properties in Relation to Pulmonary Toxicology and Workplace Safety *Toxicological Sci.* **92** 5–22

[24] Wang A, Liang X, McAllister J P, Li J, Brabant K, Black C, Finlayson P et. al 2007 Stability of and inflammatory response to silicon coated with a fluoroalkyl self-assembled monolayer in the central nervous system *J. Biomed. Mater. Res.* Part A **81** 363

[25] Trojanowicz M 2006 Analytical applications of carbon nanotubes: a review *TrAC* **25** 480

[26] Landolt-Bornstein, New Series, Group III, **17** B, 22, 41B (Ed.: U. Rossler), Springer, Heidelberg, 1999.

[27] Emanetoglu N W, Gorla C, Liu Y, Liang S and Lu Y 1999 *Mater. Sci. Semicond. Process* **2** 247

[28] Chen Y, Bagnall D and Yao T 2000 ZnO as a novel photonic material for UV region *Mater. Sci. Eng. B* **75** 190

[29] Wang Z L 2004 Nanostructures of Zinc Oxide *Materials Today* 7 26

[30](a) Huang M, Mao S, Feick H, Yan H, Wu Y, Kind H,Weber E, Russo R and Yang P Room-temperature ultraviolet nanowire nanolasers 2001 Science 292 1897

(b) Johnson J, Yan H, Schaller R, Haber L, Saykally R and Yang P 2001 Single nanowire lasers *J. Phys. Chem. B* **105** 11387

(c) Sun X W, Yu S F, Xu C X, Yuen C, Chen B J and Li S 2003 Room temperature ultraviolet lasing from zinc oxide microtubes *Japan. J. Appl. Phys.* **42** L1229

(d) Kind H, Yan H, Messer B, Law M and Yang P 2002 Nanowire ultraviolet photodetectors and optical switches *Adv. Mater.* **14** 158

(e) Arnold M S, Avouris P, Pan Z W and Wang Z L 2003 Field-effect transistors based on single semiconducting oxide nanobelts *J. Phys. Chem. B* **107** 659

(f) Lee C J, Lee T J, Lyu S C, Zhang Y, Ruh H and Lee H J 2002 Field emission from well-aligned zinc oxide nanowires grown at low temperature *Appl. Phys. Lett.* **81** 3648

(g) Zhu Y W, Zhang H Z, Sun X C, Feng S Q, Xu J, Zhou Q, Xiang B, Wang R M and Yu D P 2003 Efficient field emission from ZnO nanoneedle arrays *Appl. Phys. Lett.* **83** 144

(h) Xu C X and Sun X W 2003 Field emission from zinc oxide nanopins *Appl. Phys. Lett.* **83** 3806

(i) Xu C X, Sun X W, Chen B J, Shum P, Li S and Hu X 2004 Nanostructural zinc oxide and its electrical and optical properties *J. Appl. Phys.* **95** 661

(j) Xu C X, Sun X W and Chen B J 2004 Field emission from gallium-doped zinc oxide nanofiber array *Appl. Phys. Lett.* **84** 1540

(k) Yang P, Yan H, Mao S, Russo R, Johnson J, Saykally R, Morris N, Pham J, He R and Choi H J 2002 Controlled growth of ZnO nanowires and their optical properties *Adv. Funct. Mater.* **12** 323

(l) Pan Z W, Dai Z R and Wang Z L 2001 Nanobelts of semiconducting oxides *Science* **291** 1947

(m) Lyu S C, Zhang Y, Lee C J, Ruh H and Lee H J 2003 Low-temperature growth of ZnO nanowire array by a simple physical vapor-deposition method *Chem. Mater.* **15** 3294

[31] Dai Z R, Pan Z W and Wang Z L 2003 Novel nanostructures of functional oxides synthesized by thermal evaporation *Adv. Func Mater.* **13** 9

[32] Choy J H, Jang E S, Won J H, Chung J H, Jang D J and Kim Y W 2004 Hydrothermal route to ZnO nanocoral reefs and nanofibers *Appl. Phys. Lett.* **84** 287

[33] Li Z Q, Xiong Y J and Xie Y 2003 Selected-control synthesis of ZnO nanowires and nanorods via a PEG-assisted route *Inorg. Chem.* **42** 8105

[34] Wang J M and Gao L 2003 Wet chemical synthesis of ultralong and straight single-crystalline ZnO nanowires and their excellent UV emission properties *J. Mater. Chem.* **13** 2551

[35] Liu B and Zeng H C 2003 Hydrothermal synthesis of ZnO nanorods in the diameter regime of 50 nm *J. Am. Chem. Soc.* **125** 4430

[36] Vayssieres L, Keis K and Lindquist S E 2001 Purpose-built anisotropic metal oxide material: 3D highly oriented microrod array of ZnO *J. Phys. Chem. B* **105** 3350

[37] Schmidt-Mende L and MacManus-Driscoll J L 2007 ZnO–nanostructures, defects, and devices *Mater. Today* **10** 40

[38] J. Jagadish and S.J. Pearton (Eds.) 2006 *Zinc Oxide Bulk, Thin Film and Nanostructures* Elsevier

[39] Pearton S J, Norton D P, Ip K, Heo Y W and Steiner T 2005 Recent progress in processing and properties of ZnO *Prog. Mater. Sci.* **50** 293.

[40] Wang X, Ding Y, Summers C J and Wang Z L 2004 Large-scale synthesis of six-nanometer-wide ZnO nanobelts *J. Phys. Chem. B* **108** 8773.

[41] Chiou J W, Krishna Kumar K P, Jan J C, Tsai H M, Bao C W, Pong W F, Chien F Z, Tsai M H et. al 2004 Diameter dependence of the electronic structure of ZnO nanorods determined by x-ray absorption spectroscopy and scanning photoelectron microscopy *Appl. Phys. Lett.* **85** 3220.

[42] Bai X D, Wang E G, Gao P X and Wang Z L 2003 Dual-mode mechanical resonance of individual ZnO nanobelts *Appl. Phys. Lett.* **82** 4806

[43] Meirovich L 1986 *Elements of Vibration Analysis* 2nd edn (New York: McGraw-Hill)

[44] Wang Z L 2004 ZnO nanostructures: growth, properties and applications *J. Phys: Condens. Matter* **16** 829

[45] Hughes W and Wang Z L 2003 Nanobelts as nanocantilevers *Appl. Phys. Lett.* **82** 2886

[46](a) Catti M, Noel Y, and Dovesi R, 2003 Full piezoelectric tensors of wurtzite and zinc blende ZnO and ZnS by first-principles calculations *J. Phys. Chem. Solids* **64** 2183.

(c) Gardeniers J G E, Rittersma Z M, and Burger G J 1998 Preferred orientation and piezoelectricity in sputtered ZnO films *J. Appl. Phys.* **83** 7844.

(e) Wuethrich C R, Muller C A P, Fox G R, and Limberger H G 1998 All-fibre acousto-optic modulator using ZnO piezoelectric actuators *Sensor Actuat. A* **66** 114.

[47] Zhao M H, Wang Z L and Mao S X 2004 Piezoelectric characterization of individual Zinc Oxide nanobelt probed by piezoresponse force microscope *Nano Lett.* **4** 587

[48] Fan Z and Lu J G 2005 Zinc oxide nanostructures: synthesis and properties *J Nanosci. Nanotechnol.* **5** 1561

[49] Arnold M S, Avouris P, Pan Z W and Wang Z L 2003 Field-effect transistors based on single semiconducting oxide nanobelts *J. Phys. Chem. B* **107** 659

[50] Park W I, Kim J S, Yi G C, Bae M H and Lee H J 2004 Fabrication and electrical characteristics of high-performance ZnO nanorod field-effect transistors *Appl. Phys. Lett.* **85** 5052.

[51] Kim S Y, Jang H W, Kim J K, Jeon C M, Park W I, Yi G C and Lee J L 2002 Low-resistance Ti/Al ohmic contact on undoped ZnO *J. Electron. Mater.* **31** 868

[52] Chang P, Fan Z, Chien C, Stichtenoth D, Ronning C and Lu J G High-performance ZnO nanowire field effect transistors *Appl. Phys. Lett.* **89** 13

[53] Ryu H W, Park B S, Akbar S A, Lee W S, Hong K J, Seo Y J, Shin D C, Park J S and Choi G P 2003 ZnO sol-gel derived porous film for CO gas sensing *Sens. Actuator B* **96** 717

[54] G. Sberveglieri 1995 Recent developments in semiconducting thin-film gas sensors *Sens. Actuator B* 23, 103

[55] G. S. Trivikrama Rao, D. Tarakarama Rao 1999 Gas sensitivity of ZnO based thick sensor to NH_3 at room temperature *Sens. Actuator B* **55** 166

[56] X. L. Cheng, H. Zhao, L. H. Huo, S. Gao and J. G. Zhao 2004 ZnO nanoparticulate thin film: preparation, characterization and gas-sensing property *Sens. Actuator B* **102** 248

[57] Z. Fan, D. Wang, P. Chang, W. Tseng, J. G. Lu, ZnO nanowire field Effect transistor and oxygen sensing Property *Appl. Phys. Lett.* **85** 5923

[58] Kim J S, Park W I, Lee C and Yi G 2006 ZnO Nanorod Biosensor for Highly Sensitive Detection of Specific Protein Binding *Journal of the Korean Physical Society* **49** 1635

[59] http://www.fda.gov/default.htm

[60] Zhou J, Xu N S, Wang Z L 2006 Dissolving behavior and stability of ZnOWires in biofluids: A study on biodegradability and biocompatibility of ZnO nanostructures *Adv. Mater.* **18** 2432

[61] Li Z, Yang R S, Yu M, Bai F, Li C, Wang Z L 2009 Cellular Level Biocompatibility and Biosafety of ZnO Nanowires *J. Phys. Chem. C.* **112** 20114.

[62] Wolfe S A, Nekludova L and Pabo C O 1999 DNA Recognition by Cys2His2 Zinc Finger Proteins *Annu. Rev. Biophys. Biomol. Struc.* **3** 183

[63] Souaya E R, Hanna W G, Ismail E H and Milad N E 2000 Studies on some acid divalent metal nitrilotriacetate complexes *Molecules* **5** 1121

[64] Nitrilotriacetic Acid (NTA) 1990 Health Canada water quality report http://www.hc-sc.gc.ca/index-eng.php

[65] Villiers A 1891 Compt Rendu **112** 536.

[66] Eastburn S D and Tao B Y 1994 Applications of modified cyclodextrins *Biotechnol. Adv.* **12** 325

[67] Szetjli J 1998 Introduction and general overview of cyclodextrin chemistry *Chem Rev* **98** 1743

[68] Del Valle E M M 2004 Cyclodextrins and their uses: a review Process Biochemistry Volume **393** 1033

[69] Szetjli J 1989 Downstream processing using cyclodextrins *TIBTRCH* 7 171

[70] Eastburn S D and Tao B Y 1994 Applications of modified cyclodextrins *Biotechnol. Adv.* **12** 325

[71] Mun˜oz-Botella S, del Castillo B and Martı´n M A 1995 Cyclodetrin properties and applications of inclusion complex formation *Ars Pharm* **36** 187

[72] Schneiderman E and Stalcup A M 2000 Cyclodextrins: a versatile tool in separation science *J Chromatogr. B* **745** 83

[73] Schmid G 1989 Cyclodextrin glucanotransferse production: yield enhancement by overexpression of cloned genes *Trends. Biotechnol.* 7 244

[74] Fujishima N, Kusaka K, Umino T, Urushinata T and Terumi K 2001 Flour based foods containing highly branched cyclodextrins *Japanese Patent JP* **136** 898

[75] Bhardwaj R, Dorr R T, Blanchard J 2000 Approaches to reducing toxicity of parenteral anticancer drug formulations using cyclodextrins *J Pharm. Sci. Technol.* **54** 233

[76] Holland L, Rizzi G and Malton P 1999 Cosmetic compositions comprising cyclic oligosaccharides and fragrance *PCT Int Appl WO* **67** 716

[77] Lezcano M, Ai-Soufi W, Novo M, Rodriguez-Nunez E and Tato J V 2001 Complexation of several benzimidazole-type fungicides with alpha and beta-cyclodextrins *J Agric Food Chem* **50** 108

[78] Dufosse L, Souchon I, Feron G, Latrasse A and Spinnler H E 1999 In situ detoxification of the fermentation medium during gammadecalactone production with the yeast Sporidiobolus salmonicolor *Biotechnol Prog* **15** 135

[79] Hedges R A 1998 Industrial applications of cyclodextrins *Chem Rev* **98** 2035

[80] Eastburn S D and Tao B Y 1994 Applications of modified cyclodextrins *Biotechnol. Adv.* **12** 325

[81] Sung M , Park C, Kim C J, Poo H, Soda K and Ashiuchi M 2005 Natural and edible biopolymer poly-glutamic acid: synthesis, production, and applications *The Chemical Record* **5** 352

[82] Ivanovics G and Bruckner V 1937 *Immunitatsforsch* **90** 304

[83] Sawamura S 1913 On *Bacillus natto J. Coll. Agric Tokyo* **5** 189

[84](a) Ashiuchi M, Kamei T, Back D H, Shin S Y, Sung M H, Soda K, Yagi T and Misono H 2001 Isolation of Bacillus subtilis (chungkookjang), a poly-gamma-glutamate producer with high genetic competence *Appl. Microbiol. Biotechonl.* **57** 764

(b) Cheng C, Asada Y and Aaida T 1989 Production of γ-polyglutamic acid by Bacillus licheniformis A35 under denitrifying conditions *Agric. Biol. Chem.* **53** 2369

[85] Shih I L and Van Y T 2001 The production of poly-(γ-glutamic acid) from microorganisms and its various applications *Bioresour. Technol.* **79** 207

[86](a) Holtzer A and Hawkins R B 1996 The state of aggregation of α-helical poly(L-glutamic acid) in aqueous salt solutions, *J. Am. Chem. Soc.* **118** 4220.

(b) Kono N and Ikegami A 1966 Potentiometric titration of poly(L-glutamic acid) in aqueous solutions and binding of divalent cations *Biopolymers* **4** 823

[87] Tsutsumi A, Perly B, Forchioni A and Chachaty C 1978 A magnetic resonance study of the segmental motion and local conformations of Poly(L-glutamic acid) in aqueous solutions macromolecules **11** 977

[88] Bhattacharyya D, Hestekin J A, Brushaber P, Cullen L, Bachas L G and Sikdar S K 1998 Novel poly-glutamic acid functionalized microfiltration membranes for sorption of heavy metals at high capacity *J. Membrane Sci.* **141** 121

[89] Hikichi K, Tanaka H and Konno A 1990 Nuclear Magnetic Resonance Study of Poly(γ-glutamic acid)—Cu(II) and Mn(II) Complexes *Polym. J.* **22** 103.

[90] Snipp R L, Miller W G and Nylund R E 1965 The Charge-Induced Helix-Random Coil Transition in Aqueous Solution1 *J. Am. Chem. Soc.* **87** 3547

[91] Malachowski L and Holcombe J A 2004 Comparison of immobilised poly-l-aspartic acid and poly-l-glutamic acid for chelation of metal cations Analytica Chimica Acta **517** 187

[92] Mark S S, Crusberg T C, DaCunha C M and Di Iorio A A 2006 A heavy metal biotrap for wastewater remediation using poly-γ-glutamic acid *Biotechnol. Prog.* **22** 523

[93] Holmes F A, Kudelka A P, Kavanagn J J, Huber M H, Ajani J A and Valero V 1995 *In Taxane Anticancer Agents: Basic Science and Current Status* ed Georg G I, Chen T T, Ojima I and Vyas D M (American Chemical Society Washington DC) p 31-57

[94] Rowinsky K E and Donehower R C 1995 Paclitaxel (Taxol) *N. Engl. J. Med.* **332** 1004

[95] Li C, Yu D F, Newman A, Cabral F, Stephens C, Hunter N, Milas L and Wallace S 1998 Complete regression of well-established tumors using a novel water soluble poly(L-glutamic acid)-paclitaxel conjugate *Cancer Res.* **58** 2404

[96] Singer J W, De Vries P, Bhatt R, Tulinsky J, Klein P, Li C, Milas L, Lewis R A and Wallace S 2000 Conjugation of camptothecins to poly(L-glutamic acid) *Ann. NY Acad. Sci. **922*** 136

[97] Otani Y, Tabata Y, Iada Y 1996 rapidly curable biological glue composed of gelatin and poly(L-glutamic acid) *Biomaterials* **17** 1387

[98] Otani Y, Tabata Y, Ikada Y 1998 Hemostatic capability of rapidly curable from gelatin, poly(L-glutamic acid), and carbodiimide *Biomaterials* **19** 2091

[99] Ben-Zur N and Goldman D M 2007 γ-Poly glutamic acid: A novel peptide for skin care *Cosmetics and toiletries* **122** 65

[100] Janeway C A et. al. 2001 *Immunobiology* 5th ed (Garland Publishing) ISBN 0-8153-3642-X.

[101] Putnam F W, Liu Y S and Low T L 1979 Primary structure of a human IgA1 immunoglobulin. IV. Streptococcal IgA1 protease, digestion, Fab and Fc fragments, and the complete amino acid sequence of the alpha 1 heavy chain *J Biol Chem* **254** 2865

[102] Berzofsky J A, Berkower I J and Epstein S L 1993 *Antigen-antibody interactions and monoclonal antibodies, in Fundamental immunology* ed Paul W E (Raven New york) 421-425

[103] Vo-Dinh T and Cullum B 2000 Biosensors and biochips: advances in biological and medical diagnostics *Fresenius J Anal Chem* **366** 540

[104] Hahn K O 2006 *Making and Using Antibodies: A Practical Handbook* ed: Howard G C and Kaser M R (Plastic Comb Publisher: CRC Press) edition: 1

Chapter 3

Scanning Probe Microscopy Technique

3.1. Introduction

Scanning probe microscopy (SPM) techniques are the basic instrumentation to image and detect various physical properties (electrical, mechanical, electromagnetic, thermal, etc) of samples at the nanoscale. All SPM techniques share the same concept of which nanometric or atomic resolution image of a surface is obtained by three dimensional scanning of a sharp nanoprobe (3-50 nm radius of curvature) across the sample surface. The nanoprobe is usually mounted on a flexible probe, enabling the nanoprobe to follow the surface profile. Although most SPM systems share similar features, they differ in signal detection mechanism. Among the most powerful and versatile SPM technique available today is the atomic force microscope (AFM). Its probe consists of a nano-sized tip, mounted on a flexible cantilever, enabling the tip to follow the surface profile. The AFM exploits the interatomic forces that exist between the tip and sample, for three-dimensional, real-time imaging of almost any sample at the nanoscale (conductor, semiconductor and insulators). Depending on the tip-sample distance, different types of interatomic forces will dominate. The electrostatic force microscopy (EFM) technique is an extension of the AFM technique that detects the long-range electrostatic forces between a conducting tip and sample. Understanding the electrostatic interaction present in a nanosystem will give a powerful insight into the mechanism controlling the electronic properties [1]. The ability of the EFM technique to discriminate the conductivity of samples from the measured phase shift has led others to refer it as the scanning conductance microscope (SCM). The rest of the work will use scanning conductance microscope (SCM) to describe this technique. In this chapter, the principle of AFM and the basic concepts of tapping mode AFM are briefly addressed. The principle of SCM, a secondary imaging mode of tapping mode AFM is then described, and details of signal detection and instrumentation for SCM are given. Lastly, to aid the understanding and interpretation of the SCM results, a literature review of other's work using this technique is presented.

3.2. Principles of tip-sample interactions

Atomic force microscopy is based on the detection of forces, up to fractions of attoneewtons (1 aN = 10^{-18} N) exerted between a sharp tip, mounted on a flexible cantilever and a sample surface [2]. These forces are highly dependent on the tip-sample separations and are measured through the deflection of the cantilever. At small tip-sample separation, short range repulsive forces are dominant and at increased tip-sample separation, long-range attractive forces will dominate.

3.2.1. Short-range interactions

Interatomic forces consists of short-range ($\leq$ 0.1 nm) Born repulsive force component and long-range (up to 10-15 nm) van der Waals (vdW) force component [3]. When the tip is placed within a few nm from the sample, vdW forces (attractive or repulsive force) are sufficiently strong to produce detectable deflection of the AFM cantilever. The vdW potential and interaction forces are dictated by the material properties and consist of three components, namely; permanent dipole–permanent dipole forces, permanent dipole–induced dipole forces and instantaneous induced dipole-induced dipole (London dispersion force). For two interacting molecules, such as two identical gas molecules, the vdW potential is given by [3]:

$$U_{vdW} = -\frac{C_1}{z^6} \qquad \textbf{Equation 3.1}$$

where the constant C_1 is known as the London coefficient, and z is the distance between the molecules. When the tip is brought nearer to the sample, the wavefunction of electrons located at the end of the tip overlaps with the wavefunction of electrons located on the surface sample. Consequently, strong repulsive Born forces are produced, which is expressed as [3]:

$$U_{Born} = -\frac{C_2}{z^{12}} \qquad \textbf{Equation 3.2}$$

where C_1 is another constant. The total intermolecular potential is then given by [3]:

$$U_T = \frac{C_2}{z^{12}} - \frac{C_1}{z^6} \qquad \textbf{Equation 3.3}$$

which is known as the Lenard-Jones potential. The sum of all repulsive and attractive potentials experienced during tip-sample interactions determines the force detected by

the AFM. The attractive vdW potential experienced between two macroscopic entities, such as two spheres of radius R, is expressed as [3]:

$$U_{vdW} = -\frac{AR}{6z} \qquad \textbf{Equation 3.4}$$

And the vdW force is given by [3]:

$$F_{vdW} = -\frac{dU_{vdW}}{dz} = -\frac{AR}{6z^2} \qquad \textbf{Equation 3.5}$$

where $A \propto \pi^2 C_1 \rho_1 \rho_2$ is the Hamaker constant and ρ_1 and ρ_2 are the densities of the two entities. The relationships relating the potential, force and force gradient are summarised in Table 3.1.

		For a Spring	For a sphere-plane, z << R
Potential	U	$= \frac{1}{2}kz^2$	$\propto \frac{1}{z}$
Force	$-\frac{dU}{dz}$	$= -kz$	$\propto -\frac{1}{z^2}$
Force Gradient	$-\frac{d^2U}{dz^2}$	$= -k$	$\propto -\frac{1}{z^3}$

Table 3.1 Relationship between potential, force and force gradient.

The Lennard-Jones potential diagram, shown on Figure 3.1, illustrates the modes of operations of the AFM as a function of tip-sample separation. The three main AFM modes of operations are the contact, tapping (intermittent contact) and the non-contact modes.

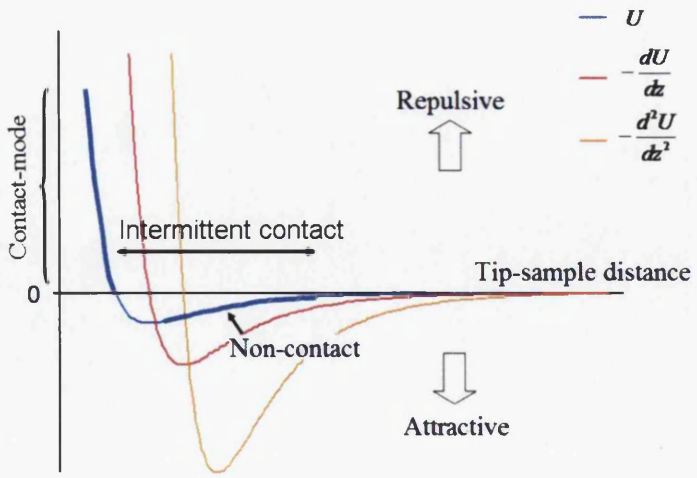

Figure 3.1 The Lennard-Jones potential diagram and the AFM modes of operation as a function of the tip-sample separation.

3.2.2. Long-range interactions

Long-range interactions include electrostatic, magnetic, and electromagnetic, or capillarity caused by surface energy of water condensed between the tip and sample. The contributions of the long-range forces are negligible at small tip-sample separations. These forces become more prominent as the tip-sample separation increases. The difference in decay length of short- and long-range forces is used to distinguish between the two types of interaction. For the detection of electrostatic or magnetic interactions, specialised conducting or magnetic AFM tips are required. These respective modes of imaging are known as the electrostatic force microscopy (EFM), also known as the scanning conductance microscopy (SCM) technique and magnetic force microscopy (MFM) technique. The simplified expression in relation to the force experienced by a tip above a homogeneous surface for electrostatic interactions is given by:

$$F_{electrostatic} = -\frac{1}{2}(\Delta V)^2 \frac{\partial C}{\partial z} \qquad \textbf{Equation 3. 6}$$

where the difference in potential between the sample and tip is given by ΔV and the tip-sample capacitance is denoted by C as a function of tip-sample separation z.
And the magnetic interaction is given by:

$$F_{magnetostatic} = \nabla(M \bullet B_{sample}) \qquad \textbf{Equation 3.7}$$

where the magnetic field emanating from the sample surface is B_{sample} and the magnetic dipole of the tip is given by M.

In this section, the principle of atomic forces in relation to the AFM tip-sample separation was discussed. In the following section, a brief overview of the AFM and the basic concept of the tapping mode AFM, which is used for imaging in this work, will be described.

3.3. Principles of atomic force microscope (AFM)

As SCM is an extension of the AFM, it is important to understand the basic operation of an AFM. The AFM probe is made up of a sharp tip, typically less than 5 μm tall and often less than 10 nm in diameter at the apex. The sharp tip is mounted at the free end of a flexible cantilever that is usually about 100-500 μm in length. The

interaction forces between the tip and a sample are monitored through the deflection of the cantilever. The amount of deflection is influenced by the strength of the surface forces acting on the tip. The schematic of the basic system design of an AFM is illustrated in Figure 3.2. The three fundamental components for an AFM are: the sample positioning system (scanner), the force detector and the feedback control system.

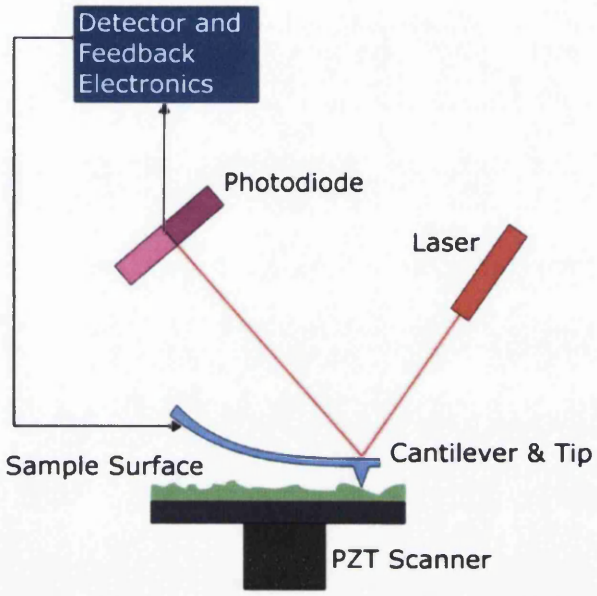

Figure 3.2 A schematic of the basic principle of AFM.

The AFM scanner is made up of piezoelectric ceramics, which changes its geometry in a direction that is perpendicular to the applied voltage. The resulting mechanical movement of this material is proportional to the applied voltage. The piezoelectric scanner is designed to precisely position a sample with nanometer resolution along the x, y and z directions. As the tip scans over the sample surface, cantilever deflections due to forces interacting with the tip are measured simultaneously. Since the cantilever behaves like a spring, these forces can be determined by measuring the amount of cantilever displacement. The deflection is measured by monitoring the laser reflections from the cantilever on to a position-sensitive photodiode (PSPD) detector. Then, the deflection sensor (PSPD) generates an output voltage that is proportional to the cantilever's deflection. The output of the deflection sensor is monitored by a feedback control system that serves to maintain the deflection of the cantilever (constant force) for each position (x, y). The feedback control system

maintains the static deflection by adjusting the applied voltage, V_z to the z piezoelectric scanner in order to bring the probe closer or further away from the sample surface. The bias voltage V_z is adjusted until the deflection of the cantilever (PSPD output) is the same as the set point value used by the feedback system. For every position of the scan, V_z is recorded, providing information in a Cartesian (x, y, z) coordinate system, generating an AFM image.

As mentioned in Section 3.2, there are different types of forces that contribute to the deflection of the AFM cantilever. At specific tip-sample separation, different forces will dominate (Figure 3.1) and thus determines the different types of AFM operations. Variations to the basic scheme shown in Figure 3.2 are used to measure topography as well as other surface features. There are numerous types of AFM modes and each mode is defined by the type of force being measured and how it is measured. The three dominant AFM modes of operation are the contact (static), non-contact (dynamic) and intermittent contact modes (dynamic). A flexible control system can also be added to allow the AFM to probe different types of surface forces such as adhesion, friction, magnetic and electrostatic force using different scanning modes. For this work, the main scanning modes are the tapping mode AFM and the electrostatic force microscope. The following will briefly describe the basic concept of the tapping mode AFM, which is used for AFM imaging of nanostructures.

3.3.1. Tapping mode atomic force microscope

The intermittent contact or tapping AFM is a type of dynamic mode in which cantilevers are mounted on actuators and deliberately oscillated. It is one of the most commonly used of all AFM modes, and is characterized by the fact that the cantilever tip lightly taps the sample surface periodically. The cantilever is oscillated near its resonant frequency by a small piezoelectric element mounted at the AFM tip holder while the tip simultaneously scans the sample surface. The cantilever oscillates at amplitude greater than 10 nm, typically 100 to 200 nm. When the tip moves close to the sample surface, forces acting on the cantilever, such as van der Waals force or dipole-dipole interaction, electrostatic forces, etc, decrease the amplitude of oscillation (Figure 3.3). The reduction in oscillation amplitude is used to identify and measure surface features.

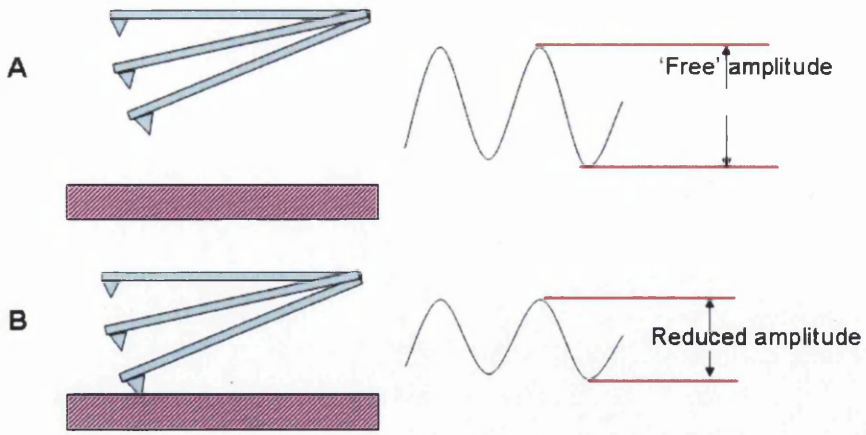

Figure 3.3 Tapping mode AFM cantilever oscillation amplitude in (A) free air and (B) during scanning.

A feedback loop is used to maintain the constant cantilever oscillation amplitude for a set of desired points on the sample surface by adjusting the cantilever tip-sample separation. When the tip scans across a 'bump' on the sample surface, the cantilever has less area to oscillate and the amplitude of oscillation decreases. Similarly, when the tip scans over a depression, the cantilever has wider area to oscillate the amplitude increases (approaching the maximum free air amplitude). The oscillation amplitude of the tip is measured by the detector and input to the SPM controller electronics. The feedback loop then adjusts the tip-sample separation to maintain constant amplitude. The feedback signal, used to regulate the vertical movement (z-direction) of the cantilever during scanning in the (x, y) place, is recorded and translated by a computer to form the topographic image of the sample surface.

3.4. Electric techniques overview

The two common electric techniques for AFM are the scanning conductance microscope (SCM) and the surface potential (SP) imaging. The SCM measures the variations in the electric field gradient between the tip and sample while the SP imaging measures the effective surface voltage of the sample by adjusting the voltage on the tip to minimise the resultant electric force exerted from the sample. Both techniques exploit a conductive AFM tip to detect long-range Coulomb forces from the sample surface. These interaction forces alter the oscillation amplitude and phase of the AFM cantilever, which are detected to produce SCM or SP images.

Both techniques employ a dual-pass LiftMode measurement, which allows imaging of relatively weak but long-range electrostatic interactions while minimizing the influence of topography. A more detailed description of the LiftMode technique is given in the next section. Only the SCM technique will be discussed in this work.

3.4.1. Dual-pass LiftMode technique

The Dual-pass LiftMode technique is usually employed when data other than topography are to be obtained. It serves to eliminate unwanted topography side effects which may diminish the reliability of SCM or SP images. For each scan line, the LiftMode records measurements in two passes, with each pass consisting of one trace and one retrace scan. The principle of the LiftMode is illustrated in Figure 3.4. During the first pass (line scan), the height (topography) profile of the sample surface is acquired using tapping mode AFM ((1) in Figure 3.4). In the second scan, the tip is lifted to a predefined lift scan height, *h* above the surface, typically 5-100nm, ((2) in Figure 3.4) and scans following the topography profile recorded during the first scan while maintaining the constant tip-sample separation, *h* ((3) in Figure 3.4). In the second pass, electric forces and potentials, magnetic fields and surface capacitance distributions can be measured [4, 5, 6, 7, 8, 9]. It is during the second pass that SCM or SP image is generated.

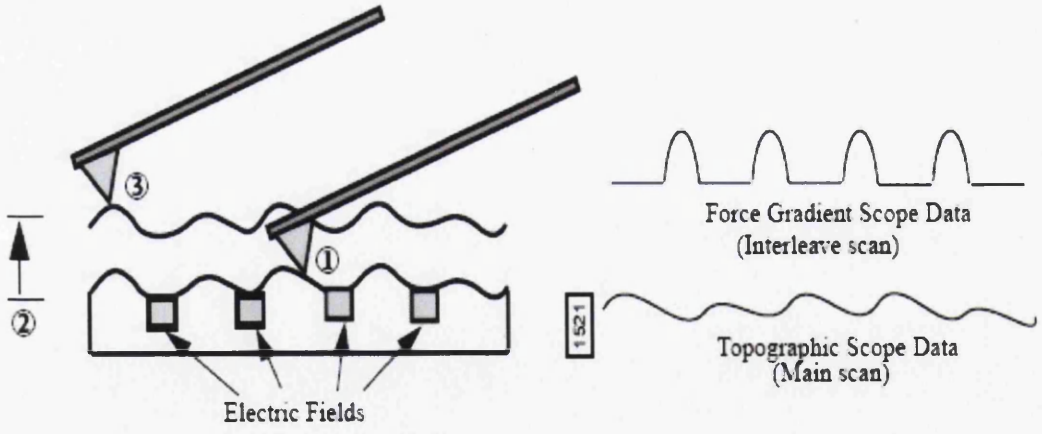

Figure 3.4 Principle of LiftMode measurement [10].

3.4.2. Scanning conductance microscope (SCM) theory

The SCM is a secondary imaging mode derived from tapping mode AFM, where topography profile of a sample surface is acquired during the first scan via tapping mode. It is also a type of dynamic imaging mode of AFM, where the cantilever tip is not in direct contact with the sample surface but is placed well above it during the second scan. The SCM is used to detect the variations in the electric field gradient between the tip and sample surface. During the SCM second scan, the cantilever is lifted to a pre-defined height, and is vibrated by a small piezoelectric element near its resonant frequency. The cantilever's effective resonance frequency will change in response to any additional force gradient exerted between the tip and sample (Figure 3.5). In the presence of attractive forces, the cantilever becomes effectively 'softer' (reduced effective spring constant, k_{eff}) , reducing the cantilever resonance frequency. Similarly, repulsive forces cause the cantilever to be effectively 'stiffer' (increased k_{eff}), increasing the resonant frequency. This change in the phase, frequency or amplitude of the cantilever oscillation, which is related to the gradient of the electric field between the tip and sample, is plotted at each in-plane coordinate x and y. In general, trapped charges on or beneath the sample surface induce a field that is sufficient to generate contrast in an SCM image. Nonetheless, a voltage can be applied between the tip and the sample to induce a stronger field.

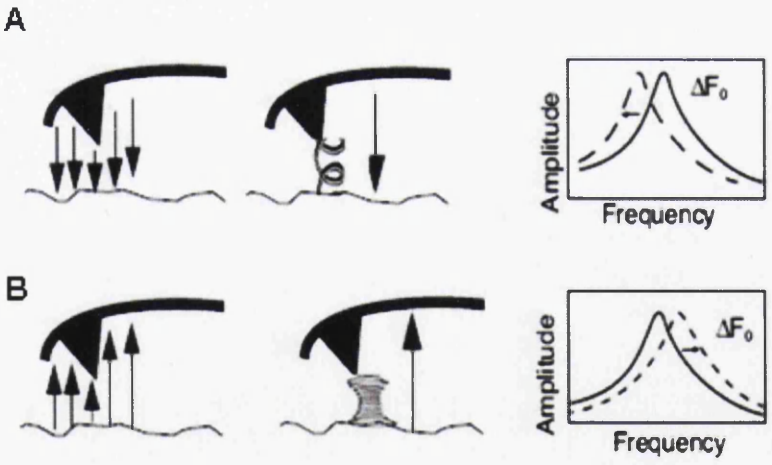

Figure 3.5 Comparison of attractive and repulsive forces. (A) An attractive tip-sample gradient is equivalent to additional spring in tension attached to the tip, thus reducing the cantilever resonance frequency. (B) A repulsive tip-sample gradient is equivalent to additional spring in compression attached on the tip, thus increasing the cantilever resonance frequency [10].

3.5. Instrumentation

3.5.1. General description

The general schematic of the experimental setup used to perform SCM measurements is presented in Figure 3.6. This experimental setup is capable of simultaneously measure both the surface topography profile (purple loop in Figure 3.6) and electrostatic force (blue loop in Figure 3.6) as a function of position. The measurements are based on the principles discussed in Section 3.4.

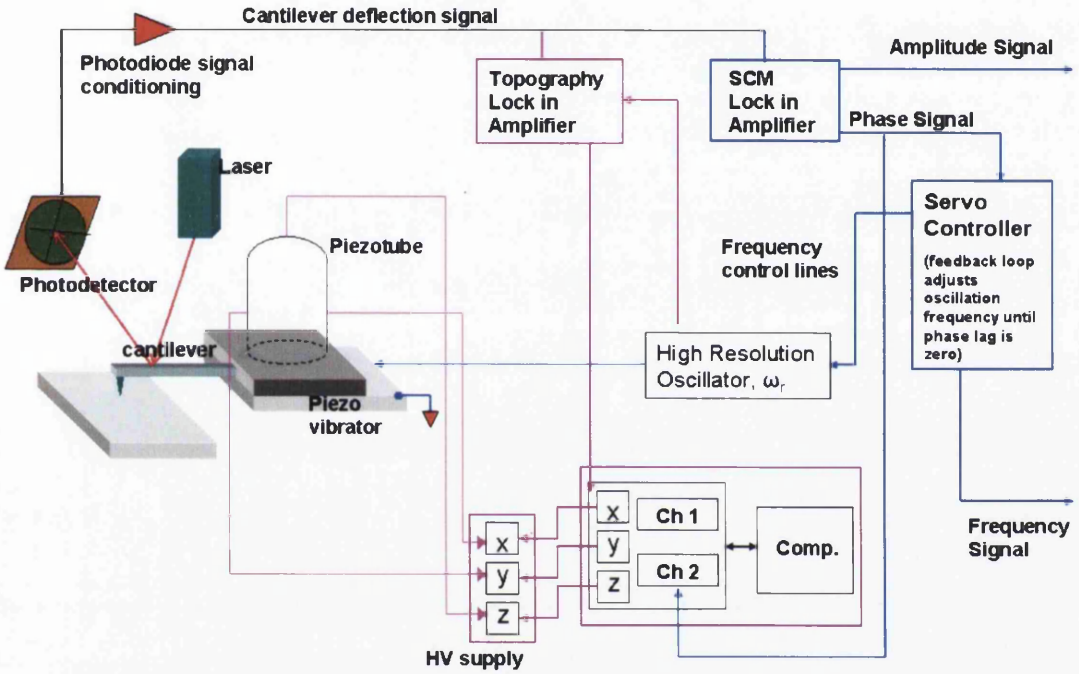

Figure 3.6 The experimental setup for SCM measurement.

The purple loop in Figure 3.6 represents the control system used to measure the surface topography. The topographic data is gathered via standard tapping mode AFM, as discussed in Section 3.3.1. The cantilever is vibrated near its resonant frequency by a small piezoelectric element, as the tip intermittently 'taps' the sample surface. As the oscillating cantilever begins to intermittently contact the surface, the cantilever oscillation is necessarily reduced due to energy loss caused by the tip contacting the surface. The surface feature of a sample is identified and measured by monitoring the changes in amplitude and phase of the cantilever oscillation.

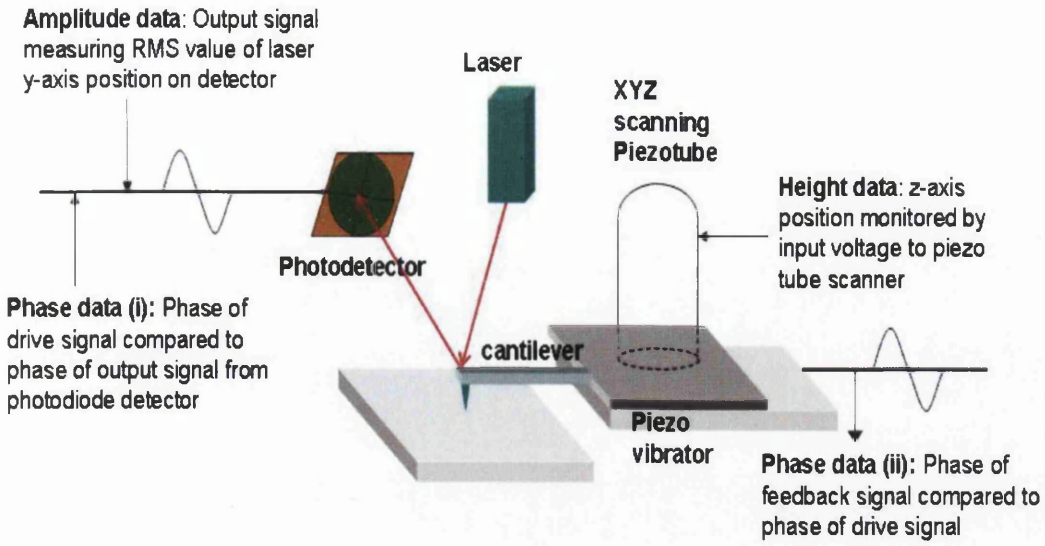

Figure 3.7 Three types of data that can be collected through tapping AFM.

Figure 3.7 summarises the various types of informative data that can be extracted via the feedback regulation system in the AFM system - amplitude, height, and phase data. As shown, changes in the cantilever oscillation amplitude of the cantilever are monitored by the optical lever beam deflection detection scheme. Laser light from a solid state diode is reflected off the back of the cantilever and collected by a position sensitive photodiode (PSPD) detector array. The PSPD array contains four photodetectors and the signal difference between the various photodetectors is monitored, amplified and transmitted to the AFM feedback system. To maintain the cantilever oscillation amplitude for each (x, y) position, the output of the photodetector is monitored by the feedback control system. The feedback control system adjusts the tip-sample separation by altering the applied voltage (feedback signal) to the z-piezoelectric scanner so as to maintain constant cantilever oscillation amplitude. The vertical movement of the probe tip (along the z direction) during scanning in the (x, y) plane is recorded and plotted as a topographical map of the sample surface (height data). Although the height data is a good measure of height of surface feature, it does not display distinct edges of the measured features. The phase data image is generated by comparing the phase offset of the piezo input drive signal to the phase offset of the cantilever response signal on the photodetector. When the cantilever is oscillating freely in air, the phase offset between the two signals is zero. The presence of tip-surface interaction forces causes the phase offset of the

oscillating cantilever to change by some angle with respect to the phase offset of the piezo input drive signal. As the tip scans across the sample surface with regions of differing elasticity, the phase angle between the two signals change due to differing amounts of damping experienced by the tip. These differences are recorded and plotted as the phase data image. The amplitude data image is extracted by plotting the variation of the RMS values of the cantilever amplitude signal. The distinctive edges of surface features can be observed through amplitude images.

The blue loop in Figure 3.6 indicates the components used to measure the electrostatic force acting on the cantilever's tip. A dc tip bias may be applied between the tip and the sample directly from the microscope's electronics under AFM software control. As shown in Figure 3.6, the SCM scans can be performed on three different modes: amplitude detection, phase detection and frequency modulation. Using the same type of phase sensitive detection as the topography loop (red loop), a separate lock-in amplifier (SCM lock-in in Figure 3.6) detects the changes in the phase and amplitude of the cantilever oscillation via the output signal of the photodetector during LiftMode. For amplitude and phase detection, the feedback during the LiftMode scan is turned off. In other words, the drive signal that oscillates the cantilever has constant frequency and any changes in amplitude or phase is recorded to form the SCM image. For frequency modulation technique, the difference between the phase of the cantilever oscillation and the phase of the drive signal from a high resolution oscillator is monitored. Any phase differences due to the presence of different tip-sample electric field gradient is used as an 'error signal' in a feedback scheme. The frequency of the drive signal is modulated ('Frequency Control lines' in Figure 3.6) until the phase lags between the two signals is zero. The modulations of the drive signal frequency are plotted versus the in plane coordinates, producing 3-D SCM image. In this work, phase detection SCM is used (explains the SCM phase signal line connection to Ch 2 in Figure 3.6) as it is faster than its amplitude response to changes in the tip-sample interactions and it is also less susceptible to height variations on the sample surface.

3.5.2. The force sensor

The basic principle of AFM is to detect, measure and control the interactions between its force sensor and the sample surface to understand the sample's properties. This is also the same for the SCM technique, a secondary imaging method of AFM. Consequently, the force sensor plays a crucial role in the scan process and determines the ultimate resolution achievable. A typical AFM probe consists of a sharp tip mounted on a small flexible cantilever, which is commercially available and ready for use. The various types of AFM tips commercially available are fabricated according to different types of applications. For electrical measurements, the specially coated cantilever tip and force constant are optimised for such applications. This type of probe yields very high force sensitivity, and at the same time allows tapping mode and LiftMode operations. This probe is also chemically inert, with high mechanical Q-factor for high sensitivity. The force sensor for electrical application is described below, firstly in terms of its cantilever properties, followed by its tip geometry.

3.5.2.1. Cantilever specifications

The spring-like cantilever act as a transducer that translates forces detected between the tip and sample surface, to its deflections. The geometry of a beam shaped cantilever is illustrated in Figure 3.8.

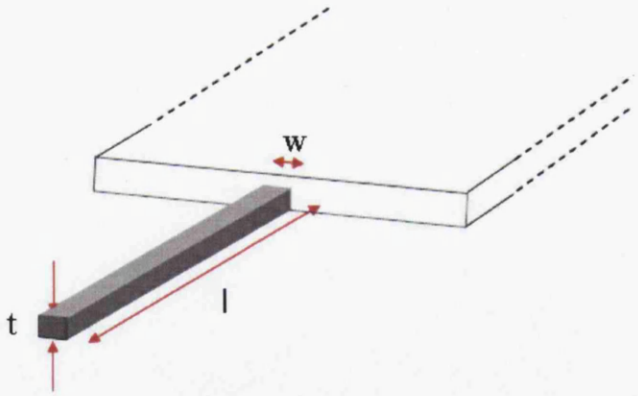

Figure 3.8 Cantilever geometries: beam-shaped.

The mechanical properties of cantilever tips are defined by the geometry, dimensions and the material used. The beam-shaped cantilever is treated as a classical, one-dimensional, lightly loaded, ''fixed-free'' beam (Figure 3.8). Therefore, the

relationship between its force constant (spring constant) k and the resonance frequency (fundamental eigenfrequency) f_0 is given by:

$$k = \frac{E}{4}\left(\frac{wt^3}{l^3}\right) \qquad \textbf{Equation 3.8}$$

and

$$f_0 = \frac{1}{2\pi}\sqrt{\frac{E}{\rho}}\frac{t}{l^2} = \frac{1}{2\pi}\sqrt{\frac{k}{m_{eff}}} \qquad \textbf{Equation 3.9}$$

where E is the Young's modulus, ρ is the density of the cantilever's material, and w, t and l are the width, thickness and length of the cantilever. These parameters can be varied to fabricate cantilevers with k =0.01 – 200 N/m and f_0 = 1- 400 kHz

The schematic of an SCM cantilever (SCM-PIT, Veeco) used in this work is shown in Figure 3.9. The SCM cantilever is fabricated from antimony (n) doped Si with Platinium/Iridium (Pt/Ir) coating on both sides of the cantilever. The coating at tip side of the cantilever (front side) serves to enhance the conductivity of the tip and allows electrical contacts. The coating at the detector side (back side) enhances the reflectivity of the laser beam and prevents light from interfering within the cantilever. The back side coating also serves to compensate the stress created by the Pt/Ir front side coating. The rectangular shaped cantilever has a nominal length (L) of 225 μm, width (w) of 28 μm and thickness (t) of 3 μm (refer schematic in Figure 3.9). In addition, the nominal force constant (spring constant, k) of the cantilever is 2.8 N/m with a nominal resonance frequency, f_0 of 75 kHz

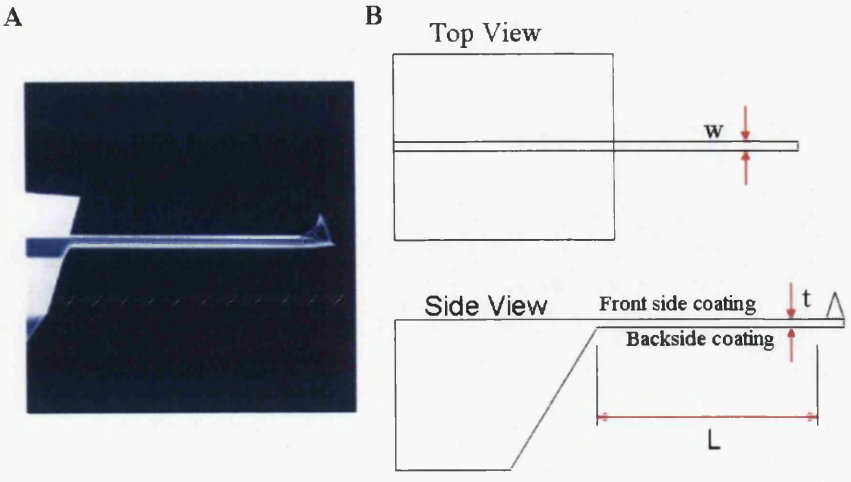

Figure 3.9 The schematic of an SCM cantilever (SCM-PIT, Veeco).

3.5.2.2. Tip specifications

The tip geometry and its characteristic dictate the ultimate resolution of AFM data. Most AFM tips are fabricated by micromachining silicon or silicon nitride, producing high aspect ratio pyramidal tips. The key properties of a standard tip are the radius of curvature r, sidewall angles θ and tip height h (Figure 3.10).

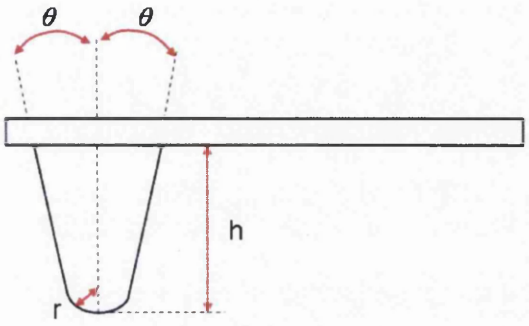

Figure 3.10 The parameters used for defining individual tips: tip height h, radius of curvature r, and sidewall angle θ.

The tip apex is approximated by a hemisphere with radius of curvature r, which is not atomically sharp. The actual sharpness of the tip is difficult to measure accurately and estimates are usually made during manufacture. The sidewall angles and the tip height influence the scanning of steep slopes, trenches and surface pits. Say, for accurate measurement of a 1 μm deep and narrow trench, the tip must be narrow enough to totally penetrate the gap. The schematic of the SCM tip (SCM-PIT, Veeco) is illustrated in Figure 3.11 [11]. As shown, the geometry of the tip is anisotropic. This tip usually has a radius of curvature r of less than 25 nm and a height h of 10-15 μm. The tip has a front angle (FA) of 25 ± 2.5°, back angle (BA) of 15 ± 2.5° and side angle (SA) of 22.5 ± 2.5°. Fabricated for electrical measurement, the front side of the tip is Pt/Ir coated to provide a metallic electrical path from the cantilever die to the apex of the tip. The added iridium alloy is used to increase the durability of the film.

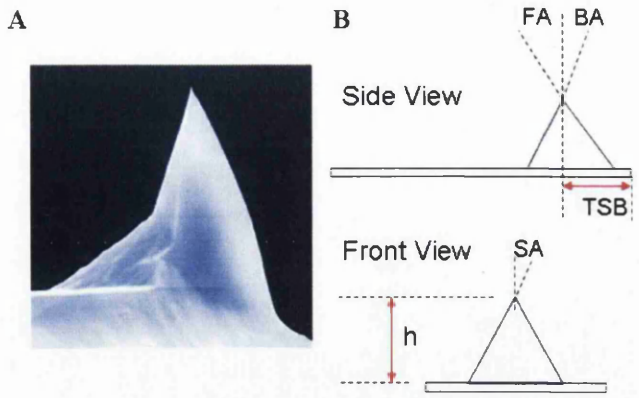

Figure 3.11 (A) The platinum-iridium coated EFM probe tip (SCM-PIT, Veeco). (B) The schematic of the tip, FA: Front angle, BA: Back angle, TSB: Tip setback, SA: Side angle, h: tip height.

3.6. Understanding Scanning Conductance Microscopy (SCM) measurements

For this work, the substrate used is a 350nm SiO_2 layer capped on top of a highly degenerately (p++) doped Si wafer (1cm x 1cm). SCM probes the electrostatic forces between the tip and the surface during LiftMode, with the metallic tip biased at V_{tip} and the cantilever drive frequency at $\omega = \omega_0$. In order to understand the dynamics of the SCM tip, the cantilever and metallic tip assembly is modelled as a damped harmonic oscillator of mass m, spring constant k and quality factor Q. Its resonance frequency ω_0 is related to m and k as $k = m\omega_0^2$. For small vertical displacements z, the AFM tip motion in response to an applied force $F(t)$ is modelled as:

$$\frac{d^2z}{dt^2} + \gamma\frac{dz}{dt} + \omega_0^2 z = \frac{F(t)}{m} \qquad \textbf{Equation 3.10}$$

where γ is the damping coefficient due to intrinsic losses and air resistance. For a given periodic driving force $F(t) = F_0\cos(\omega t)$, the response $z(t)$ will also be periodic;

$$z(t) = A\cos(\omega t + \varphi) \qquad \textbf{Equation 3.11}$$

with [12]

$$A = \frac{F_0}{m} \bullet \frac{1}{\sqrt{(\omega^2 - \omega_0^2) + \omega^2\gamma^2}} \qquad \textbf{Equation 3.12}$$

$$\tan(\varphi) = -\frac{\gamma\omega}{{\omega_0}^2 - \omega^2} \qquad \textbf{Equation 3.13}$$

The phase shift φ (in radians) of the free oscillator is expressed as:

$$\varphi = \tan^{-1}(-\frac{m\omega\omega_0}{Q(k - m\omega^2)}) \qquad \textbf{Equation 3.14}$$

As a function of ω, this phase varies sharply around ω_0. Equation 3.14 described the response of an oscillating AFM cantilever far from the sample. At resonance (with the tip driven at $\omega = \omega_0$), the phase shifts between the driving force and the cantilever oscillation is $\varphi = -\frac{\pi}{2}$ and the force gradient is zero (tip far away from sample). As standard convention of AFM, all measured phase shifts Φ, are with respect to this value. As such, $\Phi = \varphi + \frac{\pi}{2}$ and at $\omega = \omega_0$ and far away from the sample, the measure phase shifts is 0.

When the tip is moved to a height h above a substrate, there is an additional force $F_s(h+z)$ between the tip and the surface that will induce a certain amount of phase shift (Figure 3.12). The resultant equation of motion (refer Equation 3.10) becomes:

$$\frac{d^2z}{dt^2} + \gamma\frac{dz}{dt} + {\omega_0}^2 z = \frac{F_0}{m} \bullet \cos(\omega t) + \frac{F_s(h+z)}{m} \qquad \textbf{Equation 3.15}$$

For a cantilever tip oscillating with small amplitude around the equilibrium height h above a substrate, the additional force is expanded to

$$F_1(h+z) \approx F_1(h) + F_s'(h) \bullet z \qquad \textbf{Equation 3.16}$$

where $F_s'(h)$ is the first derivation of the force evaluated at the equilibrium position. Now, the equation for a driven harmonic oscillator is recovered, when we substitute Equation 3.16 into Equation 3.15. It should be noted that this is only true if we also make the substitution ${\omega_0}^2 \rightarrow {\omega_0}^2 - \frac{F'_s(z)}{m}$. As a result, we can conclude that the position-dependent force $F_s(h+z)$ between the tip and the sample alters the resonant frequency of the cantilever. For small forces, this frequency shift is proportional to the force gradient:

$$\Delta\omega \approx -\frac{\omega_0}{2k} F_s'(h) \qquad \textbf{Equation 3.17}$$

The presence of an attractive force between the cantilever tip and substrate will have a positive force derivative. This effectively softens the cantilever and reduces its resonance frequency. Figure 3.12 illustrates the change in the cantilever resonant frequency from free oscillation resonance ω_0 (tip far from substrate) to a lower value ω_L (tip at height from substrate) due to the presence of electrostatic force F_s. During the LiftMode SCM scan, the cantilever is driven at its original (free) oscillation frequency ω_0 and thus the phase shifts takes on a negative value Φ_0 (Figure 3.12B).

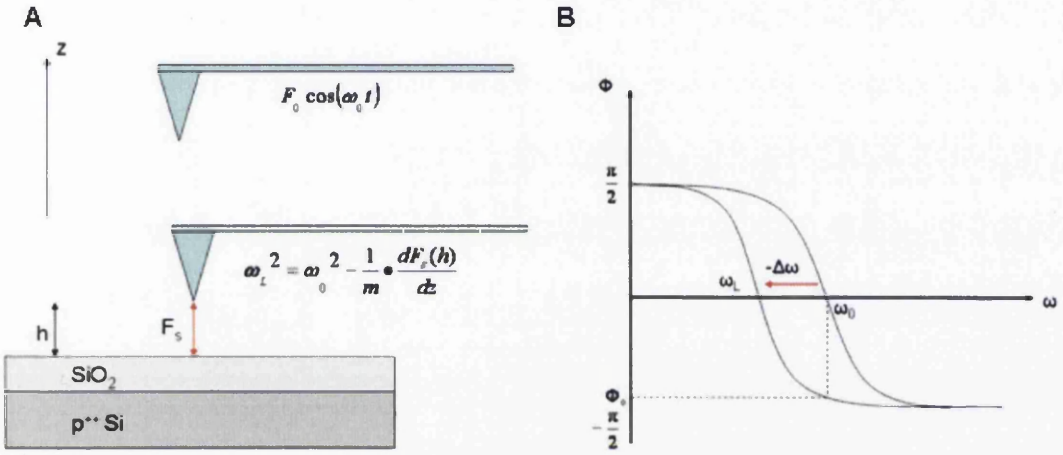

Figure 3.12 The schematic of tip-substrate interaction. (A) As the tip move closer to the substrate (height, h above substrate), the presence of electrostatic force changes the free oscillation resonance ω_0 to a lower value ω_L. (B) Phase Φ versus cantilever drive frequency ω. The phase-frequency diagram shifts to the left (lower resonant frequency) due to the presence of tip-substrate attractive force.

To a first approximation, the resultant of tip-sample force interactions is to change the force constant (spring constant, k) of the cantilever to a new effective value $k_{eff} = k + F_s'(h)$. For very small $F_s'(h)$ compared to k, the phase shift φ (refer Equation 3.14) can be expressed as

$$\varphi = \tan^{-1}\left(-\frac{m\omega\omega_0}{Q(k + F_s' - m\omega^2)}\right) \qquad \textbf{Equation 3.18}$$

Using the standard AFM convention ($\Phi = \varphi + \frac{\pi}{2}$ with $\omega = \omega_0$), the measured phase shift Φ is expressed as:

$$\Phi = \tan^{-1}(-\frac{k}{QF_s'}) + \frac{\pi}{2} \approx -\frac{QF_s'}{k} \qquad \textbf{Equation 3.19}$$

The electrostatic force exerted between the metallic top and the substrate F_s can be described in terms of the effective capacitance between the metallic tip and the SiO_2/Si substrate. For an applied tip voltage V_{tip},

$$F_s(h) = \frac{1}{2}C_s'(h)V_{tip}^2 \qquad \textbf{Equation 3.20}$$

where $C_s'(h)$ is the first derivative of tip-substrate capacitance.

When a dc voltage is applied between the tip and the highly degenerate Si, the resulting electrostatic forces will alter ω_0 and Φ. On bare SiO_2/Si substrate, the electrostatic forces are independent of the position (x, y) of the metallic tip and the phase Φ takes on the background value Φ_0. From Equation 3.19 and Equation 3.20, we relate the measured Φ_0 to the applied tip voltage, V_{tip} as:

$$\Phi_0 = -\frac{Q}{2k}C_s''(h)V_{tip}^2 \qquad \textbf{Equation 3.21}$$

Consider the metallic tip scans at the same distance h above a material deposited on the SiO_2/Si substrate. The total effective capacitance of the tip-material-substrate assembly is now $C_m(h)$. Due to the electrical properties of the material, an electrostatic force, $F_m(h)$ exerted between the tip-material changes the phase to Φ_m. So, the phase shift relative to that over the bare substrate $\Delta\Phi$ is given by:

$$\Delta\Phi = (\Phi_m - \Phi_0) = -\frac{Q}{2k}(C_m''(h) - C_s''(h))V_{tip}^2 \qquad \textbf{Equation 3.22}$$

which gives the relation between the measured phase shifts $\Delta\Phi$ and the changes in the effective capacitive coupling between the bare substrate and the material.

3.6.1. SCM studies on nanomaterials - a literature review

The SCM, based on the electrostatic force microscopy (EFM) technique, is an elegant route for the qualitative studies of the conductance of nanomaterials without the need to fabricate metal contacts. However, this technique is not widely used and so, a brief literature review on the SCM technique is presented in this section to further aid the understanding and interpretation of our SCM results.

Bockrath et. al demonstrated the capability of the SCM as a 'metal detector' for nanosize wires including those with extremely low conductivity [13]. In a typical SCM scan, a Si wafer capped with 1 μm of SiO_2 was used. *Bockrath et. al* observed that the single wall carbon nanotubes (SWNTs) deposited on the Si/SiO_2 substrate were detected as dark lines against a uniform white background (Figure 3.13A).

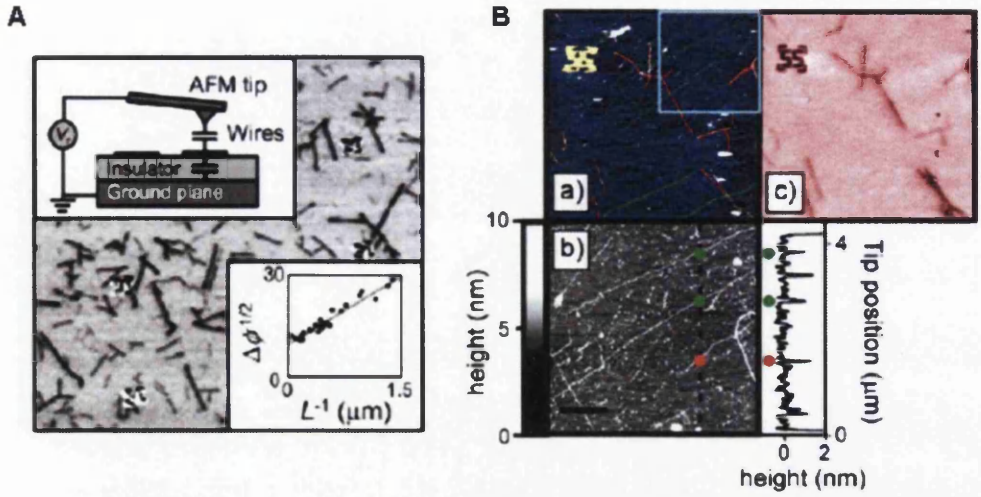

Figure 3.13 (A) Upper inset: The experimental setup with the tip scanned at 30nm above the sample deposited on a Si wafer capped with 1 μm SiO_2 as substrate. Main: The SCM phase image of SWNTs. The dark lines are detected (negative phase shifts relative to background value) when the tip scan above a CNT. (B) (a) The topographical image of SWNTs (red lines) and λ-DNA (green lines) deposited on the Si/SiO_2 substrate. (b) The topography image of the region enclosed in the blue square in (a), showing clearer topographic features. (c) The SCM phase image of the region shown in (a). Clear signals (black lines) are detected when the tip hovers above the SWNTs, while none was detected for the λ-DNA.

It was found that the dark lines of the shorter length nanotubes were relatively fainter with length shorter than 0.4 μm not detectable. The observation was explained by modeling the tip-nanotube-substrate as two capacitors arranged in series, where shorter nanotubes have less capacitance to the grounded substrate (upper inset in Figure 3.13A). As such, the potential across the tube-ground-substrate capacitor floats nearer to the applied tip voltage (V_{tip}), resulting in smaller phase shift. In the same work, a comparison study of the conductivity of SWNTs and lamda-DNA (λ-DNA) was also performed (Figure 3.13B). SCM images of the nanotubes and λ-DNA deposited on the same substrate revealed that while the SWNT (marked as red lines) yield clear signal, the λ-DNA (marked as green lines) yield no signal (Figure

3.13B). With this result, *Bockrath et. al* concluded that λ-DNA is an electrical insulator with an extremely low conductivity.

Y Zhou et. al distinguished between conducting and insulating polyaniline/polyethylene oxide (Pan/PEO) nanofibers using the SCM [14]. As a control, metal and semiconducting SWNTs were also scanned. In agreement with [13], negative phase shifts were detected when the probe tip hovers above the SWNTs, suggesting their conductive nature. It was observed that insulating PEO nanofibers always exhibited positive phase shifts that increase with diameter (Figure 3.14C), while conducting nanofibers showed 'negative-positive-negative' phase shifts (Figure 3.14B).

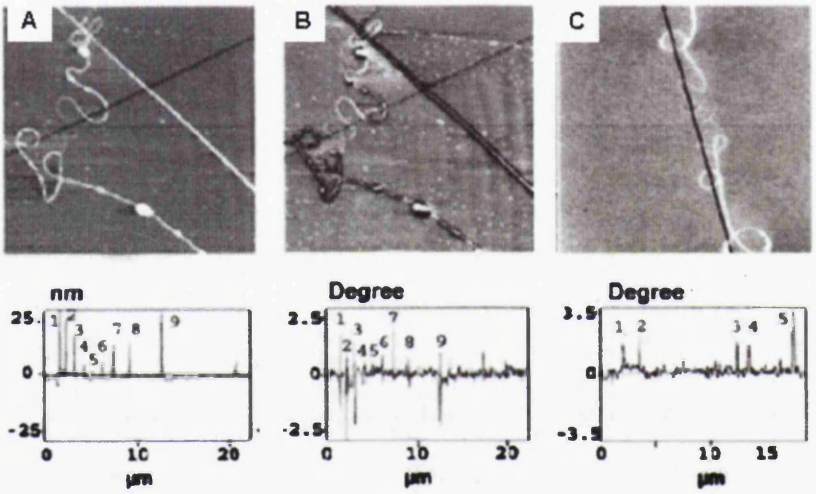

Figure 3.14 (A) AFM and (B) SCM images of PAn.HCSA/PEO nanofiber and (C) SCM image of insulating PEO nanofiber, with their respective line profile (below) taken along the black line in each images. The diameter of the insulating nanofiber in (C) varies from 40nm near the top of the image , to 4nm at its thinnest and to 60nm at the bottom of the image. Negative-positive-negative phase shift contrast were detected for a conducting nanofiber (peaks 1,2,3 and 9 in (B)) and positive phase shifts were detected for insulating nanofiber (C).

Cristian Staii et. al presented a quantitative analysis of SCM on SWNTs, conducting PAn.HCSA/PEO nanofiber and insulating PEO nanfibers (Figure 3.15) [15]. They observed similar results to *Y. Zhou et. al* [14] and explained these observations quantitatively using an improved SCM model. They suggested that the sign of the phase shift in SCM is determined by the change in the second derivative of the total capacitance of the system from Equation 3.22. By approximating the SCM probe tip as a circular plate of radius R, *Cristian Staii et. al* suggested simplified models for

the geometry of the bare substrate, the thin SWNT, and the polymer nanofiber (A, B and C respectively in Figure 3.16).

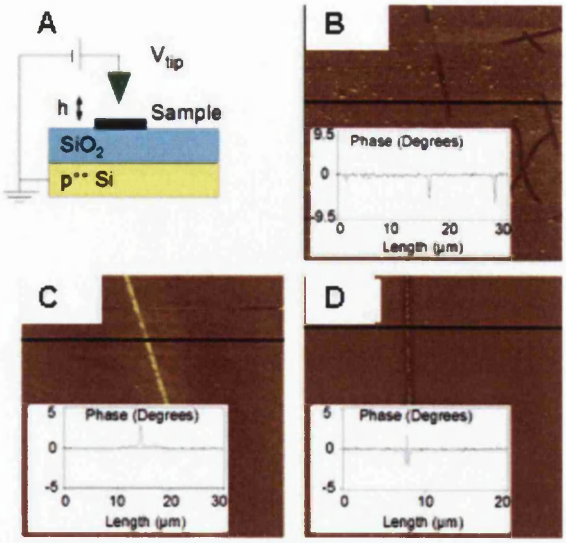

Figure 3.15 (A) Schematic of the SCM set up. SCM phase image for (A) single wall carbon nanotubes (SWNTs) (B) insulating PEO nanofiber and (C) conducting PAn.HCSA/PEO nanofiber.

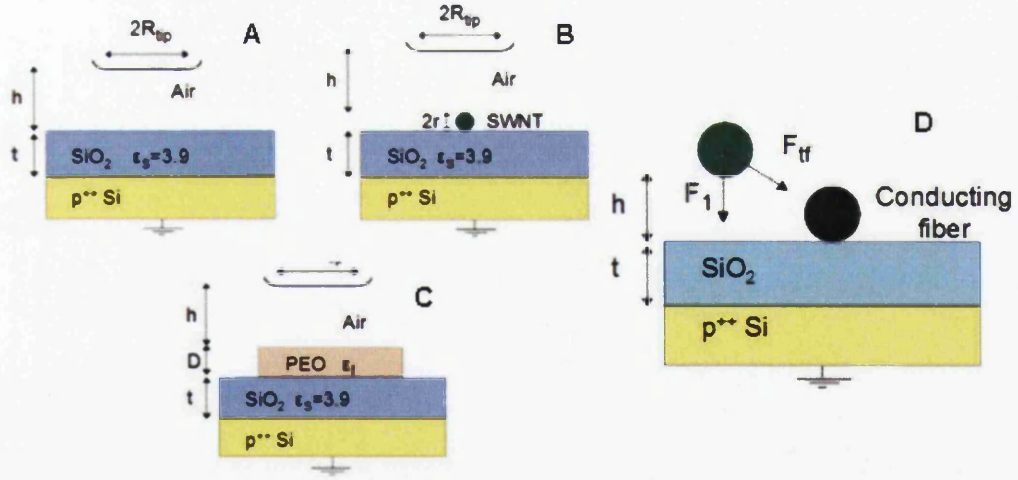

Figure 3.16 (A)-(C) Models for the tip-sample geometry with the tip approximated as a circular disk with radius, R_{tip}=30-50 nm, scans at height h above the sample. (B) The tip and SWNT are modelled as conducting plates with the SWNT approximated as a cylinder of radius r, and length L. (C) The PEO fiber is modelled as a dielectric plate of thickness D. (D) The schematic of the interaction between the AFM tip and a conducting PEO fiber, which is expressed mathematically as Equation 3.24.

For bare substrate, the AFM cantilever was estimated as a flat circular disk sitting at a distance h above the bare substrate, mathematically modeled as (Figure 3.16A):

$$C_1'' = \frac{2\pi R_{tip}^{\ 2}\varepsilon_0}{(h+\frac{t}{\varepsilon_s})^3} \qquad \textbf{Equation 3.23}$$

To calculate the dielectric constant of the PEO fiber, *Cristian Staii et. al* approximated the nanofiber as an insulating plate of thickness D and dielectric constant ε_f (Figure 3.16C):

$$C_2'' = \frac{2\pi R_{tip}^{\ 2}\varepsilon_0}{(h+\frac{t}{\varepsilon_s}+\frac{d}{\varepsilon_R})^3} \qquad \textbf{Equation 3.24}$$

Cristian Staii et. al also explained the observed negative-positive-negative' phase shifts, is due to an additional attractive force F_{tf}, originated from the tip-fiber interaction (Figure 3.16D). When the tip approaches or moves away from a conducting sample at a height h above the sample, there exist two forces that influence the cantilever oscillations. These forces originate from the capacitive interaction between tip and substrate, F_1 and the additional attractive force due to the tip-sample interaction, F_{tf}. Due to this additional attractive force, the cantilever experiences a decrease in phase, Φ, and subsequently a negative phase shift, $\Delta\Phi$. When the tip hovers directly above the sample, the influence of the finite dielectric constant of the sample overcomes the capacitive force and thus, positive phase shifts is detected by the probe tip, they expressed this mathematically with the following equation [15]:

$$\Phi = -\frac{Q}{k}(F_1' + F_{tf}') < -\frac{Q}{k}(F_1') \qquad \textbf{Equation 3.25}$$

T S Jespersen et. al reported the use of SCM as simple and efficient characterisation method for standard CNT samples. They reported the use of SCM as a quick method to identify special CNT structures such as CNT loops with respect to predefined alignment marks in a large scan area (Figure 3.17A). In addition, by using the statistical analysis of the SCM data, *T S Jespersen et. al* also demonstrated fast density characterisation of as grown CNT samples (Figure 3.17B-D) [16].

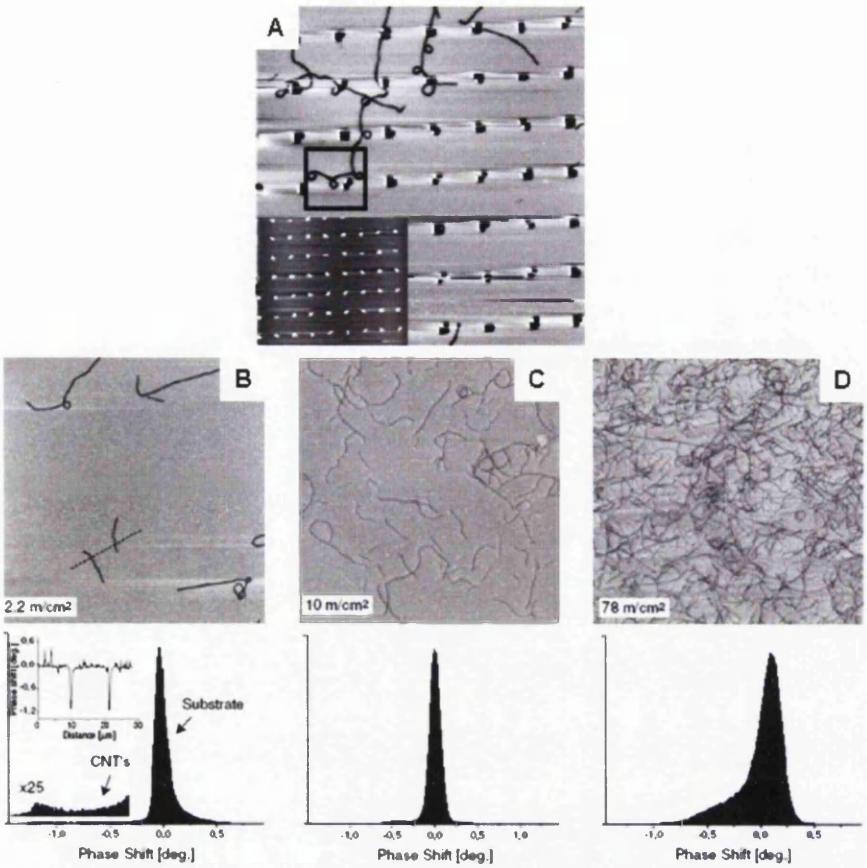

Figure 3.17 (A) 100 μm X 100μm SCM scan of SWNTs and metal alignment marks deposited on a Si/SiO_2 substrate. Lower inset: the corresponding topographic image where the CNTs were not observable. (B), (C), (D) 90 μm X 90μm SCM images of SWNTs with varying density and (below) their histogram of measured phase shift values respectively [17].

Recently, *Jespersen et. al* have shown that SCM can be used to extract useful information from intentionally induced defects in single wall CNTs (SWNTs) and also from unintentionally induced defects in as grown SWNTs [17]. In the reported work, defects were intentionally imparted in the SWNTs via oxygen plasma etching [18]. SCM scans on the SWNTs bundles before (Figure 3.18A) and after (Figure 3.18B) etching showed that significant decrease in SCM signals were detected after etching. Repetitive scans on the same sample after one month yield the same results, ruling out charging effects as the cause of the loss of SCM signals but concluded the observed results as defect induced changes in the SWNT properties.

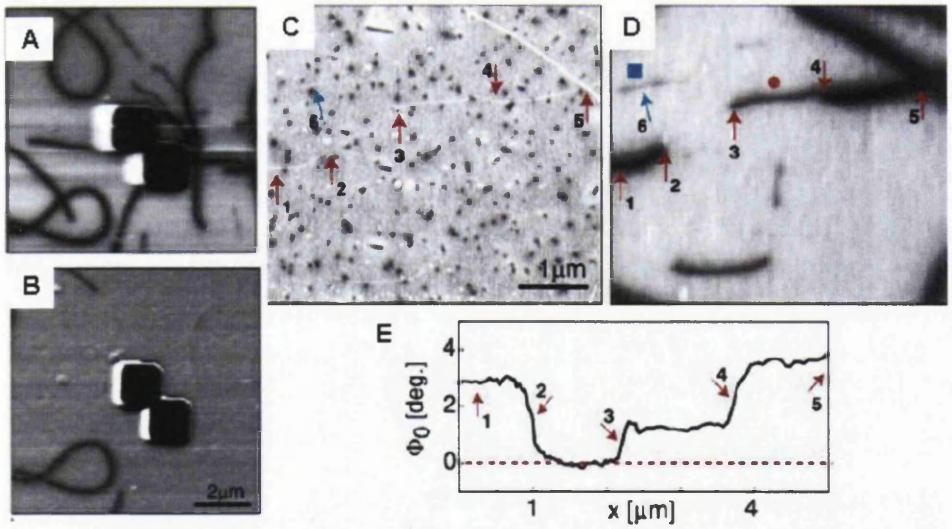

Figure 3.18 SCM phase images of CVD grown SWNTs (A) before and (B) after oxygen plasma etch. The squares are metal alignment marks. No signals were detected on almost all SWNTs after the etch. (C) Topography AFM image and (D) the corresponding SCM phase image of as grown SWNTs. The arrows point to the defect related effects on the SWNT. (E) Line profile taken along the SWNT labelled by arrows (1)-(5) in (D). No SCM signals were detected along 2-3 while a significant change in phase was detected at 4, suggesting the presence of defects on the SWNT.

Besides that, as grown SWNTs with defects were detected as weakly coupled short and highly conducting segments, which otherwise were unobservable in the standard topographic measurements (Figure 3.18C-D). As shown, the significantly thinner 2-3 segment (Figure 3.18C) was completely absent in the SCM image (Figure 3.18D), suggesting that this segment is highly defective. In addition, line profiles taken along the SWNT showed varying SCM signals with distinctive defects points (3-4) (Figure 3.18E).

The feasibility of using SCM as an analytical tool to probe the charge degradation in polypropylene electret fibers was demonstrated by *J Kim et. al* [19]. The charged polarity of the electret fiber was determined by monitoring the change in phase shift with respect to the polarity of the tip biased voltage. SCM scans with negative tip bias voltage that induced negative phase shifts (attractive tip-sample force) whereas a positive tip bias voltage induced positive phase shifts (repulsive tip-sample force), indicating that the electret fiber was positively charged. For electret fibers immersed in isopropanol (IPA), only an attractive force (negative phase shift) was detected for

either sign of the tip bias voltage, indicating charge degradation in the IPA treated electret fibers.

H Cohen et. al were able to differentiate the electrical properties of G4-DNA, a four-stranded DNA structure formed by DNA oligonucleotides with a repeat that contained three or more consecutive guanines, from that of a normal double stranded DNA (dsDNA) using SCM [20]. They reported that single G4-DNA gives polarisability signals while no observable signal was observed for dsDNA (Figure 3.19).

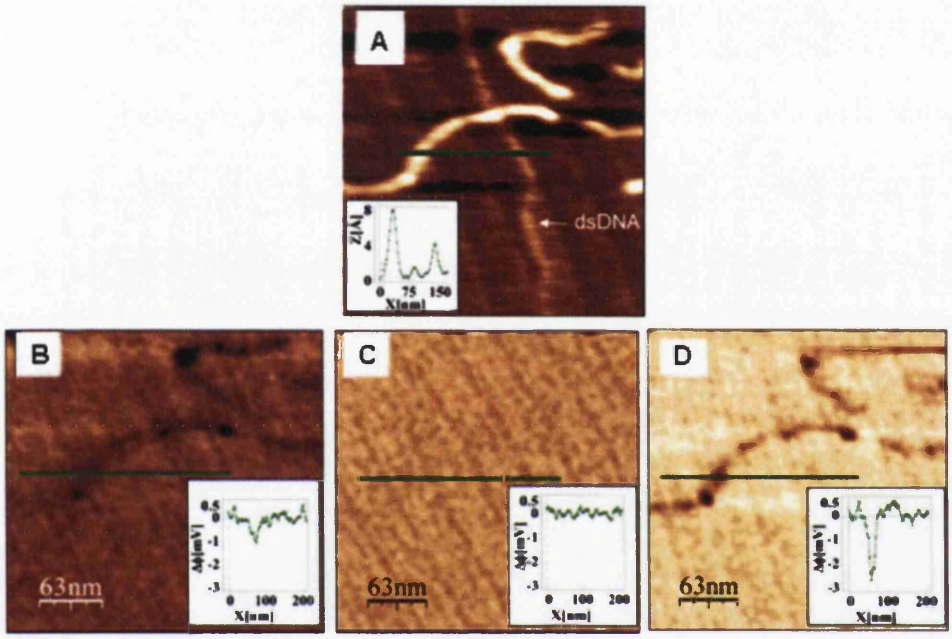

Figure 3.19 (A) Topographic image of co-adsorbed G4-DNA and dsDNA deposited on a mica substrate. Inset: Line profile taken along the green line in the image, showing that the height of the G4-DNA is twice higher than the ds-DNA. (B), (C), (D) SCM phase images of the same area in (A) with the tip biased at -3V, 0V and +3V respectively. The results clearly show that phase shifts were only detected when the tip scans above the G4-DNA and only when applying bias voltage [20].

Recently, SCM was also used to investigate the electrical properties of chromosomes for the first time [21]. By using the same model (Equation 3.24) proposed by *Cristian Staii et. al* [15], the value of the dielectric constant of the fixed chromosome deposited on the Si/SiO_2 substrate was estimated to be around 10.

3.7. Summary

This chapter has provided the theory of tip-sample forces and how these forces are exploited by the AFM to obtain information on a sample surface. Two different electric measurement techniques were introduced with emphasis on the SCM technique (electric field gradient measurement). The instrumentation needed for SCM measurement has been discussed. To understand the SCM measurement, a section relating the applied tip voltage, scan height, resultant capacitance and measured phase is addressed. Finally, a literature review on previous work using SCM on various samples is presented. This is to aid the interpretations of our SCM results discussed in chapter 6.

3.8. References

[1] Krauss T D and Brus L E 1999 Charge, polarizability, and photoionization of single semiconductor nanocrystals *Phys. Rev. Lett.* **83** 4840

[2] Stowe T D, Yasumura K, Kenny T W, Botkin D, Wago K and Rugar D 1997 Attoneewton force detection using ultrathin silicon cantilevers *Appl. Phys. Lett.* **71** 288

[3] Dragoman M and Dragoman D 2006 *Nanoelectronics-principles and devices* (Artec House, Boston)

[4] Wiesendanger R 1994 *Scanning Probe Microscopy and Spectroscopy: Methods and Applications* (Cambridge University Press, Cambridge)

[5] Bonnell D A 2001 *Scanning Probe Microscopy and Spectroscopy, Theory, Techniques and Applications* 2nd ed. (John Wiley and Sons: New York)

[6] Bachtold A, Fuhrer M S, Plyasunov S, Forero M, Anderson E H, Zettl A and McEuen P L 2000 Scanned Probe Microscopy of Electronic Transport in Carbon Nanotubes *Phys. Rev. Lett.* **84**, 6082

[7] Kalinin S V and Bonnell D A 2001 Local potential and polarization screening on ferroelectric surfaces *Phys. Rev. B.* **63**, 125411

[8] Alvarez T, Kalinin S V and Bonnell D A 2001 Magnetic-field measurements of current-carrying devices by force-sensitive magnetic-force microscopy with potential correction *Appl. Phys. Lett.* **78**, 1005

[9] Brezna W, Schramboeck M, Lugstein A, Harasek S, Enichlmair H, Bertagnolli, E. Gornik, and J. Smoliner 2003 Quantitative scanning capacitance spectroscopy *Appl. Phys. Lett.* 4253

[10] *Electric Force Microscopy (EFM) Support Note* 1996 No. 230 Rev. A (Digital Instruments)

[11] Online resource: http://www.veecoprobes.com/p-3392-scm-pit.aspx (Veeco Instruments)

[12] Feynman R P, Leighton R B, Sands M Feynman 1963 *Lectures on Physics* (Addison, Wesley Publication Co.)

[13] Bockrath M, Markovic N, Shepard A, Tinkham M, Gurevich L, Kouwenhoven L P, Wu M W and Sohn L L 2002 Scanned Conductance Microscopy of Carbon Nanotubes and λ-DNA, *Nano Letters* **2**, 187

[14] Zhou Y X, Freitag M, Hone J, Staii C, Pinto N J and MacDiarmid A G 2003 Fabrication and electrical characterization of polyaniline-based nanofibers with diameter below 30nm *Appl. Phys. Lett.* **83** 18

[15] Staii C, Johnson A T and Pinto N J 2004 Quantitative analysis of scanning conductance microscopy *Nano Lett.* **4** 859

[16] Jespersen T S, Lindelof P E and Nygard J 2005 Characterization of carbon nanotubes on insulating substrates using electrostatic force microscopy *AIP Conf. Proc.* **786** 135

[17] Jespersen T S and Nygård J 2007 Probing induced defects in individual carbon nanotubes using electrostatic force microscopy *Applied Physics A* **88** 309

[18] Zhi C Y, Bai X D and Wang E G 2002 Enhanced field emission from carbon nanotubes by hydrogen plasma treatment *Appl. Phys. Lett.* **81** 1690

[19] Kim J, Jasper W and Hinestroza J 2007 Direct probing of solvent-induced charge degradation in polypropylene electret fibres via electrostatic force microscopy *J. Microscopy* **225** 72

[20] Cohen H, Sapir T, Borovok N, Molotsky T, Felice R D, Kotlyar, Porath A B and Porath D 2007 Polarizability of G4-DNA observed by electrostatic force microscopy measurements *Nano Lett.* 7 981

[21] Clausen C H, Lange J M, Jensen L B, Shah P J, Dimaki M I, Svendsen W E 2008 Scanning conductance microscopy investigations on fixed human chromosomes *Biotechniques* **44** 475

Chapter 4

Surface Plasmon Resonance (The Biacore System)

4.1. Introduction

The road to the discovery of the surface plasmon resonance (SPR) starts as early as the 1900s [1,2]. It was not until 1968 that a complete explanation of the SPR phenomenon was plausible with the discovery of excitation of surface plasmons by Otto [3], Kretshcmann and Raether [4]. In the 1980s, an increase in the use of the SPR and other related techniques for the interrogation of thin films, biological and chemical interactions were observed [5]. The SPR is a powerful technique to measure real-time biomolecular interactions in a label free environment. The first commercial SPR product, the Biacore instrument, was launched by Pharmacia Biosensor AB, later known as BIAcore AB (was acquired by GE Healthcare in 2006), in 1990 [6]. The instrument was the most advanced, sensitive, accurate, reliable, reproducible direct biosensor technique and SPR became the 'golden standard' of the transducer principles for measuring real-time biomolecular interactions. The SPR based Biacore technology involves attaching one target interactant on the surface of a sensor chip and allowing another interactant of interest free in solution, to pass over the sensor surface for binding studies. The successful binding of molecules to the sensor surface will generate a response which is proportional to the bound mass. The sensitivity of the Biacore detection system can be down to a few picograms or less per square milimeter on the sensor surface. This corresponds to concentrations in the picomolar or nanomolar range in the sample solution. These binding interactions are monitored in real-time, as association or dissociation which will be measured in arbitrary units (SPR response) and displayed as a function of time on a graph called the sensorgram. In this chapter, the principles of the SPR with its application to the Biacore X system are described and the details of the signal detection and instrumentation are given.

4.2. Principle of surface plasmon resonance (SPR)

To understand what exactly surface plasmon resonance (SPR) is, consider the experiment setup shown in Figure 4.1. When a light beam propagates through a

prism (denser medium) to air, the light is refracted towards the interface (Figure 4.1A). On increasing the angle of incidence, a point is reached where the refracted light beam is parallel to the surface of the prism. At angles higher than this point, all light will be reflected into the prism: total internal reflection phenomenon is observed (Figure 4.1B).

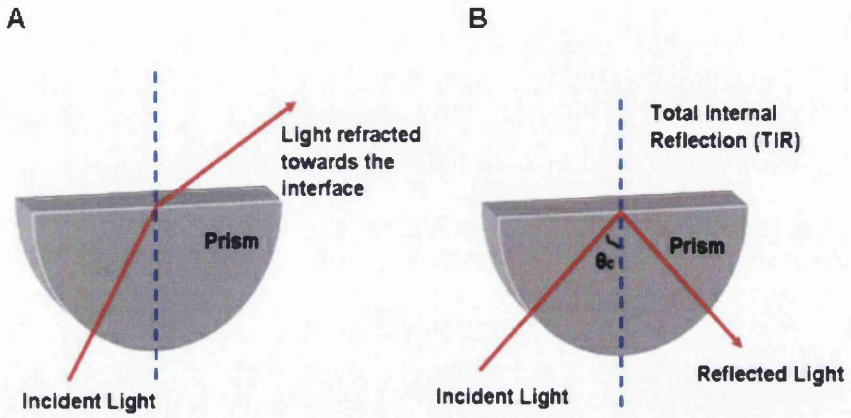

Figure 4.1 Experimental set-up to understand the principle of surface plasmon resonance (SPR).

Although the incident light is totally reflected (no net energy loss), its electric field intensity will penetrate a short distance, across the interface into the medium with lower refractive index (air). The electric field intensity component is called the evanescent wave field. The evanescent field wave has similar wavelength to the incident light but its amplitude decreases exponentially with distance from the reflecting interface. When the evanescent field wave is allowed to interact with a layer of conducting material (metal), a new phenomenon is generated.

Now, the prism is coated with a layer of thin gold film as shown in Figure 4.2. When the light is totally reflected, the p-polarised component of the evanescent field wave will interact with the delocalised electrons in the gold film, and electromagnetic waves, called the surface plasmons are excited. These surface plasmons are similar to photons that represent the particle properties of light waves, which propagate within the metal surface at the interface (Figure 4.2).

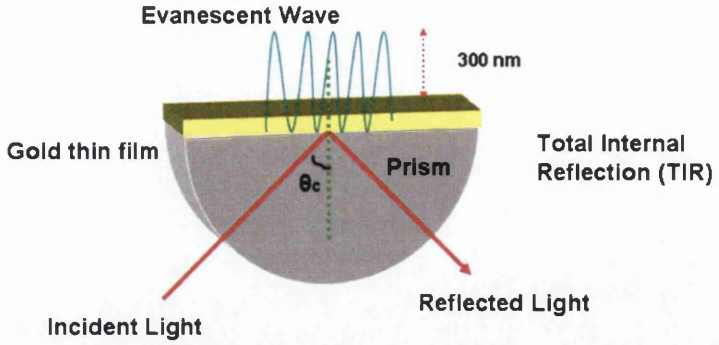

Figure 4.2 Surface plasmon resonance (SPR). The prism is coated with a layer of thin film. Incident light travel across the prism and the reflected light intensity is measured. At a certain angle of incidence, excitation of surface plasmons occurs.

At this angle of incidence, a decrease in the intensity of the reflected light will be observed (Figure 4.3A). On changing the angle of incidence, and monitoring the intensity of the reflected light, the angle at which the maximum loss of the reflected light intensity (minimum intensity) occurs is called the resonance angle or the SPR angle (Figure 4.3A). The SPR angle is mainly dependent on the properties of the metal film, the wavelength of the incident light and the optical characteristic of the system (e.g. on the refractive indices of the media at both sides of the gold) [7]. By keeping the incident light, the metal and the refractive index at the prism side constant, the SPR angle is directly dependent on the change in the refractive index in the immediate vicinity of the gold surface. Consequently, any changes on the gold surface (e.g. molecule adsorptions) will change the surface plasmon resonance conditions and the SPR angle can be used to provide information on such changes.

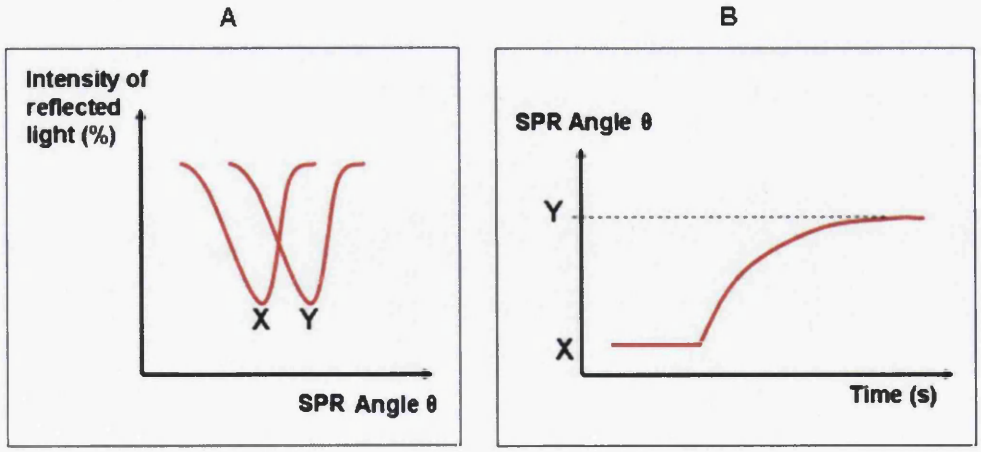

Figure 4.3 Illustration of SPR real-time measurement.

SPR is not only an excellent method to monitor the changes of the refractive index in the near vicinity of the metal surface, but it can also monitor these changes in real time. This is especially advantageous for the measurement of the kinetics of bio-molecules interactions. Figure 4.3 illustrates how real-time measurement can be carried out. When the refractive index above the gold surface changes, the SPR angle will shift as shown in Figure 4.3, where (X) represents the original plot of the reflected light intensity versus the incident angle and (Y) represents the plot after the change in the refractive index (Figure 4.3A). Therefore, by monitoring the shift of the resonance angle at which the dip is observed as a function of time, real time changes between two different states can be observed (Figure 4.3B). As a result, if these changes are due to molecular interactions, the kinetics of the interactions can be observed and studied in real time.

4.3. The Biacore system

The Biacore system exploits the surface plasmon resonance (SPR) as the detection principle to monitor the interaction between molecules. It is a bench-top instrument, connected to an associated personal computer for controlling operation and collecting results. Like all SPR-based instrument, the Biacore system utilises an optical method to monitor the changes in the refractive index near a sensor surface (within ~300nm to the surface). The Biacore system comprises of three essential units; the SPR optical detection unit, microfluidics system (liquid flow channel) and the sensor chip (Figure 4.4). These three units are integrated in the Kretshmann configuration [8], where all units are fixed in position and the reflected light intensity is monitored over a range of angles simultaneously. By eliminating all moving parts, the Biacore provides a robust and precise system, enabling rapid process to be monitored in real time.

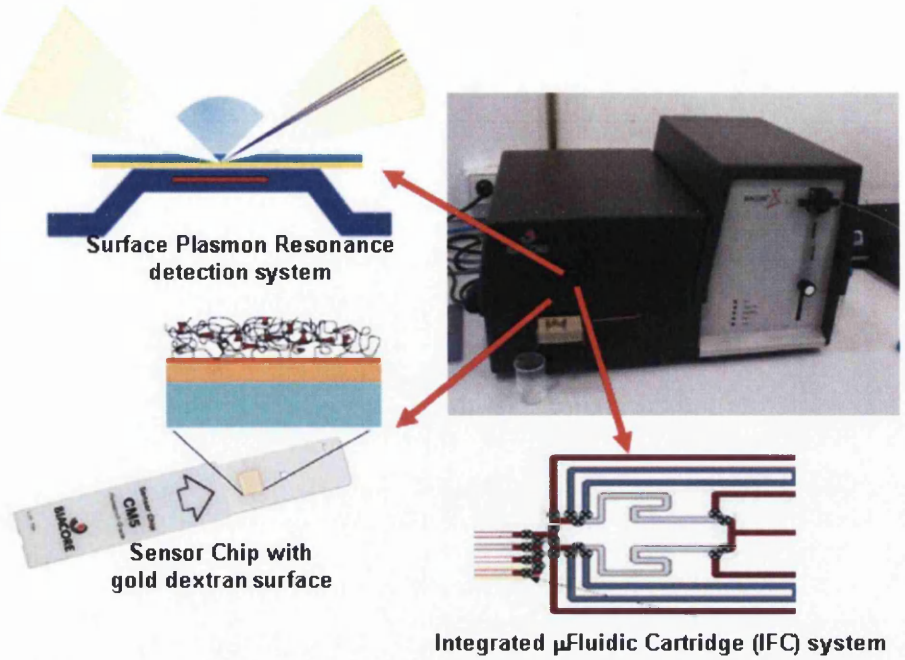

Figure 4.4 The three cornerstones technologies of the Biacore System consist of the SPR detection optical unit, the sensor chip and the microfluidic system [7].

The SPR is a phenomenon that requires a conducting film at the interface between media of different refractive index, so that photons can be converted into plasmons. In the Biacore system, the conducting film is a thin layer of gold on the removable glass sensor chip surface. The sensor chip is optically coupled to a semi-cylindrical prism (part of the SPR optical unit) through a silicone opto-interface. The opto-interface, with matched refractive index to the glass, provides good optical contacts between the sensor chip surface and the prism. With the sensor chip automatically docked, the microfluidic system ensures a continuous flow of sample across the sensor surface in a controlled manner. In the following sub-sections, more detailed description of each unit will be discussed.

4.3.1. The SPR optical detection system

The Biacore optical based SPR detector comprises of a prism, a light emitting diode, and a fixed photo-sensitive diode array detector, all configured in fixed position (Figure 4.5).

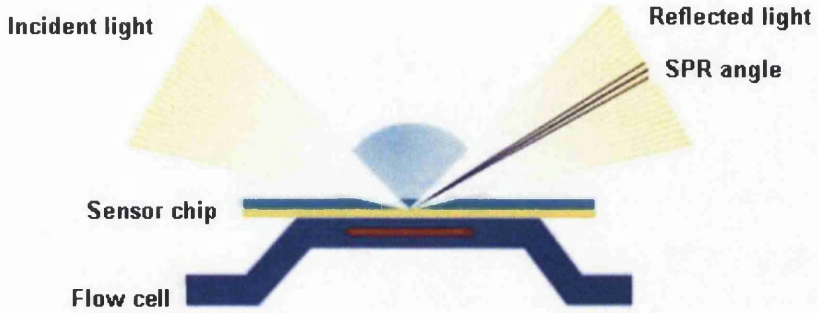

Figure 4.5 The Biacore SPR based optical detection unit.

The emitted light is wedge-shaped and has a wavelength of 760 nm. The wedge-based beam allows a broad distribution of incident light, covering a wide range of incident light angles. The polarised light is focused on the sensor chip under conditions of total internal reflection, which results in a reduction of the intensity of light reflected from the sensor surface at a specific angle. The corresponding reflected light hits the detector at different points and the two-dimensional diode detector array continuously records the angles of the reduced light intensity. The reflectance data is then calculated by computer interpolation algorithms, producing highly precise SPR angles.

As mentioned in Section 4.2, the SPR angle is dependent on the refractive index in the immediate vicinity of the gold surface. The Biacore detection system exploits this SPR criterion to measure molecular interactions. The binding of two different molecules is studied by attaching one to the surface of the sensor chip and injecting a sample containing the other over the sensor surface. A successful binding event will result in the increase of the mass concentration at the sensor surface, which corresponds to a change in refractive index of the solution close to the sensor surface. This leads to changes in the SPR conditions causing a shift in the position of the SPR angle. Similarly, when the molecules dissociates, a decrease in mass concentration followed by changes in the refractive index near the sensor surface will cause the

SPR angle to shift. These SPR angle shifts are converted to response units, called Resonance units (RU), where 1000 RU correspond to an arc angle change of ~0.1°. For most interactions, 1 ng/mm of analyte bound to the sensor surface is needed to cause an increase in signal of 1000 RU. The changes in SPR signal are recorded over time, producing a sensorgram – a continuous, real-time monitoring of the association and dissociation of the interacting molecules (Figure 4.6).

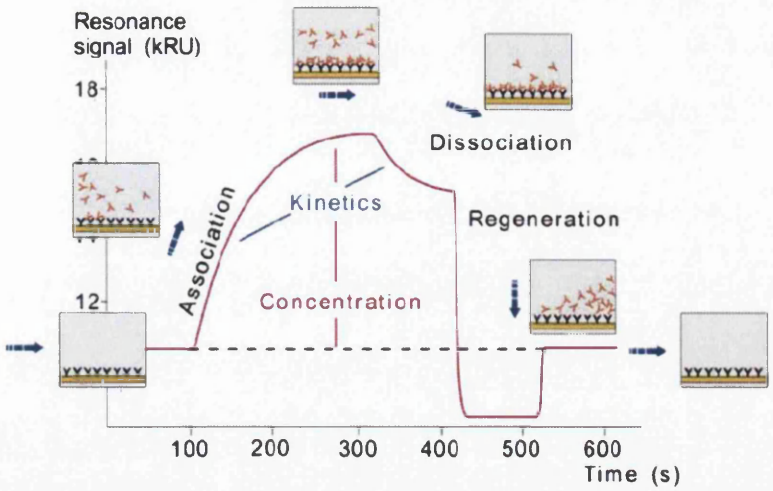

Figure 4.6 An illustration of a standard sensorgram [9]. The small inserts with the respective arrows indicate the binding interactions on the sensor surface.

4.3.2. The integrated micro-fluidic cartridges (IFC) system

The liquid flow channel system developed by Biacore is based around the integrated micro-fluidic cartridges (IFC). The IFC consists of a series of channels and valves in a plastic block (Figure 4.7). The micro-fluidic cartridge (IFC) system ensures precise sample delivery to the sensor surface, with very small dead volumes. Alternating switching between sample and running buffer flow is handled through microcomputer controlled pneumatics microvalves. Therefore, the delivery of reagents, buffer and samples to the flow cells is in a continuous, pulse-free and controlled flow through a precision liquid handling system.

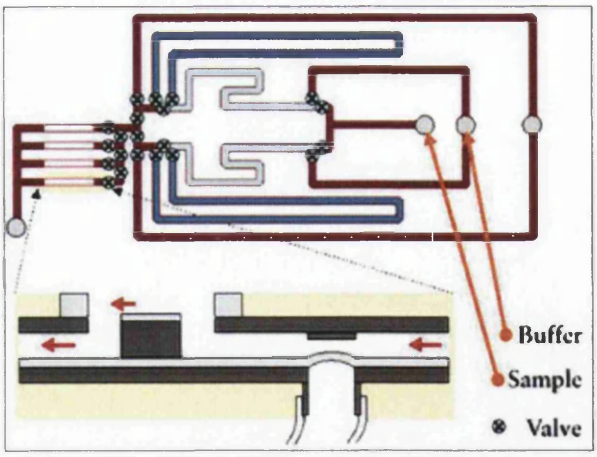

Figure 4.7 The micro-fluidic cartridges system and flow cells of a Biacore 2000 system [7].

The binding interactions and detection occurs in flow cells, which are formed on the sensor chip surface when the chip is automatically docked against a set of open channels on the surface of the IFC (Figure 4.8). As shown in Figure 4.8, three sides of the flow cells formed parts of the IFC walls, while the other side is formed by the surface of the sensor chip. The typical volumes of flow cells are of the order of 60 nl. Standard Biacore systems have two to four flow cells on each sensor chip, which can be used separately or in sequence. The high precision in sample delivery, combined with integrated micro-fluidics and detection, ensure that sample is delivered to the flow cells at constant concentration, under controlled condition. Therefore, interpretation and evaluation of the results is not only easier but also precise with high reproducibility.

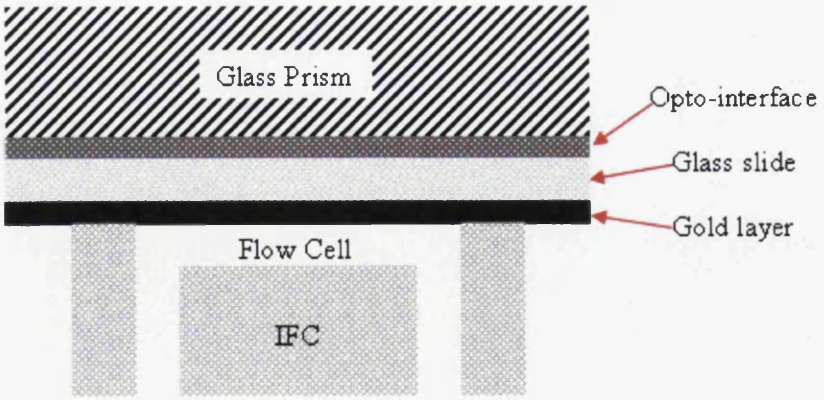

Figure 4.8 The IFC channels are pressed against the sensor surface to form the flow cell. The silicone opto-interface ensures good optical contact between the prism and the sensor chip surface [9].

4.3.3. The sensor chip

The sensor chip forms the physical barrier between the SPR optical unit (dry section) and the flow channel (wet section). It is the heart of the Biacore technology as it provides the right physical condition to generate the SPR signal. The sensor chip surface also serves as the platform for the immobilisation of a target molecule (ligand), of which one or more molecules can interact with. Therefore, the sensor chip plays a vital role on the quality of the interaction measurement, where it acts as a transducer by converting the mass change on the surface to an SPR signal. Figure 4.9 shows the range of Biacore sensor chips which are commercially available. As shown, a complete sensor chip consists of a sensor chip (gold film on glass), a plastic carrier and a protective sheath. The sensor surface is mounted on the plastic carrier for ease of handling. The carrier is in turn held in the protective plastic sheath [9].

Figure 4.9 The range of Biacore sensor chips. Standard sensor chip consists of a sensor chip (gold film on glass), a plastic carrier and a protective sheath.

A typical Biacore sensor chip consists of two essential features, which are a glass surface covered with a thin gold layer and a coating on the gold layer (Figure 4.10). The thin gold layer (50nm) is common to all Biacore sensor chips, as it provides the condition required for the generation of the SPR signal. Compared to other conducting materials, gold is not only inert in physiological buffer conditions, but also able to produce well-defined reflectance minimum at easily handled visible light wavelengths.

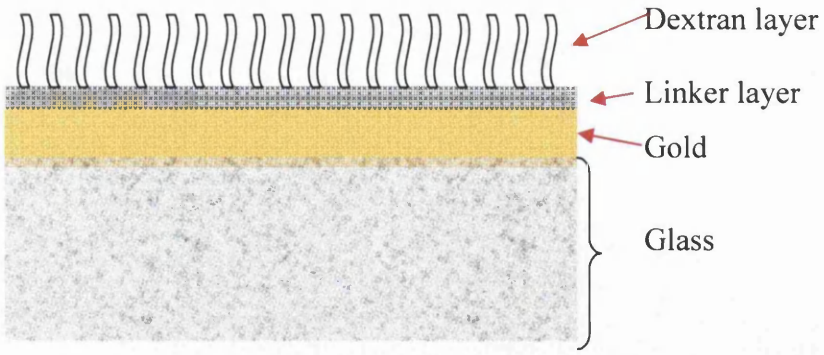

Figure 4.10 Cross section of a typical sensor chip.

The gold surface is covered with a covalently bonded monolayer of alkanethiol molecules linker layer (Figure 4.10). The monolayer serves as a protective barrier that protects biological samples from contact with the gold. On most sensor chips, a matrix of carboxymethylated dextran, a flexible unbranched carbohydrate polymer is covalently attached to the gold film through this linker layer. The dextran matrix provides the following advantages:

- It provides a hydrophilic environment favourable to most-solution based biomolecular interactions.
- It serves as a platform for the attachment of biomolecules through various well-defined chemistries.
- Due to its low isoelectric point (pI=4.5), it improves the immobilisation efficiency of positively charged molecules from dilute ligand solutions.
- It increases the net binding capacity of the surface, as compared to a flat surface.
- It reduces non specific binding of molecules to the gold surface.

There are several types of sensor chip designed to meet different types of applications. Table 4.1 summarises the essential features of each of the different sensor chips [9]:

Sensor chip	Surface Type	Uses
Sensor chip CM5	CM-dextran	General purpose
Sensor chip CM4	CM-dex CM with lower carboxymethylation level than CM5	For low immobilisation levels and reduced non-specific binding
Sensor chip CM3	CM-dextran with shorter dextran matrix than CM5	For large ligand molecules and particles
Sensor chip C1	Flat carboxylated surface, no dextran matrix	For applications where dextran interferes
Sensor chip SA	CM-dextran with immobilised streptavidin	For capture of biotinylated ligands
Sensor chip NTA	CM-dextran with immobilised NTA	For capture of poly-histidine tagged ligands
Sensor chip L1	CM-dextran with lipophilic modification	For capture of liposomes and supported lipid bilayers
Sensor chip HPA	Flat hydrophobic surface	For capture of lipid monolayers
Sensor chip Au	Plain gold surface	For surface interaction studies and custom design of surface chemistry
SIA kit Au	Plain gold surface, not mounted on chip carrier	For surface modifications outside Biacore systems

Table 4.1 Summary of the different type of sensor chip available in Biacore.

4.4. Biacore terminologies

The Biacore system is a real time bio-molecular detection system, which employs surface plasmon resonance (SPR) as the principle of detection. The quantitative measurements are made under continuous flow, with one molecule attached to a sensor chip surface, and another molecule in free solution flowing over the attached molecule to allow interactions. In this section, for the ease of the readers, the terms used in a standard Biacore assays are presented in Table 4.2.

Biacore Terminology	Description
Ligand	The molecule that is attached to the sensor surface (Figure 4.11).
Analyte	The molecule that is passed in solution over the attached ligand (Figure 4.11).
Flow cells	The area on a sensor surface where interactions occur. Flow cells are formed when a sensor surface is brought in contact against a set of open channels on the surface of the sample flow system.
Running buffer	Sample is injected over the sensor surface in a continuous flow of buffer, in a carefully controlled fashion. This buffer is termed running buffer.
Regeneration	The process of preparation for a new cycle, where bound analyte is removed from the sensor surface after an analysis cycle. This process should not damage the attached ligand.
Regeneration buffer	The buffer used for the regeneration process
Resonance Unit (RU)	The unit used to measure binding response. The response is directly proportional to the mass of biomolecules on the sensor surface.
Sensorgram	The real-time plot of response against time (Figure 4.6).

Table 4.2 The terms used in a standard Biacore assay [9].

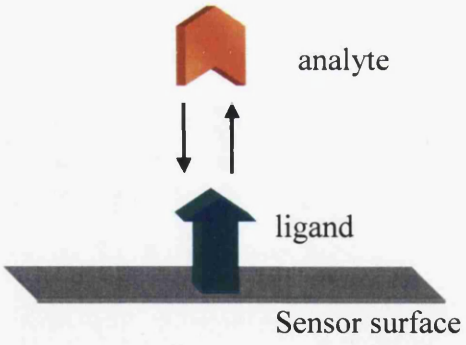

Figure 4.11 The ligand is the molecule that is attached to the sensor surface. The analyte, free in solution, is passed over the immobilised ligand to allow interactions.

4.5. General steps of Biacore experiments

A typical Biacore assay usually involves a few standard steps, as summarised in Figure 4.12.

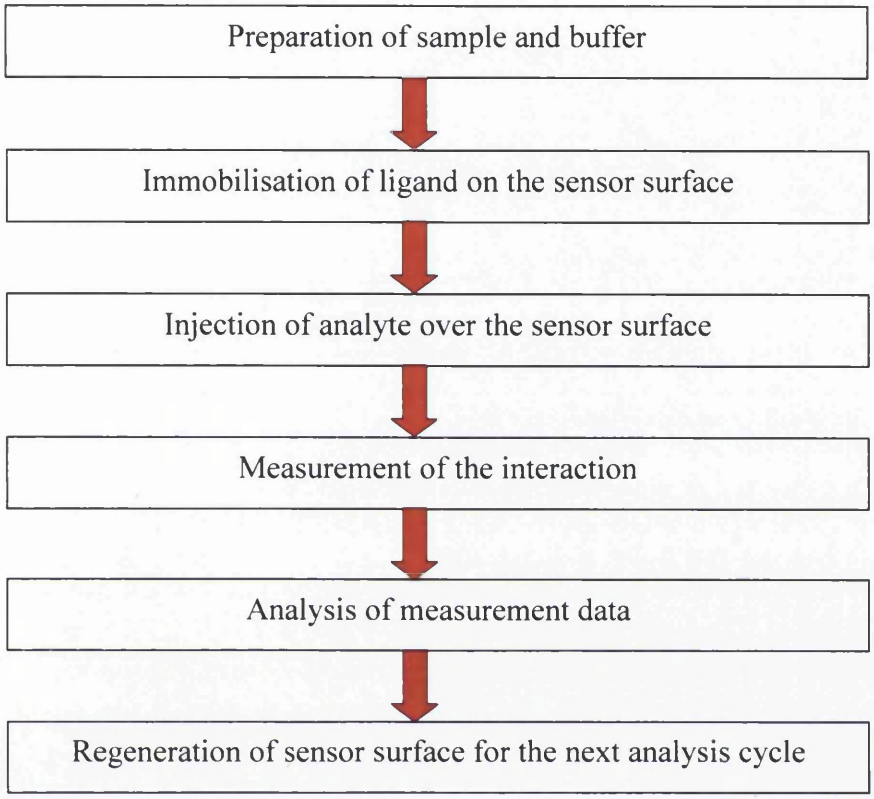

Figure 4.12 Standard steps in a typical Biacore assay.

4.6. Surface preparations : immobilisation methods

The most important and challenging step when setting up a Biacore assay is the immobilisation of ligands on the sensor chip surface. The immobilisation can be divided into two classes: (a) direct/permanent, where the ligand is covalently coupled to the dextran layer on the sensor surface and (b) indirect/capturing, where the ligand is bound, with high affinity, to another capturing molecule which was immobilised to the sensor surface. The covalent immobilisation to the dextran matrix of the sensor chip is the method of choice for attaching ligands to the surface. This is mainly due to the existence of free carboxymethyl groups on the sensor chip surface (Sensor chip CM5, various CM-series chips, Sensor chip L1 and Sensor chip C1), which serve as the basis for a range of covalent immobilisation chemistries. Among the most

common are amine coupling: exploit the presence of amine groups on the ligand after the activation of the surface with 1-ethyl-3-(3-dimethylaminopropyl)carbodiimide (EDC) and N-hydroxysuccinimide(NHS), thiol coupling: exploits the thiol-disulfide exchange between thiol groups and active disulfides introduced on either the ligand or the surface matrix and aldehyde coupling: exploit the reaction between hydrazine or carbohydrazide groups introduced on the surface and aldehyde groups obtained by oxidation of cabohydrates in the ligand (Figure 4.13) [9].

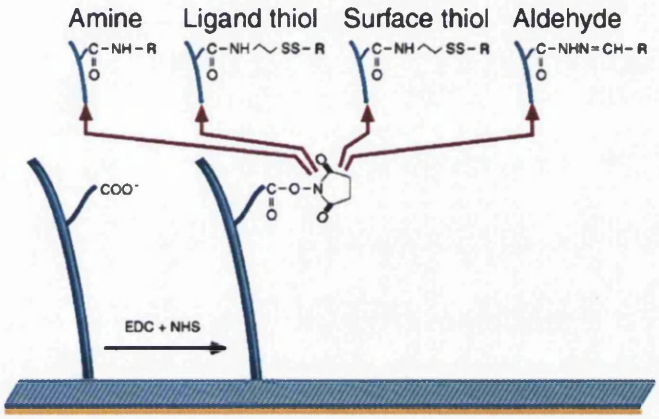

Figure 4.13 Covalent derivatives for direct immobilisation on the sensor chip surface.

Covalent immobilisation ensures the stable attachment of the ligand to the sensor surface under standard buffer conditions. During the regeneration cycle, bound analyte will be removed without affecting the ligands which are covalently coupled to the surface. For the capturing method, it relies on the high affinity binding of the ligand to the capturing molecule which was pre-immobilised on the sensor surface through covalent chemistry. In other words, the ligand will not be covalently bond to the surface and will be removed during the regeneration step. The most common capturing methods are streptavidin- or avidin–biotin capture, antibody-based capture and capture of tagged proteins. For these capturing methods, dedicated sensor chip (Table 4.1) and reagents kits are commercially available. Among these different types the capture of tagged proteins using Sensor chip NTA will be discussed in this work.

4.6.1. Sensor chip NTA

The Sensor chip NTA contains carboxymethylated dextran pre-immobilised with chelating agent nitrilotriacetic acid (NTA). This sensor chip provides a convenient approach of capturing his-tagged constructs via chelated divalent cations, such as Ni^{2+} (Figure 4.14). Proteins such as antibodies tagged with poly-histidine can be immobilised on the surface through this method.

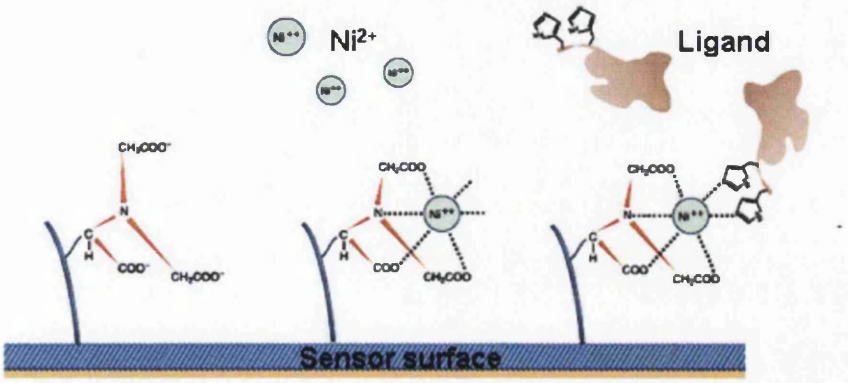

Figure 4.14 Ligand with poly-histidine tags is bound to the sensor surface via chelated nickel ions.

When using Sensor chip NTA, the running buffer used must not contain any divalent cations that may compete with the chelated Ni^{2+}. For reproducible results, it is also recommended to clean the flow system with a buffer containing 0.35 M EDTA the day before the experiment followed by continuous running buffer flow. For standard Biacore assay using the Sensor chip NTA, the sensor surface is firstly saturated with Ni^{2+} by injecting 500 μM $NiCl_2$ over the surface [9]. In general, the flow rate used is 2-10 μl/min and the ligand concentration is in the range of 10-200 nM. The capture amount can be monitored by changing the ligand concentration and the contact time (flow rate). The surface is usually regenerated for the next analysis cycle using buffer containing a high concentration of chelating agent (e.g. 0.25 M EDTA). The regeneration cycle will remove the chelated nickel as well as the ligand.

4.7. Summary

This chapter provided the theory of surface plasmon resonance and how it can be exploited by the Biacore system. The instrumentation needed for Biacore has been discussed and the details regarding the particular Biacore system used in this work are given in Chapter 5.

4.8. Reference

[1] Wood R W 1902 On a remarkable case of uneven distribution of light in a diffraction grating spectrum *Philysophical magazine* **4** 396

[2] Wood R W 1912 Diffraction gratings with controlled groove form and abnormal distribution of intensity *Philysophical magazine* **23** 310

[3] Otto A 1968 Exitation of nonradiative surface plasma waves in silver by the method of frustrated total reflection *Z Phys* **216** 398

[4] Kretschmann E and Reather H 1968 Radiative decay of nonradiative surface plasmon excited by light *Z.Naturf.* **23A** 2135

[5] Homola J, Yee S S and Gauglitz G 1999 Surface plasmon resonance sensors: review *Sensors and Actuators B* **54** 3

[6] Liedberg B, Nylander C and Lundstrom I 1995 Biosensing with surface plasmon resonance—how it all started *Biosensors Bioelectron.* **10** i

[7] *BIAcoreTechnology Handbook* 1998 (BIACORE AB)

[8] Kretschmann E 1971 Determination of optical constants of metals through the stimulation of surface plasma oscillations Z. *Phys* **241** 313

[9] *BIAcore Sensor Surface Handbook* 2003 (BIACORE AB)

Chapter 5

Experimental Techniques

5.1. Introduction

The various technique used in this work are discussed in this chapter. The Dimension 3100 AFM system was used for imaging and characterising samples in air. The operation of the AFM system will be discussed in terms of the apparatus and feedback mechanism. The Biacore X system was used to study the binding interactions between different functional molecules with the surface of ZnO. The apparatus and sample loading technique for the Biacore system will be presented. In addition, other techniques; fluorescence detection, thermogravimetric analysis (TGA), thin layer chromatography (TLC) and the gel permeation chromatography (GPC) were also used in this work. The fluorescence detection technique, fluorescence & confocal microscopy, and the TGA were used to verify the functionalisation of biomolecules of interest on ZnO surface. The former is in terms of fluorescence light detection and the later of temperature dependent weight loss. The TLC technique was used as a quick and easy analytical tool to check the success of synthesised compounds, while the GPC technique was used to measure the molecular weight of synthesised polymer. These experimental techniques will be briefly described in terms of their basic working principle with the relevant apparatus.

5.2. The Dimension 3100 AFM

5.2.1. General description

The Digital Instruments' Dimension 3100 AFM (DI 3100) was used for imaging and investigating the electrical properties of samples in air. The overall instrument as shown in Figure 5.1, is mounted on a vibration isolation table with an acoustic hood. These features ensure minimal vibrations and keep air flow and temperature stable around the microscope during imaging. The instrument is connected to a desktop PC via the Nanoscope IV Controller as shown in the schematic diagram in Figure 5.2 [1]. This system is capable of scanning in various different modes, for example contact-, non-contact-, magnetic force microscope, electrostatic force microscope and more.

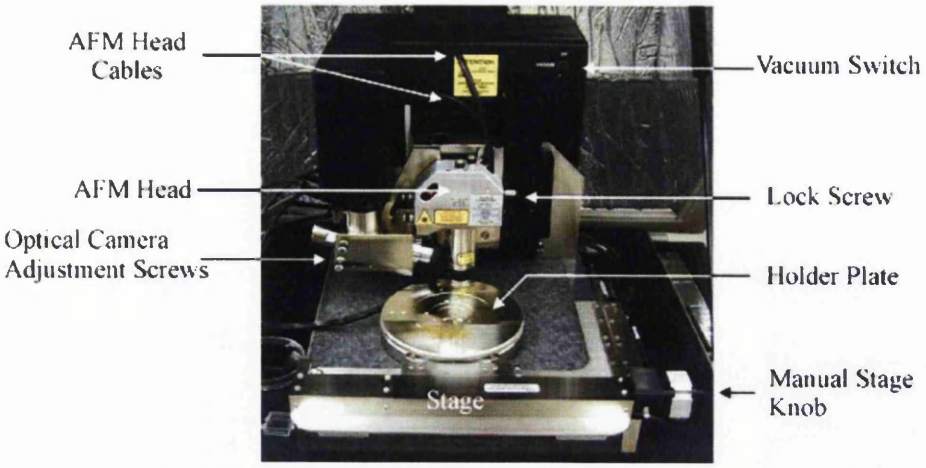

Figure 5.1 The overall instrument view of the Dimension 3100 AFM system [1].

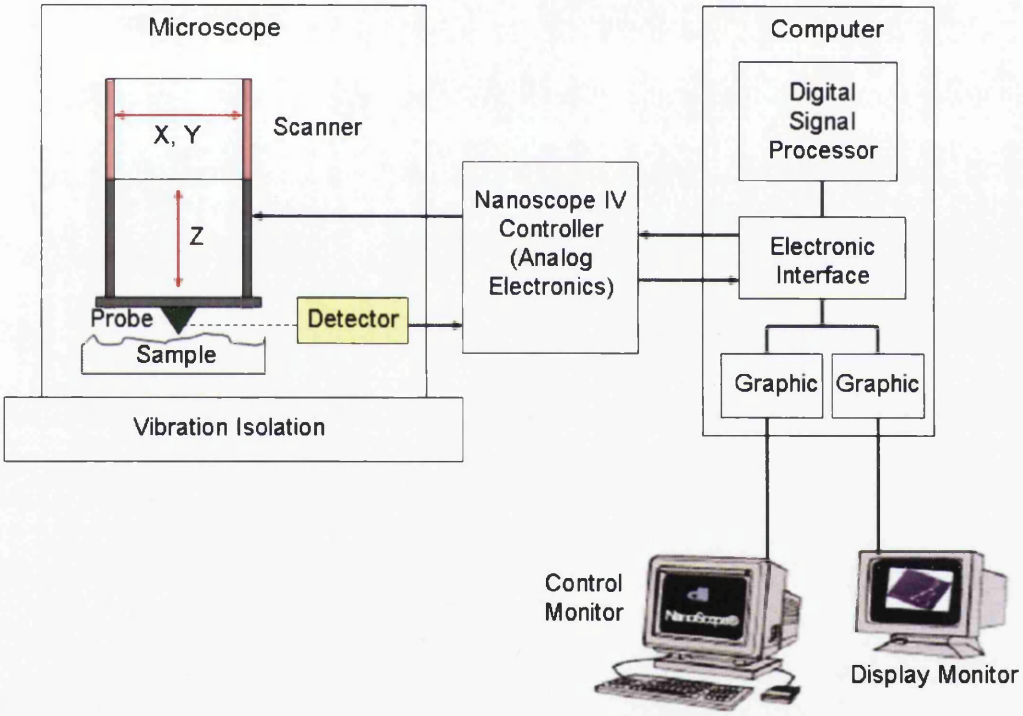

Figure 5.2 The schematic of the basic components in the Dimension 3100 AFM system [1].

5.2.2. Sample and tip positioning

The Digital Instruments scanners are made from piezoelectric material and consist of a single tube of independently operated piezo electrodes (Figure 5.3) [1]. The five independently operated piezo electrodes X (two segments: X and $\overline{X}$), Y (two segments Y and $\overline{Y}$) and Z enable the scanner to manipulate and probe samples with

high precision in 3 dimensions. For the Dimension 3100, the sample is kept stationary while the scanner moves the tip in a raster motion.

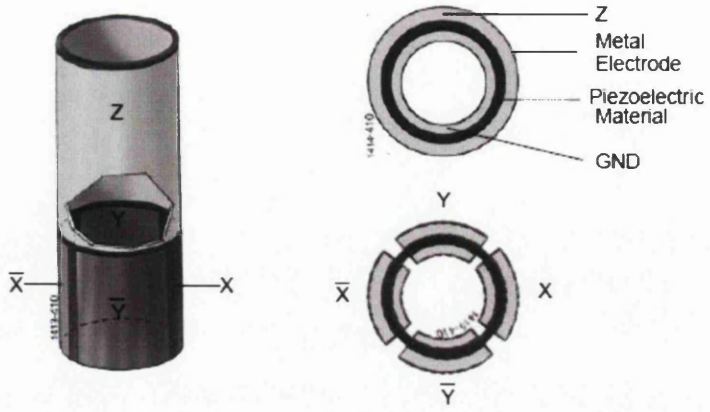

Figure 5.3 The typical scanner piezo tube in the X-Y-Z configuration.

5.2.3. Feedback control system

The DI 3100 system uses the feedback signals derived from laser beam deflections from the back of the cantilever onto a position sensitive photodiode detector (PSPD). The laser beam path in the system's scanner head is shown in Figure 5.4 [1].

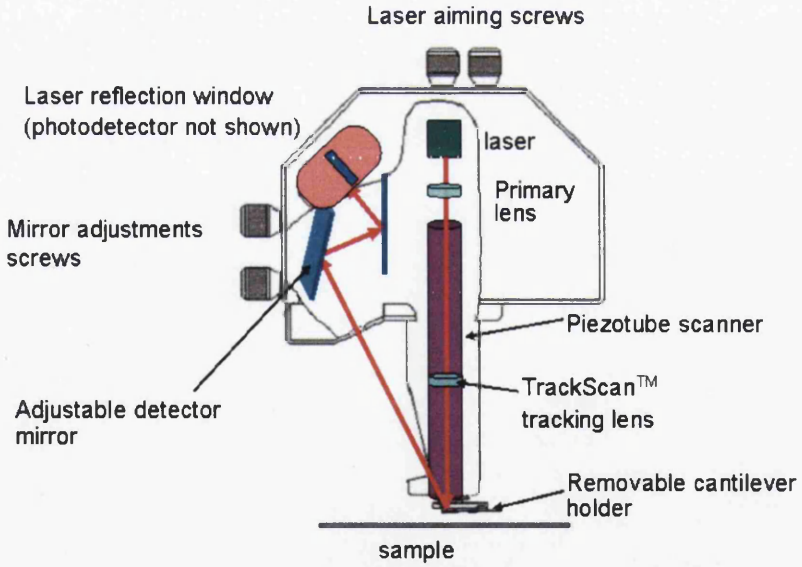

Figure 5.4 Schematic diagram of the laser beam deflection path for the Dimension 3100 AFM system [1].

The laser beam is aligned on the back of the cantilever using the laser aiming screws to give a sum signal of about 4V. The laser reflection is centralised on the laser reflection window using the mirror adjustments screws to give a vertical deflection

of 0V. The tip and the sample surface are located and focused using the PC control software. The cantilever frequency is also tuned using the PC control software. The desired scan area is chosen and an auto approach activated to start scanning.

For the electrostatic force microscope (also known as the scanning conductance microscopy) measurement, three different detection modes are used in the DI 3100 feedback loop: amplitude detection, phase detection and frequency modulation (FM) techniques (Figure 5.5).

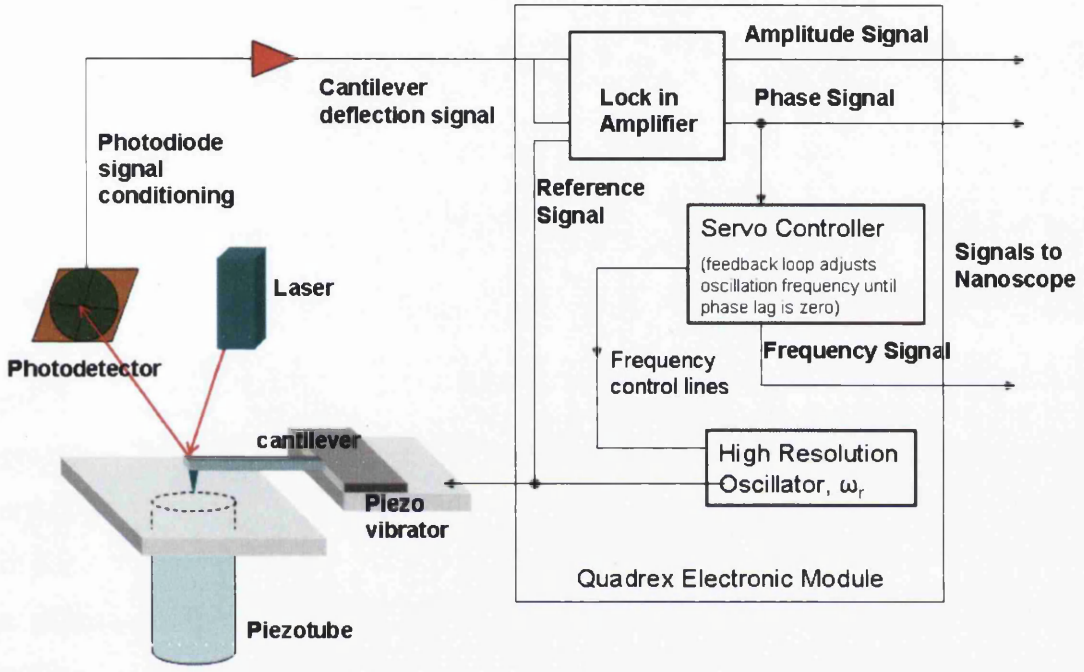

Figure 5.5 The different types of detection modes for EFM measurement: amplitude detection, phase detection and frequency modulation (FM).

5.2.4. AFM electronics and software

The Dimension 3100 microscope is connected to the computer via the nanoscope controller (Nanoscope IV). The nanoscope controller acts as the interface between the computer and the AFM microscope by converting the user commands (from computer) into signals that are used to direct the microscope. The controller is also responsible for obtaining data from the photodetector and conveys it to the computer for analysis. For electrostatic force microscope measurement, the tip voltage may be applied directly from the Nanoscope IV controller electronics via the AFM computer software interface.

Further information regarding the DI 3100 AFM system can be found in the manufacturers' notebook [1].

5.2.5. Data analysis and image processing

Data images are captured in Realtime scanning mode and almost all captured images have some artifacts/noise associated with them due to instrumental defects. Therefore, image processing is required to remove these artifacts before viewing and analysing the captured images. The Nanoscope software (V. 6.13) is equipped with a variety of analysis/modification functions for quantifying the surface properties of different samples. One of the most common analysis procedures is the measurement of depth, height and width which is done via Section analysis command in the Nanoscope software. This simple command works by drawing a cross-sectional line on any part of the AFM image (height, phase or amplitude data) and the vertical profile along the line will be displayed. Almost all AFM images possess certain amount of deviation in the background plane due to the movement of the piezoelectric scanner in a curved motion over a sample surface ('bow' artifact) and also the impossibility to align the probe tip exactly perpendicular to the sample surface ('tilt' artifact). The background artifacts are removed from the AFM images by using the Modify Plane Fit command in the Nanoscope software. The Plane Fit command calculates a single polynomial of a selectable order for an entire image (or selected areas) and then subtracts the polynomial fit from the image [2]. This command allows operation in either or both X-Y directions. In other words, a plane in the X-direction can be modified without affecting the plane in the Y-direction. Figure 5.6A illustrates an image of a test grid with 'bow' background, which was removed using Plane Fit 2^{nd} order command in both XY directions (Figure 5.6B). Flatten modify command is also sometimes used to eliminate low frequency noise and tilt from an AFM image resulted from a vertical offset between scan lines. The Flatten command is a filter that modifies the image on a line-by-line basis and in the fast scan directions. It calculates the best least-squares fit polynomial of a specified order (1^{st} order: 'tilt' background, or 2^{nd} or 3^{rd} order: 'bow' background) for each scan line and then subtracts the polynomial fit from the original scan line [2]. Consequently, the average Z value of each scan line is fitted to 0V out of the +/- 220V Z range. More detailed information on the various analysis and modify functions can be found in the Command Reference Manual [3].

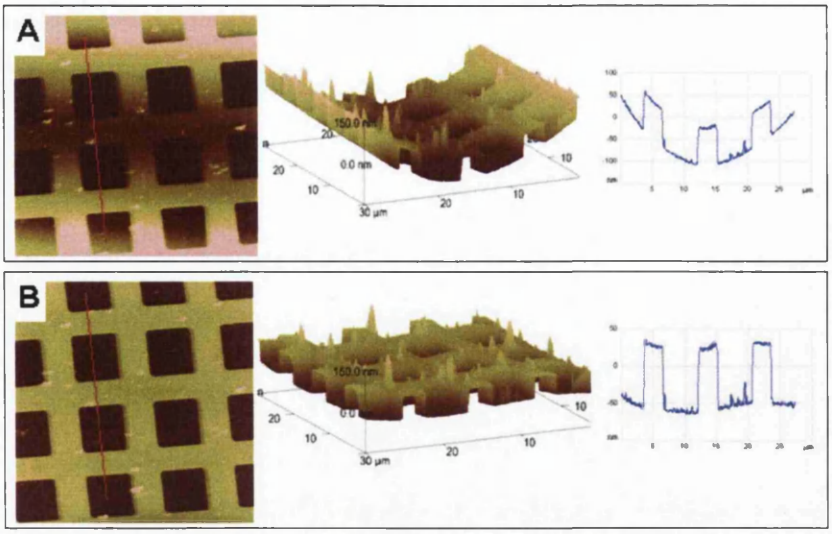

Figure 5.6 (A) AFM image of a test grid with 'bow' artefact with its 3D representation and line profile taken across the red line. (B) AFM image of (A) after plane fit command with its 3D representation and line profile taken across the red line.

5.3. The Biacore X system

The Biacore X system from GE Healthcare was used to study the interactions between various molecules in a controlled environment. The instrumentation for the Biacore X is shown in Figure 5.7. The name and functions of each part, labelled from A to H, are presented in Table 5.1.

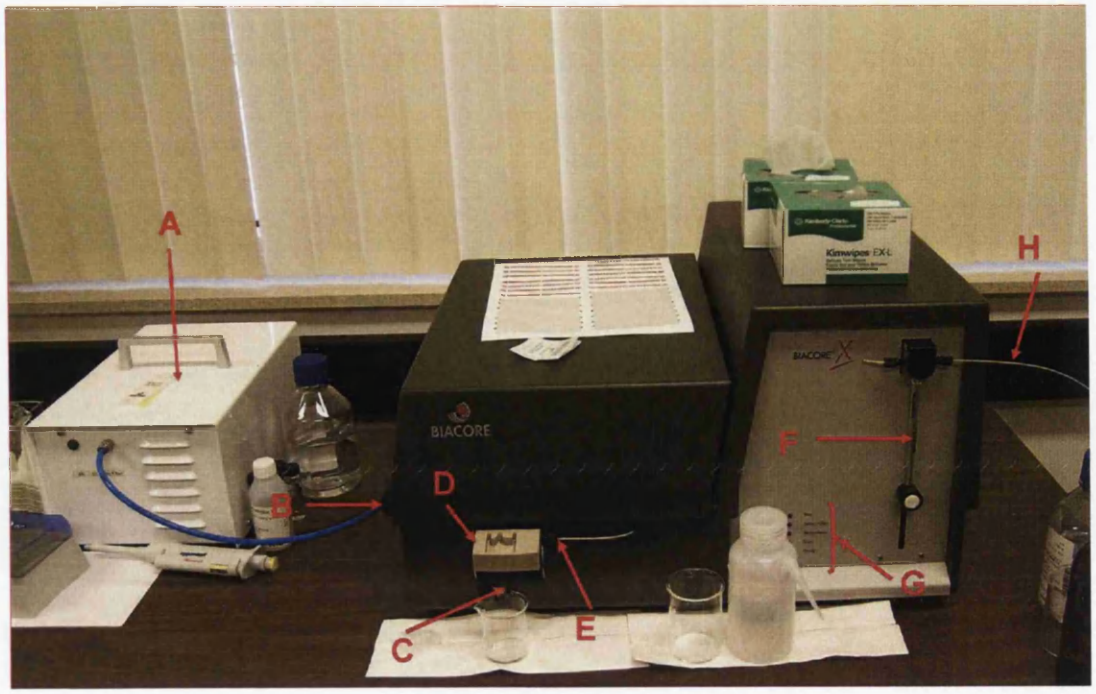

Figure 5.7 The Biacore X system instrumentation.

Label	Parts	Function
A	Stepper motor pump	Designed for smooth pulse-free flow.
B	Sensor chip docking port	Sensor chip is inserted and docked against the integrated fluidic cartridge (IFC).
C	Waste out port	Outlet for waste from flow cells.
D	Connector block	The connector block has one inlet port, a pump port for buffer flow with a screw-nipple fitting for the pump tubing and an injection port for manual injection of sample and reagents. The injection port is connected directly with flow channels in the IFC. There are three outlet ports for waste and for recovered sample (from the sample loop and from the sensor chip surface) (Figure 5.8).
E	Pump tubing	Allow buffer pumped by the syringe pump into the IFC inlet via the connector block
F	Syringe pump	Designed for accurate pulsefree flow at rates down to 1 µl/min. The continuous flow pump takes liquid from a buffer bottle and pumps it directly into the IFC inlet through the connector block.
G	LED status indicator	Indicate the status of the instrument in terms of ready, error temperature, sensor chip, and run.
H	Buffer tubing	Aspirate running buffer into the IFC using the syringe pump.

Table 5.1 The relevant parts in the Biacore X instrumentation as shown in Figure 5.8.

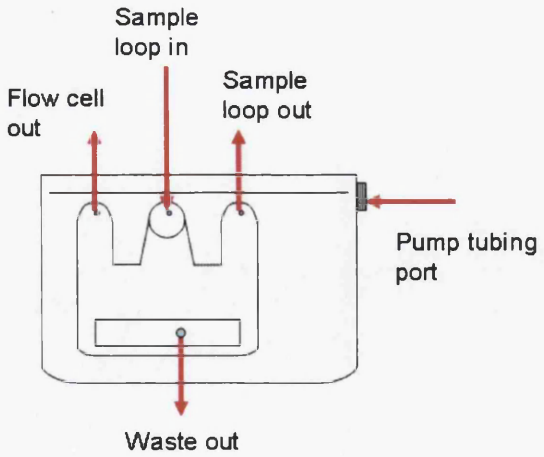

Figure 5.8 Ports available on the connector block.

5.3.1. The integrated microfluidic system

The microfluidic pathway of the Biacore X is shown in Figure 5.9.

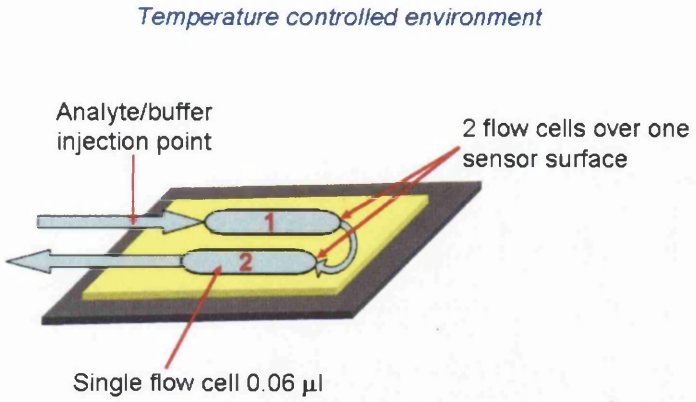

Figure 5.9 The microfluidic system (IFC) of the Biacore X. The IFC is housed in a temperature controlled environment and there are two available flow cells over one sensor surface.

As shown, there are two available flow cells on a single sensor surface and each with a volume of 0.06 µl. The advantage of having two flow cells is that one flow cell can be used as a true reference during a single sample injection. The Biacore X comes equipped with an automatic in-line reference subtraction for a single sample injection, using flow cell 2-1 or 1-2. The automatic reference subtraction and the controlled environment of the flow path enable measurements of weak binding and also measurement of small molecules.

5.3.2. The sample loading technique

The Biacore X is a semi-automatic instrument. The sample of interest is loaded manually into the sample loop of the IFC and is injected over the sensor surface automatically under precise control of the computer. The sample is loaded into the loop via an injection port on the connector block ('sample loop in' in Figure 5.8) by using a standard micropipette. When injecting the sample using the micropipette, it is important to maintain the sample dispersion at the beginning and end of the injection to a minimum. This can be done by introducing small air bubbles to separate the sample from the buffer in the sample loop. This 'air bubbles technique' is achieved by aspirating small volumes of air and sample alternately into the pipette tip after the main sample volume, as shown in Figure 5.10. The sample is then injected, by placing the pipette tip vertically and firmly into the connector block injection block.

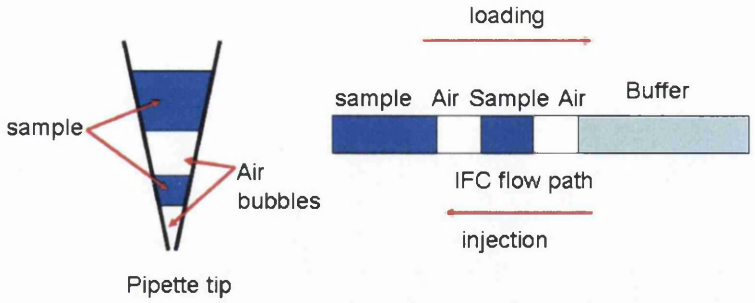

Figure 5.10 The 'air bubbles technique' to reduce sample dispersion.

5.3.3. Data analysis

The operation of the Biacore X instrumentation is controlled from a separate personal computer. The control software enable user interface to the complete system, from pump control and sample injection to data collection. The logistic of the instrument and the data collection (from diode detection arrays) are controlled by a built-in microcomputer embedded in the instrument. During an experiment, the progress of the analysis is presented in real time and displayed as sensorgram on the computer screen. BIAevaluation, a software package consists of powerful numerical integration, global fitting algorithm and also includes pre-defined kinetic models for homogeneous or heterogeneous interactions, is used to analyse sensorgram data [4]. This data evaluation software ensures that results are well analysed and presented clearly.

In general, data analysis is divided into two categories; (a) quantitative analysis; to determine whether specific interaction occurs between a given analyte and ligand (yes or no binding) and (b) qualitative analysis; to compare and evaluate the binding kinetics. For quantitative analysis work, it is important to have a test negative control to exclude any false positive results. In this work, only quantitative analysis was used. As mention in Section 4.3.1, positive/negative binding interactions on the sensor chip surface changes the SPR angle, which are converted into Response Unit (RU) on a sensorgram. Consequently, quantitative analysis is simple and straight forward, where specific interactions (yes/no binding) are detected directly from the sensorgram as increased in RU relative to the initial baseline. As illustration, the

affinity analysis of bovine serum albumin (BSA) to antibody BSA is discussed in the following sub section.

Further information regarding the Biacore X can be found in the manufacturers' handbooks [5, 6, 7], which described the technology and its application in more detail.

5.3.3.1. Affinity analysis of BSA to antibody-BSA

BSA (66 kDa) and antibody BSA (150 kDa) were both purchased from Sigma Aldrich. Running buffer (HBS-EP: 10 mM HEPES pH7.4, 150 mM NaCl, 3 mM EDTA, 0.005 % (v/v) surfactant P20), regeneration buffer (10 mM glycine-Hcl, pH 2.5) and immobilisation buffer (10 mM sodium acetate pH5) were purchased from Biacore, GE Healthcare UK Ltd. The antibody BSA was immobilised on a Sensor Chip CM5 using an amine coupling kit (750 mg 1-ethyl-3-(3-dimethylaminopropyl)carbodiimide hydrochloride (EDC), 115 mg N-hydroxysuccinimide (NHS), 2 x 10.5 ml 1.0 M ethanolamine-HCl pH 8.5) purchased from Biacore, GE Healthcare UK Ltd.

The result of the amine coupling of anti-BSA on Sensor Chip CM5 is shown in the sensorgram of Figure 5.11. The surface of the Sensor Chip CM5 is coated with a matrix of carboxymethylated dextran, a flexible unbranched carbohydrate polymer [7]. The carboxylic acid groups on the dextran are activated using 1:1 of EDC/NHS to reactive succinimide esters ((1) in Figure 5.11). The amine groups on the antibody BSA will react spontaneously with these reactive esters forming strong covalent bonds. The sensor surface was stabilised by injecting ethanolamine to remove any excess reactive groups. The immobilised amount of anti-BSA is extracted from the sensorgram (Figure 5.11) by comparing the RU at (3) to the initial baseline response unit at (2). For this case, the immobilised anti-BSA RU was ~ 11000 RU equivalents to concentration of 10 ng/mm^2 on the sensor chip (1000 RU ~1 ng/mm^2).

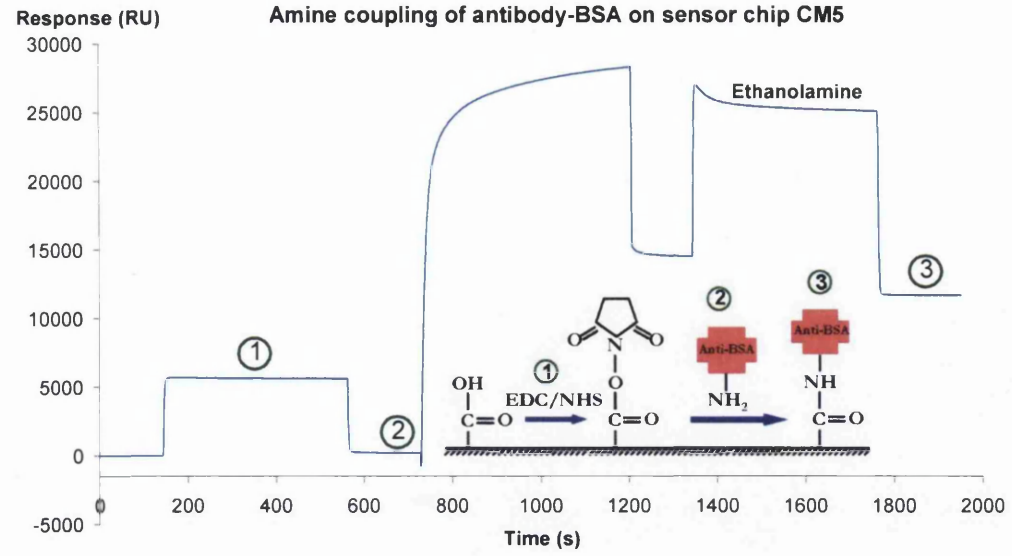

Figure 5.11 Sensorgram showing the result of the amine coupling of antibody BSA on Sensor chip CM5. (1) The sensor surface is activated with 1:1 of EDC/NHS to give reactive sucinimide esters. (2) Antibody BSA is injected over the surface and the esters react spontaneously with the amine groups on the antibody. Ethanolamine is injected to deactivate excess reactive groups on the surface. (3) The resultant bound antibody BSA.

Figure 5.12 shows the sensorgram data of the interaction of BSA with the immobilised anti-BSA. The interactions of BSA to anti-BSA immobilised on the sensor chip are illustrated in the inset in Figure 5.12. The bound BSA can be removed by injecting regeneration buffer across the sensor chip surface, in preparation for the next analysis cycle.

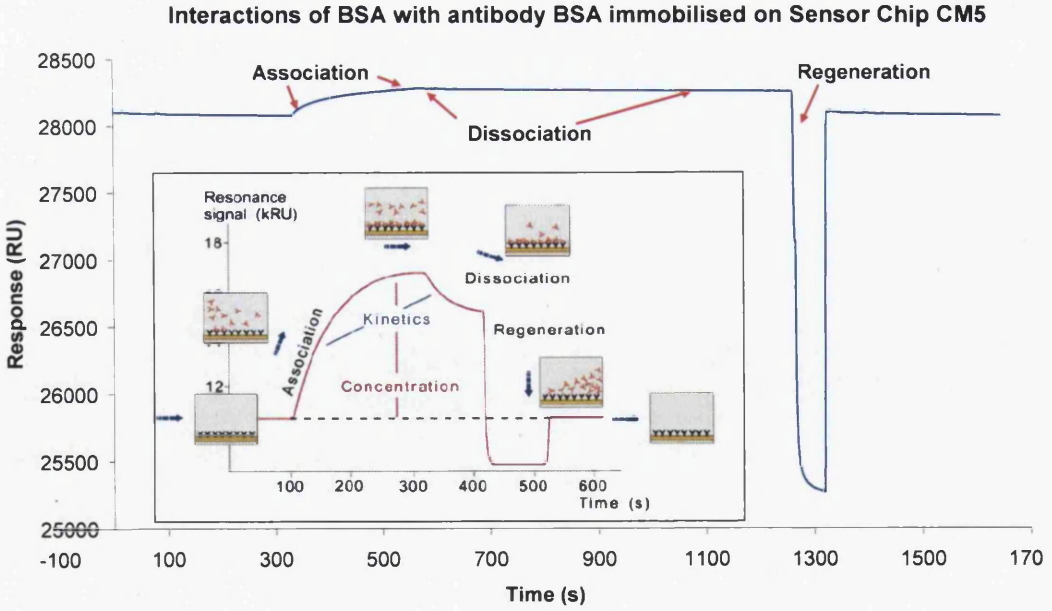

Figure 5.12 Sensorgram of the interaction of BSA (20 µg/ml) to anti-BSA. Inset: illustration of a standard sensorgram [7].

BIAevaluation software was used to combine the results of the interactions of BSA at various concentrations (2.5 μg/ml, 5 μg/ml, 10 μg/ml and 20 μg/ml) as shown in Figure 5.13. Using the software, the respective sensorgrams baseline was aligned to 0 RU and the amount of bound BSA were measured by comparing the final RU to the baseline.

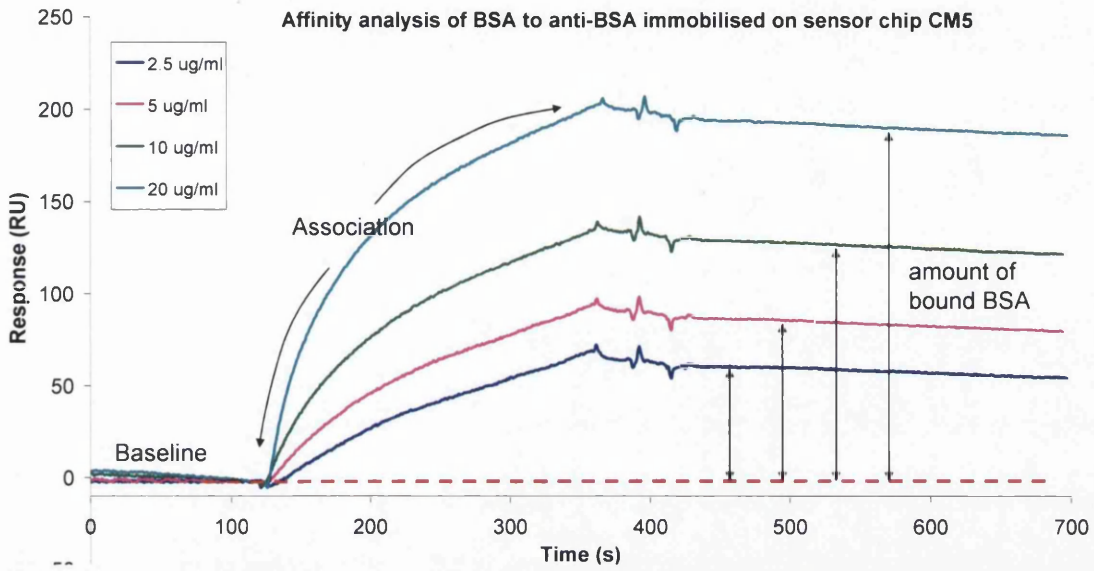

Figure 5.13 Sensorgrams of the interactions of BSA (2.5 μg/ml (blue), 5 μg/ml (violet), 10 μg/ml (green) and 20 μg/ml (dark blue)) to anti-BSA. The amount of bound BSA is measured as shown.

5.4. Other Techniques

5.4.1. Fluorescence detection techniques

The fluorescence and confocal microscopy are two common techniques used in medical and biological science. In this section, a brief outline of the principles and techniques of these fluorescence detection methods will be discussed.

5.4.1.1. General description: The fluorescence process

Fluorescence is the property possessed by a substance (molecule) which absorbs light at a particular wavelength and subsequently emits light of a longer wavelength after a brief interval. This substance is better known as a fluorophore or fluorescent dye. In general, the fluorescence process is divided into three stages: excitation, excited-state lifetime and fluorescence emission. The electronic-state diagram (Jablonski diagram) in Figure 5.14 illustrates the fluorescence process [8].

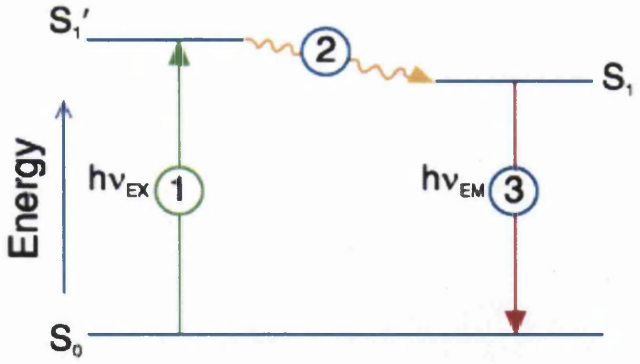

Figure 5.14 Jablonski diagram illustrating the processes involved the creation of an excited electronic singlet state by optical absorption and subsequent emission of fluorescence.

When light from an external source such as an incandescent lamp or laser shines on some molecule (fluorophore), the light photon of energy $h\nu_{EX}$ is absorbed by the molecule. This additional absorbed energy causes the molecule to be excited from the electronic ground state (S_0) into a higher electronic single state (S_1') (labelled (1) in Figure 5.14). During the excited state lifetime (typically 1-10 nanoseconds), the molecule will undergo conformation changes and may also interact with the molecular environment. Consequently, the photon energy S_1' will be partially dissipated, lowering the energy state to S_1 (labelled (2) in Figure 5.14). It is from this relaxed singlet excited state S_1 that fluorescence emission originates. Then, as the molecule returns to its initial ground state S_0, a photon of energy $h\nu_{EM}$ is emitted (fluorescence). The energy of this photon is lower due to the energy dissipation during the excited-state lifetime. As such, the wavelength of this photon is longer than that of the excitation photon $h\nu_{EX}$. The difference in energy or wavelength represented by ($h\nu_{EX}$ –$h\nu_{EM}$) is called the Stokes shift. The Stokes shift is fundamental to the sensitivity of fluorescence techniques because it allows emission photons to be detected against a low background, isolated from excitation photons. The four basic elements of a fluorescence detection system are; a) an excitation source, b) a molecule (fluorophores), c) wavelength filters to isolate the emission photons from the excitation photons, d) a detector that records the emission photons and transduces the signal into readable output (electrical signal or image).

Typical fluorescence images are shown in Figure 5.15.

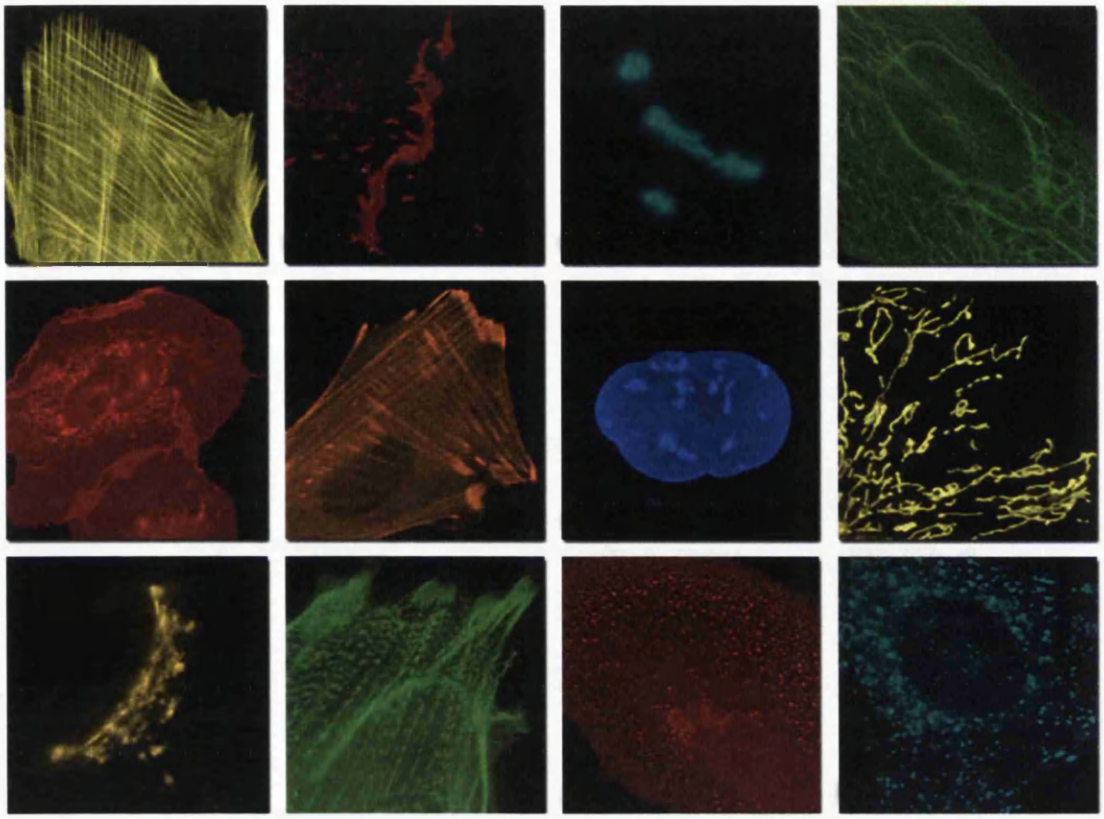

Figure 5.15 Fluorescence imaging of Anthozoa fluorescent protein sub-cellular localisation fusions [9].

5.4.1.2. The fluorescence microscope (Zeiss Axio Imager Z1)

The fluorescence microscope is based on the phenomenon that when certain substances are irradiated with the light of a specific wavelength, these substances will emit energy that is detectable as visible light (Section 5.4.1.1). Modern fluorescence microscopy techniques combine the power of high performance optical components with computerised control of the instrument and digital image acquisition. In general, the light source of the microscope must be powerful enough to generate the excitation light intensity in very narrow ranges of the spectrum. Most commonly used light sources are the mercury or xenon arc (burner) lamps. Figure 5.16 illustrates the actual beam path in a microscope equipped with fluorescence equipment [10].

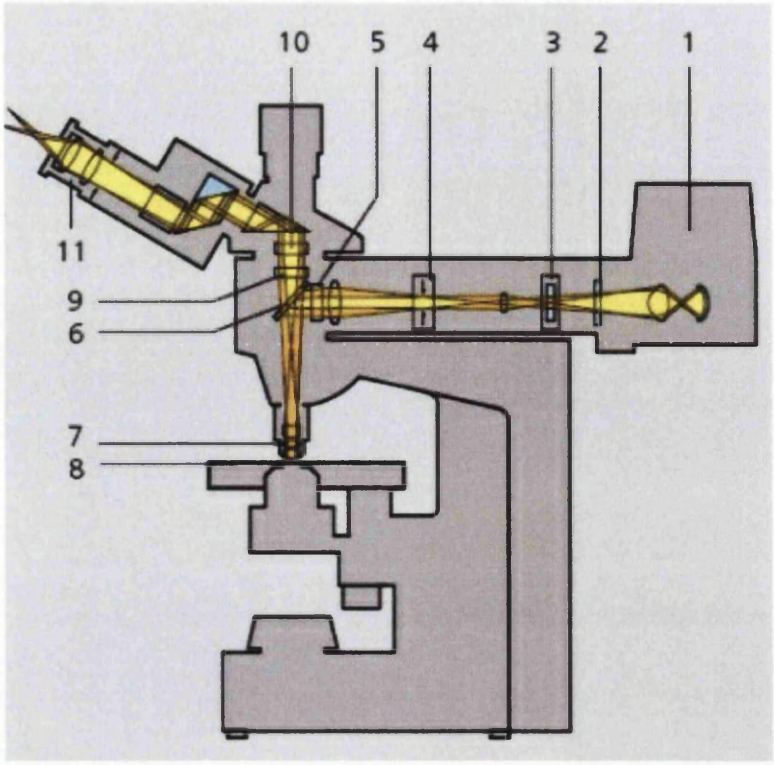

Figure 5.16 The beam path in a microscope equipped with fluorescence equipment [5].

As shown, the microscope is made up of a combination of a dichroic mirror (the dichroic beam splitter (**6**) in Figure 5.16) and optimum quality fluorescence filters (the excitation filter (**5**), the heat-protection filter (**2**), the red attenuation filter/barrier slider (**3**) and the emission filter (**9**) in Figure 5.16), that are responsible to transmit the required wavelengths to excite the fluorescent chromophores, and block the un-required ones as completely as possible. The light from an additional light source (**1**) travels to the excitation filter (**5**) via the heat-protection filter (**2**), the red-attenuation filter/barrier slider (**3**) and the luminous-field diaphragm (**4**). The excitation filter is integrated into the reflector slider which also contains the beam splitter (**6**). The short wave exciting light is reflected by the dichroic beam splitter into the specimen (**8**) via the objective (**7**). The objective gathers the resultant emission light which is transmitted by the dichroic beam splitter (**8**) and passed through the emission filter (**9**). The dichroic beam splitter (**8**) only allows the emission light with longer wavelengths than the excitation light to pass through while the emission filter (**9**) or better known as the barrier filter serves to block out the remaining excitation light. Finally, the microscope image, which only consists of fluorescence light, is formed at the tube lens and the eyepiece. A specific combination of excitation filter, emission

filter and dichroic mirror is needed to visualise and/or quantitate the fluorescence emission from a particular fluorescent chromophore. The dichroic mirror is mounted on an optical block referred to as a filter cube. The excitation and emission filters are usually fixed to the filter cube. The cube serves as a convenient means to change the dichroic mirror without having to directly change either the mirror or filters. For ease of changing optical elements, the microscope is equipped with several filter cubes to detect the different types of available fluorophores.

The fluorescence microscopy system used in this work is the Zeiss Axio Imager Z1 with Isis software 5.1 (Figure 5.17).

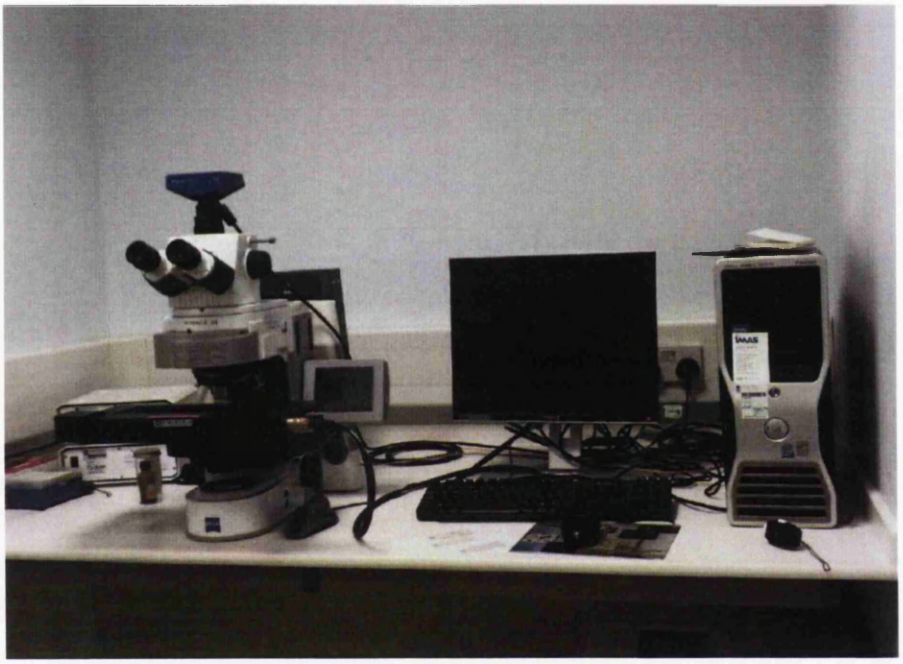

Figure 5.17 The Zeiss Axio Imager Z1 instrumentation.

It is a trinocular, fully motorised, PC controlled high performance research microscope with transmittance and reflectance modes for optical imaging. This upright microscope system is equipped with a sensitive monochrome camera (Zeiss, Axiocam MRm) and has filter cubes for UV (Dapi, Hoechst), CFP, FITC, YFP, TRITC and Cy5 (far red). The user interface is very simple and the entire system is straightforward and easy to use. It has a TFT display touch screen that allows user to manipulate the motorised microscope and change between cube filters, without using the external PC as a 'stand along' system. Among the available filter cubes, only

DAPI, FITC and TRITC according to the traditional fluorochromes that are commonly used for blue, green, and red fluorescence, will be used in this work. The imaging equipment includes a high quality B&W digital camera, PC computer, Samsung 19" LCD monitor, and AxioVision software.

5.4.1.3. The scanning confocal microscope (Zeiss LSM 510 metasystem)

The confocal microscope is a modified fluorescence microscope with superior imaging quality. This technique exploits two main ideas which are point by point illumination of the sample and the rejection of out of focus light [11,12,13]. The Zeiss LSM 510 metasystem was briefly used in the early part of the fluorescence detection analysis work. Due to the nature of the work, the fluorescence microscope later was found to be sufficient. This section will briefly describe the basic working principle of a confocal microscope. Figure 5.18 shows the basic set up of a confocal microscope. A beam from the intensive light source travels through the objective and the scanners, to excite the fluorescence sample. The resultant fluorescence light from the sample travels back through the objective and the scanners. The light then passes through the beam splitter and is focused on the pinhole placed in the conjugate confocal (hence the term the confocal) plan of the sample. After the pinhole, the fluorescent light is separated from the excitation light by the barrier filters and is measured by the light detector. The pinhole ensures that only fluorescent light from the focal point of the objective is allowed through (rejecting all out of focus light). Hence, light from say, plan X (Figure 5.18), will be blocked out by the pinhole.

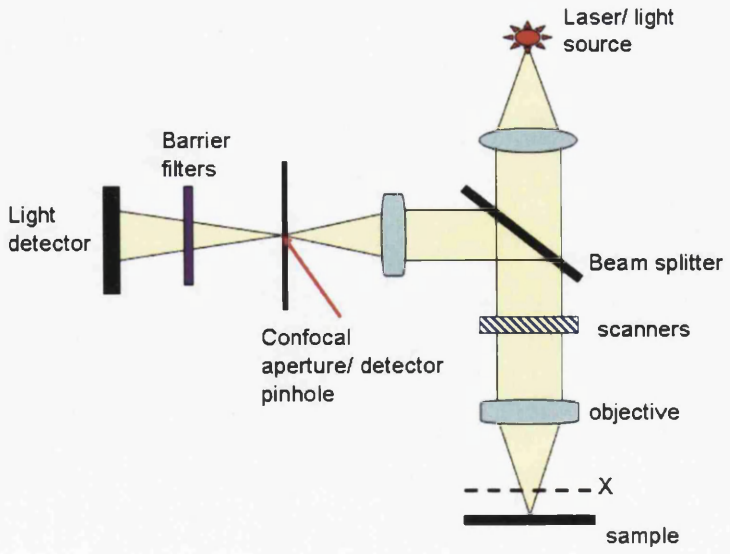

Figure 5.18 Schematic setup of a scanning confocal microscope.

5.4.2. Thermogravimetric analysis (SDT Q600 TA Instrument)

Thermogravimetic analysis (TGA) is an analytical technique used to monitor the weight loss (or weight gain) of a material as a function of temperature. The TGA measurement is normally carried out in air or in an inert atmosphere. As materials are heated, drying or chemical reactions that liberate gasses can cause them to loose weight. On the other hand, some materials can also gain weight by reacting with the atmosphere in the testing environment. These weight loss and gain are disruptive processes to the sample material, and thus by monitoring three crucial measurements: weight, temperature and temperature change, a material's thermal stability and the fractions of components present in the material can be evaluated.

The SDT Q600 model from TA Instrument was used in this work to examine the binding of samples to ZnO surface. The main components in the SDT Q600 are the thermobalance and the temperature and control system (Figure 5.19A), the furnace and the purge gas system (Figure 5.19B) [14]. The thermobalance features a horizontal dual-balance mechanism that ensures high sensitivity and accuracy in weight signal measurements. For temperature control and measurements, a thermocouple pair of matched platinum/platinum-rhodium within the ceramic beams provides direct sample, reference and differential temperature measurements. It allows a wide range of the temperature measurement from ambient up to 1500°C.

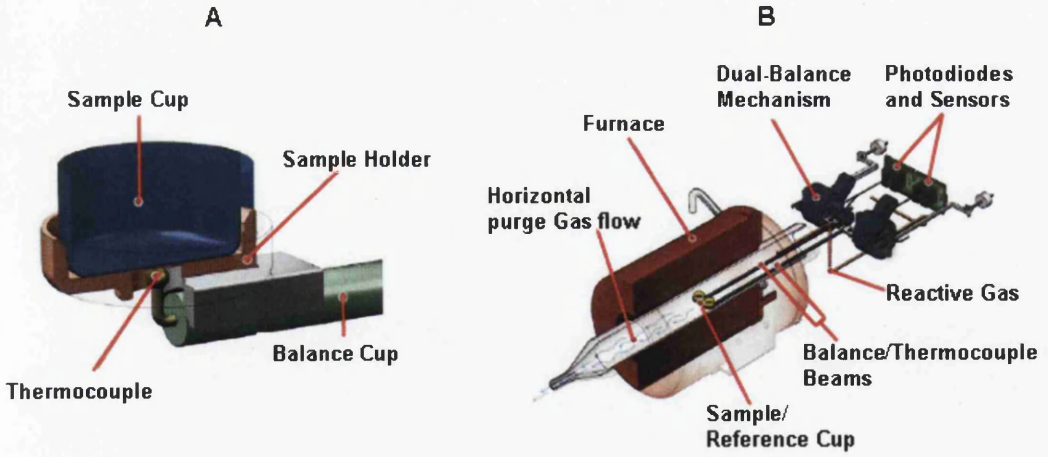

Figure 5.19 The main components in the SDT Q600 model from TA Instrument [14].

For such a wide temperature range, the Q600 has a reliable, horizontal furnace encased in a perforated stainless steel cowling, which ensure accurate and precise delivery of programmed and isothermal operation. In addition, the furnace is designed with an automatic furnace opening/closing, easy sample loading and rapid post-experiment furnace cool down. The horizontal purge gas system is equipped with a digital mass flow control and integral gas switching, and is responsible for the precise metering of purge gas to the sample and reference pans. It is designed to help produce a better baseline, prevent back diffusion and efficiently remove decomposition products from the sample area.

The TGA analysis in this work was performed by Mr Robert Jenkins from Cardiff University.

5.4.3. Thin layer chromatography (TLC)

Thin layer chromatography (TLC) is a type of column chromatography, however instead of a column, a strip of plastic (with one side coated with a thin layer of alumina or silica gel) is used as the adsorbent. This technique is simple, reasonably quick, inexpensive and requires only small amount of sample. It serves as an analytical tool to check the purity of a compound or to determine the number of components in a mixture. In addition, TLC is also useful as an initial check on the identity of a compound. This can be done by spotting the plate with the sample as well as with a known compound for comparison. Figure 5.20 shows the typical steps in a TLC analysis. A pencil line is first drawn near one end of the plate to mark the original position. The substance to be tested is placed in a single spot, X on the pencil line (about 10 μl) using a micro capillary (Figure 5.20A). The plate is then 'developed' by placing it in a developing jar (beaker covered with watch glass) with a small amount of solvent (Figure 5.20B). Due to capillary action, the solvent rises up the plate, carrying the component of the sample with it. Different components in the sample are carried to different distances up the plate since they differ in their adsorption on the adsorbent coating (Figure 5.20C). As such, with the presence of several components in the sample, a column of spots is seen on the developed plate. The bottom of the plate will have more polar compounds, whereas the top plate will have less polar compounds.

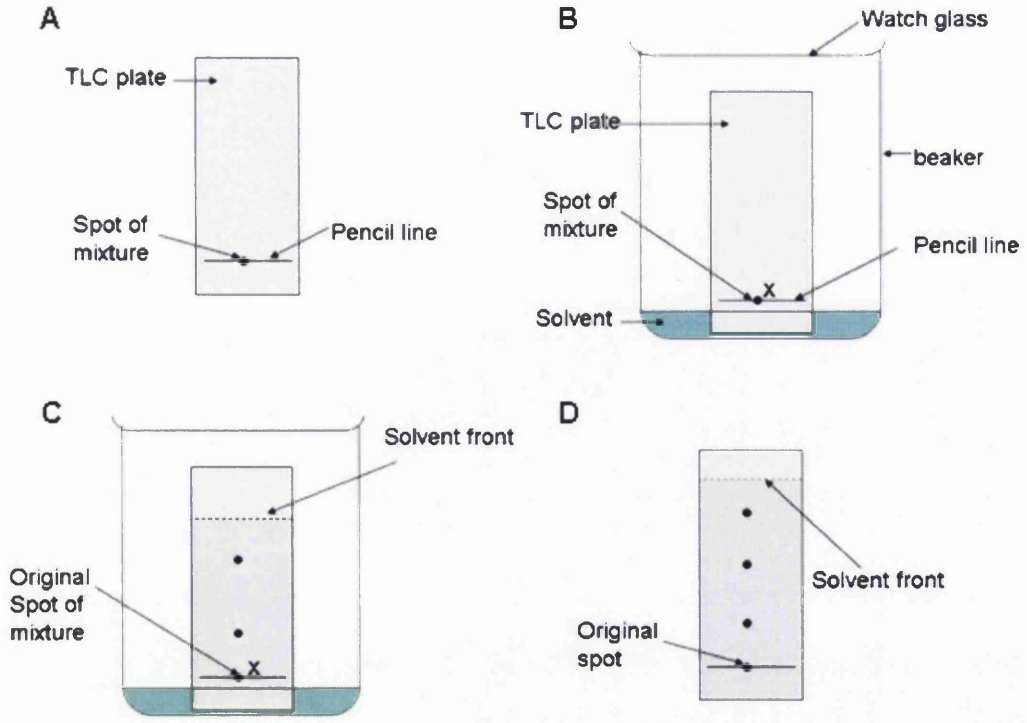

Figure 5.20 Thin layer chromatography (TLC). (A) A pencil line is drawn at one end of the TLC plate and a spot of sample is placed on it. (B) The spotted plate is placed in a beaker filled with the appropriate solvent. The beaker is covered with a glass watch is to ensure that the atmosphere is saturated with the solvent vapour. (C) As the solvent travels up the plate, the different components of the mixture travel at different rates. (D) The final developed plate.

The distance that the spot of a particular compound moves up the plate relative to the distance moved by the solvent front is called the retention factor, or R_f value. When all variables are held constant: solvent, adsorbent, thickness of adsorbent and amount of compound on the plate, the R_f value for a compound is constant. Figure 5.21 shows how the identity of a compound maybe be determined by comparing the unknown sample with a known compound on the same plate.

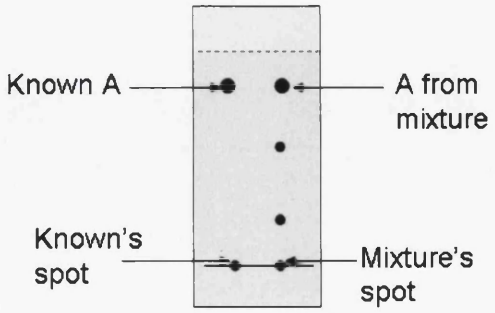

Figure 5.21 A known and unknown sample may be analysed on the same plate at the same time under the same environment.

5.4.4. Gel permeation chromatography (GPC)

Gel permeation chromatography or in short GPC is a technique for measuring molecular weight and molecular weight distribution. This technique involves passing a solution of polymer through a tubular column packed with polymeric gel (cross linked) beads. As the polymer passes through the gel beads under high pressure flow, some fractions of the polymer will be separated into the pores of the gels, while others pass by the gel beads. The residence time of a given polymer chain in the packed column depends on its molecular weight. Low molecular weight chain will easily be force into pores of the gel and thus takes longer travel through the column while a high molecular weight chain will by pass the pores of the gel and thus take a shorter time to travel down the column. For the measurement of the polymer's molecular weight averages and distribution, a calibration curve using monodisperse standard is required. The most commonly used standard is the polystyrene standards, which are available from most chemical suppliers.

The GPC was performed by Smithers Rapra Technology Ltd using Viscotek 'Evolution', with associated pump and autosampler. The analysis was aqueous based GPC, with columns appropriate to low/medium molecular weight polymer. The column used was PL Aquagel guard plus 1 x P2* and 1 x P3*, 30 cm, 8 μm. The experiment was performed at 1.0 ml/min flow rate and 30 °C temperature. A single solution of the sample was prepared by adding 10 ml of eluent (0.2 M $NaNO_3$, 0.01 M NaH_2PO_4, pH 7) to 20 mg of synthesised sample and left overnight to dissolve. The sample solution was well mixed before part was transferred to an autosampler vial, without filtration, prior to chromatography.

5.5. Summary

The nature of this work, involving multidisciplinary fields from nanotechnology, biological life science to chemistry requires a variety of experimental techniques/methods. The Dimension 3100, equipped with nanosize tip and precise feedback and control system, is a versatile technique for the characterisation of nanomaterials. The Biacore X provides a way to monitor interactions between molecules in real time under a controlled environment. The semi-automatic nature of Biacore X instrumentation ensures that samples are injected over the sensor surface in an accurate pulse free flow at rates down to 1 μl/min, under precise control of the computer. Therefore, Biacore X, with its complete integrated system, ensures effective, precise and label free detection analysis of interactions between molecules of interest. The other techniques, namely the fluorescence & confocal microscopy, the thermogravimetric analysis (TGA), the thin layer chromatography (TLC) and lastly the gel permeation chromatography (GPC), are all well known techniques in biological science and chemistry. Each of these techniques was chosen due to their availability and also their suitability to the relevant experimental parts of this work discussed in chapters 6 and 7.

5.6. References

[1] *Scanning Probe Microscopy Training notebook Version 3* 2000 (Digital Instruments) Veeco Metrology Group, SantaBarbara, USA, 2001

[2] *NanoScope Software 6.13 User Guide* (Digital Instruments) Veeco Metrology Group, SantaBarbara, USA, 2001

[3] *Nanoscope Command Reference Manual* (Digital Instruments) Veeco Metrology Group, SantaBarbara, USA, 2001

[4] *BIAevaluation Software*, version 3.2 1994–2001 (BIAcore AB) GE Healthcare

[5] *BIAtechnology Handbook* 1998 (BIAcore AB) GE Healthcare

[6] *BIAapplication Handbook* 1994-1998 (BIAcore AB) GE Healthcare

[7] *Sensor Surface Handbook* 2003 (BIAcore AB) GE Healthcare

[8] Online resource: http://www.invitrogen.com/site/us/en/home/References/Molecular-Probes-The-Handbook/Introduction-to-Fluorescence-Techniques.html

[9] Online resource: http://zeiss-campus.magnet.fsu.edu/articles/probes/anthozoafps.html

[10] Kapitza H G and Lichtenberg S 1997 *Microscopy from the very beginning 2nd revised edition* Carl Zeiss Jena GmbH

[11] Sheppard C J R and Shotton D M 1997 *Confocal Laser Scanning Microscopy* (New York: Springer)

[12] Inou´e S and Spring K R 1997 *Video Microscopy: The Fundamentals* (New York: Plenum)

[13] Pawley J B 1995 *Handbook of Biological Confocal Microscopy* (New York: Plenum)

[14] Online resource: http://www.tainstruments.com/

Chapter 6

Qualitative Conductance Studies of Zinc Oxide Nanostructures

6.1. An overview

One-dimensional nanostructures have well-defined nanoscale dimension and high surface-to-volume ratio, where surface and interface properties (i.e. electronic conductance) are extremely sensitive to minor surface perturbations (e.g. binding of biomolecules). Biosensors based on these nanomaterials are extremely sensitive, and it was estimated that the detection levels can be down to the single molecule level. Therefore, nanowires can serve as a bridge between biomolecules and micro solid-state device, so that biological processes occurring on the surface of the nanowire can be transduced into measurable signals through electrodes to computers.

The structural and characteristic knowledge of the nanostructures used as a platform for biosensor is crucial for the successful implementation of the device. Since the principle of the biosensor detection is mainly due to the change in conductivity of the nanostructure upon the binding of biological molecules, it is important to ensure that the chosen nanostructures are conductive. Prior to the invention of SCM, metal contacts were needed to characterise the electrical properties of nanostructures. Typical metal contact fabrication processes involved a number of different steps depending on the chosen method. Fabrication of metal contacts across nanostructures is time consuming and impractical for characterising a number of different samples.

Scanning conductance microscopy (SCM) is a valuable technique that provides a direct means of characterising the electrical properties of nanostructures, without having to fabricate metal contacts, which often require expensive lithography equipments. Contact resistance issues and unwanted Schottky barriers also hinder direct electrical measurements, especially on nanostructures. By monitoring the electrostatic force between the probe tip and sample, the SCM is able to provide a quick conductivity screening of various nanostructures. Furthermore, the topography of the samples is mapped out simultaneously for better understanding of the properties. The principle operation of the SCM was presented in Chapter 3.

In this work, SCM was used to compare the electronic properties of different ZnO nanostructures synthesised via two different methods. The SCM studies were performed using a Dimension 3100 atomic force microscope (AFM) equipped with the Nanoscope IV controller (Veeco Instruments Inc.). Preliminary work looked at bare silicon substrate capped with an oxide layer to test the feasibility of the SCM technique. The SCM phase results for each of the respective nanostructures were then presented followed by a comparison study between them.

6.2. Sample preparation

The probe tip used was a Platinum-Iridium coated silicon tip doped with antimony (n) with curvature radius R = 20-40 nm, quality factor Q ~ 200 ± 2, spring constant k ~ 2.8 N/m and resonant frequency f = 68 ± 3 kHz (SCM-PIT, Veeco probes). The substrates for all experiments are p-type degenerately doped Si wafer with a 350 nm oxide layer on top. During an interleave scan, the probe tip was biased from 8V to -8V in steps of 2V.

6.2.1. Silicon substrates

Silicon dioxide layer on a 1 cm x 1 cm highly degenerated (p++) Si wafer was grown using standard thermal growth method. The 1 cm x 1 cm silicon wafers were placed in a furnace under inert nitrogen gas environment. The nitrogen flow rate was 0.6 L/min and the initial temperature was 650 °C. Once the furnace reaches the process temperature of 1100 °C, pure oxygen gas was flowed at the rate of 0.6 L/min and the duration of the oxidation process was 5 hours. The estimated thickness of the SiO_2 layer was 350 nm. The silicon substrates were cleaned by soaking with acetone in an ultrasonic bath for 5 minutes. This was followed by thorough scrubbing of the substrate surface with a clean cotton swab drenched with acetone and blown dry with Nitrogen gun.

6.2.2. ZnO nanostructures

The hydrothermally grown ZnO nanorod samples were courtesy of Professor Shu Ping Lau of Nanyang Technological University, Singapore. The nanorods were prepared from an aqueous solution of zinc nitrate hydrate polyethyleneimine and

hexamethylenetetramine [1]. The seed layer on Si substrate was prepared from zinc acetate solution [2]. The CVD nanorods and nanowires were grown in a tube furnace by carbothermal reduction of ZnO powder (C:ZnO ratio of 1:1 in weight) at 1080°C in a flow of Ar and O_2 (5%) at 100sccm. The structures grew on Si substrates placed downstream at a temperature of about 500 °C and 700 °C for the nanorods and nanowires, respectively. No catalyst was used on the substrates. The as grown nanorod/nanowires were dispersed in ethanol and sonicated for 30 minutes. 5 µl of the dispersion was then deposited onto a thoroughly cleaned Si/SiO_2 substrate and blown dry with nitrogen.

6.3. Calibration studies on bare silicon substrate capped with oxide layer

Quantitative calibration of the SCM phase measurements were carried out on bare Si substrate with a thermally grown oxide layer. Such study is important to test the feasibility of the SCM technique. The thickness of the as-grown oxide layer on the silicon substrate was verified using the quantitative analysis method proposed by Cristian Staii *et. al* [4]. Figure 6.1A shows a typical result of the SCM-phase measurements of the bare Si substrate. The tip-sample separation was 60 nm and 25 - 30 line scans were obtained for each values of bias voltage (8V to -8V in step of 2V) applied to the tip. The SCM measurements were repeated for tip-sample separation of 35 nm, 70 nm, 80 nm, 90 nm and 100 nm. The values of phase shift as a function of V_{tip} and as a function of V_{tip}^2 for each different tip-sample separation are plotted in Figure 6.1C and Figure 6.1D respectively. By using least square method, the graphs in Figure 6.1D are fitted to Equation 3.20 (refer Chapter 3) and the second derivative capacitance C'' for each graph is evaluated (from the slope of the respective graph). The thickness of the oxide layer is verified by substituting these experimental values into Equation 3.23 (refer Chapter 3) with $\varepsilon_s = 3.9$ and $R_{tip} \sim 30$ nm. The calculated oxide thickness has the average value of 340 nm, which is in excellent agreement with the estimated thickness of the as-grown oxide layer on the silicon substrate.

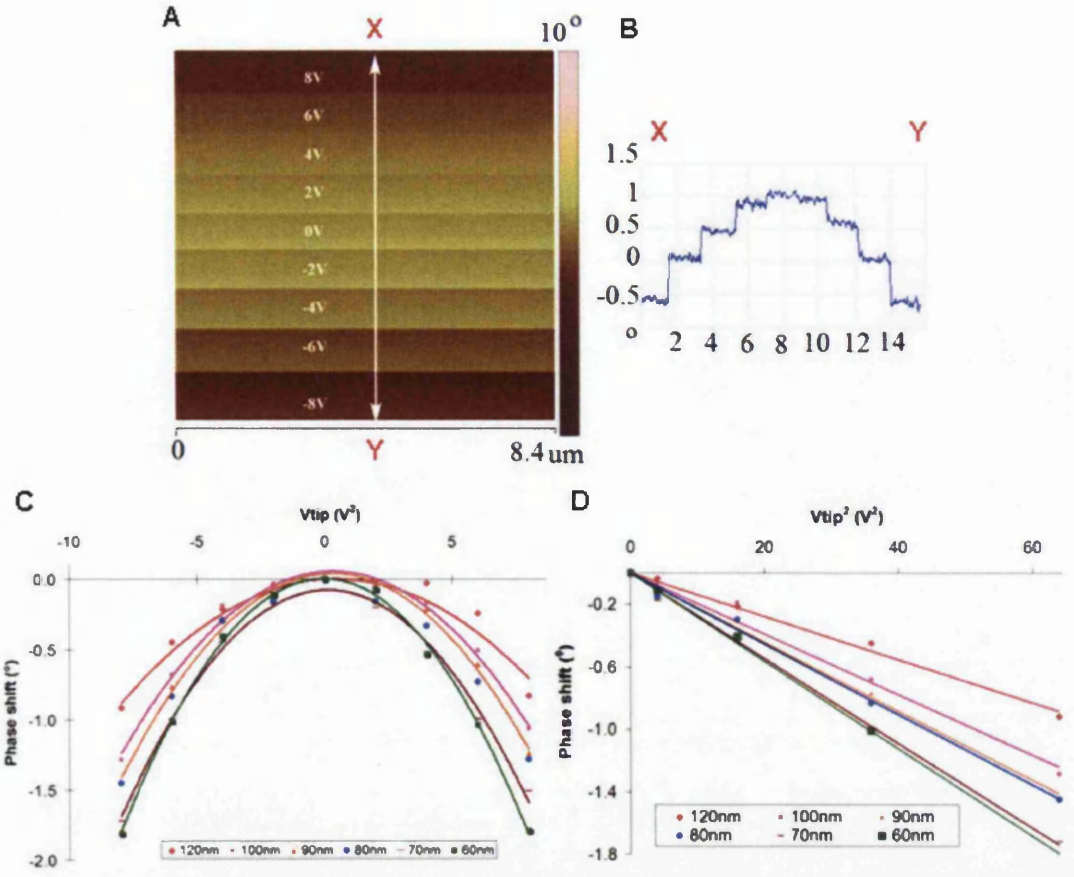

Figure 6.1 (A) Typical SCM image of bare Si substrate capped with an as grown oxide layer. Experiment was performed by varying the tip voltage from 8V to -8V (A to B) in step of 2V for every 25-30 line scans with 60nm tip-sample separation. (B) Line profile taken across the Si substrate, shown as white line (X to Y) in (A). (C) SCM phase shift as a function of V_{tip} for bare Si substrate at different tip-sample separation. The solid curves are the least square fit of each respective data. (D) SCM phase shift as a function of V_{tip}^2. The solid curves are fitted to: $\Delta\Phi = -\frac{Q}{2k}C''V_{tip}^2$. All phase shifts are measured with respect to zero tip bias voltage.

6.4. Scanning conductance microscopy (SCM) analysis of different ZnO nanostructures.

The SCM analysis on bare Si/SiO_2 substrate has demonstrated the viability of the technique, satisfying the theory and equations discussed in Chapter 3. In this section, SCM analysis on ZnO nanostructures synthesised using two different techniques, namely the hydrothermal and chemical vapour deposition (CVD) method, is presented. Brief descriptions on both of the synthesis techniques can be found in Chapter 2 (Section 2.3.2).

6.4.1. Hydrothermally grown ZnO nanorod

The geometry of the hydrothermally grown ZnO nanorod was obtained using standard tapping mode AFM. The height, phase and amplitude images of the nanorod are presented in Figure 6.2A, B and C respectively. A line profile was taken across the cross section of the nanorod and is presented in Figure 6.2D. The nanorod has a height of ~100 nm and length of about 1.2 μm.

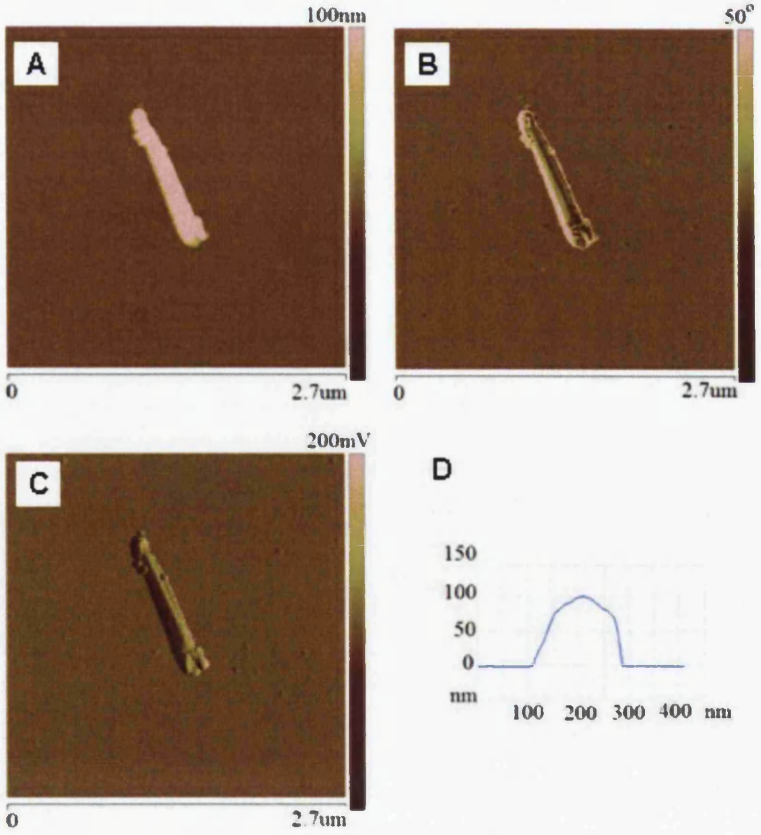

Figure 6.2 Tapping mode AFM images of a hydrothermally grown ZnO nanorod. (A) Height image. (B) Phase image. (C) Amplitude image. (D) Line profile taken across the ZnO nanorod.

The SCM-phase results of the ZnO nanorod is shown in Figure 6.3. The tip voltage was biased from 2V to 8V (Figure 6.3A-D) and from -2V to -8V (Figure 6.3E-H) in step of 2V.

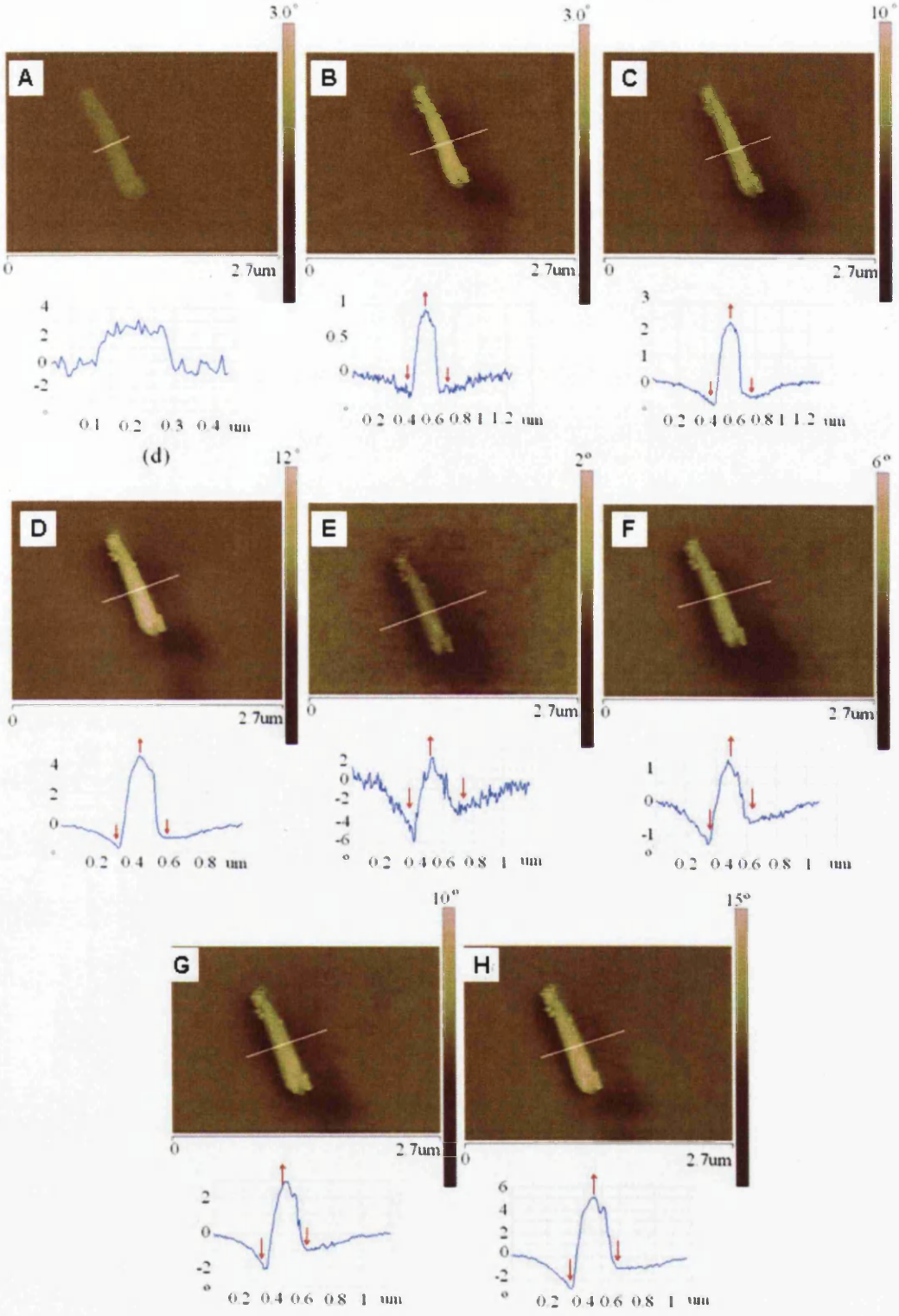

Figure 6.3 SCM phase images for hydrothermally grown ZnO nanorod with respective line profiles taken across the nanorod. The lift height was 30nm and the tip voltage was biased from -8V to 8V in step of 2V.

By measuring the phase change, $\Delta\phi$ from the respective line profiles, it was observed that the phase increases with applied tip voltage, V_{tip}. By plotting the measured $\Delta\phi$ against the applied V_{tip}, it is shown that the $\Delta\phi$ and V_{tip} has a quadratic relationship which satisfies Equation 3.22 (Figure 6.4A). From the line profiles taken across the nanorod at the respective V_{tip}, decrease in phase shift as the tip travel towards and away from the nanorod and increase in phase shift when the tip hovers above the nanorod were observed. A closer look at the results (Figure 6.3) shows that the surrounding area of the nanorod is dark. These observations suggest the presence of attractive forces between the tip and the sample as the tip travels towards and away from the nanorod.

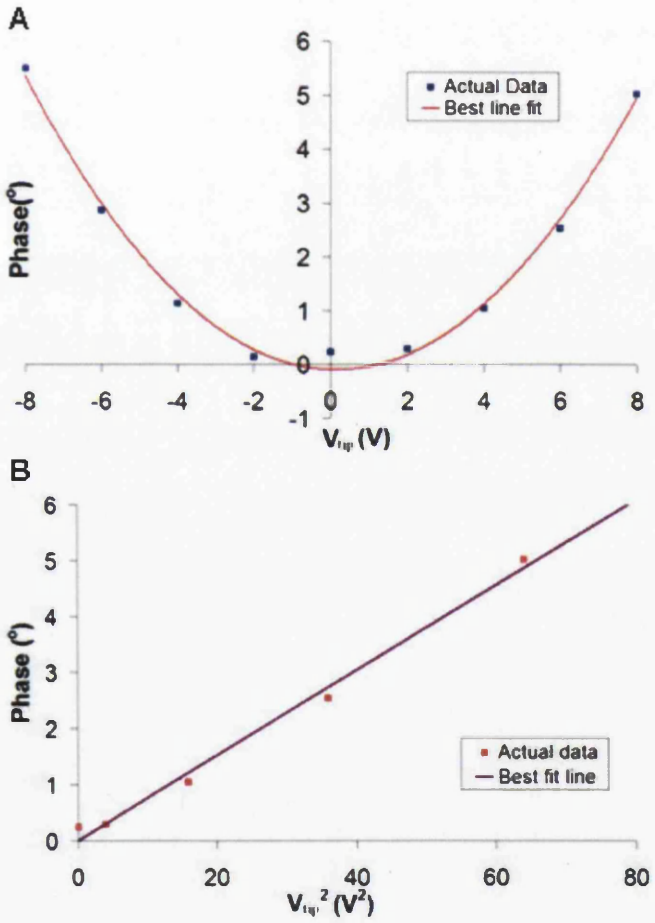

Figure 6.4 (A) SCM phase shift as a function of V_{tip} for hydrothermally grown ZnO nanorod. The solid curves are the least square fit of each respective data. (B) SCM phase shift as a function of V_{tip}^2. The solid curves are fitted to: $\Delta\Phi = -\frac{Q}{2k}C''V_{tip}^2$.

6.4.2. Chemical vapour deposition grown ZnO nanowire

The topography data of the CVD grown ZnO nanowire are presented in Figure 6.5. The result was obtained by tapping mode AFM (Veeco Dimension 3100). From the line profile (Figure 6.5D), the CVD grown ZnO nanowire has a diameter of ~12 nm and length of ~1 μm. It should be noted that the measured diameter of the nanowire is smaller than the diameter of the AFM probe tip (~30 nm). As such, the actual size of the nanowire may be smaller than the measured value due to tip convolution effect.

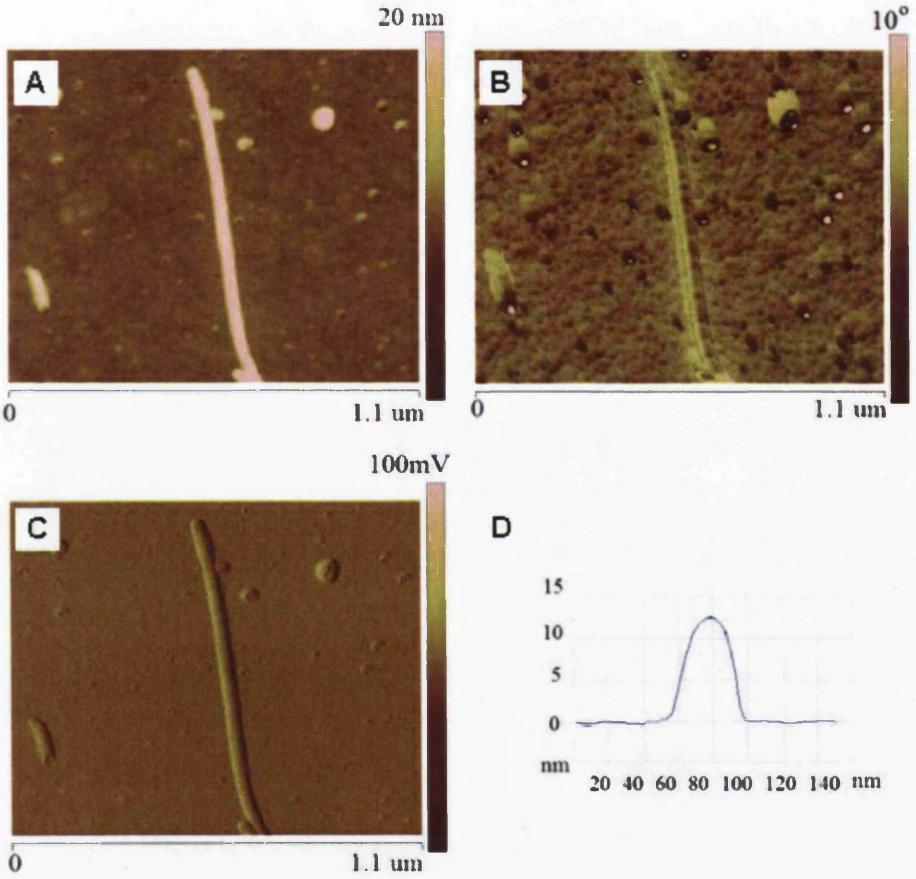

Figure 6.5 Tapping mode AFM images of a CVD grown ZnO nanowire. (A) Height image. (B) Phase image. (C) Amplitude image. (D) Line profile taken across the ZnO nanowire.

The SCM-phase results of the nanowire are presented in Figure 6.6. The SCM lift height was fixed at 30 nm and V_{tip} was biased from 0V to 8V (Figure 6.6(A)-(E)) and from -2V to -8V (Figure 6.6(F)-(I)) in step of 2V for each SCM scan. The SCM phase result shown in Figure 6.6J was obtained at 35 nm lift scan height and V_{tip} = -8V.

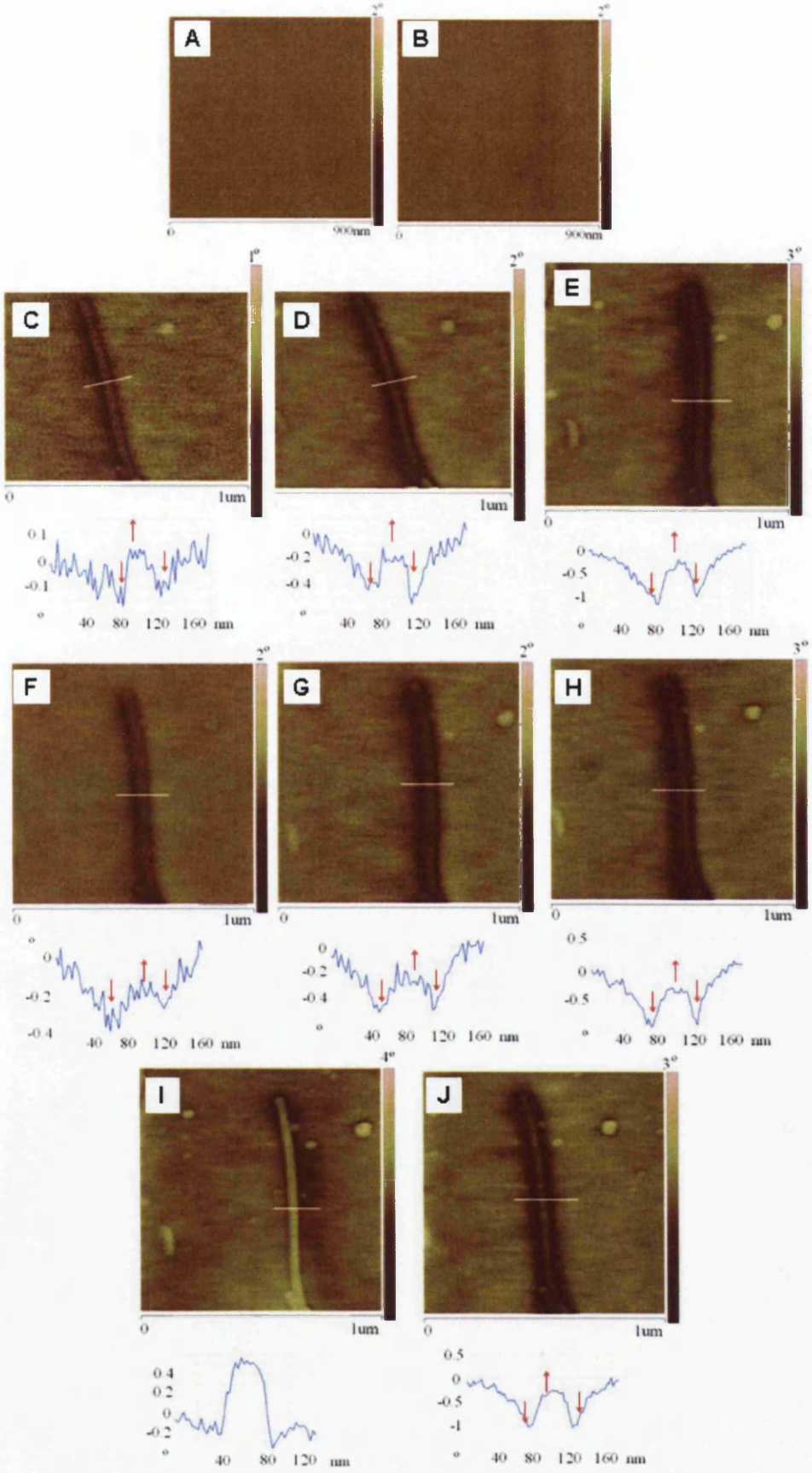

Figure 6.6 SCM phase images for CVD grown ZnO nanowire with respective line profiles taken across the nanowire. The lift height was 30nm and V_{tip} was biased from (A)-(E) 0V to 8V and (F)-(I) in step of 2V. (J) The lift height was 35nm and V_{tip}= - 8V.

From the results, it was observed that the SCM phase change is negligible at V_{tip}=0V and V_{tip}=2V, at 30nm lift height (Figure 6.6A and B). Whereas, at -6<V_{tip}<8V, with similar lift height (30nm), an overall negative phase shifts was observed across the cross section of the nanostructure. This is superimposed onto a 'dip-rise-dip' profile across the nanowire (see arrows in the line profiles) as shown in the respective line profiles (Figure 6.6 (C)-(H)). This indicates a decrease in phase shifts when the tip approaches or move away from the nanowire and an increase in phase shifts when the tip hovers above the nanowire. It was noted that the overall negative phase shifts for the CVD grown nanowire were observable at high electric field gradient (V_{tip}> 4V). The detected overall negative phase shift was plotted against the respective tip voltage as shown in Figure 6.7. As shown, the phase shifts increases (negatively) with increased tip voltage. The best fit line plotted using least square method relates the change in phase shift quadratically to the applied tip voltage satisfying the Equation 3.22 (Chapter 3). The detected negative phase shifts suggest the presence of tip-nanowire attractive force, which increases with applied V_{tip} (at both voltage polarities).

At V_{tip}= -8V, positive phase shift was detected (Figure 6.6I), implying the presence of tip-nanowire repulsive force. As mentioned, at -6V<V_{tip}<10V, the tip-nanowire attractive force increases with applied V_{tip}. Consequently, at V_{tip} = -8V, it is believed that the said attractive force was increased to such a degree that at the defined lift height, the tip may be 'pulled' towards the nanowire, resulting in shorter lift scan height. As a result, short range tip-sample forces may dominate over the long range electrostatic force. This can be clarified by comparing the SCM phase image with the TM-AFM phase image, where both images exhibit similar features [3]. The SCM scan was repeated with 35 nm lift height and V_{tip} = -8V (Figure 6.6J). As shown, an overall negative phase shift was again detected across the nanowire. Therefore, by increasing the lift height, the tip-sample force gradient was decreased, ensuring that the probe tip is at a safe distance from the nanowire, where long range electrostatic force dominates.

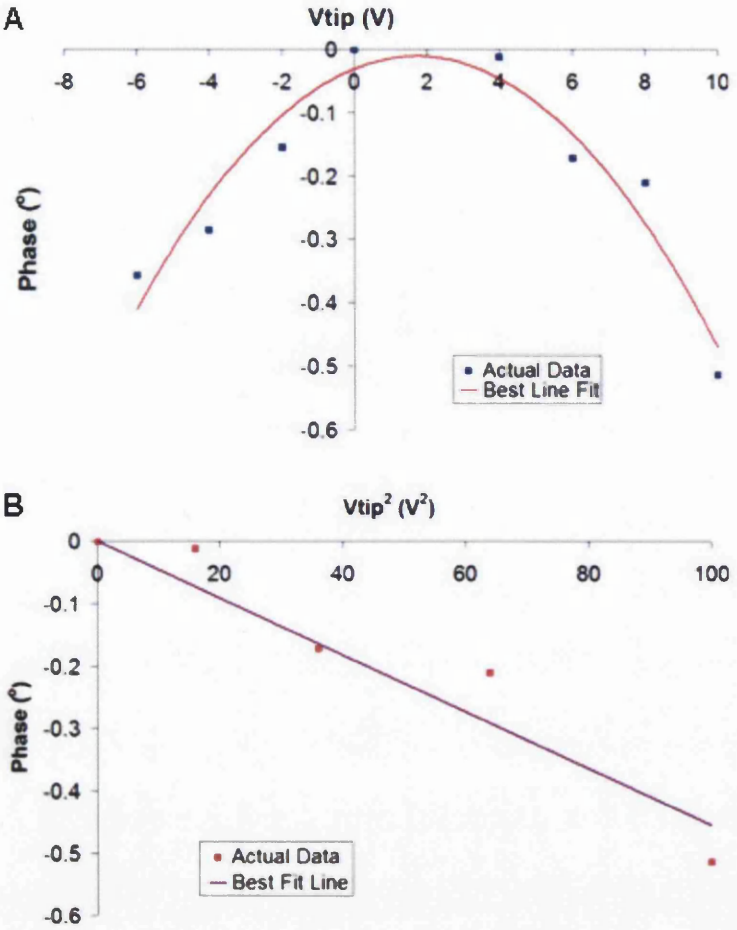

Figure 6.7 (A) SCM phase shift as a function of V_{tip} for CVD grown ZnO nanowire. The solid curves are the least square fit of each respective data. (B) SCM phase shift as a function of Vtip^2. The solid curves are fitted to: $\Delta\Phi = -\frac{Q}{2k} C'' V_{tip}^{\ 2}$.

6.4.3. Chemical vapour deposition grown ZnO nanobelt

The topography data of CVD grown ZnO nanobelt was obtained using standard tapping mode AFM (Veeco Dimension 3100) and are presented in Figure 6.8. From the line profile, the CVD grown ZnO nanobelt has a rectangular shape-like structure with ~35 nm height and ~200 nm width (Figure 6.8D). The belt-like nanostructure is more than 12 μm long.

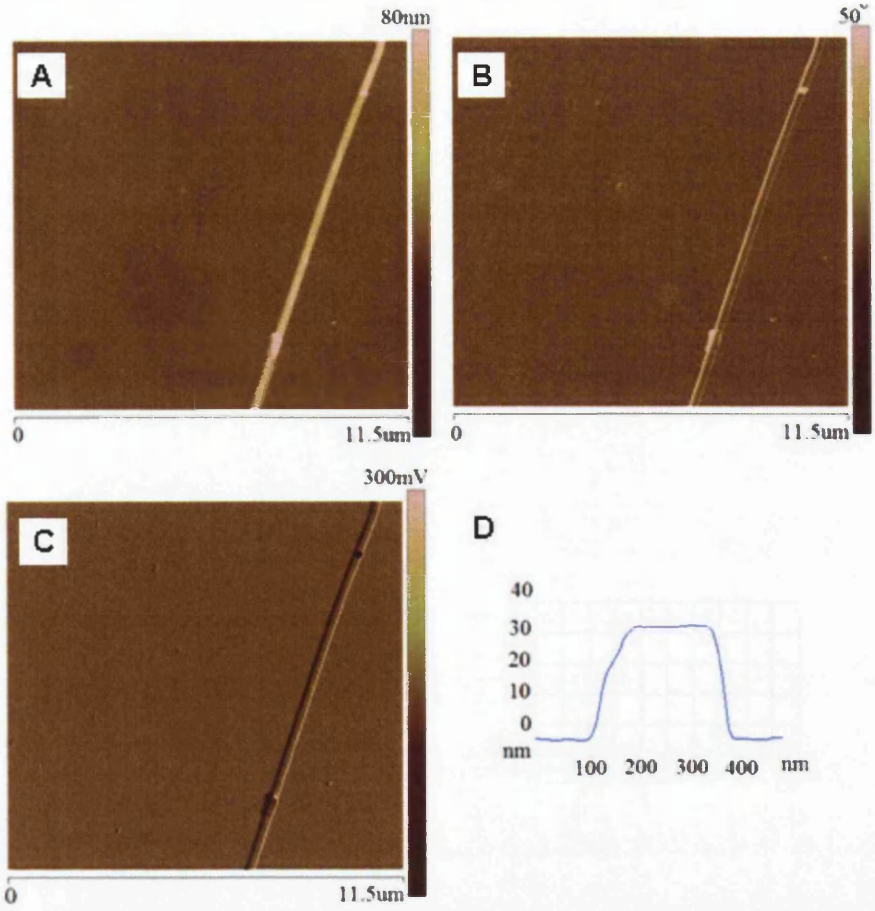

Figure 6.8 Tapping mode AFM images of a CVD grown ZnO nanobelt. (A) Height image, (B) phase and (C) amplitude images. (D) Line profile taken across the ZnO nanobelt.

Figure 6.9 shows the SCM-phase results obtained at 30 nm lift height and V_{tip}= ± 6V. Line profile taken across the nanobelt exhibit distinctive negative phase shifts. Referring to Figure 6.9B, the SCM phase image has similar feature to the TM-AFM phase image Figure 6.8B. The feature is observed as the double lines (indicated by red arrows) on the sides of the nanobelt. This similarity suggest that during the SCM scan, instead of only detecting long range electrostatic force, van der Waals force was also detected. Therefore, to ensure that only long range electrostatic force was detected, the following SCM scans were performed at 50 nm lift height.

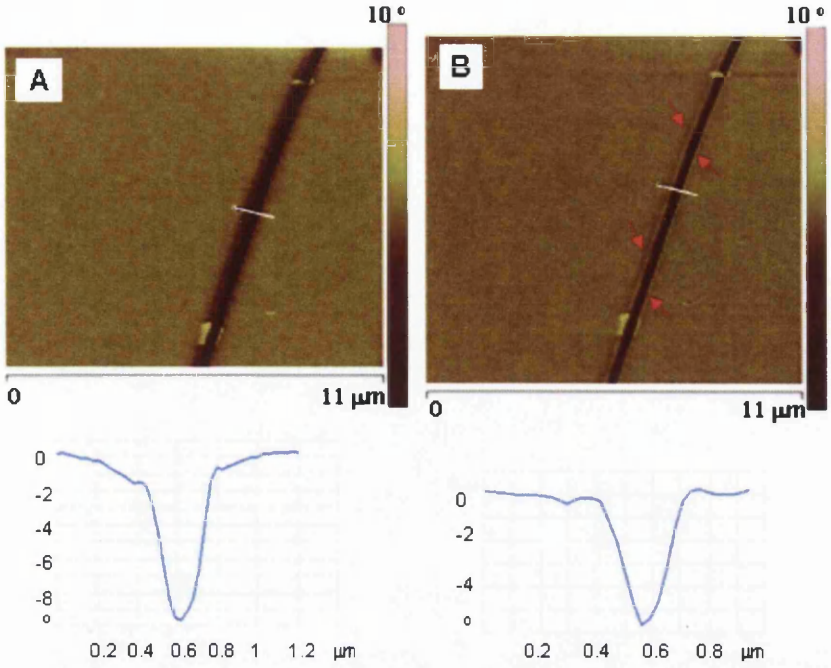

Figure 6.9 SCM phase images for CVD grown ZnO nanobelt with respective line profiles taken across the nanobelt. The lift height was 30nm and the tip voltage was biased at (A) Vtip = 6V and (B) Vtip = -6V.

The SCM phase scan results for 50 nm lift height are shown in Figure 6.10. The V_{tip} was biased from 0V to 8V (Figure 6.10A-E) and 2V to -8V (Figure 6.10F-I) in steps of 2V. From the SCM results, no phase change was detected at V_{tip}= 0V (Figure 6.10A) and distinctive negative phase shifts were detected for all other applied V_{tip}, as shown in each respective line profiles. The detected negative phase shift increases (by magnitude) as a function of V_{tip} at both polarities. These results imply the presence of an attractive force between the tip and the nanobelt. The measured phase data was plotted and the relationship between the change in phase and applied tip voltage are illustrated in Figure 6.11. As shown from the best fit lines the phase shifts and V_{tip} satisfies the SCM relation of Equation 3.22 (Chapter 3).

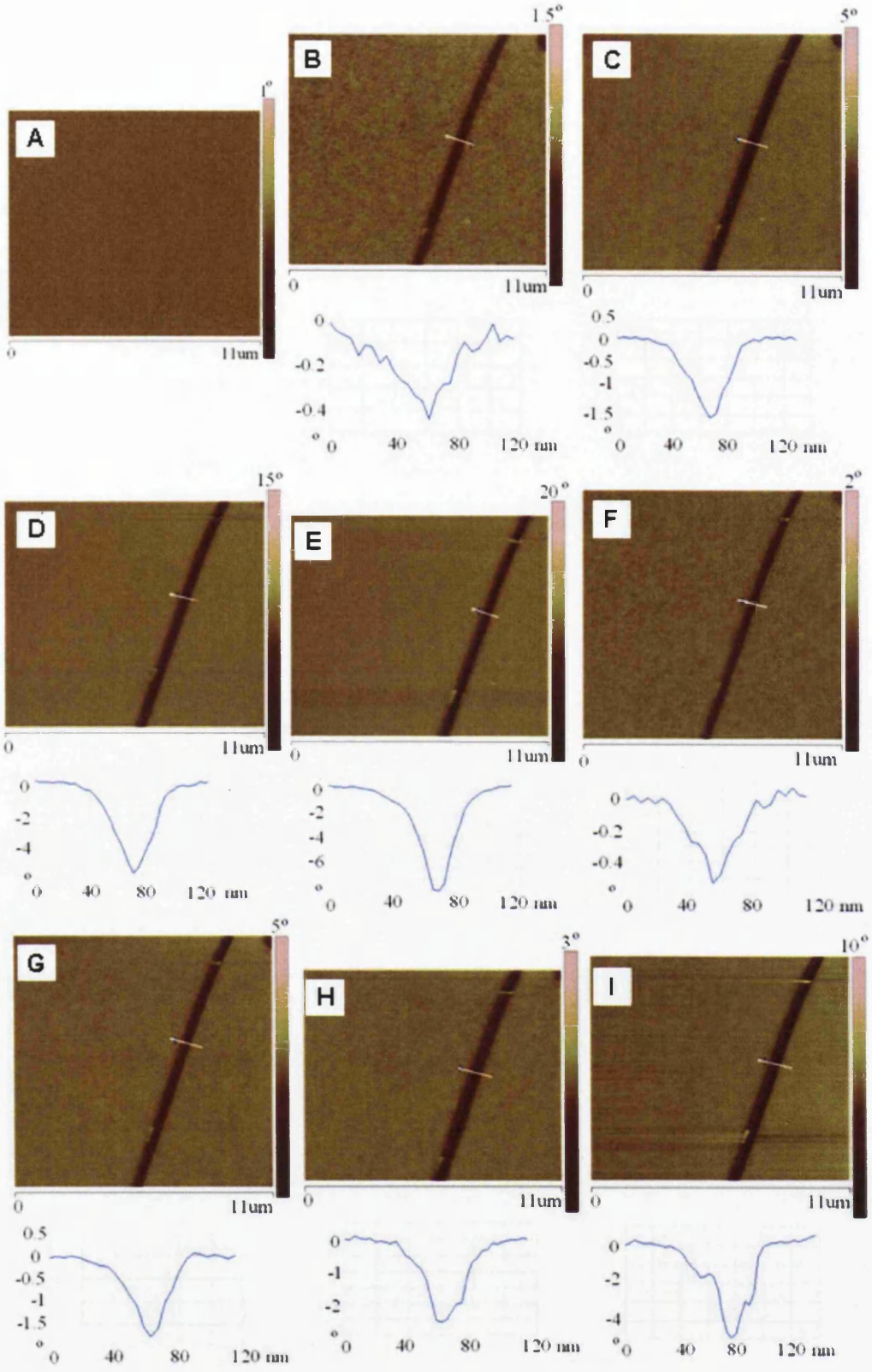

Figure 6.10 SCM phase images for CVD grown ZnO nanobelt with their respective line profiles taken across the nanobelt (white line). The lift scan height was 50nm and V_{tip} was biased from (A)-(E) 0V to 8V and (F)-(I) -2V to -8V in steps of 2V.

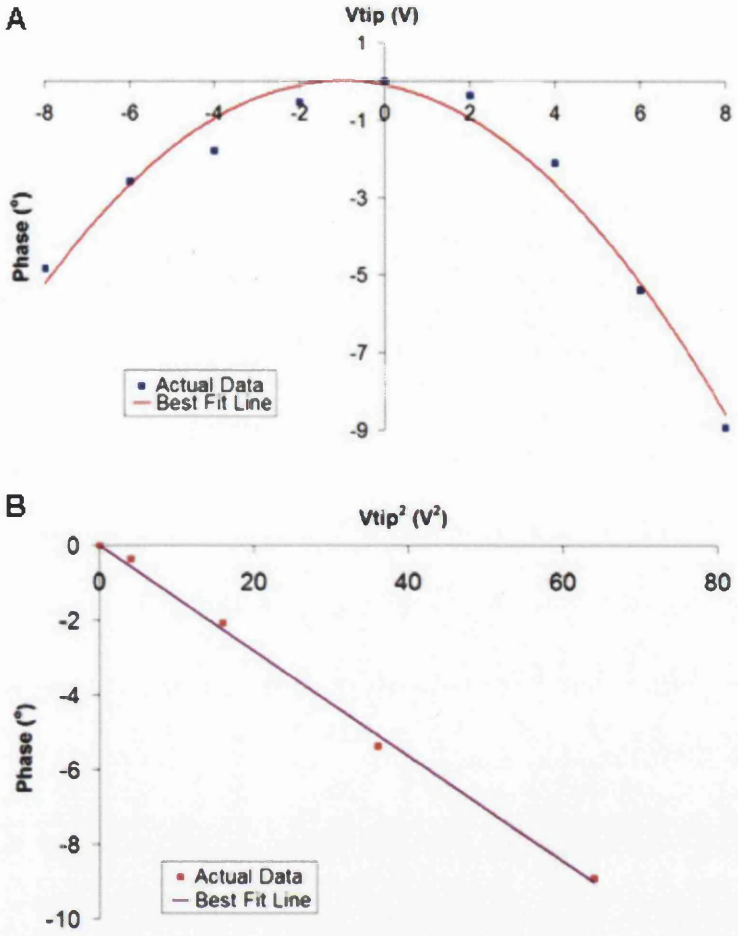

Figure 6.11 (A) SCM phase shift as a function of V_{tip} for CVD grown ZnO nanobelt. The solid curves are the least square fit of each respective data. (B) SCM phase shift as a function of V_{tip}^2. The solid curves are fitted to: $\Delta\Phi = -\frac{Q}{2k} C'' V_{tip}^2$.

6.4.4. Chemical vapour deposition grown ZnO nanorod

The topography data of CVD grown ZnO nanorod was obtained using standard tapping mode AFM in air (Dimension 3100). The height, phase, amplitude images and line profile taken across the nanorod are presented in Figure 6.12A, B, C and D respectively. From the line profile, the nanorod has a diameter of ~300 nm and length of ~2 μm.

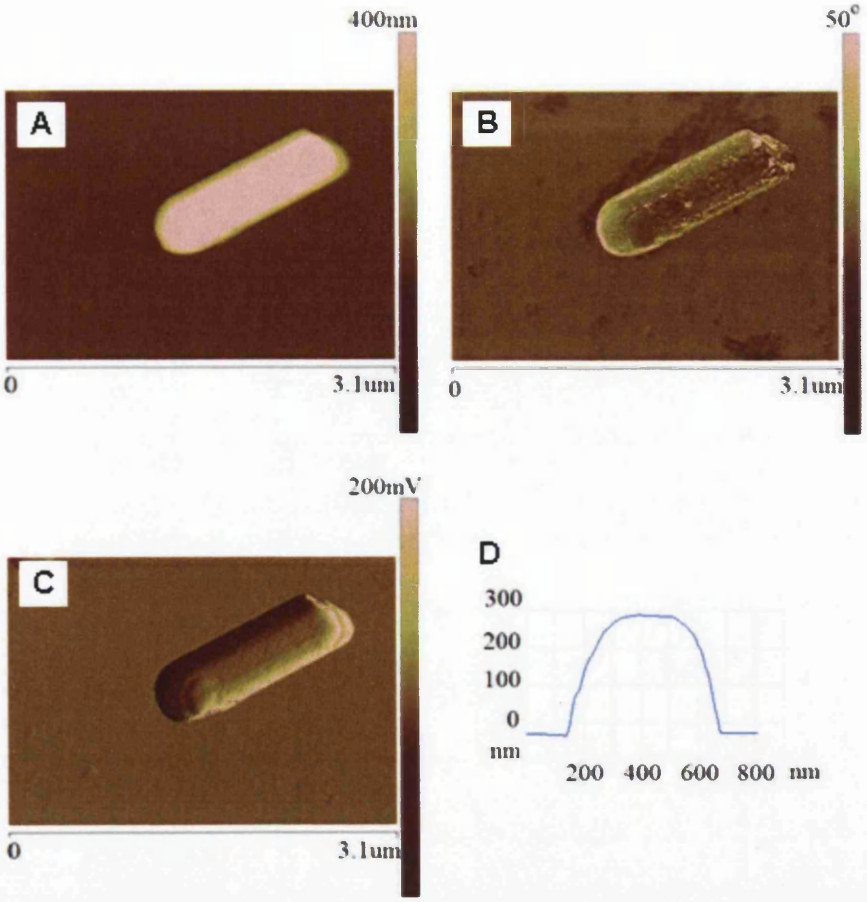

Figure 6.12 Tapping mode AFM images of a CVD grown ZnO nanorod. (A) Height image. (B) Phase image. (C) Amplitude image. (D) Line profile taken across the ZnO nanorod.

The SCM phase results of the CVD grown ZnO nanorod are shown in Figure 6.13. The lift scan height was predefined to 100 nm and V_{tip} was biased from 0V to 8V (Figure 6.13A-E) and from -2V to -8V (Figure 6.13F-I) in steps of 2V. As the nanorod is relatively large, initial higher lift height (100 nm) was chosen as a precaution to ensure that strong tip-nanorod forces will not 'pull' the probe tip too close to the sample. For each SCM scan, the change in phase with respect to the substrate was measured from the line profiles taken across the nanorod.

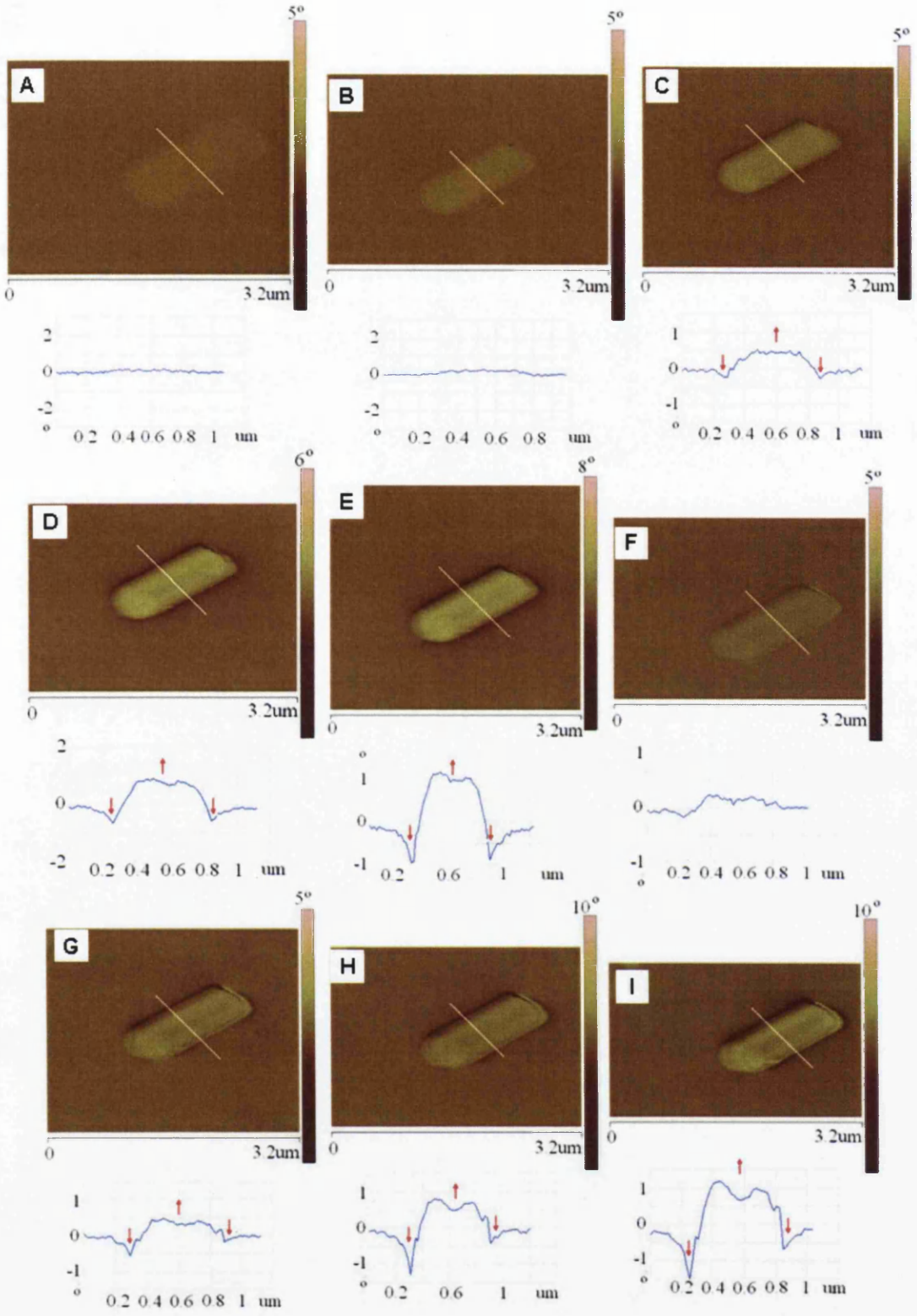

Figure 6.13 SCM phase images for CVD grown ZnO nanorod with respective line profiles taken across the nanorod. The lift height was 100 nm and the tip voltage was biased from (A)-(E) 0V to 8V and (F)-(I) -2V to -8V in step of 2V. The arrows show the 'dip-rise-dip' behaviours.

A closer look at the line profiles taken across the nanorod for each respective scan showed the decrease in phase shifts when the tip approaches or move away from the nanorod and an increase in phase shifts when the tip hovers above the nanowire. The decrease in phase shifts is observed as 'dark' contrasts surrounding the ZnO nanorod. As the magnitude of V_{tip} increases, 'dark' contrasts were observed at the centre of the nanorod. The observed 'dark' contrast from the SCM phase images is measured from the line profile taken at the cross section of the nanorod, as decrease in phase. It was noted that such observation is more pronounced at the negative polarity of V_{tip} (Figure 6.13(F)-(I)).The relationship between the phase shift and applied tip voltage is plotted in Figure 6.14. As shown, the change in phase increased as a function of V_{tip} and has a quadratic relationship which meets Equation 3.22 (Figure 6.14A).

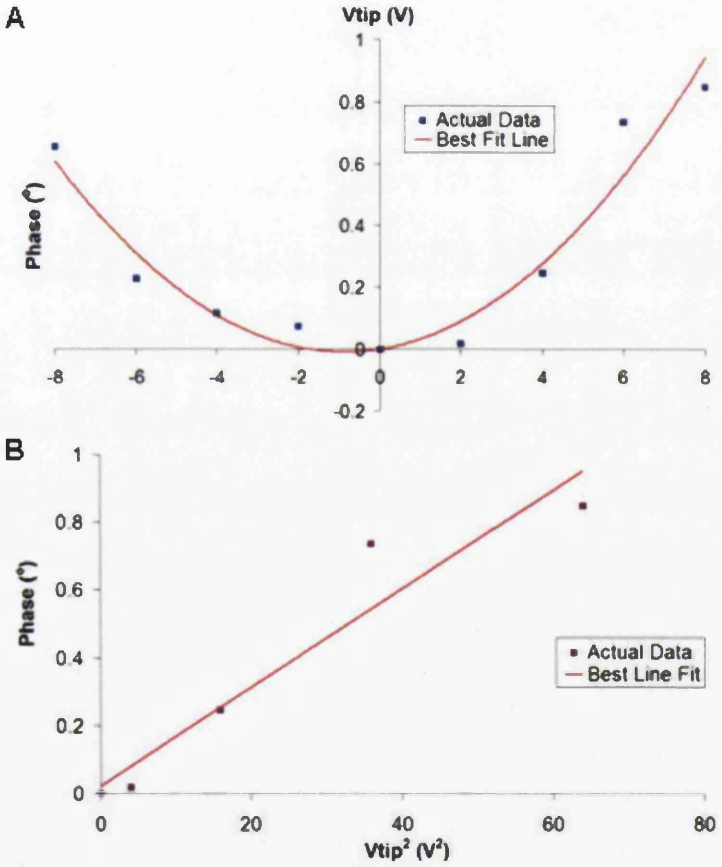

Figure 6.14 (A) SCM phase shift as a function of Vtip for CVD grown ZnO nanorod. The solid curves are the least square fit of each respective data. (B) SCM phase shift as a function of V_{tip}^2. The solid curves are fitted to: $\Delta\Phi = -\frac{Q}{2k} C'' V_{tip}^{\ 2}$.

The change in phase at the centre of the nanorod is better observed by plotting V_{tip} (of negative polarity) as a function of the change in phase (Figure 6.15). The plotted phase data at each applied voltage was obtained as an average value of five random points taken along the centre of the nanorod. The error bars shown in the graph (Figure 6.15) is the standard deviation of each of the respective phase data point. As shown, the phase shift increases steadily with applied V_{tip} and an evident decrease in phase is observed at V_{tip} = -10V. From the graph (Figure 6.15), it was noted that the overall measured phase shift is positive with respect to the substrate for all SCM phase scan. However, it should be reminded that the SCM probe tip detects point-to-point changes in phase. As such, from the line profiles, the phase change at the centre of the nanorod with respect to its side is measured as a negative phase shift. This decrease in phase observed from the respective SCM phase result suggests the presence of an attractive force between the tip and the nanostructure (centre of nanorod). Furthermore, this attractive force appears to be stronger at higher electric field gradient and can be attributed to induced polarisation effect.

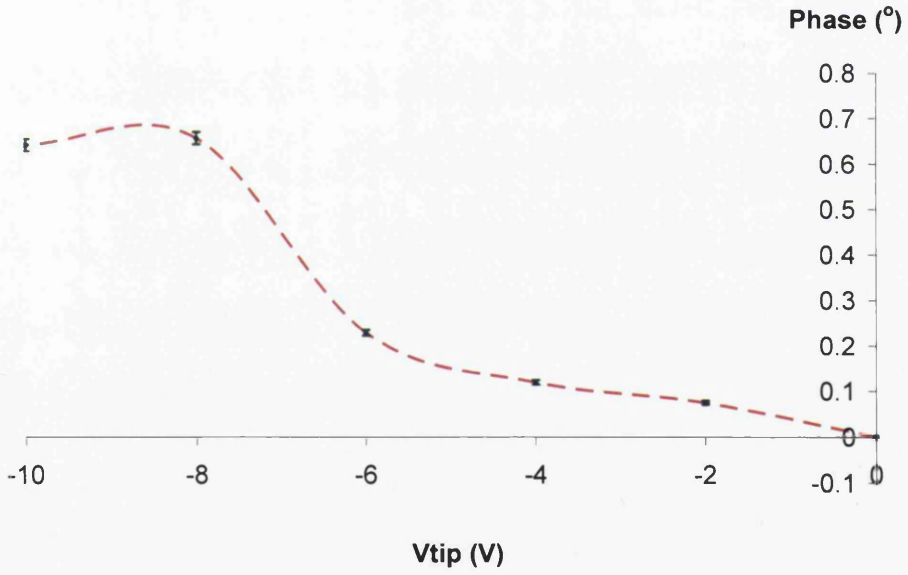

Figure 6.15 SCM phase shift plotted as a function of V_{tip} (negative polarity) for 100 nm lift height. At V_{tip}= -10V, a decrease in phase shift was observed. Error bars (green) indicate the standard deviation of each measured data.

As observed, the induced polarisation is more pronounced at negative V_{tip}, especially at high electric field gradient. As such, the SCM phase scans were repeated at -8V $\leq V_{tip} \leq$ -2V with lift scan height of 30 nm. The results of the SCM scan are shown in Figure 6.16.

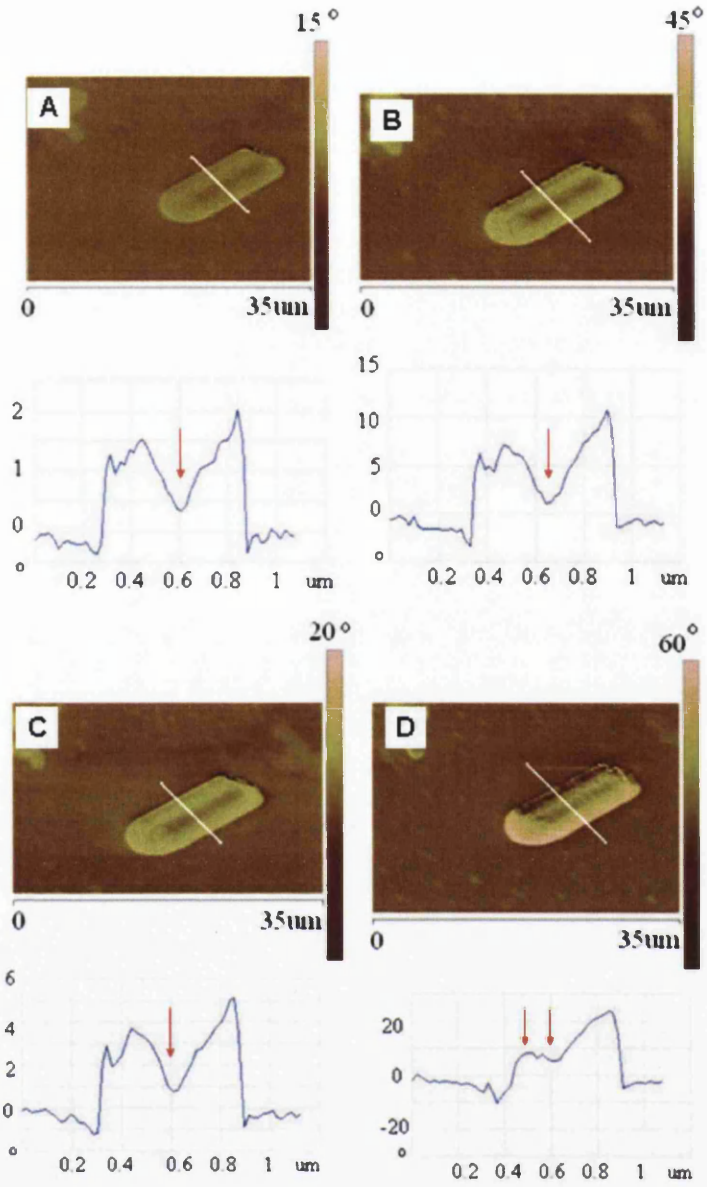

Figure 6.16 SCM phase images of CVD grown ZnO nanorod with the respective line profiles taken across the nanorod. The lift height was 30nm and V_{tip} was biased from -2V to -8V in steps of 2V. The arrows indicate decrease in phase shifts due to tip induced polarisation effect.

With a stronger electric field gradient (smaller lift height), the induced polarisation at the centre of the nanorod is more prominent (Figure 6.16). At V_{tip} = -8V, dark contrasts (decrease in phase) were observed at the centre and at the side of the nanorod (Figure 6.16D). Similarly, the observed dark contrast suggests the presence of an attractive force between the tip and the nanostructure, attributed to tip induced polarisation. The change in phase is plotted against the applied V_{tip}, shown in Figure 6.17. The error bars of the graph indicate the standard deviation of the measured

phase shift of five different points taken along the centre of the nanorod. As shown, the tip-sample repulsive force reaches saturation at V_{tip}= -8V. From these results, it can be concluded that the CVD grown nanorod experience tip induced polarisation effect, especially at high tip-sample electric field gradient. The tip induced polarisation of the nanorod starts from the centre, spreading to the side of the nanorod.

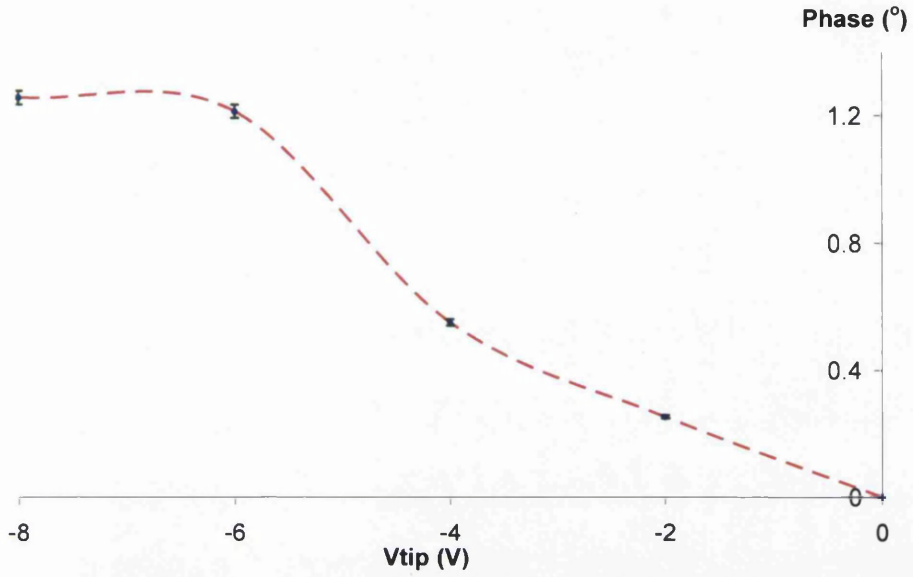

Figure 6.17 The SCM phase shift plotted as a function of V_{tip} at 30nm lift height. At Vtip= -8V, tip-sample repulsive force reaches saturation. Error bars (green) indicate the standard deviation of each measured data.

6.5. Discussion on the scanning conductance microscopy (SCM) phase results

This section compares and discusses the results obtained from the SCM scans on the hydrothermal grown ZnO nanorod and the CVD grown ZnO nanorod, nanobelt and nanowire, as presented in Section 6.4.

Figure 6.18 shows the SCM-phase results of the CVD grown nanowire and nanobelt. As shown, an overall negative phase shift was observed across the cross section of the CVD nanowire (Figure 6.18A). This is superimposed onto a 'dip-rise-dip' profile across the nanowire as shown from its line profile. This indicates a decrease in phase shifts when the tip approaches or move away from the nanowire and an increase in phase shifts when the tip hovers above the nanowire. The overall negative phase

shifts for the CVD grown nanowire were observable at high electric field gradient (V_{tip} > 4V). As for the CVD grown nanobelt, a distinctive negative phase shift was detected, as shown from the line profile taken across the nanostructure (Figure 6.18B).

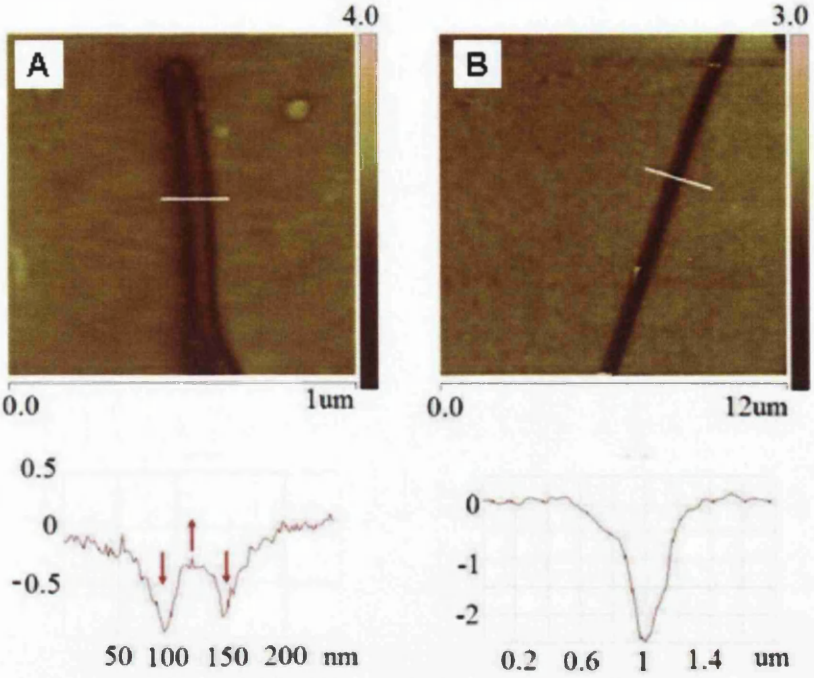

Figure 6.18 SCM-phase results of CVD grown ZnO (A) nanowire and (B) nanobelt deposited on Si substrate (oxide thickness = 340 nm). The lift scan height = 30 nm and V_{tip} = -6V. (A) The arrows on the nanowire line profile illustrate the 'dip-rise-dip' characteristic.

Although an overall negative phase shift was detected for both the CVD grown nanowire and nanobelt, the line profiles taken across the respective nanostructures were considerably different. While the 'dip-rise-dip' line profile was observed for the nanowire, a distinctive decrease in phase shift was observed for the nanobelts. An interesting finding from an SCM scan on another ZnO nanowire showed that at high electric field gradient (V_{tip}= 8V), a distinctive negative phase shift was observed (Figure 6.19A-B). A line profile taken across one of the particles surrounding this nanowire portrayed the 'dip-rise-dip' attribute (Figure 6.19C).

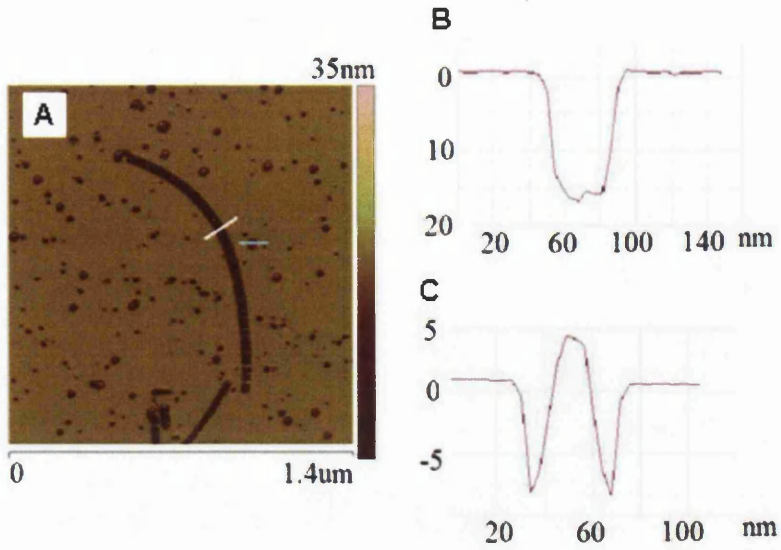

Figure 6.19 (A) SCM phase image of a fully polarised CVD grown nanowire. Result was obtained with Vtip=-8v and tip-sample separation of 35nm. (B) Line profile taken across the nanowire (white line). (C) Line profile taken across a particle, showing the dip-rise-dip attributes (blue line).

Figure 6.20 compares the SCM phase results on a CVD grown nanorod scanned at different lift scan height (100 nm and 30 nm) but the same V_{tip} (-6V). For the CVD grown nanorod with diameter 15 times of the nanowire, the 'dip-rise-dip' phenomenon was again observed (Figure 6.20A). Similarly, a decrease in phase shifts were observed when the tip move toward and away from the nanorod, and an increase in phase shift was observed when the tip hovers above the sample. The line profile taken across the nanorod did not show an overall negative phase shift (observed for CVD nanowire) instead a 'negative-positive-negative' phase shift. At higher electric field gradient, a decrease in phase shift was observed in the centre of the nanorod, as shown in Figure 6.20B. This is believed to be the tip-induced polarisation due to the applied field gradient.

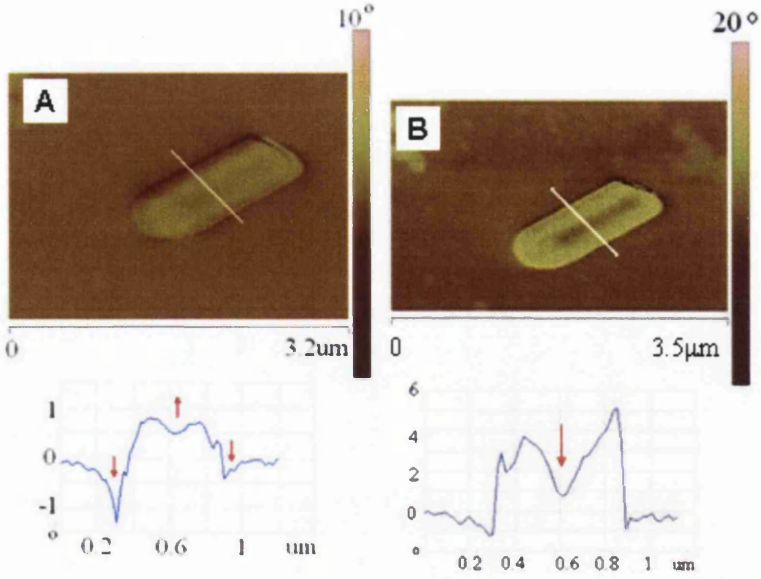

Figure 6.20 SCM-phase images of CVD grown ZnO nanorod (diameter ~300nm). (A) The lift scan height = 100nm and the V_{tip} = -6V. The arrows indicate the 'dip-rise-dip' characteristic. (B) The lift scan height = 30 nm and the V_{tip} = -6V. The arrows indicate decrease in phase shift due to tip induced polarisation.

Figure 6.21 shows the SCM-phase images of the hydrothermally grown ZnO nanorod. The SCM phase result is similar to the result observed for the CVD grown ZnO nanorod scanned at low electric field gradient (Figure 6.20A). More explicitly, a decrease in phase shifts were observed when the tip move toward and away from the nanorod and an increase in phase shift was observed when the tip hovers above the sample. However, the hydrothermal nanorod did not polarise at high electric field gradient, but experienced an increased in phase shift with applied electric field gradient.

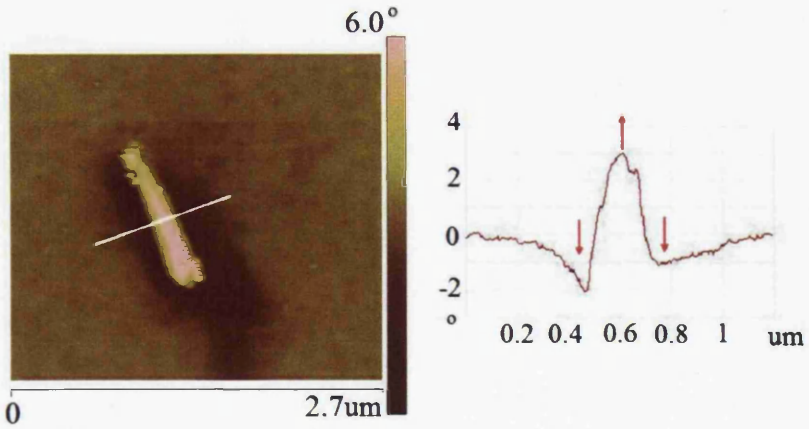

Figure 6.21 SCM phase image of the hydrothermally grown ZnO nanorod. The line profile is taken across the nanorod as indicated by the white line in the SCM phase image. The applied tip voltage was 6V and lift scan height was 30nm.

From these SCM-phase results, the explanation for the observed behaviours of each 1-D ZnO nanostructure will be discussed as follows. During the SCM interleave scan, the cantilever is oscillated near its resonance frequency. Any additional force gradient due to the sample will be translated into changes in the cantilever's resonant frequency and consequently shifts in the phase of the oscillations. There are two main factors which contribute to the SCM images, firstly the capacitance between the tip and the sample which is influenced by the tip-sample distance, material (dielectric) and sample geometry. Secondly, the potential difference applied between the tip and sample, which depends linearly on the sample charge since the tip voltage is kept constant. In general, for the capacitance variations, SCM images obtained with positive and negative tip bias should exhibit the same phase shifts. Whereas for sample charge potential variations, the SCM images should exhibit complementary phase shifts at opposite tip voltage polarity. In this work, all SCM-phase measurements were taken on uncharged samples and any change in the SCM phase shift were solely due to the electrical properties of the nanostructures. For rapid sample conductivity discriminations, SCM displays distinctive negative phase shifts for metallic samples and distinctive positive phase shifts for insulating samples [12-14]. For metallic samples, when the tip hovers above the sample, the tip and sample act like a parallel plate capacitor. Under applied voltage, these parallel plates (effective tip-sample) capacitor experience an additional attractive force due to tip-induced charge polarisation within the sample. Thus, the cantilever experiences a decrease in its effective spring constant, which is translated into negative phase shifts. As for insulating and semiconducting samples, the effective capacitance is influenced by the dielectric permittivity and the geometry of the samples (Equation 3.24). Due to the high dielectric permittivity of insulating samples, the SCM cantilever probe detects an overall positive phase shift [6, 7]. However, conducting samples with a finite dielectric permittivity showed negative-positive-negative phase shifts, as measured by Cristian Staii *et. al* [4]. When the tip approaches or moves away from a conducting sample at a height h, there exist two forces that influence the cantilever oscillation. These forces originate from the capacitive interaction between the tip and the substrate, F_{ts} and the additional attractive force due to the tip-sample interaction, F_{tz} (Figure 6.22).

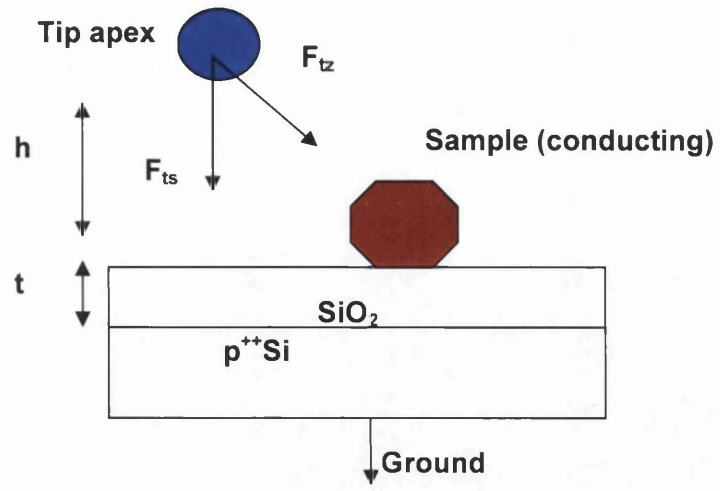

Figure 6.22 Schematic diagram of the interaction forces between the SCM probe tip and the conducting sample [4].

Due to this additional attractive force, the cantilever experiences a decrease in phase, Φ, and subsequently a negative phase shift, $\Delta\Phi$. Mathematically, this can be expressed as follows [4]:

$$\Phi = -\frac{Q}{k}(F_{ts}^{'} + F_{tz}^{'}) < -\frac{Q}{k}(F_{ts}^{'}) \qquad \textbf{Equation 6.1}$$

When the tip hovers directly above the sample, the influence of the finite dielectric constant of the sample overcomes the capacitive force and thus, positive phase shifts are detected by the probe tip [4]. As a result, negative-positive-negative phase shifts are observed across the sample. Previous work using SCM includes a comparison study between single-wall carbon nanotubes and λ-DNA where metallic carbon nanotubes exhibited negative phase shifts while the λ-DNA strands were not detectable on the phase image due to their length and insulating properties [5]. Other SCM work on polyaniline/polyethylene oxide(Pan/PEO) nanofibres showed positive phase shifts that increased with the fibre diameter for insulating samples and negative-positive-negative phase shifts across conducting nanofibers, with finite dielectric permittivity [6]. Further SCM work on dielectric human chromosomes resulted in positive phase shifts [7]. More detailed literature reviews can be found in Section 3.6.1.

Therefore, for the CVD nanowire (Figure 6.18A), when the tip approaches or moves away from the nanowire, the conducting nature of the nanowire induces an attractive force between the tip and nanostructure. As such, when the tip nears the nanostructure, this additional attractive tip-sample force, F_{tz} interacts with the capacitive tip-Si substrate force, F_{ts} , resulting in the decrease of the cantilever oscillation phase, Φ, and subsequently a decrease in phase shift, $\Delta\Phi$. Also, when the tip hovers above the nanowire, the dielectric constant of the nanowire alters the effective capacitance, resulting in the increase in phase shift, which explains the 'dip-rise-dip' line profile. Furthermore, the relatively smaller diameter of the nanowire (12 nm) compared to the radius of the probe tip (25-30 nm) would cause the tip to hover between the Si substrate and the nanowire. To which, the tip will always detect the additional tip-sample attractive force, F_{tz} which results in the observed overall negative phase shift. As for the CVD nanobelt (Figure 6.18B), the distinctive negative phase shift detected implies the presence of attractive force between the nanostructure and the probe tip. The tip-sample attractive force is caused by tip-induced polarisation within the nanostructure, where the tip and nanobelt act as parallel capacitor plates under applied voltage. This is similar to SCM-phase scan on metallic carbon nanotubes performed by other research groups [5]. For the CVD and hydrothermally grown ZnO nanorods, negative-positive-negative phase shift was detected on both samples under low applied field gradient. As mentioned, this is due to the existence of two forces; the capacitive interaction between tip and substrate F_{ts} and the additional tip-sample attractive force, F_{tz} which originate from the conducting nature of the CVD and hydrothermal nanorods. This can be explained mathematically as before by Equation 6.1 and as illustrated in Figure 6.22[4].

When a higher tip voltage (V_{tip}) was applied, a decrease in phase shift was detected in the centre of the CVD nanorod (Figure 6.20B). Although the detected phase shift (centre of nanorod) is not in the negative region when taking the Si background as phase reference, it should be noted that the SCM measures the point-to-point variations in the tip-sample force gradient. Therefore, the decrease in phase shift suggests that the attractive force was detected in the centre of the nanorod as the tip scanned across the nanostructure. As for the hydrothermal nanorod, an overall positive phase shift that increased with applied tip voltage was detected.

The SCM phase shift is influence by the electrostatic force gradient detected between the tip and the sample. Consequently, for uncharged nanostructures, the detected change in the SCM phase shift is expressive of the sample electronic properties. From former observations, at high electric field gradient, the tip-induced attractive force within the sample was detected for all the CVD grown nanostructures, but not for the hydrothermally grown nanorod. More explicitly, negative phase shifts were detected within the entire length of the CVD nanowire and nanobelt, and a decrease in phase shift was detected in the centre of the CVD nanorod. The detected attractive force is believed to be caused by tip-induced polarisation, where mobile charges within the nanostructures are polarised in such a way that charges of opposite sign are attracted to the probe tip. It was also noted that the phase shifts (reflecting attractions) for the CVD nanowire and nanorod are only prominent at high electric field gradient (relation to applied tip voltage). This suggests that these mobile charges require a certain amount of energy (ionisation energy) to exert movements. By using the polarisability as a qualitative measure of charge mobility, a comparison between the SCM-phase results proposes that the mobile carriers within the CVD nanostructures have greater degree of freedom in movement, than the hydrothermal nanorod. The difference in the electrical properties of these nanostructures is believed to be influenced by the presence of various defects at different density in the nanostructures due to their growth methods.

Since nanostructures have a large surface-to-volume ratio, surface defects play an important role in controlling their electrical properties. Zn interstitials and oxygen vacancies are known to be the predominant defects in native undoped ZnO, where one is a shallow donor and the other is a deep donor [8, 9]. Because of the different ionisation energy of these defects, the growth temperature can influence the concentration of various defects in a ZnO nanostructure [8]. The crucial factor in the electrical properties of ZnO is having the right density of defects to facilitate charge carrier movement. The growth methods for CVD and hydrothermal nanostructures are different in terms of growth temperature and oxygen/zinc environment. The hydrothermal growth method is known to produce higher concentration of defects [10] namely oxygen vacancies due to low O_2 concentration in the water and low temperature growth [8]. Oxygen vacancies, requiring a much higher ionisation energy than interstitial Zn, were found to contribute negligibly to the n-type ZnO

conduction and also to be deep level traps which dilute the hole concentration in any p-type ZnO [11]. The CVD method on the other hand uses high temperature and an oxygen rich environment to produce higher crystal quality structure (reduced oxygen vacancies). When grown with the right amount of Zn interstitial sites, these shallow donor levels under the conduction band can facilitate electron mobility and improve conductivity. Although there is still much controversy of the actual influence of various defects on the conductivity of ZnO nanostructures, it is believed that the difference in the electrical properties of these nanostructures was mainly due to the difference in their defects density. From the SCM results and using polarisability as a qualitative measure of charge mobility, CVD ZnO nanostructures are found to be of better conductivity than the hydrothermal nanostructure.

6.6. Summary

This chapter has demonstrated the difference in electrical properties of two differently grown ZnO nanostructures, analysed via the scanning conductance microscope (SCM). The conductivity of ZnO nanostructures grown via the two different methods were investigated by monitoring the electrostatic force between the samples and a SCM probe tip. Tip induced polarisation as well as surface/volume trapped charges within the nanostructure may influence the total electrostatic force experienced by the tip [12]. In this work, all SCM-phase measurements were taken on uncharged samples and any change in the SCM phase shift were solely due to the electronic properties of the nanorods. At high electric field gradient, an attractive force (polarisation) was induced between the SCM probe tip and all the CVD grown nanostructure. The high field gradient caused the mobile carriers within the nanostructures to polarise in such a way that charges of opposite sign were attracted to the probe tip. The hydrothermal grown nanorods maintain their overall positive phase shifts even at high electric field gradient. A comparison between the SCM results showed that the electrical properties of the CVD and hydrothermal nanostructure are significantly different. This was expected since the different growth temperature and environment influence the presence of various defects which can affects the electrical behaviour of each nanostructure. Although polarisability is only a qualitative measure of carriers' mobility, a viable comparison between the SCM-phase results of the differently grown nanostructures proposes that the mobile carriers within the CVD nanostructures are freer to move than the hydrothermal nanorod. This implies that the hydrothermal nanorods are less electrically active. Therefore, it is believed that the CVD nanostructures are more conducting than the hydrothermal grown nanorod. In addition, the CVD nanobelt appears to have better polarisability and can therefore be used in the later work on the fabrication of biosensor. The SCM study has demonstrated qualitative conductivity measurement of ZnO nanostructures. However, quantification of the conductivity of nanostructures is not straightforward. Nonetheless, the versatility of SCM as a useful initial conductivity characterisation of nanomaterials has been demonstrated. The next step, having successfully confirmed that ZnO nanostructures are conducting, is to investigate surface functionalisation methods of ZnO, as will be discussed in Chapter 7.

6.7. References

[1] Greene L E, Law M, Goldberger J, Kim F, Johnson J C, Zhang Y, Saykally R J and Yang P 2003 Low-temperature wafer-scale production of ZnO nanowire Arrays *Angew. Chem. Int. Ed.* **42** 3031

[2] Greene L E, Law M, Tan D H, Montano M, Goldberger J, Somorjai G and Yang P 2005 General route to vertical ZnO nanowire arrays using textured ZnO seeds *Nano Lett.* **5** 1231

[3] *Electric Force Microscopy (EFM) Support Note No. 230 Rev. A* 1996 (Digital Instrument Santa Barbara CA)

[4] Staii C, Johnson A T and Pinto N J 2004 Quantitative analysis of scanning conductance microscopy *Nano Lett.* **4** 859

[5] Bockrath M, Markovic N, Shepard A, Tinkham M, Gurevich L, Kouwenhoven L P, Wu M W and Sohn L L 2002 Scanned conductance microscopy of carbon nanotubes and λ-DNA *Nano Lett.* **2** 187

[6] Zhou Y X, Freitag M, Hone J, Staii C, Pinto N J and MacDiarmid A G 2003 Fabrication and electrical characterization of polyaniline-based nanofibers with diameter below 30nm *Appl. Phys. Lett.* **83** 18

[7] Clausen C H, Lange J M, Jensen L B, Shah P J, Dimaki M I and Svendsen W E 2008 Scanning conductance microscopy investigations on fixed human chromosomes *BioTechniques* **44** 225

[8] Schmidt-Mende L and MacManus-Driscoll J L 2007 ZnO –nanostructures, defects, and devices *Materials Today* **10** 5

[9] Janotti A and Van de Walle C G 2007 Native point defects in ZnO *Phys Rev B* **76** 16

[10] Kwok W M, Djurišić A B, Leung Y H, Li D, Tam K H, Phillips D L and Chan W K 2006 Influence of annealing on stimulated emission in ZnO nanorods *Appl. Phys. Lett.* **89**, 18

[11] Yu ZG, Wu P and Gong H 2007 Theoretical and experimental studies on oxygen vacancy in p-type ZnO *Phys. B* **401** 417

[12] Kalinin S and Bonnell D 2000 *Electrostatic and magnetic force microscopy in scanning probe microscopy and spectroscopy* (New York: Wiley-VCH) pp 205-251

Chapter 7

Surface Functionalisation of Zinc Oxide (ZnO)

7.1. An overview

Biosensors are functional hybrid systems, combining three essential components, namely a biological recognition system which is usually made up of biological molecules (antibodies) that detect specific analyte (antigens), a physico-chemical transducer (ZnO nanowire) which converts biological signals into quantitative measurable signal, and an output system to display the measured signal into an appropriate format. The key to the successful implementation of biosensors is inextricably related to the interface between the biological molecules and the transducer. Thus, the method for the coupling of biological molecules to the 1-D ZnO nanostructure, or in other words, immobilisation, is crucial to the effectiveness of a biosensor.

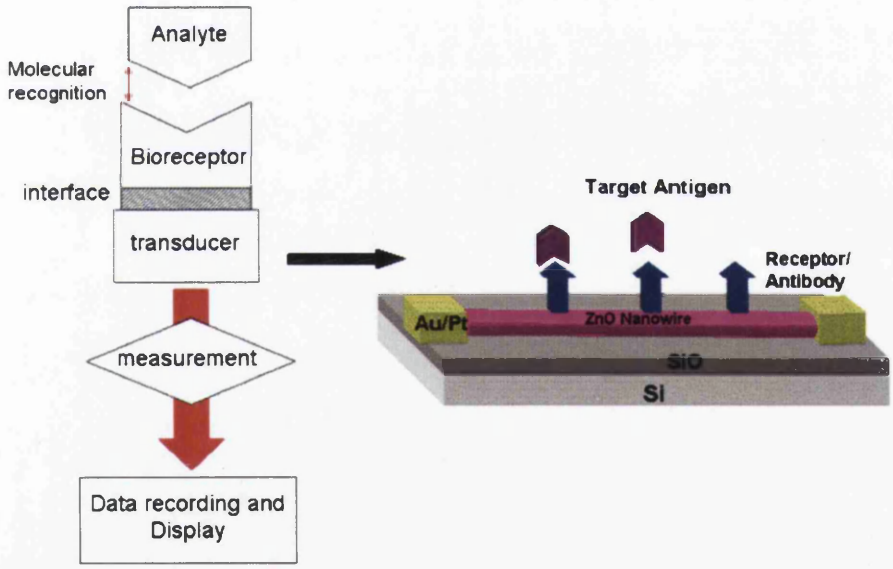

Figure 7.1 Schematic representations of a biosensor.

For efficient bio-sensing, there are a few essential criteria that the immobilisation technique should meet. Firstly, the immobilised biological molecules must be correctly orientated, retaining their structure and functionality. The immobilised biological molecules must also be durable and securely tethered to the sensor surface. In addition, for practicality, the biological molecules must possess a high degree of specificity to a particular analyte of interest. Other criteria include the ability for

immobilised biological molecules to adapt to different environments and able to have more than one immobilised active component on the sensor surface for multiplex sensing. The immobilisation technique employed must be reproducible and not impair the physical and electronic properties of the nanostructure surface. In this work, we look for a specific bio-friendly functional group that permits strong and flexible linkage of biological molecules to the surface of ZnO nanostructures. Different types of functional moieties were investigated for their affinity to ZnO surface. Below is a list of possible surface functionalisation strategies:

- Strategy I: Hexahistidine tag (His-tag)
- Strategy II: Zinc finger moieties
- Strategy III: Fluorescence nitrilotriacetic acid (NTA)
- Strategy IV: Nitrilotriacetic acid (NTA) bio-receptor mimic
- Strategy V: Polyamino acid as the intermediate linker

For each respective strategy, various evaluation techniques were exploited, namely the Biacore X system, a surface plasmon resonance detection technique (Strategy I and II), thermogravimetric analysis and thin layer chromatography technique (Strategy IV), confocal and fluorescence microscopes (Strategy V). The principles behind each technique are presented in Chapter 3, 4 and 5.

7.2. ZnO surface preparation

For Strategy I and II, Biacore X system (GE healthcare Ltd.) was used to investigate the binding affinity of various functional groups to ZnO surface. As mentioned in Chapter 4, the Biacore system detects molecules interactions by monitoring mass changes on the surface of a sensor chip. This section explores ways to create a ZnO surface layer on a sensor chip, so that the binding interactions of biomolecules (with functional group of interest) injected across the ZnO surface can be monitored. Two different routes were attempted; the first by coating a plain gold sensor chip (Sensor chip Au) with a layer of ZnO thin film and the second by binding ZnO nanoparticles (ZnO NPs) on Sensor chip NTA, a type of commercial available sensor chip with pre-immobilised nitrilotriacetic acid on its surface.

7.2.1. ZnO thin film coated on Sensor chip Au

7.2.1.1. Sample preparation

SIA Kit Au (GE Healthcare Ltd), which contains unmounted gold (Au) sensor surfaces, adhesive strips, sensor chip supports, a protective sheath and an assembly unit, was used (Figure 7.2). The SIA Kit Au allows design of customised sensor surfaces using a variety of coating techniques, including those using harsh conditions that the chip carrier would not withstand.

Figure 7.2 The SIA Kit Au is made up of 10 unmounted gold surfaces, 12 adhesive strips, 10 sensor chip supports, a protective sheath and an assembly unit.

The results were analysed using BIA evaluation software [1]. The customised ZnO sensor surface was prepared by coating the unmounted Au sensor surface with a thin layer of ZnO thin film by filtered cathodic vacuum arc at room temperature [2]. The ZnO thin film has a thickness of ~60 nm and the carrier concentration measured using Hall Effect on quartz substrate was about 7×10^{19} cm^{-3}. This customised sensor chip was then assembled by mounting the as prepared ZnO/Au surface on a sensor chip support using the provided adhesive strips and then inserted into a protective sheath. The ZnO/Au Sensor chip was then docked onto the Biacore X system and ready for subsequent bio-molecules and ZnO surface binding experiments. A plain Sensor chip Au was used as a control.

7.2.1.2. Results and discussion

Before injecting any bio-molecule samples across the ZnO surface, a baseline and signal check is required to ensure the competency of the modified sensor chip ZnO/Au. Figure 7.3 shows the evaluated (BIAevaluation software) result sensorgram for the baselines with continuous running buffer flow (10 µl/min) across the plain Sensor chip Au (pink), Sensor chip ZnO/Au before (blue) and after (green) overnight

continuous buffer flow with response of ~41000 RU, ~95000 RU and 48000 RU respectively.

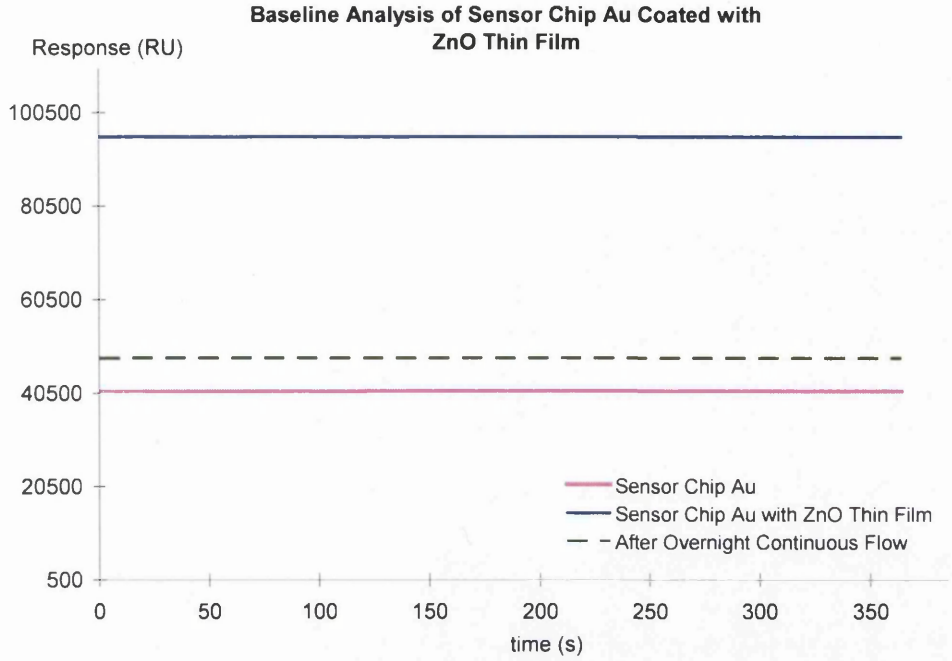

Figure 7.3 Baselines of bare Sensor chip Au (pink) and Sensor chip Au coated with 60 nm ZnO thin film before (blue) and after (green) overnight continuous Buffer flow.

By comparing the baselines, there was a difference of ~47000 RU between the plain Sensor chip Au and the ZnO/Au Sensor chip (blue). The Biacore X has a dynamic range of 1.33-1.4 refractive index range, equivalent to absolute response unit up to 70,000 RU [3]. The measured response of ~95000 RU for the ZnO thin film coated Sensor chip Au is significantly higher than the maximum dynamic range of the Biacore system. A quick signal check using the Biacore X control software confirmed that the SPR signal was indeed dynamically out of range. It can be concluded that the ZnO thin film, although transparent, was too thick, causing obstruction to the SPR signal. Moreover, when the ZnO/Au Sensor chip was docked and left overnight under continuous running buffer flow (5 µl/min), the thin film appear to have been removed by the buffer flow. This was observed from the lower baseline response (green) in Figure 7.3 (from ~95000 RU down to ~48000 RU). Therefore, an alternative surface preparation step was needed as the ZnO thin film has not only obstructed the SPR signal but also did not bond well on the Au sensor chip surface. An alternative route for ZnO surface preparation will be discussed in the next section.

7.2.2. ZnO nanoparticles pre-immobilised on Sensor chip NTA

Sensor chip NTA, with nitrilotriacetic acid (NTA) pre-immobilised on a dextran matrix is designed to capture polyhistidine-tagged recombinant proteins using the free coordination sites of chelated metal ions. Because of the high affinity of NTA to various divalent metal ions, such as Ni^{2+}, Mg^{2+}, Zn^{2+}, Ca^{2+} etc [4], the possibility of NTA ligands to chelate ZnO nanoparticles (ZnO NPs) was investigated as a preliminary study to prepare a suitable ZnO surface layer on the sensor chip.

7.2.2.1. Sample preparation

A Biacore X system and Sensor chip NTA (GE Healthcare) were used. The results were analysed using BIA evaluation software [1]. ZnO NPs (average molecular weight = 81.39 g/mol, size ≤ 100 nm, and with surface area = 15–25 m^2/g) was purchased from Sigma Aldrich. The running buffer used in the Biacore experiments was made up of 10 mM HEPES, 0.15 M NaCl, 0.0005% P20, and 8% glycerol (pH 7.3). Regeneration buffer was made up of 10 mM HEPES, 0.15 M NaCl, and 0.35 M EDTA (pH 8.3). A 0.5 M stock solution of the ZnO NPs was diluted using the as-prepared running buffer to 2, 4, 6, and 8 mM. Each binding and dissociation cycle was performed with a constant flow rate of the running buffer of 5 µl/min. For each cycle, 35 µl of each ZnO NP solution of different concentration was injected onto the NTA sensor chip surface. Sample injection was followed by a 1 min washing step using the running buffer at a flow rate of 100 µl/min. The ZnO NP dissociation was then monitored under a continuous flow of the running buffer (t ~2000 s). The surface was regenerated using the regeneration buffer to remove all the ZnO NPs. An illustration of the interactions between ZnO NPs and the NTA sensor chip surface is shown in Figure 7.4.

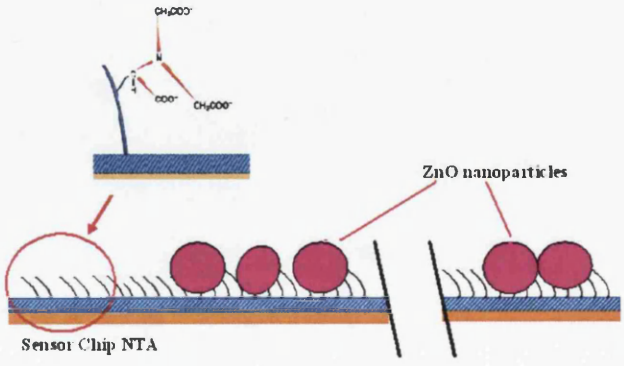

Figure 7.4 Illustrations of the interactions between ZnO NPs and Sensor chip NTA.

7.2.2.2. Results and discussion

Figure 7.5 shows the results of the Biacore affinity analysis of ZnO NPs to the surface of Sensor chip NTA. Under continuous running buffer flow conditions (rate: 5 µl/min), the sensor chip initially gives a baseline response (see A, Figure 7.5). Upon injection of ZnO NPs an increase in response is observed as a result of the particles present both in the flow and now binding to the NTA surface (see B, Figure 7.5). A washing step follows, which utilises the running buffer at a flow rate of 100 µl/min to remove loosely bound ZnO NPs. The amount of ZnO NPs bound was then determined by measuring the maximum response signal determined at point C (Figure 7.5). After washing, the running buffer continues to flow at a rate of 5 µl/min and desorption of the ZnO NPs from the chip surface can be monitored (from points C–D).

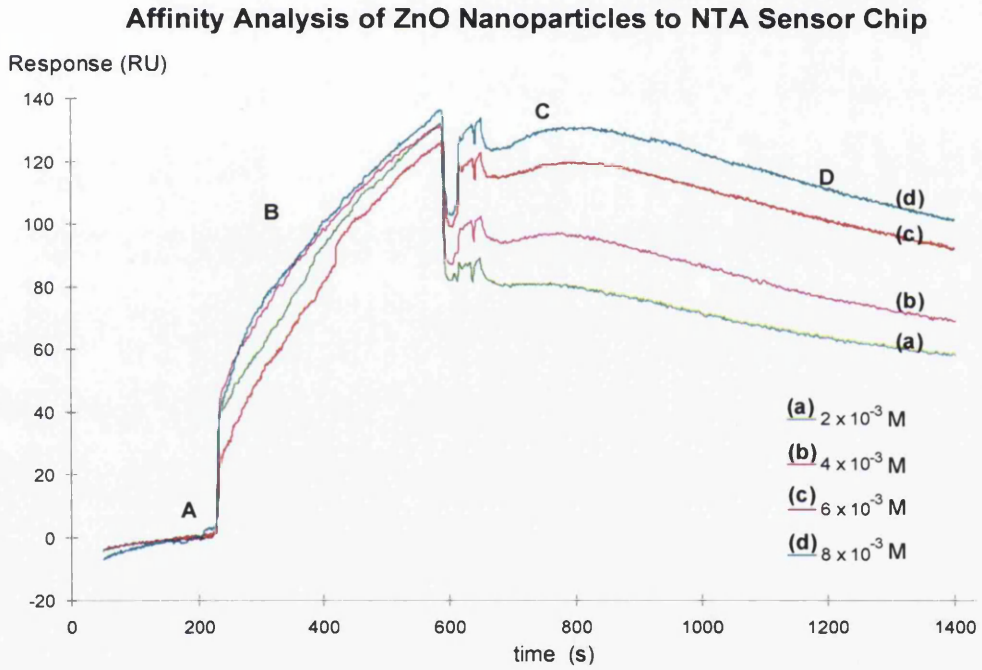

Figure 7.5 Plot of the SPR response upon binding of ZnO NPs at different concentrations (2, 4, 6, and 8 mM) to the NTA sensor chip surface. After the baseline is reached, NPs were injected (A) allowed to associate for 7 minutes (B). The injection is stopped and the surface thoroughly washed with running buffer to remove any unbound ZnO NPs. The maximal binding, R_{max} is determined at point C and the dissociation of the NPs can be monitored (C to D).

While the concentration necessary to saturate the chip surface with ZnO particles was not determined, the results clearly show a high binding affinity between the surface of the ZnO NPs and the NTA ligands. It was noted that the change in response unit (RU) due to the association of ZnO NPs (2, 4, 6, and 8 mM) to the

Sensor chip NTA surface were low in the range of 60-100 RU. This shows the high sensitivity of the Biacore system, being able to detect the binding of small analytes down to macromolecule size [3]. Following these results, as a surface preparation step, subsequent experiments utilised pre-immobilised ZnO NPs on the Sensor chip NTA to investigate the affinity of different functional moieties to ZnO.

7.3. ZnO surface functionalisation strategies

In this section, four different ZnO surface functionalisation strategies (Strategy I-IV) are discussed. The first two strategies investigate the binding of two common biological entities, the hexahistidine tags (His_6 tags) (Strategy I) and the zinc fingers (Strategy II), to ZnO NPs surface using the Biacore X system. Following the results in Section 7.2.2, ZnO NPs were pre-bound on Sensor chip NTA, as a means to provide a ZnO sensor surface for the binding studies. Strategy III and IV investigate the prospect of exploiting NTA as the functional linker group between ZnO surface and organic material. Two compounds were synthesised, a fluorescence tagged NTA (Strategy III) and a bio-receptor mimic incorporated with the NTA (Strategy IV).

7.3.1. Strategy I : Hexahistidine tags (His_6)

While NTA itself proved effective in binding ZnO, attention was turned to Hexahistidine (His_6) peptide, a well known biological linker. The His_6 peptide, which consists of a single amino acid sequence, is able to coordinate metal ions by the multiple imidazole side chains of the histidine units. It is known to strongly bind to Zn^{2+} ions and is often used to link biomolecules to zinc (and other) fluorescent probes for labelling. In addition to purify proteins by acting as a coordinating ligand to metal ions that are pre-immobilised as chelate complexes to NTA-bound solid supports [5]. As such, the first part of the work looks at the ability of Hrs1 protein (SAC) tagged with His_6 to bind to the surface of the pre-immobilised ZnO NPs sensor chip NTA. As further investigation, the experiment was repeated with His_6 peptide. Control studies were also performed with pre-immobilised Ni^{2+} ions on the Sensor chip NTA for both Hrs1 protein (tagged with His_6) and His_6 peptide respectively. Ni^{2+} ions were used as a control since its affinity to His_6 tag is sufficiently high and such NTA/Ni^{2+}/His-tag complexes are well known [3,6,7].

7.3.1.1. Sample preparation

A Biacore X system and Sensor chip NTA (GE Healthcare) were used. The results were analysed using BIA evaluation software [1]. ZnO NPs (molecular weight = 81.39 g/mol, average diameter < 100 nm, and with surface area = 15–25 m^2/g) and $NiCl_2$ were purchased from Sigma Aldrich. Histidine-tagged Hrs1 proteins (molecular weight ~44 kDa, p*I* ~9.13), which were expressed in *Escherichia coli*, were courtesy of the Institute of Life Sciences, Swansea University [8]. Hexahistidine peptide (His_6 peptide, sequence (Ac-)HHHHHH(-COOH), molecular weight of 883 Da, 95% purity) was purchased from Innovagen. The running buffer used in the Biacore experiments was made up of 10 mM HEPES, 0.15 M NaCl, 0.0005% P20, and 8% glycerol (pH 7.3). Regeneration buffer was made up of 10 mM HEPES, 0.15 M NaCl, and 0.35 M EDTA (pH 8.3).

7.3.1.2. Results and discussion

The results for the binding interactions between Hrs1 proteins with Ni^{2+} and ZnO nanoparticles are depicted in Figure 7.6 and Figure 7.7 respectively.

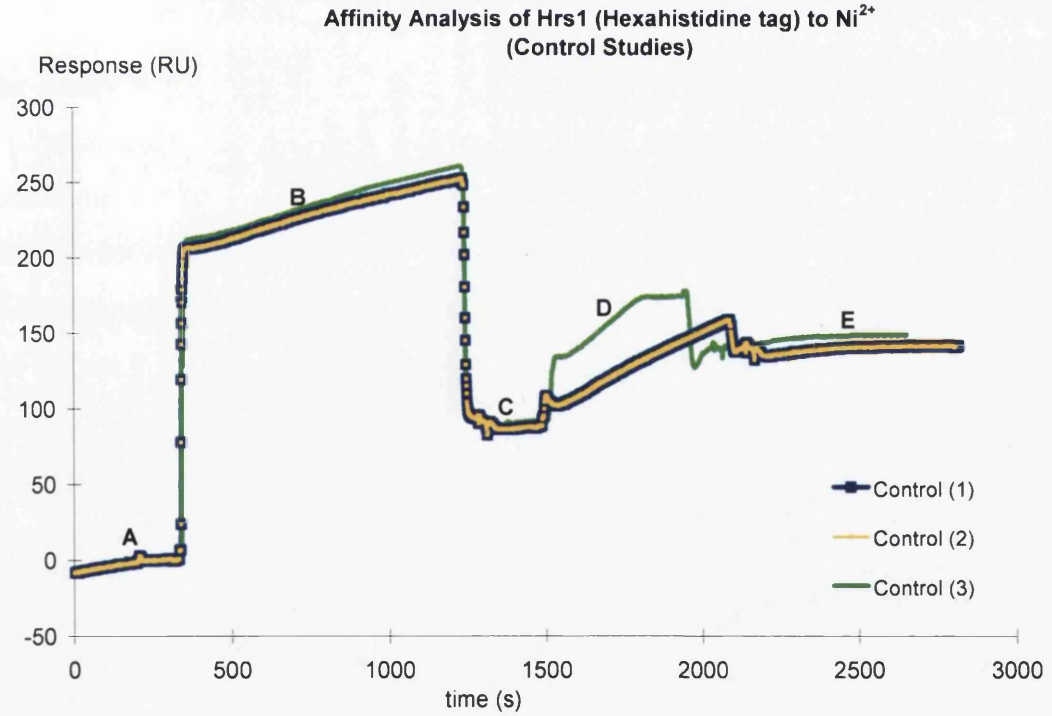

Figure 7.6 Overlay plots of the binding of His-tag protein (Hrs1) to Ni^{2+}. After obtaining a stable baseline (A), 1mM $NiCl_2$ solution was injected and allow to charged up the sensor chip surface (B). After charging the NTA surface (C), 20 µl of the His tag protein (Hrs1) was injected and its binding response was measured (E). 10ng/ul of Hrs1 protein was injected for Control (1) and Control (2) and 20 ng/µl for Control (3).

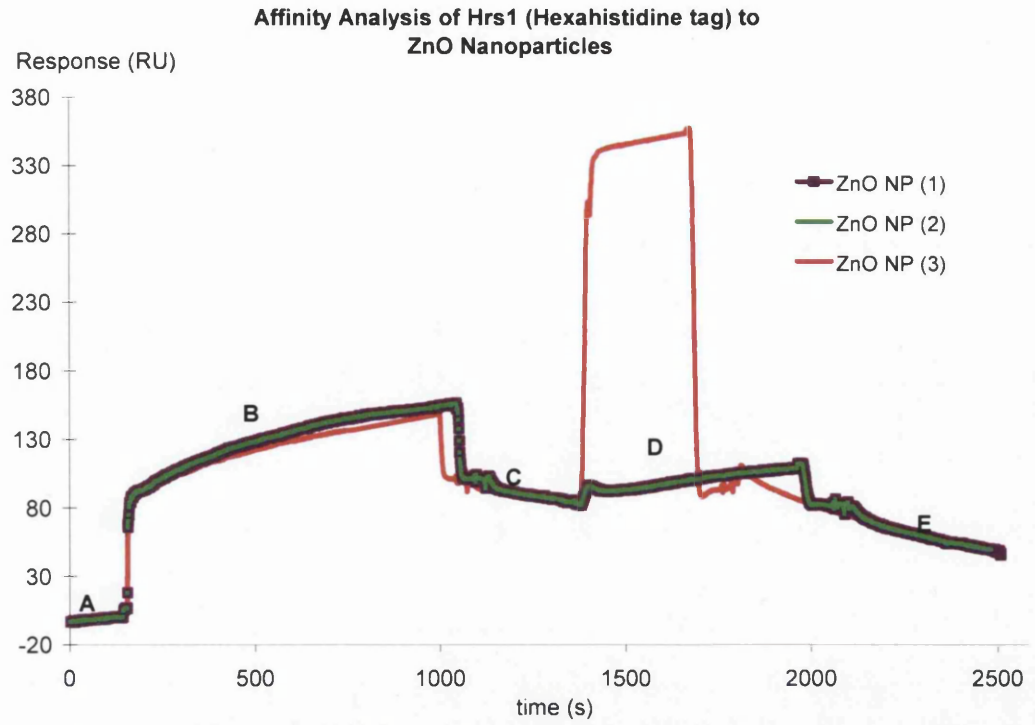

Figure 7.7 Overlay plots of the binding of His-tag protein (Hrs1) to ZnO NP. After obtaining a stable baseline (A), 10 mM ZnO solution was injected and allow to charged up the sensor chip surface (B). After charging the NTA surface (C), 20 µl of the protein (Hrs1) was injected and its binding response was measured (E). 10 ng/µl of Hrs1 protein was injected for ZnO NP (1) and ZnO NP (2) and 40 ng/µl for ZnO NP (3).

The binding cycle was performed at a constant flow rate of running buffer of 2 µl/min. Before sample injection, a stable baseline response was obtained under continuous buffer flow (see A, Figure 7.6 and Figure 7.7). The Sensor chip NTA was loaded with ZnO NPs (or Ni^{2+}) by injection of 20 µl of a 0.01 M ZnO NP (or 1 mM of $NiCl_2$) solution where an increased in response was observed (see B, Figure 7.6 and Figure 7.7). After a washing step and ~1200 s of continuous running buffer flow (see C, Figure 7.6 and Figure 7.7), 20 µl of his-tagged Hrs1 protein was injected. Upon injection of the protein, an increased in response was observed as the proteins flow across the sensor chip surface to allow interactions (see D, Figure 7.6 and Figure 7.7). Then, a second washing step follows and any binding response was observed (see E, Figure 7.6 and Figure 7.7). The surface was then regenerated with regeneration buffer until the initial baseline was obtained. The binding assay was repeated at different concentration of his-tagged Hrs1 protein which is represented by the respective sensorgrams as labelled in Table 7.1.

Sensorgram	Hrs1 Concentration (ng/μl)
Control (1)	10
Control (2)	10
Control (3)	20
ZnO NP (1)	10
ZnO NP (2)	10
ZnO NP (3)	40

Table 7.1 Different concentrations of Hrs1 protein injected across the sensor chip with respect to each sensorgram.

Referring to Figure 7.6 and Figure 7.7, upon injection of higher concentration of Hrs1 proteins, (see D, Control (3) in Figure 7.6 and ZnO NP(3) in Figure 7.7 respectively), a higher response was observed as a result of more concentrated protein present both in the flow and interacting with the sensor chip surface (as compared to Control (1), Control (2), ZnO NP (1) and ZnO NP (2)). Also, it was noted that Hrs1 proteins (40ng/μl) injected across modified sensor surface ZnO (see D, ZnO NP(3) in Figure 7.7) induced about twice the response unit to that of Hrs1 proteins (20 ng/μl) injected across the Ni^{2+} modified surface (D, Control (3) in Figure 7.6). These observations were expected since the response of the SPR detector is influenced by the changes in refractive index across the surface of the sensor chip. The final binding response for both Ni^{2+} and ZnO chelated sensor chips showed consistent results (see E) with stable binding response for the Ni^{2+} and the lack of binding for the ZnO NP.

As a further investigation, the Hrs1 protein and ZnO NP binding assays were repeated using hexahistidine peptide (His_6). The Sensor chip NTA was loaded with ZnO NPs (or Ni^{2+}) by injection of 20 μl of 0.01 M ZnO NP (or 0.01 M $NiCl_2$) solution (see B, Figure 7.8 and Figure 7.9). The concentration of the His_6 peptide used in this binding assay was 10 ng/μl for all repeated experiments. The results are shown in Figure 7.8 and Figure 7.9 for His_6 peptide binding to Ni^{2+} and ZnO NP respectively.

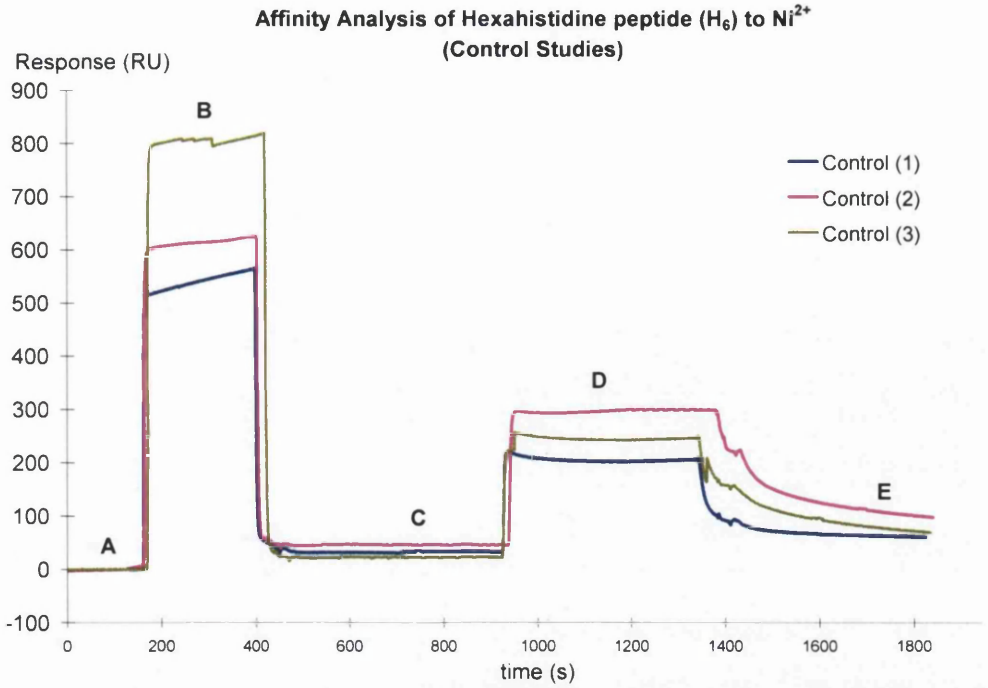

Figure 7.8 Overlay plots of the binding of hexahistidine peptide (His_6) to Ni^{2+} modified sensor surface. After obtaining a stable baseline (A), 0.01M $NiCl_2$ solution was injected and allow to charge up the sensor surface (B). After charging the NTA surface (C), 20 µl of His_6 at 10 ng/µl was injected and its binding response was measured (E).

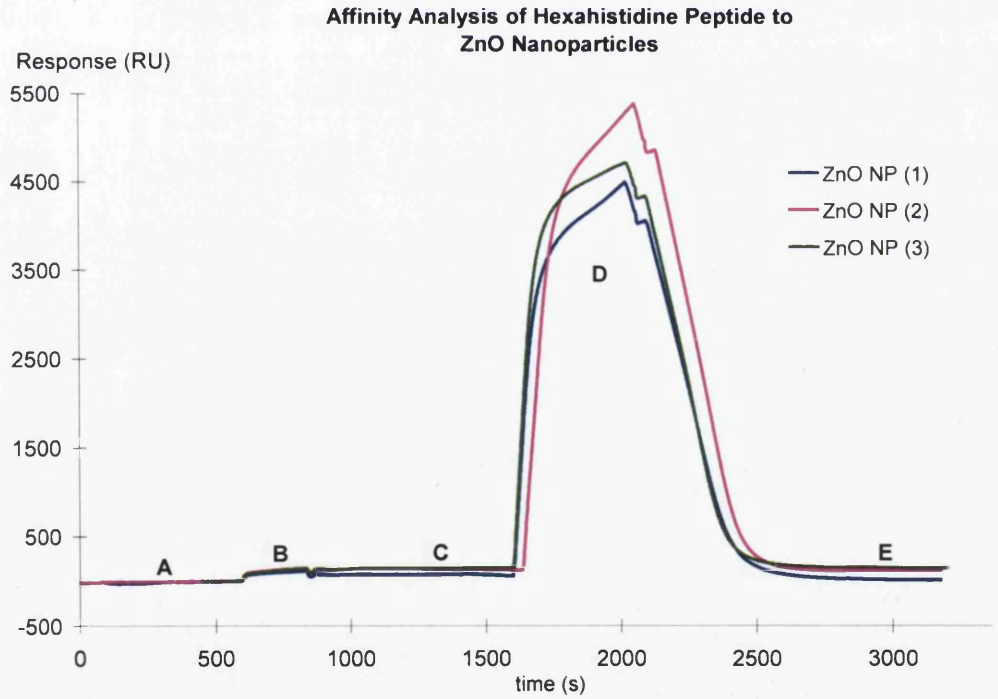

Figure 7.9 Overlay plots of the binding of hexahistidine peptide (His_6) to ZnO NPs modified sensor surface. After obtaining a stable baseline (A), 0.01M ZnO solution was injected and allow to charge up the sensor surface (B). After charging the NTA surface (C), 20 µl of His_6 at 10 ng/µl was injected and its binding response was measured (E).

Similar to previous results, the Ni^{2+}-bound NTA chip showed the expected strong binding response upon exposure to His_6 peptide and Hrs1 his-tag protein and the ZnO NP-bound NTA chip demonstrated poor response. An interesting observation is that the response unit when His_6 peptide was injected across the ZnO NPs modified sensor surface (see D, in Figure 7.9) was almost 10-fold higher than that of His_6 peptide injected across the Ni^{2+} modified surface (see D, Figure 7.8). The pre-bound ZnO NPs appear to have caused a certain amount of optical enhancement to the sensor detector. A closer look at the at the sensorgram in Figure 7.9, suggests some sort of transient response between the His_6 peptide and ZnO NPs bound sensor surface (see D, Figure 7.9). While the His_6 peptide is able to strongly bind Zn^{2+} ions free in solution, it is likely that its ability to chelate Zn 'ions' in the ZnO lattice is compromised by space limiting ability to adopt the tetrahedral geometry usually associated with hexahistidine-Zn^{2+} coordination and as a result of the decreased number of coordination sites available on Zn 'ions' in the ZnO surface.

7.3.2. Strategy II: Zinc fingers

Zinc fingers are small, functional, independently folded domain that requires coordination of one or more zinc ions to stabilise its structure [9]. These fingers bind to a single zinc ion that is tetrahedrally coordinated between an α-sheet and two-stranded anti-parallel β-sheet to form an αββ domain [10]. The oestrogen receptor (ERα), a DNA-binding transcription factor that regulates gene expression, possesses two zinc fingers (refers Chapter 2 for details). In this section, the affinity of the ERα to ZnO NP (through its zinc fingers) is examined.

7.3.2.1. Sample preparation

A Biacore X system and Sensor chip NTA (GE Healthcare Ltd.) were used. The results were analysed using BIA evaluation software [1]. ZnO NPs (average molecular weight = 81.39 g/mol, size < 100 nm, and with surface area = 15–25 m^2/g) and $NiCl_2$ were purchased from Sigma Aldrich. Oestrogen receptor (ERα) was purchased from Active Motif. The recombinant ERα is specific for the ERα subunit and the full length was expressed (accession number NM 000125) with an amino terminal polyhistidine tag in a baculovirus system and purified by an affinity column in combination with FPLC chromatography. The supplied stock concentration was

200 ng/µl in AM1 buffer (20 mM Tris-Cl (pH 8), 20% glycerol, 100 mM KCl, 1 mM DTT, and 0.2 mM EDTA). The running buffer used in the Biacore experiments was made up of 10 mM HEPES, 0.15 M NaCl, 0.0005% P20, and 8% glycerol (pH 7.3). Regeneration buffer was made up of 10 mM HEPES, 0.15 M NaCl, and 0.35 M EDTA (pH 8.3). A stock solution of ERα (200 ng/µl in 20 µl of AM1 buffer) was diluted with the running buffer to three different concentrations of 2, 4 and 8 ng/µl.

7.3.2.2. Results and discussion

The results for the binding studies of ERα to ZnO NPs pre-bound on Sensor chip NTA are given in Figure 7.10. For each binding cycle, 20 µl of ZnO NPs (4 mM) was injected to generate a ZnO sensor surface for interaction studies (not shown in sensorgram). Subsequently, a stable baseline response under continuous running buffer flow across the pre-bound ZnO NP sensor surface was achieved (see A, Figure 7.10). 35 µl of ERα protein solution was then injected across the sensor surface (see B, Figure 7.10) and the response was observed 100 s after the end of the ERα protein injection (see C, Figure 7.10). The binding interactions was repeated for different concentration of ERα protein; 2, 4 and 8 ng/µl.

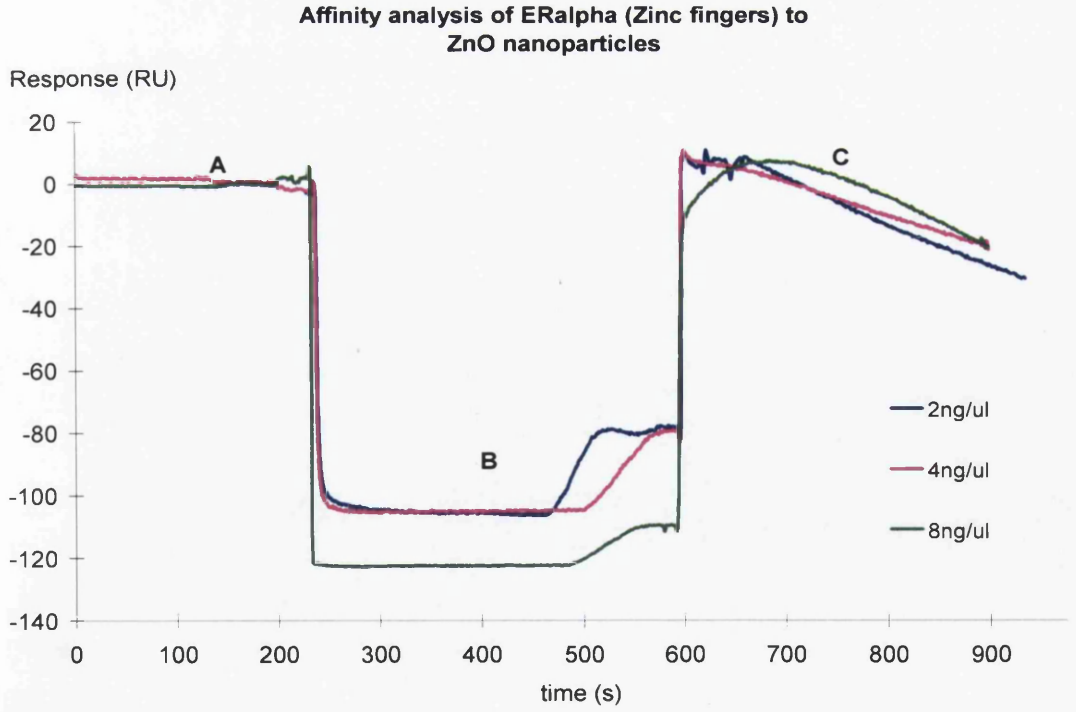

Figure 7.10 Overlay plot showing the binding of zinc fingers protein (ERα) to ZnO – NTA. After charging the NTA surface with 4 mM of ZnO nanoparticles (A), 35 µl of the ERα was injected and its binding response was measured after 100 s.

A decrease in response unit (RU) during ERα protein injection (see B, Figure 7.9) can be observed. This was due to the difference in refractive index between the running buffer and the sample dilution buffer (AM1). From this analysis, the ERα zinc fingers protein showed lack of binding to the ZnO NPs immobilised on the NTA sensor chip (Figure 7.10). The seemingly incongruous (i.e., negative) result for the detected response with ERα is indicative of a complete lack of binding of the protein and the continual, gradual desorption of ZnO from the chip surface in the continuous buffer flow.

The inability of the ERα protein to bind the ZnO particles is possibly a reflection of the zinc binding site being located within 'pockets', easily accessible to free Zn^{2+} ions but unavailable to zinc held in the ZnO surface. This inaccessible zinc fingers pocket can be illustrated in Figure 7.11.

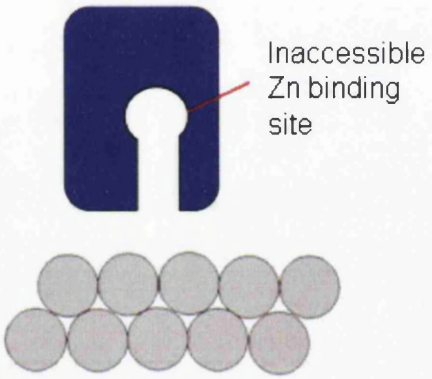

Figure 7.11 Illustration of an inaccessible Zn^{2+} binding site of a zinc finger moiety.

7.3.3. Strategy III: Fluorescence tagged nitrilotriacetic acid (NTA)

In an attempt to visualise the attachment of NTA to ZnO surface, the synthesis of fluorescence tagged NTA mimic compound (Et-NTA) was carried out. Ethidium Bromide (EtBr), is a non-radioactive marker that fluoresces reddish-brown when exposed to ultraviolet (UV) light, was chosen as the fluorescent candidate. This compound is well known and widely used as intercalating agent for the staining of DNA in molecular biology. The Et-NTA compound was formed by conjugating EtBr to ethylenediaminetetraacetic acid (EDTA), which has similar structure to the NTA. Like the NTA compound, EDTA is also known as a strong chelating agent that binds to di- and trivalent metal ions via carboxylate groups.

7.3.3.1. Sample preparation

Ethylenediaminetetraacetic acid (EDTA) and ethidium bromide (EtBr) were purchased from Sigma Aldrich. 1-Ethyl-3-(3-dimethylaminopropyl)carbodiimide (EDC) and N-hydroxysulfosuccinimide (NHS) were purchased from Invitrogen. The synthesis steps of Et-NTA are shown in Figure 7.12.

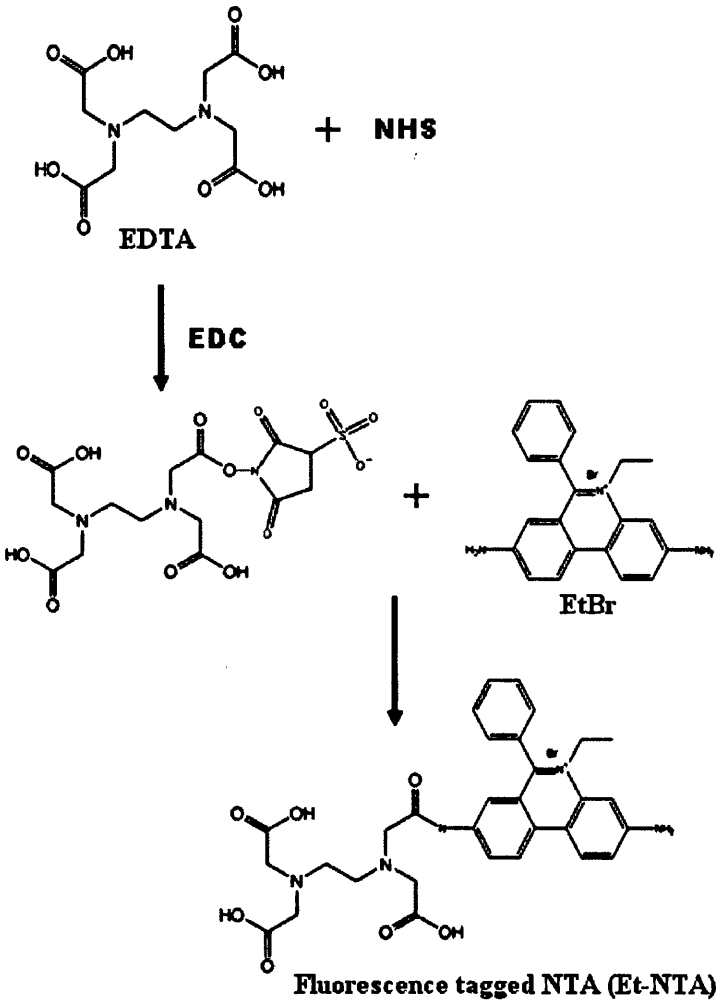

Figure 7.12 Synthesis route for fluorescence tagged NTA compound (Et-NTA) via carbodiimide chemistry.

With the presence of amine and carboxylic groups in each respective compound, the conjugation of the EtBr to EDTA was carried out by the well known carbodiimide chemistry. 50 ml of EDTA (0.47202 g in DI water) was mixed with 1.0144 ml of NHS (0.1 M) and 0.25361 ml of EDC (0.4 M) was then added into the solution. The pH of this mixture was adjusted to pH 7.5-8.5 using 1 M of NaOH. After 15 minutes of activation time, 4 ml of EtBr (25 mM) was added into the mixture and the mixture

was left overnight under continuous stirring. After the overnight reaction, the product was made acidic (pH 1–2) using 1 M HCl to change the remaining free carboxyl groups a free acid form.

7.3.3.2. Results and discussion

The EDTA compound has four carboxylic groups (COOH) while the EtBr has amine group (NH_2) on both terminuses. To conjugate both compounds together, one of the carboxylic acid (EDTA) was first converted to a succinimide ester using EDC and NHSS. The succinimide ester-modified EDTA then spontaneously reacts with one of the amine on the EtBr (Figure 7.12). For quick and easy analysis, thin layer chromatography (TLC) was carried out on the resultant synthesised Et-NTA. The TLC measures the R_f values, which is a measure of movement of a compound relative to the movement of the solvent. With the R_f of a known compound, the identity of a compound in a mixture can be resolved. To ensure the reliability of the result, the TLC spotting was repeated, as shown in 1, 2 and 3 of Figure 7.13. The results show that the R_f values of the product (P) and the EtBr (reference spot) are the same. This is observed by the same distance travelled from the original position by both of the spot solution (P and EtBr). In other words, non Et-NTA was detected in the synthesised mixture solution. The failure in the conjugation of EtBr to EDTA may be due to the fact that the amine groups of EtBr are bound to a stable aromatic ring. Further research is needed to explore a better synthesis route, which will not be discussed further in the present work.

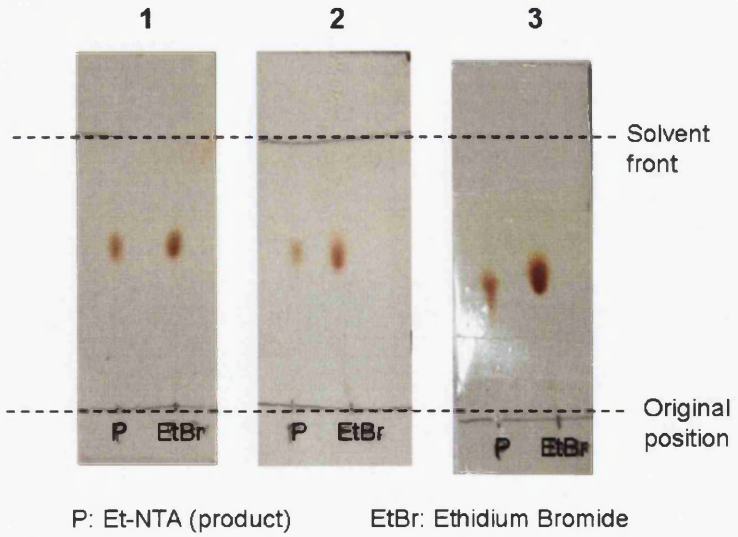

Figure 7.13 The results of the thin layer chromatography (TLC) plates of the fluorescence tagged NTA moieties (Et-NTA). The TLC spotting was repeated as shown in 1, 2 & 3.

7.3.4. Strategy IV: Nitrilotriacetic acid (NTA) bio-receptor mimic

The idea to have a functional customised linker that can bind to ZnO surface is explored in this section. The surface functionalisation strategies discussed thus far have shown that NTA moieties bound to ZnO NPs surface promisingly. As such, a customised NTA-like linker moiety was incorporated to a model organic compound and its binding capability to ZnO NPs was investigated. Beta-cyclodextrin (βCD) naturally occurs in starch by means of an enzymatic conversion from the bacteria *Bacillus macerans* and is part of a family of cyclic oligosaccharides. The host–guest properties of cyclodextrins and their modified analogues have led to their use as 'enzyme mimics', drug delivery vehicles, food stabilisers, etc (for some recent reviews on the uses of cyclodextrins, see refs. [11,12]). Therefore, βCD serves as a good model for the eventual binding of antibodies on ZnO nanostructures for specific antigen detection. More descriptions of the structure and applications of βCD can be found in Chapter 2 (Section 2.4.3). In the synthesis steps of the bio-receptor mimic, βCD was first modified by substitution of a primary hydroxy group with diaminopropane (pn) to give βCD-pn [13,14], followed by reaction with chloroacetic acid to give an NTA-like moiety covalently linked to the cyclodextrin. Such carboxylated amino-cyclodextrins are known to strongly bind various metals [14,15]. For example, the Zn^{2+} complex of 6^A-[bis(carboxylatomethyl)amino]-6^Adeoxy-β-cyclodextrin, [Zn(βCD-ida)], has a stability constant of log K = 6.08 dm^3/mol. This is slightly lower than that of the Zn^{2+} complex of the non-cyclodextrin bound bis(carboxylatomethyl)amino moiety [Zn(ida)] (log K = 7.24 dm^3/mol). The presence of the bulky cyclodextrin does lower the metal binding strength of the carboxylated linker, however, is it not expected to prevent βCD-NTA from binding to the ZnO surface.

7.3.4.1. Sample preparation

β-cyclodextrin (βCD, > 99%) was purchased from Fluka and dried to a constant weight in a vacuum oven at approximately 50 °C and 700 bar of pressure. Toluene-4-sulfonyl chloride (> 97%) was also purchased from Fluka. 1,3-Diaminopropane, chloroacetic acid, and *N*-methylpyrolidone were used as received from Aldrich. Pyridine was purchased from Lancaster and was distilled over calcium hydride under a nitrogen atmosphere. Thin layer chromatography (TLC) was carried out using

Whatman 250 μm silica gel coated aluminium sheets and developed using 7 : 4 : 5 : 7 propan-2-ol/ammonia/water/acetic acid. For the detection of amino groups in the compound, the developed plates were dipped into a solution of 1% ninhydrin in ethanol and heated over a Bunsen burner. As for the detection of cyclodextrins, the developed plates were dipped into a solution of 1% H_2SO_4 in ethanol and heated over a Bunsen burner.

7.3.4.2. General procedure for the synthesis of NTA bio-receptor mimic

The synthesis steps of the NTA bioreceptor mimic, βCD-NTA, are shown in Figure 7.14.

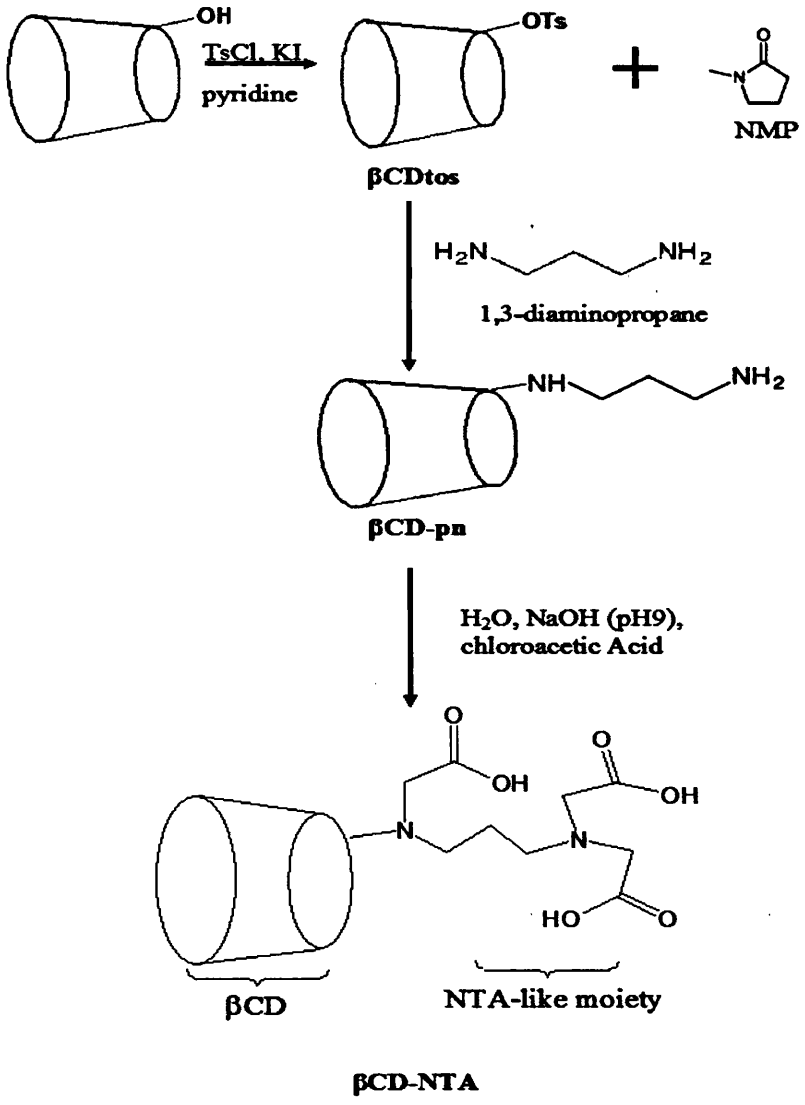

Figure 7.14 Synthesis route for βCD-NTA compound.

βCD was tosylated with 1:1 mole ratio of p-toluenesulfonyl chloride (TsCl) in dry pyridine. 0.33 g of TsCl in 50 ml distilled pyridine was added drop wise into a mixture solution of βCD (2.0 g) and pyridine (50 ml). The reaction was left overnight in continuous stirring under nitrogen gas environment. Excessive pyridine was removed by using rotary evaporation and acetone. The product, mono-6-p-toluenesulfonyl-β-cyclodextrin (βCDtos) was dried under vacuum in a desiccator overnight. 6^A-deoxy-(ω-aminopropylamino)-β-cyclodextrin (trβCD-pn) was synthesised as reported in the literature [13]. A solution of βCDtos (2.0 g, 1.55 mmol), KI (0.025 g, 0.15 mmol) and diaminopropane (5 mmol) in dry NMP (5 ml) was stirred at 70 °C in a lightly stoppered flask for 4-8 hour. The resultant light yellow solution was cooled to room temperature and added drop wise into cooled ethanol solution (100 ml). The resulting white precipitates were collected by vacuum filtration, washed successively with ethanol (100 ml) to remove any un-reacted diaminopropane and dried under vacuum. The crude product was then dissolved in water (10 ml) and loaded onto a column (4.5 x 4.5 cm) H^+ form Amberlite IR-120, 16-45 mesh (Fluka). The column was washed repeatedly with water (400 ml) to remove excessive βCD and βCD-NTA was eluted with 1 mol/dm^3 ammonium hydroxide (NH_4OH). Fractions containing the βCD-NTA were combined and evaporated to dryness under vacuum. The residue was then dissolved in water and the resultant solution was evaporated under reduced pressure to remove excess ammonia. For thorough removal of the ammonia, this step was repeated several times. The product was dried under vacuum over phosphorus pentoxide (P_2O_5) to give βCD-pn. The next step involved the carboxylation of βCD-pn by a literature procedure [14,15] to produce the final product, βCD-NTA. A solution of chloroacetic acid (0.25 g, 2.5 mmol in 1 ml H_2O) was neutralised by the addition of an aqueous solution of sodium hydroxide (0.1g, 2.5 mmol in 1 ml H_2O). This mixture was then added to an aqueous solution of βCD-pn (0.4 g, 0.3 mmol in 5 ml H_2O) and heated at 80 °C under continuous stirring for 2-3 hours. The pH was maintained by the addition of small amount of NaOH as required. The reaction mixture was then left stirring and cooled to room temperature until analysis by thin layer chromatography (TLC) showed the presence of only one product and some native βCD (approximately 12 hours). The solution was acidified, diluted and loaded onto a column (1 x 0.15 m) containing H^+ form Amberlite IR-120, 16-45 mesh

(Fluka). The column was then washed with H_2O (100 ml) and the product eluted with 1 mmol/ml NH_4OH. The solvent of the collected portions was removed by vacuum evaporation. The residue was then diluted with water and resultant solution was evaporated under reduced pressure (repeated several times). The product was dried under vacuum over phosphorus pentoxide (P_2O_5) to give an off white solid, βCD-NTA. Electrospray mass spectrometry analysis was performed on the ZQ4000 (Waters, UK) in positive ionisation mode.

7.3.4.3. Binding assay for thermogravimetric analysis

TGA is a simple and straightforward analytical technique to determine the weight loss or weight gain of a material as a function of increasing temperatures. When materials are heated, some will experience weight loss due to simple process like evaporation/drying, while some will experience weight gain due to reactions with the atmosphere of the testing environment. Therefore, with the knowledge of the magnitude and temperature range in which certain materials experience weight loss or weight gain (i.e. melting point), TGA analysis can be used to detect the presence of materials in a sample. In this work, thermogravimetric analysis (TGA) was performed on apparatus from TA Instruments (Model SDT Q600). The ZnO NPs were coated with βCD-NTA by stirring in a concentrated aqueous solution of the NTA-bioreceptor mimic for 24 hours. The mixture was then centrifuged and the supernatant removed. The pellet was washed by resuspending the ZnO–(βCD-NTA) in deionised water by sonification, followed by centrifugation, and removal of the supernatant. This process was repeated until the supernatant showed no trace of βCD-NTA (monitored by charring a droplet of supernatant previously placed and dried on a TLC plate and exposed to 1% H_2SO_4 in ethanol). A similar procedure was employed to coat ZnO NPs with native βCD. Native βCD, βCD-NTA, ZnO NPs, ZnO–(βCD-NTA), and ZnO–βCD were analysed by TGA. Samples were heated from 50 to 800 °C at 20 °C/min under a nitrogen flow of 100 ml/min.

7.3.4.4. Results and discussion

βCD was first modified by substitution of a primary hydroxy group with diaminopropane (pn) to give βCD-pn [13]. This was followed by reaction with chloroacetic acid to give the NTA-like moiety covalently linked to the cyclodextrin,

βCD-NTA (Figure 7.14). The electrospray mass spectrometer analysis (ES^+ MS *m/z*) of the product is shown in Figure 7.15.

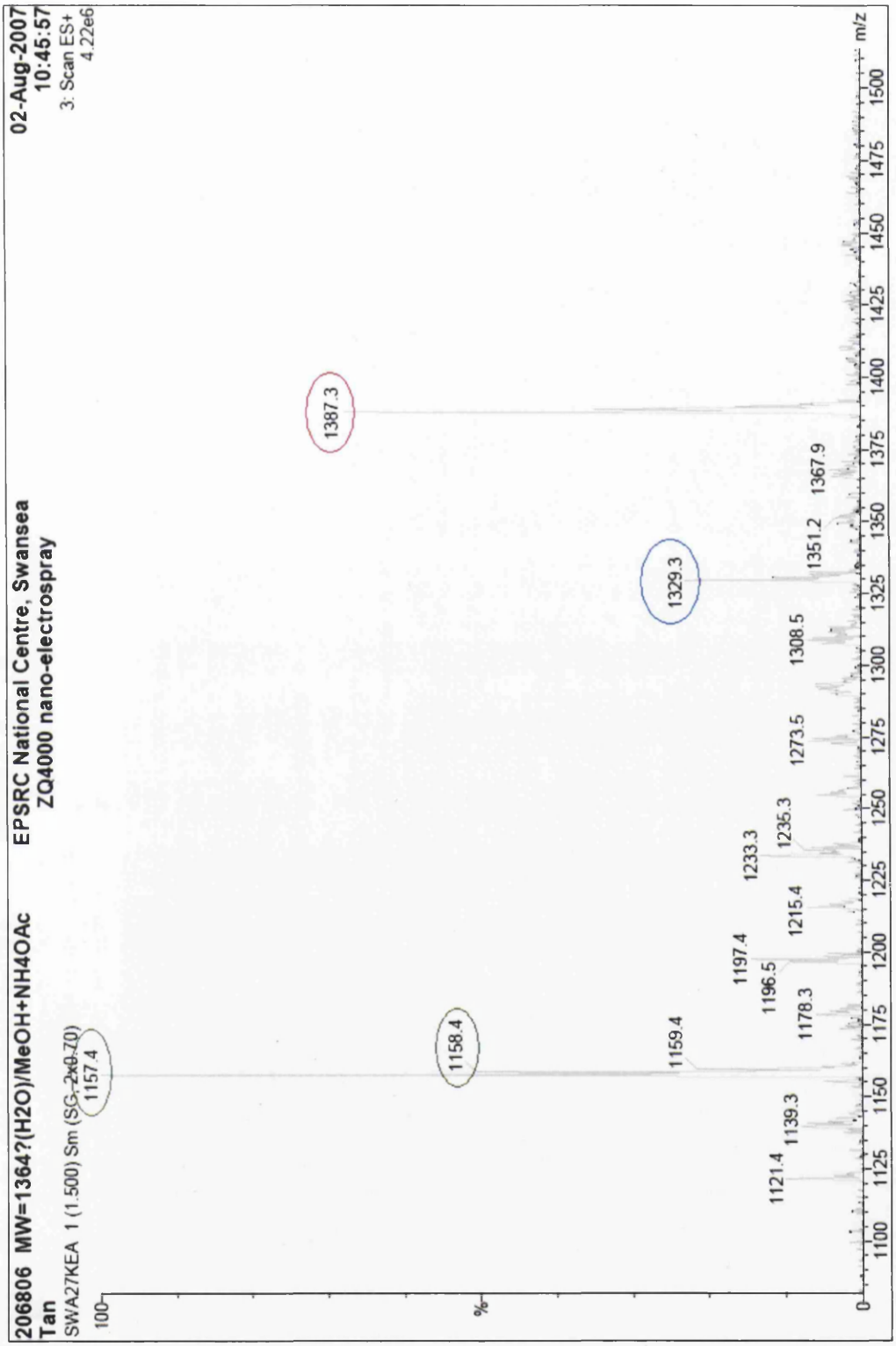

Figure 7.15 Electrospray mass spectrometry analysis of βCD-NTA performed on the ZQ4000 (waters, UK) in positive ionisation.

The result shows the presence of the product with sodium (βCD-NTA + Na^+): 1387 (red circle, Figure 7.15) and also other by products, such as (βCD with two spacer arms + Na^+): 1329 (blue circle, Figure 7.15) and (βCD + Na^+): 1157, 1158 (green circles, Figure 7.15). The presence of these fragments may be due to the disintegration of the 'NTA arms' caused by strong ionisation energy during mass spectrometer analysis.

Since visualising βCD-NTA molecules using scanning probe microscopy is difficult, the ability of βCD-NTA to bind to ZnO NPs was determined by TGA analysis. The binding assays were as described in Section 7.53. ZnO NPs were coated with βCD-NTA by stirring in a concentrated solution of the NTA-bioreceptor mimic for 24 hr and removing any unbound βCD-NTA by centrifugation washing. Native cyclodextrin is also able to bind to metal by its primary and secondary hydroxy groups. As such, ZnO NPs were also exposed to a concentrated solution of native βCD to help elucidate the mode of binding of βCD-NTA (i.e., by the NTA-like moiety or by the native OH groups). The samples were heated from 50 to 800 °C at a rate of 20 °C/min. The result of the TGA analysis of uncoated ZnO NPs is shown in Figure 7.16. As expected, the uncoated ZnO NPs showed negligible weight loss over this range (ZnO melting point: 1975 °C).

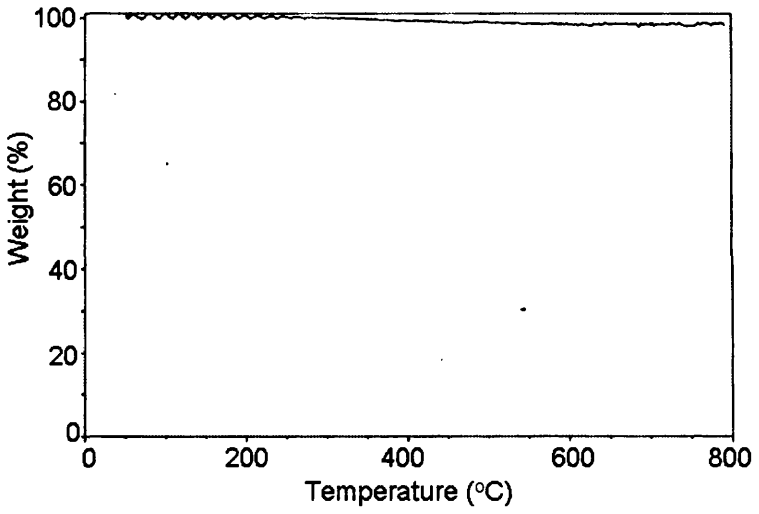

Figure 7.16 Thermogravimetric analysis (TGA) of ZnO nanoparticles (ZnO NPs). The result shows that uncoated ZnO NPs experienced negligible weight loss between the 50 to 800 °C temperature range.

The TGA analysis of native βCD and βCD-NTA are shown in Figure 7.17A and B respectively. The native βCD gave a sharp single decomposition signal at ~340 °C (Figure 7.17A), while βCD-NTA fully decomposed (broad single-step response) between 250 and 350 °C (Figure 7.17B). As βCD-NTA is made up of βCD, diaminopropane linker and NTA-like moiety (Figure 7.14); the melting point for each 'part' is different, which explains the broad single step response.

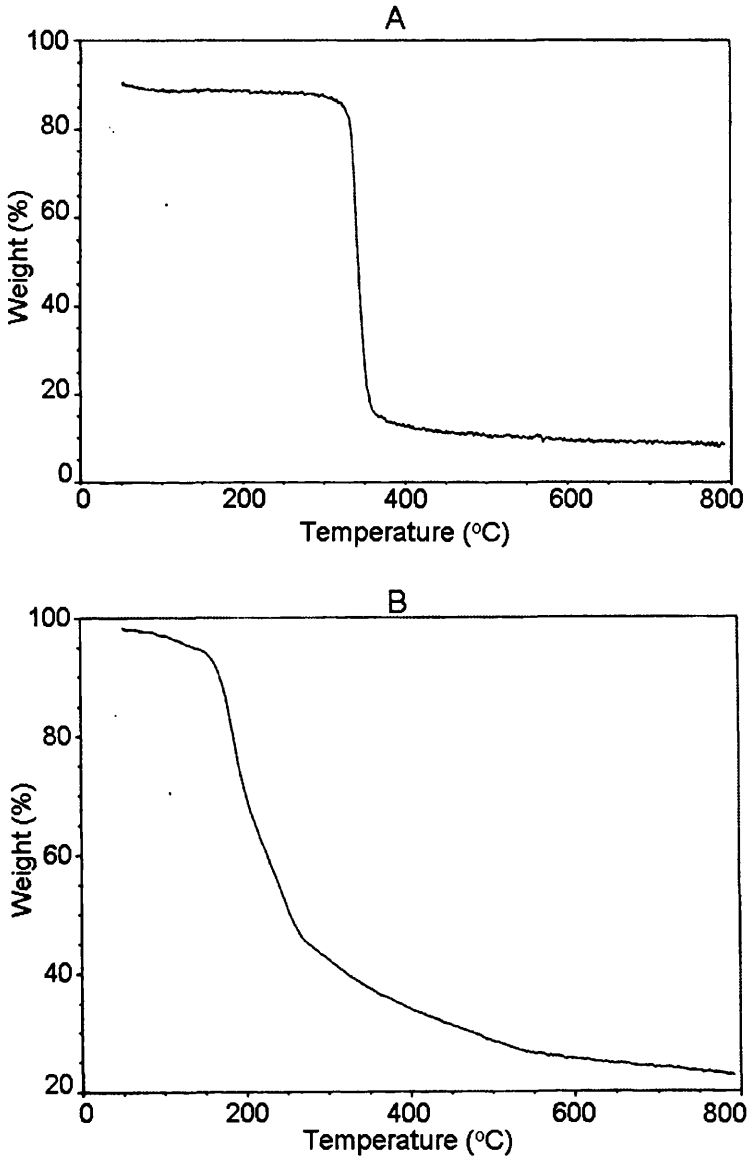

Figure 7.17 Thermogravimetric analysis (TGA) of (A) native βCD and (B) βCD-NTA. (A) Native βCD experienced a sharp single decomposition at 340°C. (B) βCD-NTA was fully decomposed between 250 and 350°C.

Figure 7.18A and Figure 7.18B show the results of the TGA analysis for native βCD coated ZnO NPs and βCD-NTA coated ZnO NPs respectively. From the results, the TGA analysis of the ZnO NPs exposed to βCD revealed the presence of βCD bound to the surface. This can be observed by the content percentage weight loss of ~5.5 wt% at ~340 °C (slightly broadened signal as shown in Figure 7.18A). This result indicates the possibility of native βCD binds to the ZnO surface. From the TGA analysis of βCD-NTA bound ZnO NPs, content percentage weight loss of ~19.3 % was detected at 250-350 °C (Figure 7.18B).

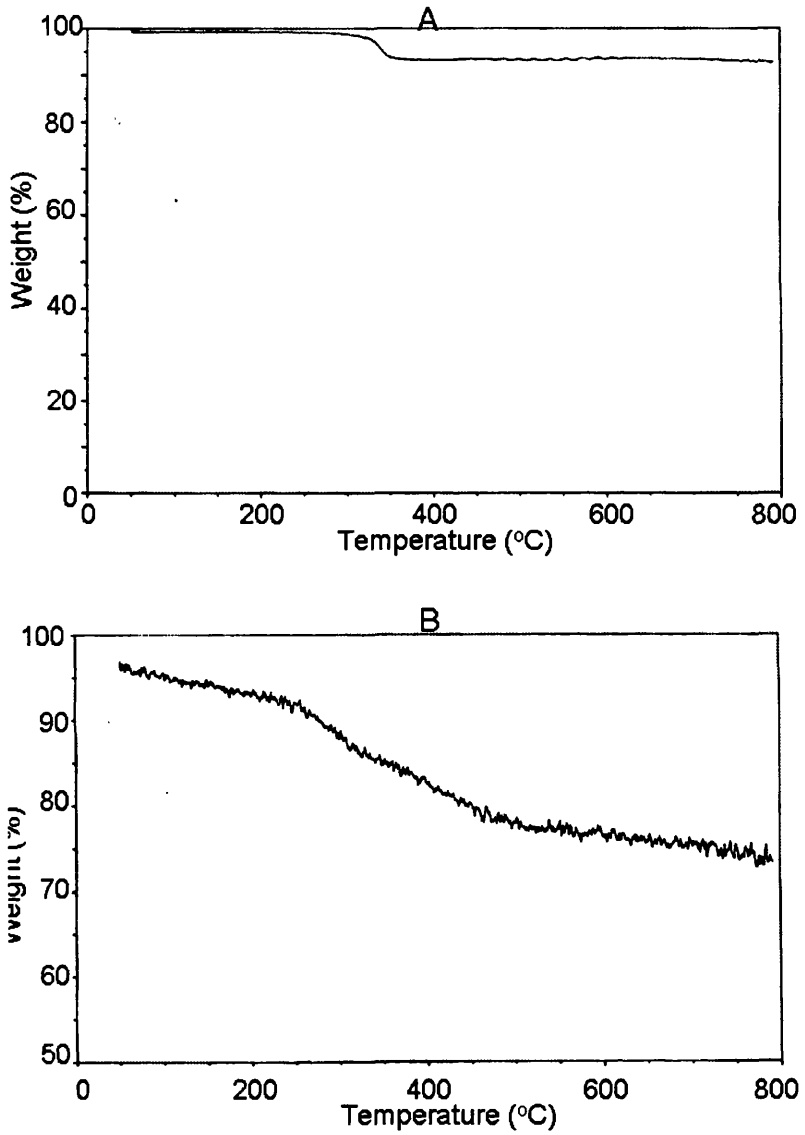

Figure 7.18 Thermogravimetric analysis (TGA) of ZnO NPs coated with (A) native βCD and (B) βCD-NTA. (A) The presence of native βCD was observed with the content percentage weight loss of ~5.5 wt% at ~340°C. (B) The presence of βCD-NTA was observed with the content percentage weight loss of 19.3% between ~250-350°C.

By comparing the results obtained via TGA analysis, the introduction of the NTA-like moiety appears to have significantly improved the ability of the cyclodextrin to bind the surface of the ZnO NPs. Therefore, it is envisioned that βCD-NTA could be used to coat ZnO nanowires in preliminary sensing devices to enable the determination of a change in electrical response upon the 'receptor' binding a guest molecule. Similar antibody-NTA mimic can also be synthesised for bio-sensing purposes.

7.3.5. Conclusion: Strategy I-IV

This section present a brief summary of the results and the conclusion obtained from the four different ZnO surface functionalisation strategies. It was found that histidine tags (His_6) and zinc fingers do not bind to ZnO NPs surface. The lack of binding for histidine tag and zinc fingers is possibly due to their restricted binding sites served to highlight the need for a customised linker to bind biomolecules to the ZnO surface. Nonetheless, ZnO NPs was found to have promising affinity to NTA pre-immobilised on sensor chip (Sensor chip NTA). Also, TGA analysis performed on bio-receptor NTA mimics (βCD-NTA) coated ZnO NPs revealed that by incorporating NTA to the βCD compound, the ability of βCD to bind to the surface of ZnO NPs has significantly improved. The quest to find a suitable method to functionalise ZnO surface with bio-molecules has led us to the discovery of NTA functional group.

A closer look at the NTA structure (Figure 7.19) reveals that it is an aminotricarboxylic acid, consisting of three spacer arms with a carboxylic acid group (COOH) at each end. It is a strong chelating agent of similar type to EDTA. However, unlike EDTA, it has insufficient amount of coordinating groups to form the bonds necessary to chelate transition metals such as Fe, Mg and Zn in a single molecules. For complete metal chelation, more than a single NTA molecule is required to form metal complex since there are only three coordinating groups in one molecule. This may explain why βCD-NTA, although showed an improvement in the binding ability of the cyclodextrin to ZnO NPs surface, this binding ability was still lower than what was expected.

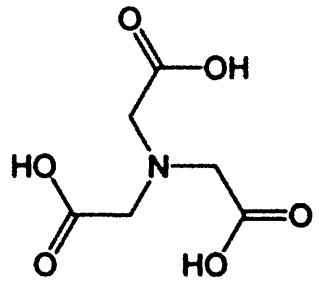

Figure 7.19 The structure of nitrilotriacetic acid (NTA), where it is made of three spacer arm with carboxylic acid groups.

It is known that the coordinating groups that are responsible for metal chelation in the NTA are the carboxylic groups. Theoretical calculations and infrared spectroscopy have shown the interactions of metal surfaces to negatively charged carboxylate groups, obtained by deprotonation of carboxylic acids [16, 17, 18]. Besides being a good metal chelator, carboxylic acids have also been known to react spontaneously with the surface hydroxyl groups of metal oxides surfaces, where bonds exhibiting good stability were formed [19]. Consequently, carboxylic acids and its derivatives are known as one of the best anchoring group for metal oxides [20] and are often used in metal oxide nanoparticles surface modifications [18]. Carboxylic acids and their derivatives were found to form stable bonds with metal oxide nanoparticles such as TiO_2, SnO_2 and ZrO_2, mainly through carboxylate bidentate bonds. Furthermore, previous work has revealed that carboxylic acid group is a suitable anchoring group for binding of Ru-poplypyridyl dyes, a type of photosensitizer to ZnO nanotips [21]. In addition, 2,2'-bipyridine-4,4'-dicarboxylate (dcbpy), was also successfully used as the bifunctional ligand to bridge the surface of ZnO thin film and lanthanide ions. This interaction was investigated using the FTIR spectroscopy, where observed spectral changes indicated that the dcbpy was bound to the ZnO surface through the bipyridine carboxylate groups [22,23].

On the basis of these revelations and the results from the binding of ZnO NPs to NTA, we proposed to use materials with an abundance of COOH groups as the intermediate between the ZnO surface and bio-molecules. Such material has to be biocompatible with the ease of functionalizing bio-molecules to its surface. One such promising candidate is polyamino acids. The following section presents an

alternative ZnO surface functionalisation strategy (Strategy V) by using polyamino acids as the intermediate between ZnO surface and biomolecules.

7.4. Polyamino acid as the intermediate linker (Strategy V)

Polyamino acids are polyamides that are made up of one type of amino acid linked by amide bonds. They are naturally occurring bio-homopolymers that are water-soluble, biodegradable, edible and non-toxic towards human and environment. Their potential applications include drug carriers for sustained release materials, biological adhesive, homeostatic or medical bonding kit, vaccines, thermoplastic, etc. Previous studies, where various types of polyamino acid chains have been immobilised onto different type of substrates have proven that these polyamino acid chains are also effective metal chelators [24, 25, 26, 27]. To meet the criteria of abundance COOH groups, two different polyamino acids were proposed, namely the polyaspartic acid (PSAP) and polyglutamic acid (PGA). The structure of each respective polymer is shown in Figure 7.20.

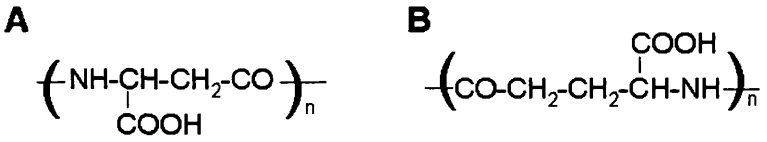

Figure 7.20 The molecular structure of (A) polyaspartic acid and (B) polyglutamic acid.

These two polyamino acids have very similar structure and despite the additional methyl group in the carboxylate side chain of PGA, both exhibit similar metal binding characteristics [28]. Studies using NMR and polarography showed that the carboxylate side chains are the main metal binding functionality for these polymers. As mentioned in Section 7.3 and 7.4, the difficulty in binding to ZnO surface is due to the restricted 'binding pockets' of the naturally occurring metal binding proteins; the hexahistidine tag (His_6) and the zinc finger protein. The PGA and PSAP, however, are proposed to not have any pre-determined binding 'cavity', unlike other metal-binding proteins or traditional metal chelators (EDTA or crown ethers). They are able to adopt to different tertiary structure which best suits the target metal surface [28]. In addition, PGA has also been successfully used to coat

superparamagnetic iron oxide nanoparticles for magnetic resonance imaging (MRI) [29]. Therefore, it is believed that these polyamino acids will also bind to ZnO surfaces. With the abundance of carboxylic acid groups on the polymer, there will be a large number of unused carboxylic acid groups when the polymers coordinate to metal or a metal oxide surface. These unused COOH groups will be very useful for further protein attachment through amide bonds using carbodiimide chemistry.

Various groups have coated different types of nanoparticles with polymers, whether to improve the nanoparticles' biocompatibility or for surface modifications purposes. The most common method used by these groups to report the success of their polymer coating was by measuring the change in diameter of the nanoparticles before and after polymer coating by using the AFM. Although this thickness measuring method is practical, there is the possibility that the change in thickness was due to contaminations. In this part of the work, a more effective method to prove the success of the binding of polyamino acids to the ZnO surfaces is presented. The polyamino acid of interest will be conjugated with fluorescence tags and the binding to the ZnO surfaces will be observed through the confocal and the fluorescence microscopy techniques.

7.4.1. Polyaspartic acid (PSAP)

7.4.1.1. Sample preparation

Maleic anhydride and ammonia were both purchased from Sigma Aldrich. 30% ammonia was prepared as stock solution.

7.4.1.2. General procedure for the synthesis of polyaspartic acid (PSAP)

The synthesis of PSAP follows a simple general procedure, as shown in Figure 7.21 [30]. A suspension made up of 14.7 g maleic anhydride (0.15 mol) and 10 ml water was formed in a 500 ml beaker. Then, 7.1 ml of ammonia (30%) was then added into the suspension. The clear mixture solution was irradiated via microwaves for 3.5 minutes, at a frequency of 2450 MHz and at 1000 W output power. The beaker was taken out after a few minutes and a golden brown solid was observed. NaOH solution was added in the beaker and the pH was adjusted to 9.5, so that the resultant polysuccinimide (PSI) was hydrolysed to PSAP. This solution was then left

overnight (12 hours) under constant stirring for complete hydrolysis process. The pH of the resultant brownish gold solution was then adjusted to 3.86 using HCl (6 M). The solution was filtrated and the filtrate was added dropwise into cooled ethanol solution (100 ml). The resulting precipitates were collected by vacuum filtration using a sintered funnel and washed successively with ethanol (100 ml). The resulting product was then dried at 70 °C and complete removal of excess solvent was monitored by repetitive cool weight method (i.e. dry product in oven, allow the product to cool, then measure the weight of the product). The final product was analysed by gel permeation chromatography (GPC) and Mass Spectrometry (MALDI).

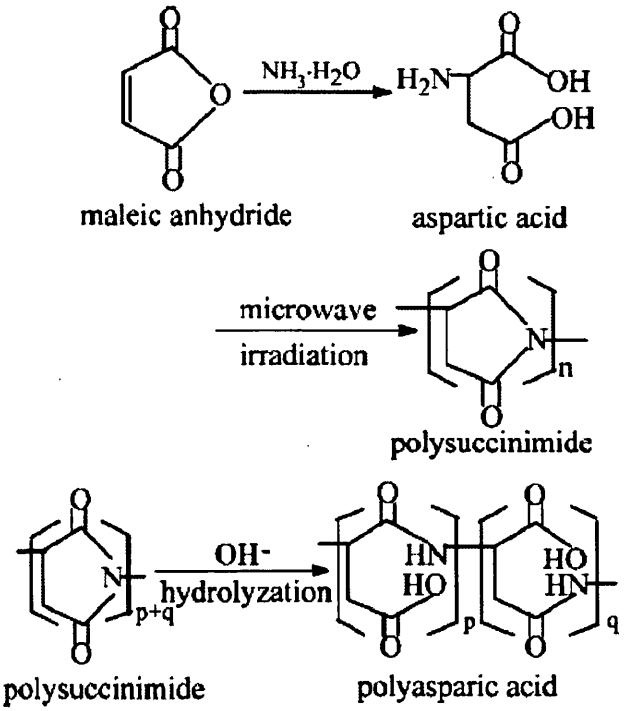

Figure 7.21 Synthesis route of polyaspartic acid [30].

GPC was performed using the Viscotek 'Evolution', with associated pump and autosampler. The column used was PL Aquagel guard plus 1 x P2* and 1 x P3*, 30 cm, 8 μm. The experiment was performed at 1.0 ml/min flow fate and 30 °C temperature. A single solution of the sample was prepared by adding 10 ml of eluent (0.2 M $NaNO_3$, 0.01 M NaH_2PO_4, pH 7) to 20 mg of synthesised sample and left overnight to dissolve. The sample solution was well mixed before part was transferred to an autosampler vial, without filtration, prior to chromatography.

7.4.1.3. Results and discussion

The microwave assisted synthesised polyaspartic acid was yellowish in colour. For the GPC analysis, the sample appeared to be readily soluble and there were no significant difficulties with the chromatography. The GPC system used for the work was calibrated with poly(ethylene glycol)/poly(ethylene oxide) and the results are therefore expressed as 'PEG/PEO equivalent' molecular weights. The results are summarised as the calculated molecular weight averages and polydispersity (Mw/Mn), as shown in Table 7.2.

Sample	Run Number	Mw	Mn	Mw/Mn
Polyaspartic acid	6*	2,560	1,810	1.4
	9*	2,570	1,820	1.4
	10	2,630	1,880	1.4

* Runs used in overlay plot.

Table 7.2 Calculated molecular weight averages and polydispersity (Mw/Mn).

Figure 7.22 shows an overlay of the computed molecular weight distributions for two runs of the sample solution. These plots are normalised with respect to area, the y-axis being a function of weight fraction. The sample is of apparently low molecular weight but with one main, higher, molecular weight component and a couple of, lesser, low molecular weight components. Electrospray mass spectrometry analysis was performed on the ZQ4000 (Waters, UK) in positive and negative ionisation mode. There was no evidence of the polymer at all. This may be due to the presence of metal impurities in the sample. As the synthesis and the characterisation of polymer can be complicated and time consuming, further synthesis work will be carried out in the future and will not be discussed in this work.

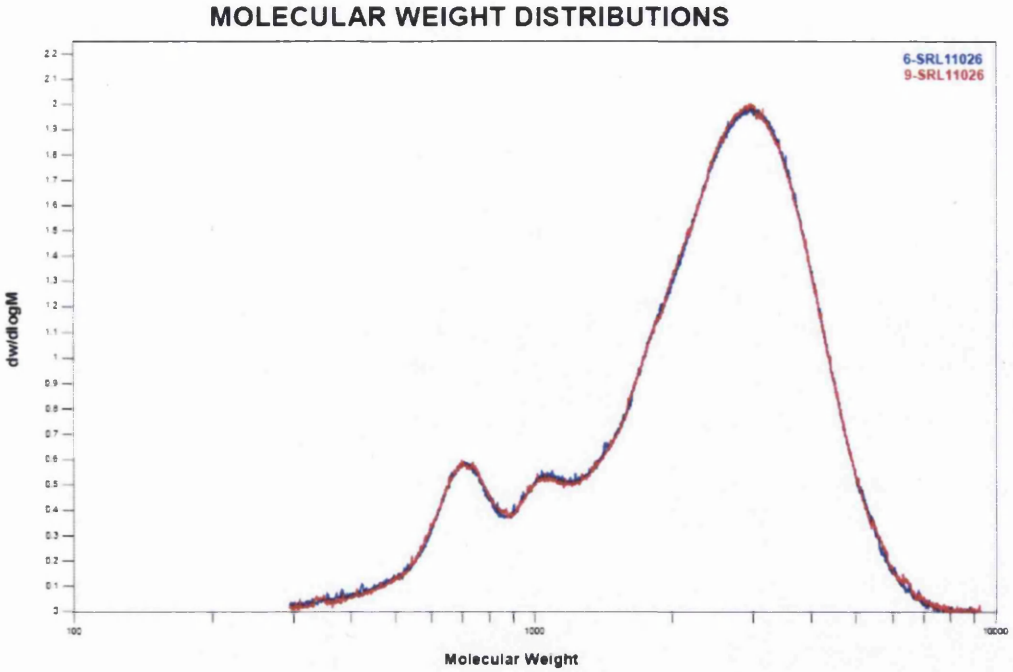

Figure 7.22 Overlay of the computed molecular weight distributions for run number 6 and 9 of the sample solution.

7.4.2. Polyglutamic acid (PGA)

As mentioned in Section 7.4, PGA has abundance of COOH groups, readily available for amine moieties conjugation through carbodiimide chemistry. Therefore, in order to view and evaluate binding of PGA to ZnO surfaces, the PGA was conjugated with carboxylic acid reactive fluorescent dyes. The structure of the chosen fluorescent dye, fluorescently glycine amide (A1363, Invitrogen) is shown in Figure 7.23. The free amine group available can be conjugated to the carboxylic groups of proteins and water soluble biopolymers using water-soluble carbodiimide chemistry.

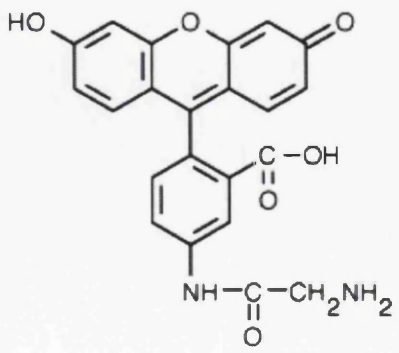

Figure 7.23 The structure of 5-(aminoacetamido)fluoresceinfluoresceinyl glycine amide.

The carbodiimide coupling process involves a two-step reaction sequence of condensation between carboxyl groups of the polymer and the amine group of the fluorescence. Firstly, the carboxyl group is activated by the carbodiimide to an amine-reactive o-acylisourea intermediate. The unstable o-acylisourea intermediate is converted to stable amine-reactive sulfo-NHS esters with the addition of NHSS. Then, the reaction of an amine-reactive ester with an amino group leads to the formation of the amide linkage between the two compounds.

7.4.2.1. Sample preparation

Poly-D-glutamic acid (sodium salt) (PGA) was purchased from Sigma and had a molecular weight range of 15-50 kDa. 5-(aminoacetamido)fluorescein (fluoresceinyl glycine amide) was purchased from Invitrogen. Water soluble carbodiimide, 1-ethyl-3-(3-dimethylaminopropyl)carbodiimide hydrochloride (EDC) and N-hydroxysulfosuccinimide (NHS) were also purchased from Invitrogen. A Visking dialysis membrane, made from natural cellulose, was purchased from Medicell International Ltd. The molecular cut off weight (MWCO) of the dialysis membrane was 12-14 kDa, with a flat diameter size of 14.3 mm. All reagents were used as received.

7.4.2.2. General procedure for the conjugation of fluorescence to polyglutamic acid (PGA)

Using the average molecular weight of 30 kDa for PGA, one molecule of the polymer will contain 200 repeat units. In other words, there should be approximately 200 free carboxylic acid group for surface binding and modification. The activation of the carboxyl acid group was carried out in a molar ratio [PGA: NHS: EDC] = 1:100:300. A solution of PGA (1.7 mg) was prepared with 5 ml DI water and the pH was adjusted to pH 5 using 1 M of HCl. Solutions of EDC (2.13 mg) and NHSS (0.6 mg) were prepared separately in a eppendorf tube with 500 µl DI water respectively. The EDC/NHS solutions were used immediately and added into the as prepared PGA solution. After 30 minutes of activation time, fluoresceinyl glycine amine (1.5 mg) dissolved in 1 ml Di water, was added into the mixture solution and the pH was adjusted to pH 8-9. The reaction was allowed to proceed in the dark and left stirring overnight, in a water ice bath. Un-reacted fluoresceinyl glycine amine, EDC, NHS

and any other by products were removed from the solution by dialysis, by using the cellulose Visking dialysis membrane (MWCO 12-14 kDa). The dialysis process was performed in the dark where the dialysis buffer was exchanged 4 times every 3-4 hours and left overnight. This was repeated twice to ensure complete removal of all unwanted substance. The final product (PGA-F) was collected in sample vials and stored in the dark at 4 ^{o}C until further use.

7.4.2.3. Binding assays for fluorescence detection

The resultant PGA-F were bound to different types of ZnO sample, namely ZnO belt-like structures in micron sizes, ZnO nanorods with ~300 nm in diameter and 2 μm in length, and ZnO nanoparticles with an average diameter of 100 nm. The ZnO microstructures were dispersed in DI water by ultrasonication bath for 3 minutes. 50 μl of the ZnO microstructures suspension was then deposited on a silicon substrate. Then, 30/50 nm chromium/gold (Cr/Au) layer was deposited on part of the Si substrate via a mask as shown in Figure 7.24. The mask was made up of tungsten wires (diameter: 0.17 mm) placed alternately on the Si substrate. The as-prepared sample was later submerged into PGA-F solution and left in the dark for 5 hours to allow interactions, followed by repetitive rinsing with DI water to remove all un-reacted compound.

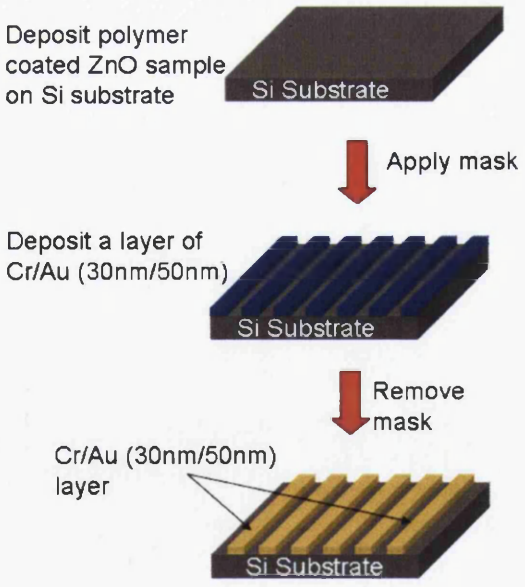

Figure 7.24 Sample preparation procedure for PGA-F coated ZnO microstructures. ZnO microstructure was first deposited on a Si substrate. A mask was then applied followed by the deposition of Cr/Au (30/50 nm) layer. The resultant sample is an alternate of Cr/Au layer with exposed ZnO microstructure on the Si substrate.

The success of the binding was investigated using confocal microscopy technique. The surface of the silicon substrate and the evaporated gold layer were used as a control surface to check the specific binding of the PGA-F to ZnO surface. In addition, a similar as-prepared sample (without interaction with PGA-F) was also used as a control sample.

For the ZnO nanorods and nanoparticles, they were respectively dispersed in DI water by ultra sonication bath for 3 minutes to give ZnO suspension (300 µl) in a 1.5 ml eppendorf tube. 200 µl of the synthesised PGA-F was mixed with the ZnO suspension. The mixture was left for 5 hours, in the dark, under rotation to allow binding. Excess PGA-Fs were removed by repeated washing by centrifugation (10 mins 5000 rpm Biofuge Fresco), removed 300 µl supernatant, redispersed with 300 µl DI water and repeat (5 times). 50 µl of the final product was deposited on silicon substrates for fluorescence detection analysis using the confocal microscope.

7.4.2.4. Results and discussion

(i) Fluorescence detection analysis: ZnO belt-like microstructures

The binding assay of PGA-F to the ZnO belt-like microstructures is as described in Section 7.4.2.3. The results of the confocal microscopy are presented in Figure 7.25. The faint line in (A) and (B) is the border between the evaporated gold layer and the exposed Si substrate surface. The region to the right of the 'border line' in (A) and to the bottom in (B) is the evaporated gold surface (Figure 7.25). As shown from these results, considerable binding of PGA-F on the surface of the ZnO microstructures were observed. A closer look at the images showed that the binding of PGA-F to ZnO microstructures was specific (i.e. no binding was seen on the Si or gold surface alone). The control sample (as-prepared sample in Figure 7.24 without interaction with PGA-F) viewed under the confocal microscope exhibited blue fluorescent signals (result not shown).

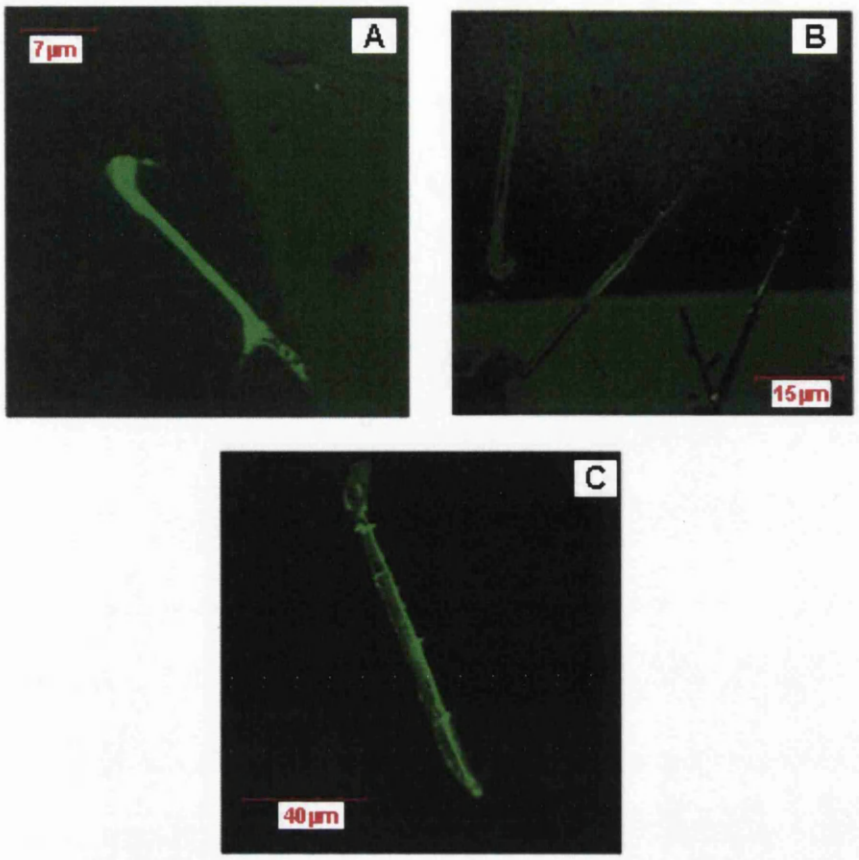

Figure 7.25 Confocal microscopy images of the PGA-F functionalised ZnO microstructures. (A) ZnO microstructure coated with PGA-F. The region to the right of the faint line is the evaporated gold suface and to the left is the Si substrate surface. (B) ZnO microstructures coated with PGA-F. The region to the bottom of the faint line is the evaporated gold surface and to the top is the Si substrate surface. (C) A ZnO microstructure coated with PGA-F. From these results, it was observed that the PGA-F only binds to the surface of the ZnO microstructures.

Due to the limited magnification of the microscope, tapping mode AFM (Veeco Dimension 3100) was used to visualise the surface of the functionalised microstructure surface. The TM-AFM data images of the microstructure of Figure 7.25A are shown in Figure 7.26. Upon PGA-F binding, the ZnO surface is observed to be uneven, which was to be expected (Figure 7.26D).

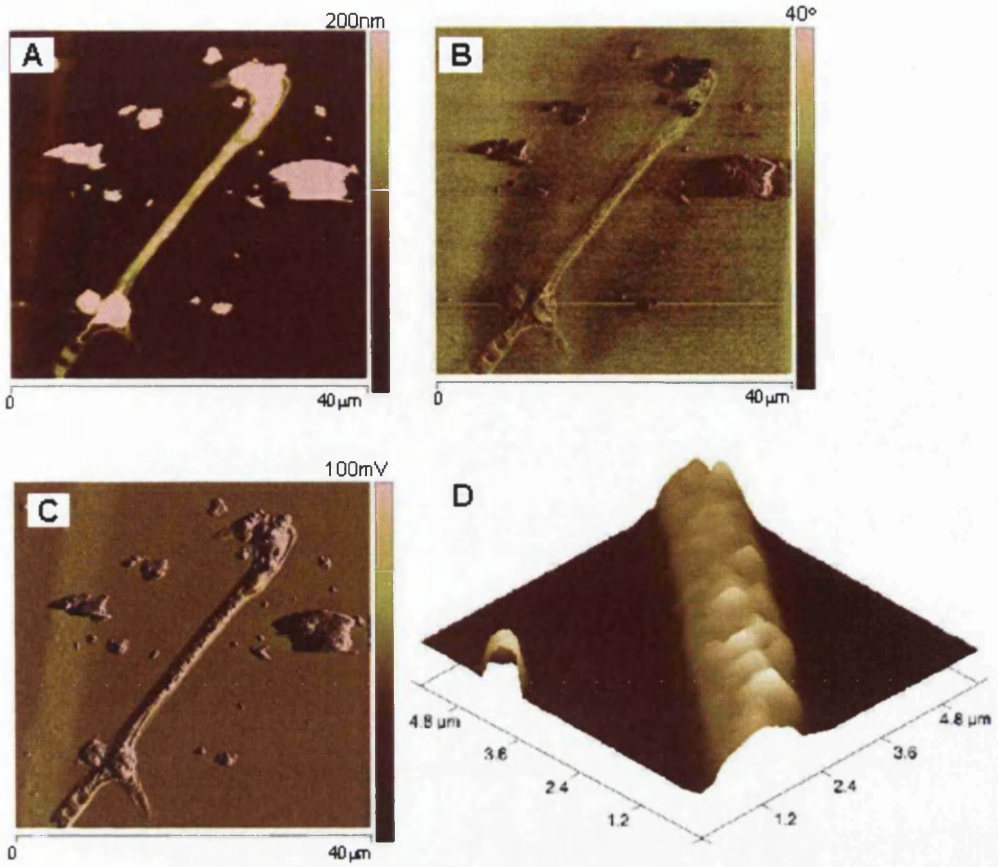

Figure 7.26 AFM images of ZnO microstructure functionalised with PGA-F. (A)-(C) The height, phase and amplitude images. (D) Higher magnification image of the functionalised ZnO surface.

(ii) Fluorescence detection analysis: ZnO nanoparticles

The binding assay of PGA-F to the ZnO nanoparticles (ZnO NPs) is as described in Section 7.4.2.3. The edge of the resultant sample droplet was imaged via the confocal microscope and the result is shown in Figure 7.27A. From this image, bare silicon (outside the droplet) did not show any fluorescence signals, and therefore, the fluorescence signals detected were entirely due to the functionalised ZnO NPs. Images of the PGA-F functionalised ZnO NPs , taken at higher magnification (40X) are shown in Figure 7.27B and Figure 7.27C. The functionalised ZnO NPs appear to be aggregated, forming circular particles with diameter of 6-12 µm. As control, bare ZnO NPs did not exhibit any fluorescence signal when viewed under the microscope.

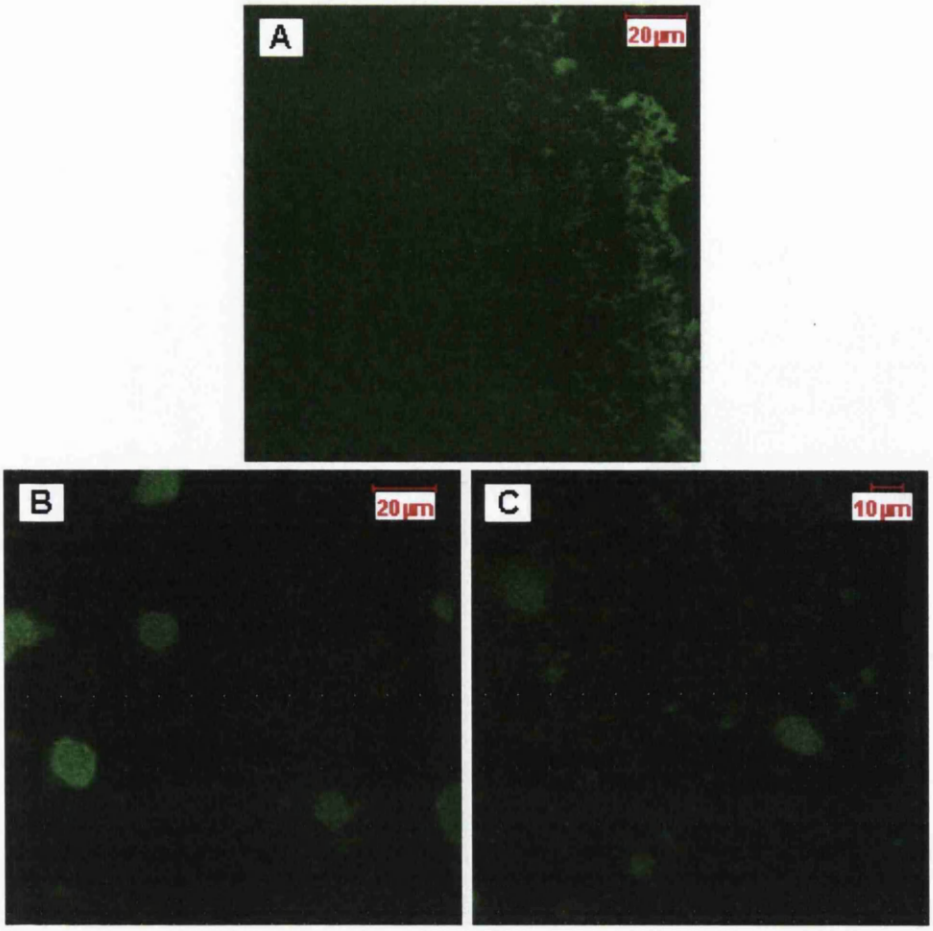

Figure 7.27 Fluorescence images of the binding PGA-F to ZnO nanoparticles (ZnO NPs) obtained via confocal microscope. (A) Image capture of the edges of the sample droplet. (B)-(C) Fluorescence images of the functionalised ZnO NPs at high magnification ((40X magnification).

(iii) Fluorescence detection analysis: ZnO nanorod

The binding assay of PGA-F to the ZnO nanorod is as described in Section 7.4.2.3. The edge of the resultant sample droplet was imaged via the confocal microscope and the result is shown in Figure 7.28A Similar to the results observed for the ZnO NPs, no fluorescence signal was detected outside the sample droplet (bare Si surface). Images of the PGA-F functionalised ZnO nanorod, taken at higher magnification (40X) is shown in Figure 7.28B. Due to the microscope limitation, the functionalised ZnO nanorods were barely distinguishable. However, from the known size (~2 µm in length) and shape of the nanorod, the red circled fluorescence structure is believed to be a functionalised ZnO nanorod. The blue circled structures are believed to be aggregates of these nanorods (Figure 7.28B).

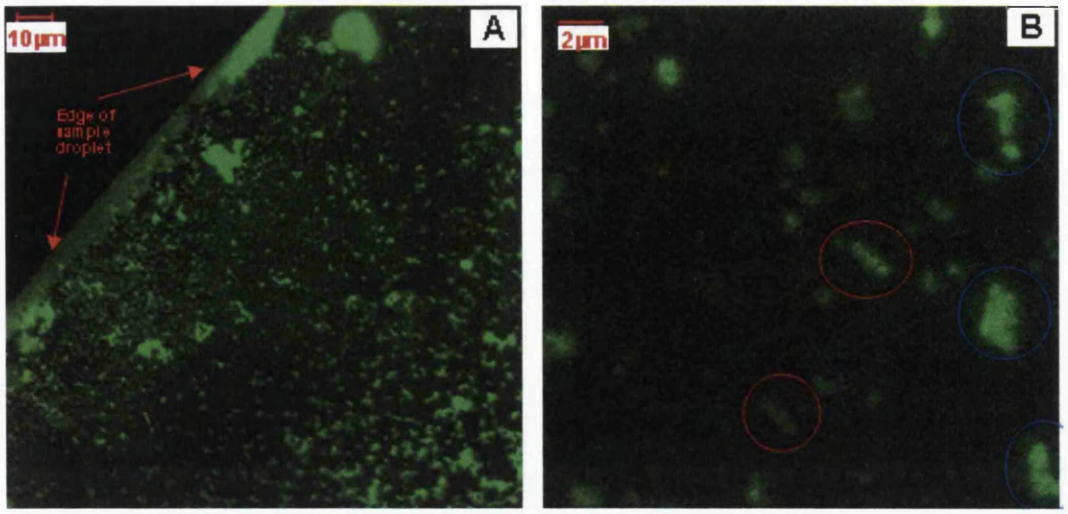

Figure 7.28 Fluorescence images of PGA-F functionalised ZnO nanorod obtained via confocal microscope. (A) Image shows the edge of the sample droplet. (B) Image of the functionalised ZnO nanorod sample taken at higher magnification (40X).

Figure 7.29(A)-(C) shows the TM-AFM scan of an area near the edge of the sample droplet. The structures (red circled, Figure 7.29) are believed to be functionalised ZnO nanorod. Higher magnification TM-AFM scans on one of these structures are presented in Figure 7.29(D)-(I). By comparing the dimension and the geometry of the functionalised ZnO nanorod with the un-functionalised ZnO nanorod (Figure 7.29(J)-(L)), we are convinced that the nanostructure in Figure 7.29(D)-(I) are PGA-F functionalised ZnO nanorods. The smaller fragments surrounding the PGA-F functionalised ZnO nanorod (Figure 7.29D and G) may be residues of unbound PGA-F.

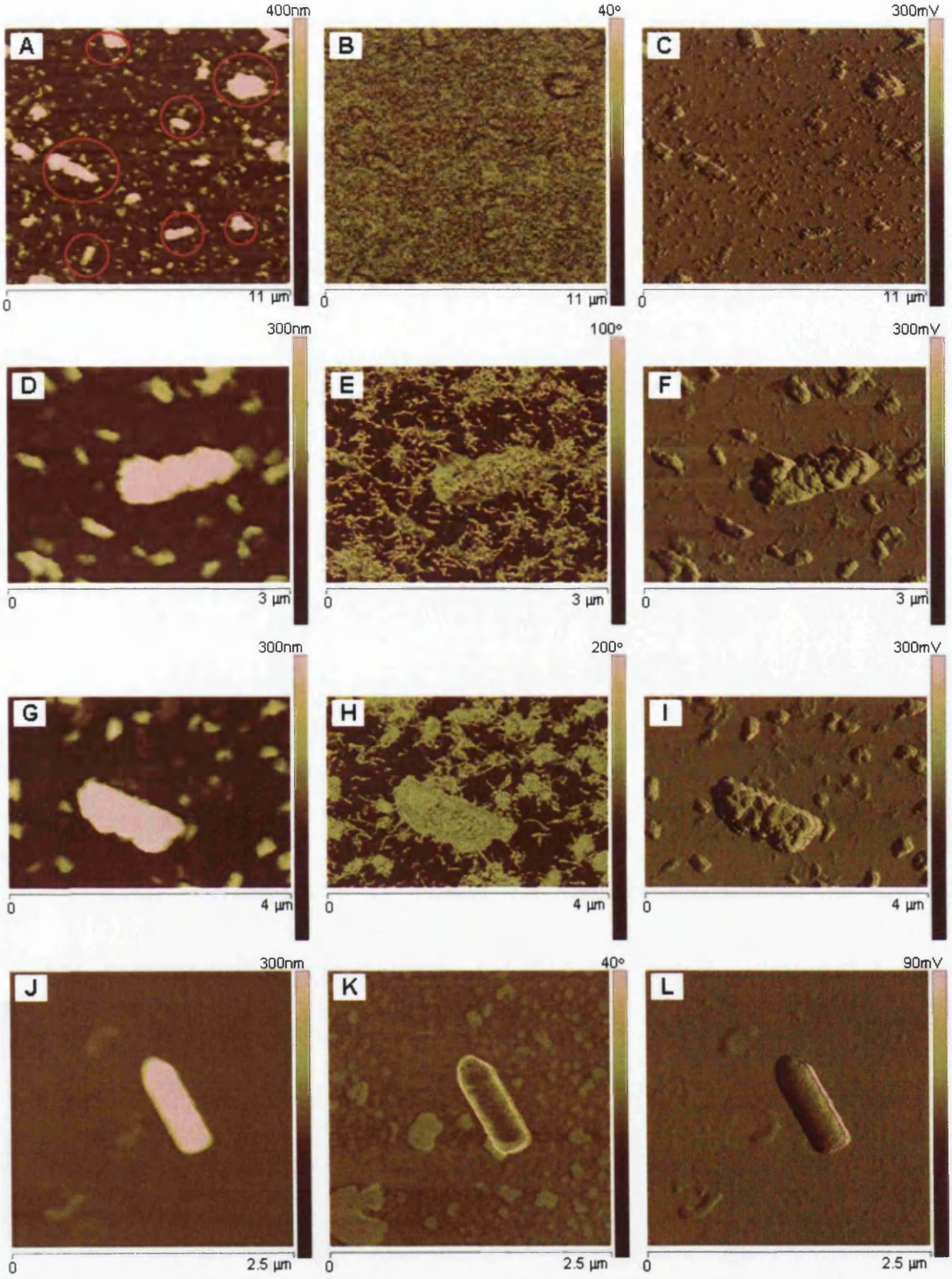

Figure 7.29 TM-AFM images of the PGA-F functionalised ZnO nanorod. (A)-(C) The respective height, phase and amplitude data image taken at the edge of the sample droplet. (D)-(F) and (G)-(I) The respective height, phase and amplitude data images of two different functionalised ZnO nanorod of (circled in A). (J)-(L) The respective height, phase and amplitude data image of a ZnO nanorod without PGA-F functionalisation.

Based on the results for the binding of PGA-F to the ZnO microstructure, the ZnO NPs and ZnO nanorod, it can be concluded that PGA can be effectively attached to ZnO surface. Due to the nature of how the fluorescent tags (fluorecein glycine amide) were covalently bound to the PGA, it is believed that the amine group on proteins or antibodies may be conjugated to the PGA surface following the same route. This proof of concept will be discussed in the Section 7.5. Due to the microscope magnification limits, the belt-like microstructures will be used as the ZnO surface platform in the following experiments.

7.5. Surface functionalisation of ZnO surface with antibodies

The feasibility of using polyglutamic acid (PGA) as the intermediate linker between ZnO and antibodies is examined in this section.

7.5.1. Sample preparation

100 ml of 10 mM phosphate buffer saline (0.8 g NaCl, 0.02 g KCl, 1.44g $NaHPO_4$) and 100 ml of 50 mM MES buffer were prepared and autoclaved. Water soluble carbodiimide, 1-ethyl-3-(3-dimethylaminopropyl) carbodiimide hydrochloride (EDC) and N-hydroxysulfosuccinimide (NHS) were purchased from Invitrogen. Stock solutions of EDC (30 mg in 1 ml of DI water) and NHS (5.75 mg in 1 ml of DI water) were prepared and ready for use.

7.5.2. Control studies

To ensure that the experimental results obtained were reliable, control experiments were carried out concurrently to ZnO surface functionalisation experiment. The control samples are (1) bare ZnO microstructures, (2) PGA coated ZnO microstructures and (3) PGA coated ZnO microstructures mixed with secondary antibody. Control sample (3) was prepared without addition of carbodiimide to the PGA coated ZnO microstructures prior to the addition of secondary antibodies. In other words without carbodiimide, the COOH groups on the surface of the PGA polymer will not be activated and amide linkage will not be formed between the polymer and the antibody. The following describes the sample preparation process followed by the observed results.

7.5.2.1. Binding assay

PGA solution was prepared by mixing 1 mg of PGA in 500 µl of DI water. ZnO microstructures suspension was prepared with ~10 mg of ZnO in 600 µl DI water in a 1.5 ml eppendorf tube. The ZnO microstructures were dispersed by ultrasonication bath for 3 minutes. For the bare ZnO microstructures, 10 µl of the as-prepared ZnO suspension was deposited on a glass slides and covered with a cover slip. As for the PGA coated ZnO microstructures, 300 µl of the as-prepared ZnO suspension is mixed with the PGA solution and allowed to interact. The resultant PGA-ZnO mixture was left for 5 hours under mixing by rotation (11 rpm, Stuart Rotator SB3), followed by repeated wash to remove excess PGA. The washing step was performed by centrifugation (10 mins 5000 rpm Biofuge Fresco), removed 600 µl supernatant, redispersed with 600 µl DI water and repeat (5 times). 10 µl of the final product was deposited on a glass slides and covered with a cover slip. 200 µl of the as-prepared PGA coated ZnO suspension was mixed with 3 µl of donkey anti-goat FITC antibody (400 µg/ml) and left in the dark, under mixing by slow rotation for 6 hours. Excess donkey anti-goat FITC was removed with repeated centrifugation wash cycles. All three control samples were examined using the fluorescence microscope.

7.5.2.2. Results and discussion

The fluorescence images of the bare and the PGA coated ZnO microstructures are shown in Figure 7.30 and Figure 7.31 respectively. Both control samples were observed using fluorescence microscope by switching between three different filter cubes, namely DAPI, FITC and TRITC. As suggested by the name of the filter cubes, DAPI, FITC and TRITC are responsible for the detection of fluorophores in the blue, green and red part of the visible spectrum respectively. From the results, both the bare and the PGA coated ZnO microstructures exhibited specific blue fluorescence signals when viewed under the DAPI cube filter of the fluorescence microscope, while no signal were detected under the FITC and TRITC cube filters (Figure 7.30 and Figure 7.31). It can be concluded that bare and PGA coated ZnO microstructures exhibited blue auto fluorescence (natural fluorescence) in the absence of fluorescence probes.

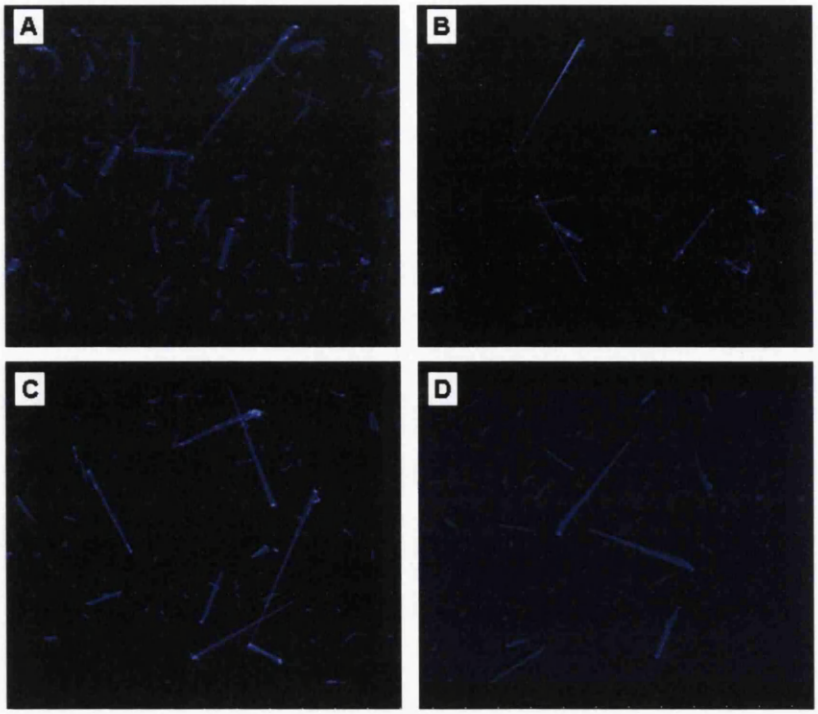

Figure 7.30 Fluorescence images of bare ZnO belt-like microstructures obtained with fluorescence microscope. The ZnO microstructures exhibited specific blue fluorescence when viewed via the DAPI cube filter of the microscope.

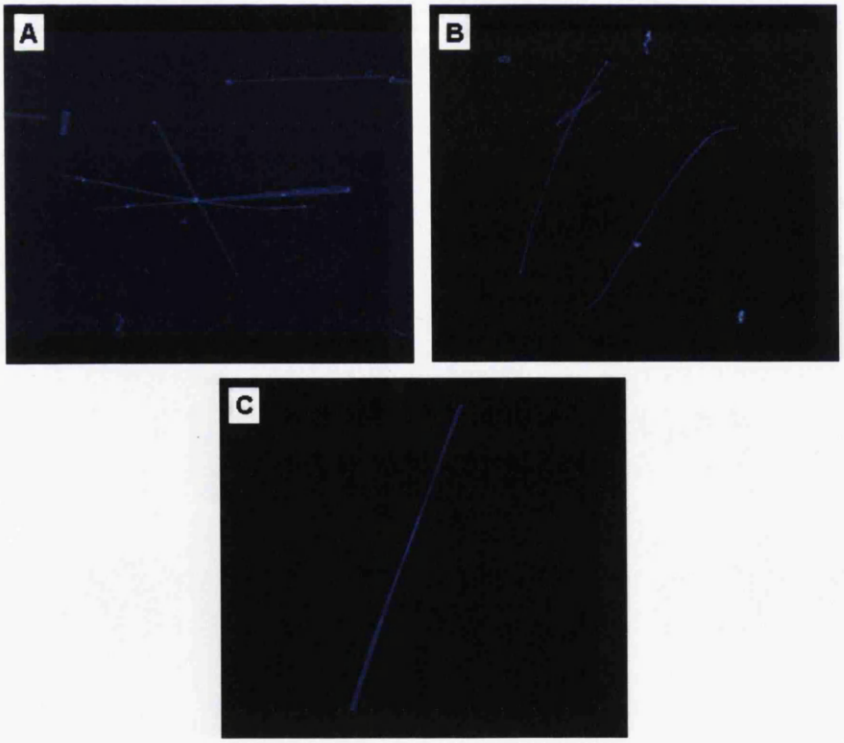

Figure 7.31 Fluorescence images of PGA coated ZnO belt-like microstructures obtained with fluorescence microscope. Similar to the bare ZnO microstructures, PGA coated sample also exhibited specific blue fluorescence when viewed via the DAPI cube filter of the microscope.

Figure 7.32 shows the fluorescence images of PGA coated ZnO microstructures which were allowed to interact with secondary antibody without carbodiimide activation.

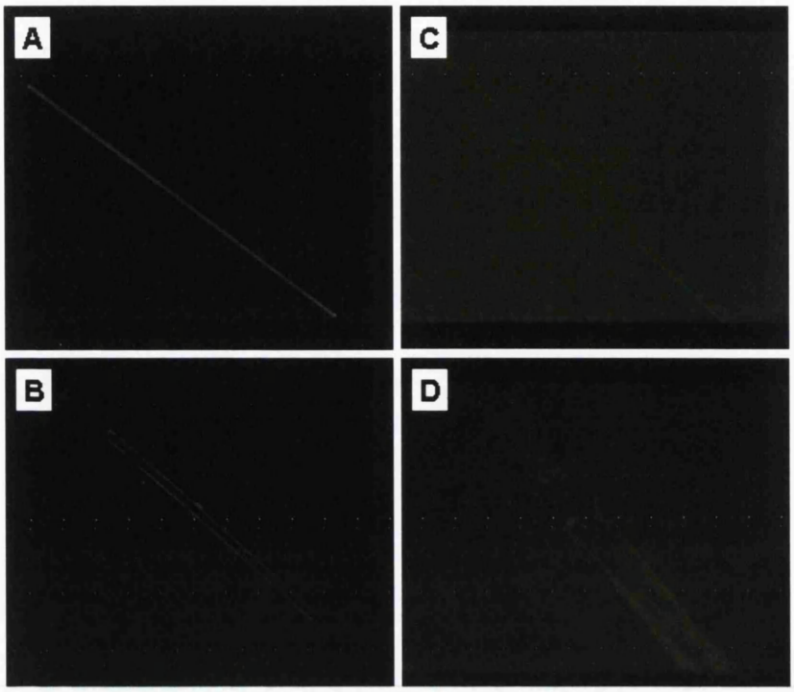

Figure 7.32 Fluorescence microscope images of PGA coated ZnO microstructures mixed with secondary antibody (without carbodiimide activation). In this experiment, the COOH groups on the PGA were not activated prior to the addition of secondary antibodies.

The modified ZnO microstructures exhibit similar blue auto-fluorescence as before when viewed under the DAPI cube filter (not shown). However, when they were viewed under the FITC cube filter, green fluorescence signals were detected only at the edges of the modified microstructures (Figure 7.32A-B). This may be due to dried up antibodies moieties trapped at the edges of the microstructure.

7.5.3. Secondary antibody

In this section, secondary antibody is conjugated to PGA following similar method discussed in 7.4.2.2. Secondary antibody is an antibody that is labeled with fluorescence probes and binds to primary antibody. By using secondary antibody, the viability of functionalising ZnO surface with antibodies can be analysed via fluorescence microscope technique. The secondary antibody used was the donkey anti-goat fluorescein isothiocyanate (FITC) antibody (400 μg/ml), which was

purchased from Santa cruz biotechnology. All other chemicals and samples used in this part of the work are mentioned in Section 7.5.1.

7.5.3.1. General procedure for surface functionalisation of ZnO with secondary antibody

ZnO microstructures suspension was prepared by diluting the sample in 500 µl Di water, followed by ultrasonication bath for 3 minutes. The as prepared ZnO microparticles suspension was then mixed with 2.5 mg of PGA solution (250 µl in DI water). The resultant mixture was left for 5 hours at RT under mixing by rotation (11 rpm, Stuart Rotator SB3). Then, un-reacted PGA was removed by 3-4 repeated wash cycle with 10 mins of centrifugation (5000 rpm Biofuge Fresco), followed by the removal of 500 µl of supernatant and resuspension of the sample in 500 µl 50 mM MES buffer. The PGA coated ZnO microstructures (ZnO-PGA) were activated after 30 minutes at room temperature by adding 100 µl NHS (5.75 mg/ml), followed by 100 µl (30 mg/ml) of EDC. Then, activated ZnO-PGA were washed three times by centrifugation (10 mins, 5000 rpm), followed by removal of 500 µl supernatant and redispersed in 500 µl of 50 mM MES. These washing cycles will remove excess EDC, NHS and any other by-products. 3 µl of the donkey anti-goat FITC antibody (400 µg/ml) was then added and the conjugation was continued at room temperature in the dark, under mixing by slow rotation for 6 hours. The final product was washed 3 or 6 times to remove excess antibody and other by-products. 20 µl of sample was deposited on a glass slides (with cover slips) for fluorescence detection analysis. All reactions were performed in 1.5 ml centrifuge tube.

7.5.3.2. Results and discussion

The surface functionalisation of ZnO microstructures with secondary antibodies follows the general procedure as described in Section 7.5.3.1. In this analysis, excess secondary antibodies were removed with three repeated cycle of centrifugation wash (wash procedures is as described in Section 7.5.3.1. The samples were observed under the fluorescence microscope by switching between three different filter cubes, namely DAPI, FITC and TRITC. The fluorescence images of the functionalised ZnO microstructures are shown in Figure 7.33.

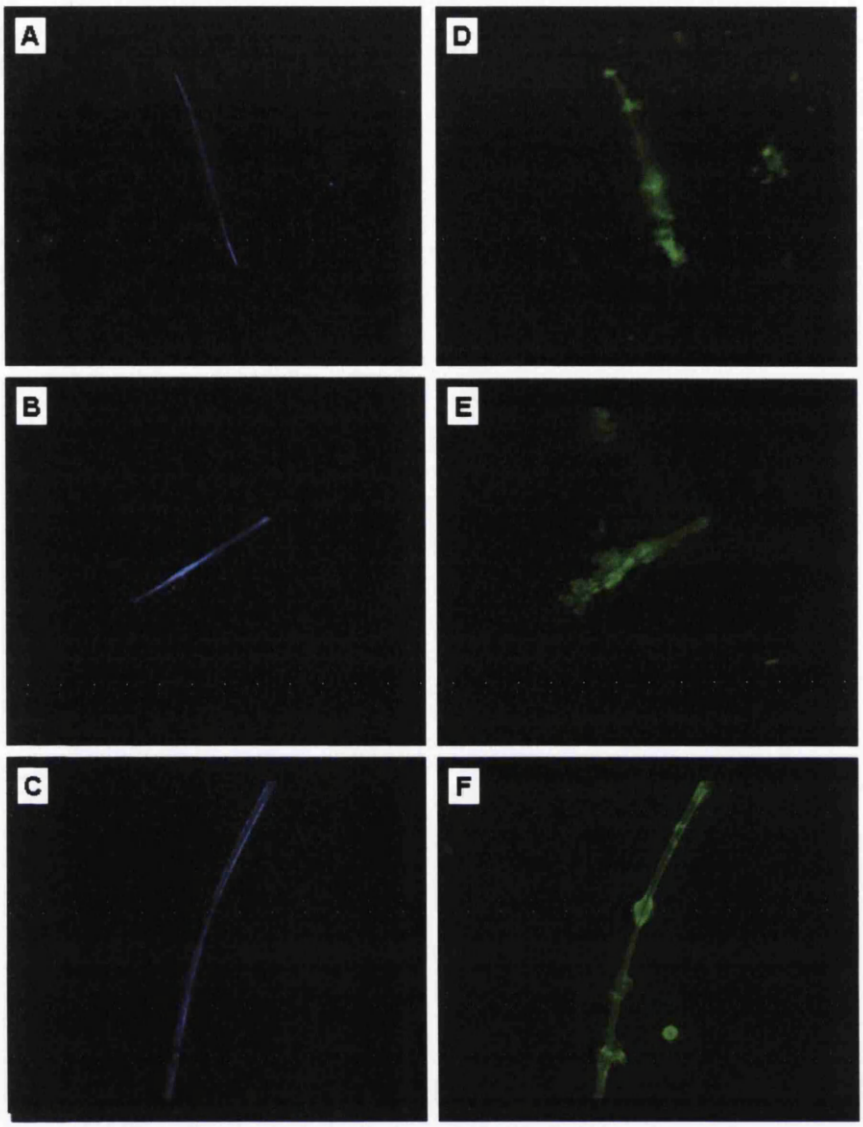

Figure 7.33 Fluorescence images of secondary antibody functionalised ZnO microstructures. (A)-(C) Samples viewed under the DAPI cube filter of the fluorescence microscope, showing the blue auto fluorescence of PGA coated ZnO structure. (D)-(F) Samples viewed under the FITC cube filter, showing specific secondary antibody-FITC signal.

The functionalised ZnO structures exhibit blue fluorescence when viewed under the DAPI cube filter (Figure 7.33A-C) and green fluorescence when viewed under the FITC cube filter (Figure 7.33D-F). As observed from the control experiments, bare and PGA coated ZnO microstructures autofluoresce in the blue part of the visible light spectrum respectively (Figure 7.30 and Figure 7.31, Section 7.5.2). Therefore, the detected specific blue fluorescence is believed to originate from the mentioned auto fluorescence. The functionalised samples appear to be saturated with secondary

antibodies, where 'green lumps' are observed on the surface of the ZnO microstructures (Figure 7.33D-F).

To ensure that these antibodies are not just co-adsorbed on the ZnO surface, the experiments were repeated with extra centrifugation wash cycles to remove excess antibodies. The wash cycle follows the procedures as mentioned in Section 7.5.3.1. Similar to previous experiment, the sample were observed under the fluorescence microscope by switching between three different filter cubes, namely DAPI, FITC and TRITC. The fluorescence images of the functionalised ZnO microstructures from the repeated experiment are shown in Figure 7.34.

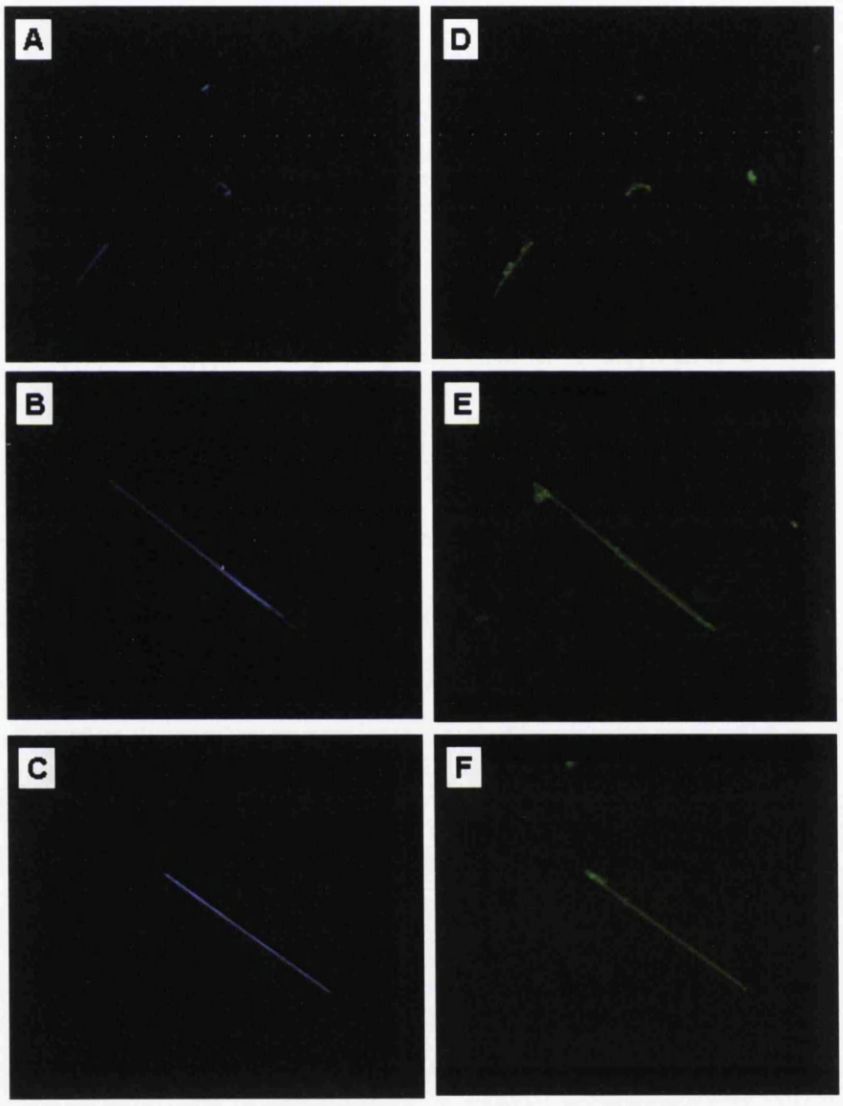

Figure 7.34 Fluorescence images of secondary antibody-FITC functionalised ZnO microstructures obtained using fluorescence microscope. (A)-(C) Samples viewed under the DAPI cube filter. The observed blue signal is believed to originate from the auto-fluorescence of PGA coated ZnO microstructures. (D)-(F) Samples viewed under the FITC filter, showing specific secondary antibody-FITC signal.

The functionalised ZnO microstructures fluoresced blue and green when viewed under the DAPI and FITC cube filters respectively (Figure 7.34). The surfaces of the functionalised ZnO microstructures are cleaner, in the absence of 'green lumps' as compared to the results in Figure 7.33D-F.

Figure 7.35 shows the fluorescence images of the antibody functionalised ZnO microstructures (of Figure 7.34) obtained at higher magnification (40X). The smoother functionalised surface suggests that additional ultracentrifugation washes had removed weakly adsorbed antibodies, leaving only the covalently bound antibodies intact.

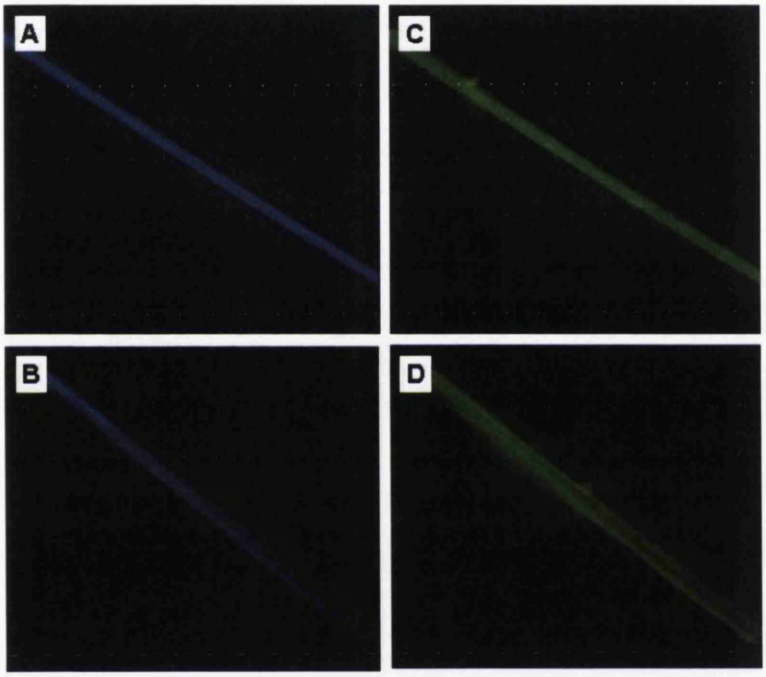

Figure 7.35 Fluorescence images of the secondary antibody-FITC ZnO microstructures taken at higher magnification (40X). Additional ultracentrifugation washes produced smoother and more uniform functionalised surface.

The difference in the magnified images of the surface of the carbodiimide mediated functionalised microstructure (Figure 7.35) and control sample (3) (Figure 7.32) is significant. While one exhibits evident fluorescence signal, the later negligible fluorescence signals. These highlights the fact that the secondary antibodies were functionalised on the PGA coated ZnO microstructures via carbodiimide (EDC and NHS) mediated chemistry. From these results, it can be concluded that the

functionalisation of the secondary antibody to the PGA coated ZnO microstructures was a success.

7.5.4. Primary antibody

With the success of functionalising ZnO microstructures surface with secondary antibodies, this part of the work focus on functionalising the ZnO surface with primary antibodies. Secondary antibody was used as a probe to detect the bound primary antibody on the ZnO surface. The primary antibody, antibody bovine serum albumin (Anti-BSA) (2 mg/ml) was purchased from Sigma Aldrich. It was developed in rabbit using purified BSA and its strong reactivity to BSA has been determined. The secondary antibody used was goat anti-rabbit Texas Red (TR) antibody (400 μg/ml) which was purchased from Santa cruz biotechnology. All other chemicals and samples used in this part of the work are mentioned in Section 7.5.1.

7.5.4.1. General procedure for surface functionalisation of ZnO with primary antibody

The surface functionalisation of ZnO with Anti-BSA follows the same general procedure in Section 7.7.2. 3 μl of goat anti-rabbit TR antibody were introduced into the resultant Anti-BSA functionalised ZnO microstructures solution, and allowed to interact at room temperature, in the dark and under mixing by slow rotation for 4 hours. The excess secondary antibodies were removed by 6 repeated wash cycle by centrifugation (10 mins, 5000 rpm) with 50 mM MES, removal of 500 μl supernatant and redispersed in 500 μl. 20 μl of the resultant sample was deposited on a glass slide and covered with a cover slips and ready for fluorescence microscope analysis.

7.5.4.2. Results and discussion

The secondary antibodies are antibodies that bind to primary antibodies of a given species, for this case, anti-rabbit. The secondary antibodies used in this work are labelled with Texas Red (TR), a common red fluorescent dye which fluoresces in the red of the visible light spectrum. The sample was observed under the fluorescence microscope by switching between three different filter cubes, namely DAPI, FITC and TRITC. By theory, the secondary antibodies (goat anti-rabbit IgG-TR) will bind to the primary antibodies (Anti-BSA) and then show the locations of the anti-BSA as

specific red shinning fluorescence spots when viewed under the TRITC filter cube using the fluorescence microscope (refer Chapter 5 for the description of fluorescence microscopy technique).

The modified ZnO microstructures displayed blue fluorescence when viewed under the DAPI cube filter (Figure 7.36), while no fluorescence signals were detected under both of the FITC and TRITC cube filters. Nonetheless, it should be emphasised that the obtained results do not mean that anti-BSA was not conjugated to the PGA coated ZnO microstructures.

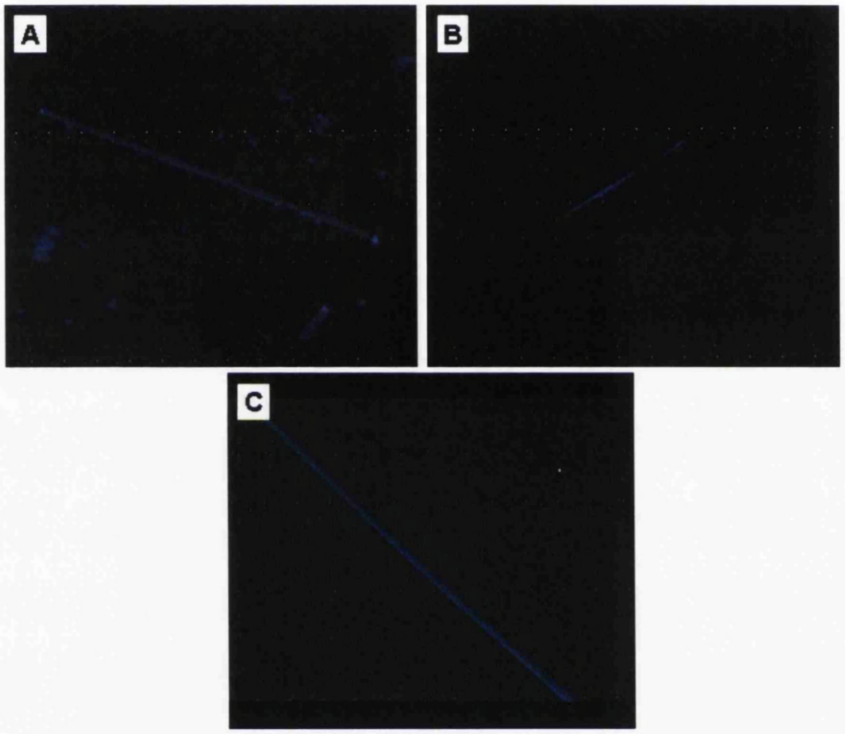

Figure 7.36 Fluorescence images of anti-BSA functionalised ZnO microstructures viewed under the DAPI cube filter. No signals were detected under the FITC and TRITC cube filters.

The results indicate that the secondary antibodies were not bound to the anti-BSA functionalised ZnO microstructures. This may be due to the orientation of the primary antibodies that may have obstructed the binding sites for the secondary antibodies. An explanation for this observation follows:

IgG antibody is composed of two subunits including two "heavy" chains and two "light" chains. These are assembled in a symmetrical structure and each IgG has two identical antigen recognition domains. The molecule itself is roughly shaped like a "Y" and the regions of the extreme tips of the "Y" are the antigen recognition domains. The stem of the "Y", the Fc region, is not involved in recognition of antigens and is fairly constant among the various classes of antibodies (refer Chapter 2 for detailed structure of an antibody). Two attributes of the Fc region are noted:

- The amines in the Fc region usually react more readily and therefore random modifications usually result in the binding to the Fc fragment of the antibody
- The Fc region can be used as an antigen that is recognizable by secondary antibodies of certain species. The binding mechanism of the primary and the secondary antibodies is illustrated in Figure 7.37.

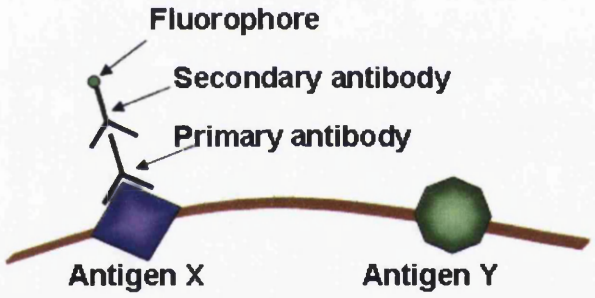

Figure 7.37 The primary antibody (in purple) binds to an antigen (in red). A labeled secondary antibody (in green), then binds to the primary antibody, through the Fc region.

Binding of the primary antibodies (Anti-BSA) to the PGA surface occurs at the Fc region. Consequently, the binding sites for the secondary antibodies (i.e. Fc region of the primary antibodies) may be blocked. Figure 7.38A illustrates how the primary antibody binding site may have been blocked after being conjugated to the PGA coated ZnO microstructures surface. An alternative method to visualise the anti-BSA functionalised ZnO microstructures is to use a secondary antibody which binds to BSA protein as depicted in Figure 7.38B. Due to time constraint, the proposed alternative will be performed in future works.

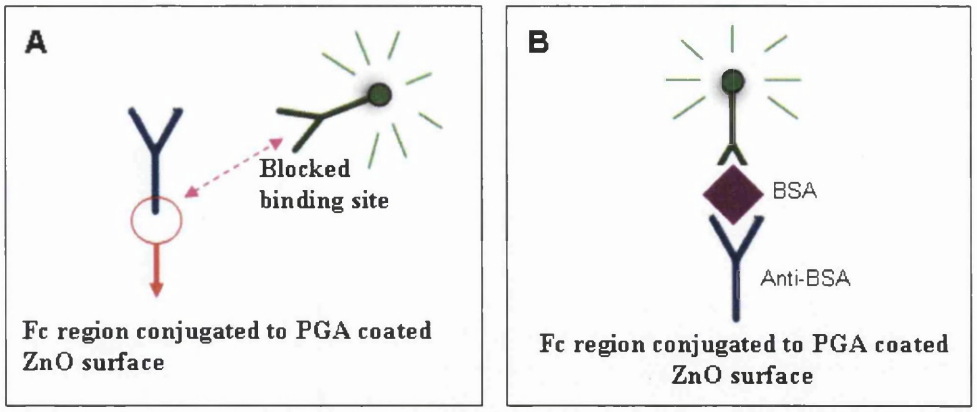

Figure 7.38 The likelihood of the Fc region of the primary antibody conjugated to the polymer may have blocked the binding site of the secondary antibody. (B) A proposed alternative of detection method using a secondary antibody which binds to BSA protein.

7.6. Summary

Ultra-sensitive and selective biosensors can be fabricated by combining nature's bio-recognition functionalities with the novel electronic properties of one dimensional nanostructures. The key to the successful implementation of such biosensors are inextricably related to the interface between the bio-molecules, which provide the specific recognition functionalities, and the surface of the nanostructure, which convert the biological signals into quantitative measurable signal. In this chapter, suitable ZnO surface functionalisation strategies were evaluated.

The Biacore system, a surface plasmon resonance based technique, was used to identify suitable functional group that has high affinity to the surface of ZnO nanoparticles (ZnO NPs). Preliminary studies involve preparing a suitable ZnO saturated sensor chip surface followed by the binding studies of various functional groups/moieties to the as-prepared ZnO surface. It was found that Sensor chip NTA served as a suitable platform to immobilise ZnO NPs due to its naturally high affinity to divalent metal ions. Subsequent experiments look at the binding interactions between the pre-immobilised ZnO NPs with the zinc fingers moieties of oestrogen receptor alpha (ER_{α}) protein and also with histidine tagged (His_6) hrs1 protein. Under the conducted experimental tests, both of these functional groups did not bind to the ZnO NPs surface. The observed lack of binding for zinc fingers and His_6 to the ZnO NPs surface may be due to their restricted binding sites. Nonetheless, the results from the Biacore system analysis showed that NTA moieties (on the Sensor chip

NTA) chelate ZnO NPs promisingly. Following these results, βCD-NTA, a bioreceptor mimic that incorporates an NTA-like linker moiety to β-cyclodextrin was synthesised and its binding interactions to ZnO NPs was analysed using thermogravimetric analysis (TGA). Results revealed that, although the βCD-NTA binding ability to ZnO NPs was lower than expected, the incorporated NTA-like moiety has significantly improved the ability of native β-cyclodextrin (βCD) to bind to the surface of the ZnO NPs. A closer look at the NTA structure has revealed that it is an aminotricarboxylic acid, consisting of three spacer arms with carboxylic acid group (COOH) at each end. It was known that more than a single NTA molecule was required for complete metal chelation, which explains why the βCD-NTA, although showed an improvement in the binding ability of the cyclodextrin to ZnO NPs surface, this binding ability was still lower than what was expected. Besides that, it was also known that the coordination groups responsible for metal chelation by the NTA are the COOH group at the end of each spacer arm. This discovery leads to finding an alternative material with an abundance of COOH groups as an intermediate between the ZnO surface and the bio-molecules. As such, polyglutamic acid (PGA), with its abundance of COOH groups on its surface in addition to its biocompatibility was chosen as the promising candidate. The PGA was first conjugated with fluoresceins (fluorescein glycine amide) using carbodiimide chemistry and the binding to ZnO surface was studied using confocal microscopy technique. The positive results lead to conjugating antibodies to the surface of the PGA via the same carbodiimide chemistry. In the first attempt to functionalised ZnO surface, FITC tagged secondary antibodies (green fluorescence) were conjugated to the surface of PGA coated ZnO microstructure surface via water-soluble carbodiimide (EDC and NHS) mediated chemistry. In this study, specific green fluorescence signal was detected suggesting the success of immobilising antibody to the surface of ZnO with PGA as the intermediate. It was noted that thorough washing of the samples are needed to ensure that loosely adsorbed antibodies were removed appropriately. The last part of the work attempted to functionalise ZnO surface with non-fluorescence primary antibodies (anti-BSA). TRITC tagged secondary antibodies (red fluorescence) were used as probes to detect anti-BSA that were immobilised on the surface of the ZnO microstructures. Results showed that these modified ZnO microstructures did not fluoresce under either the TRITC or the FITC cube filters. However, the sample exhibited the common blue auto fluorescence

when viewed using the DAPI cube filter. It was postulated that due to the high probability of conjugating anti-BSA via its Fc region, the binding site for the secondary antibodies (also the Fc region of anti-BSA) was blocked.

In conclusion, this chapter has demonstrated a successful method in immobilising antibodies on the surface of ZnO by using PGA as the intermediate.

7.7. References

[1] *BIAevaluation Software* 3.2 1994–2001 (Biacore AB) GE Healthcare Life Science

[2] Wang Y G, Lau S P, Lee H W, Yu S F, Tay B K et. al 2003 Comprehensive study of ZnO films prepared by filtered cathodic vacuum arc at room temperature *J. App. Physics*, **94** 1597

[3] *BIAcore X Instrument Handbook* 1996 (Biacore AB) GE Healthcare Life Science

[4] Souaya E R, Hanna W G, Ismail E H and Milad N E 2000 Studies On Some Acid Divalent-Metal Nitrilotriacetate Complexes. *Molecules* **5** 1121

[5] Hauser C T and Tsien R Y 2007 A hexahistidine-Zn^{2+}-dye label reveals STIM1 surface exposure *Proc. Natl. Acad. Sci.* **104** 3693

[6] A. N. Kapanidis, Y. W. Ebright, R. H. Ebright, *J. Am. Chem. Soc.* **2001**, *123*, 12123.

[7] C. R. Goldsmith, J. Jaworski, M. Sheng, S. J. Lippard, *J. Am. Chem. Soc.* **2006**, *128*, 418.

[8] M. P. Chronakis, R. S. Conlan, N. Gounalaki, T. Copf, D. Tzamarias, *J. Biol. Chem.* **2000**, *275*, 8397.

[9] Sekhon B S 2006 Zinc finger proteins: An overview *Natl. Acad. Sci. Lett. Ind.* **29** 387.

[10] Wolfe S A, Nekludova L and Pabo C O 2000 DNA recognition by Cys_2His_2 Zinc finger proteins *Annu. Rev. Biophys. Biomol. Struct.* **29** 183

[11] Carrier R L, Miller L A and Ahmed M 2007 The utility of cyclodextrins for enhancing oral bioavailability *J. Controlled Release* **123** 78

[12] Del Valle E M M 2004 Cyclodextrin and their uses: A review *Proc. Biochem.* **39** 1033

[13] Kean S D, May B L, Easton C J and Lincoln S F 1997 Preparation and characterization of 6A-polyamine-mono-substituted β-cyclodextrins *J. Chem. Soc., Perkin Trans. 1* 3157

[14] Sandow M, May B L, Clements P, Easton C J and Lincoln S F 1999 Complexes of 6A-(2-Aminoethylamino)-6A-deoxy-b-cyclodextrin and 6A-[Bis(carboxylatomethyl)amino]-6A-deoxy-b-cyclodextrin with (R)- and (S)-Tryptophanate and (R)- and (S)-Phenylalaninate in Aqueous Solution. A pH Titrimetric and N.M.R. spectroscopic study *Aust. J. Chem.* **52** 1143.

[15] Kean S D, Easton C J, Parker D and Lincoln S F 2001 A preparative and solution study of a modified β-cyclodextrin and its Europium(III) complex, and their interactions with Racemic amino acid anions *Aust. J. Chem.* **54** 535

[16] Lee M S, Hong S-S and Mohseni M 2005 Synthesis of photocatalytic nanosized TiO2–Ag particles with sol–gel method using reduction agent *J Molec Catal A Chem* **242** 135

[17] Sen S, Mahanty S, Roy S, Heintz O, Bourgeois S and Chaumont D 2005 Investigation on sol–gel synthesized Ag-doped TiO_2 cermet thin films *Thin Solid Films* **474** 245

[18] Neouze M A and Schubert U 2008 Surface modification and functionalization of metal and metal oxide nanoparticles by organic ligands *Monastsh. Chem.* **139** 183

[19] Kalyanasundaram K and Grätzel M 1998 Applications of functionalized transition metal complexes in photonic and optoelectronic devices *Coord. Chem. Rev.* **177** 347

[20] Galoppini E 2004 Linkers for anchoring sensitizers to semiconductor nanoparticles *Coord. Chem. Rev.* **248** 1283

[21] Taratula O, Galoppini E, Wang D, Chu D, Zhang Z and et. al 2006 Binding Studies of Molecular Linkers to ZnO and MgZnO Nanotip Films *J. Phys Chem. B.* **110** 0506.

[22] T. pauporte, T. Yoshida 2006 Hybrid layers of ZnO/lanthanide complexes with high visible luminescences *J. Mater. Chem.* **16** 4529

[23] T. Pauporte, T. Yoshida, D. Komatsu , H. Minoura 2006 Highly Porous Electrodeposited Zinc Oxide Films Functionalized for Red/Green Luminescence *Electrochem. Solid-State Lett.* **9** H16

[24] Miller T C and Holcombe J A 2001 Comparison and evaluation of the synthetic biopolymer poly-L-aspartic acid and the synthetic "plastic" polymer poly-acrylic acid for use in metal ion-exchange systems.*J. Hazard. Mater.* **83** 219

[25] Malachowski L and Holcombe J A 2003 Immobilized poly-Image -histidine for chelation of metal cations and metal oxyanions *Anal. Chim. Acta* **495** 151

[26] Ritchie M C, Kissick K E, Bachas L G, Sikdar S K, Parikh C and Bhattacharyya D 2001 Polycysteine and Other Polyamino Acid Functionalized Microfiltration Membranes for Heavy Metal Capture *Environ. Sci. Technol.* **35** 3252.

[27] Hestekin J A, Bachas L G and Bhattacharyya D 2001 Poly(amino acid)-Functionalized Cellulosic Membranes: Metal Sorption Mechanisms and Results *Ind. Eng. Chem. Res.* **40** 2668

[28] Malachowski L and Holcombe J A 2004 Comparison of immobilized poly-Image-aspartic acid and poly-Image -glutamic acid for chelation of metal cations *Anal. Chim. Acta* **517** 187

[29] Kaufner L, Cartier R, Wustneck R, Fichtner I ,Pietschmann S, Bruhn H, Schütt D, Thünemann A F and Pison U 2007 Poly(ethylene oxide)-block-poly(glutamic acid) coated maghemite nanoparticles: in vitro characterization and in vivo behaviour *Nanotechnology* **18** 115710

[30] Huang J, Zhang Y, Cheng Z and Tao H 2007 Microwave-assisted synthesis of polyaspartic acid and its effect on calcium carbonate precipitate *J. Appl. Poly. Sci.* **103** 358

Chapter 8

Conclusion and Future Challenges

8.1. Conclusion

The ultimate aim of this research was to fabricate an ultrasensitive and selective biosensor based on a 1-D ZnO nanostructure. The biosensor has three essential components: a biological recognition system which is usually made up of a biological receptor that detects a specific analyte, a physico-chemical transducer which converts the biological signals into a quantitative measurable signal (for this case, a ZnO nanobelt), and an output system to present the measured signal into an appropriate format. The interfaces between each of these components play crucial roles in the feasibility of the biosensor. Consequently, the nature of this work involved multidisciplinary fields, requiring extensive knowledge and skills.

The work in the thesis contributes towards the development of a highly sensitive and selective biosensor based on one-dimensional (1-D) ZnO nanostructures. Emphasis was put on two very important areas for a feasible biosensor;

(i) The 1-D nanostructure used as the transducer platform of the biosensor must be conducting.

(ii) The ZnO surface functionalisation strategy employed must be reproducible, robust and not require harsh chemicals/conditions which may affect the activity of the bioreceptor or the ZnO nanostructure.

From the conductivity study of 1-D ZnO nanostructure using the scanning conductance microscopy (SCM), the polarisation of ZnO nanostructures synthesised via chemical deposition vapour (CVD) method was observed for the first time. The tip induced polarisation effect was most evident within the CVD ZnO nanobelt. It is proposed that nanostructures synthesised via CVD method were more conducting and thus is proposed as the biosensor's primary transducer. This finding supports the work done by others claiming that a different defect density, due to a variation in growth conditions, on similar materials can affect their electrical conductance [1]. By using polarisability as a qualitative measure of carriers' mobility, the ZnO nanobelt

was found to be of better conductivity among the examined CVD ZnO nanostructures. As the detection mechanism of the proposed biosensor relies strongly on the change in conductivity of the 1-D nanostructure upon the binding of the target molecule, this part of the work was important to ensure that the chosen 1-D ZnO nanostructure is not only conducting, but also of better conductivity among the available samples. In addition, SCM was shown to be a valuable technique to provide quick and direct means of characterising the electrical properties of nanomaterials. Unlike other common techniques, SCM discriminates the conductivity of nanomaterials without having to fabricate metal contacts, which often require time consuming processes or/and expensive techniques. Contact resistance issues and unwanted Schottky barriers that hinder direct electrical measurements are avoided. This is crucial and practical as a quick initial characterisation tool, especially for analysis work on large number of nanomaterials.

This work also reports for the first time, the binding of ZnO nanoparticles to nitrilotriacetic acid (NTA), a well known aminotricarboxylic chelating agent. From this revelation, a novel NTA bioreceptor mimic, made up of beta-cyclodextrin (β-CD) was synthesized. With a modified NTA linker, analysis showed the improved binding of β-CD to ZnO surface leading to the discovery of the metal binding functionality of carboxylic groups. Subsequently, the work reports for the first time, the functionalisation of ZnO nanostructures with natural occurring polyamino acid, the polyglutamic acid (PGA). The functionalisation strategy exploited the PGA's abundance of carboxylic groups on its surface for coordination onto the ZnO surface and also for attachment of the bioreceptor (i.e. antibodies) by forming amide linkages. The process was done under mild conditions, using safe and simple water-soluble carbodiimide. Others' work on functionalising ZnO nanorod with a synthetic polymer, namely the biotin-polyethylene-glycol (biotin-PEG) [2] is not suitable for in vivo sensing due to the controversial toxicity of the PEG polymer [3]. Therefore, PGA, known for its biocompatibility and biosafety, serves as a better alternative and is proposed as a better surface functionalisation strategy for ZnO nanostructure in the later fabrication work of ultrasensitive biosensor.

8.2. Future Challenges

The vision of the research was to produce a variable method to fabricate a microchip biosensor packed with enormous arrays of addressable functionalised nanowires for highly specific and sensitive antibody/antigen detections. The arrays of independent nanodevices would be fully integrated with the fast parallel electronic signal processing capability of an on-chip computation and wireless communication. In recent years, progresses made in the applications of one-dimensional nanostructures in biosensors provide novel opportunities for the development of such device. However, with the research in its preliminary stage, there are several issues and challenges that should be addressed based on the outcomes of the work in this thesis.

In a standard development process of nanowires biosensing device, the nanowires are first grown off-chip and then dispersed onto a wafer, contact leads are then individually aligned to the randomly placed nanowires, followed by surface functionalisation of the nanowires for specific detection. One of the challenges of large scale integration of such device is to ensure the uniformity of the nanowires in terms of dimensions, properties and morphology. The nanowire growth process must be optimised to produce nanowires with consistent quality. Besides that, assembling and aligning addressable nanowire device along an identical direction with correct registry to any underlying circuitry is a great challenge. Several efforts have been made to overcome this issue through the development of different alignment techniques, namely micro-fluidic alignment [4, 5], electric field alignment [6, 7] and magnetic field alignment [8, 9] techniques. The possibility of placing a single nanowire on a desired location in a patterned substrate with relative ease and simplicity was demonstrated using the magnetic alignment technique [10]. In addition, it is also essential to fabricate highly reliable ohmic contact between the nanowires and electrode contact to realise a high performance biosensor. Biological molecules possess unique structures and functions; understanding the mechanism of interaction between biomolecules and nanomaterials is still at its infancy and remains a challenge. Also, the 'holy grail' for medical biosensing is an implantable device and several trials to develop such a device to detect specific bio-molecules and chemicals in the body over a period of time have been reported [11]. One of the main issues for an implantable biosensor is the degradation of sensitivity over time, which

is primarily caused by non-specific binding, wound healing and inflammation (biofouling phenomenon). Therefore, much consideration must be put on tissue biocompatibility and inflammation behaviour in the design of an implantable biosensor. The sensor surface may be modified and coated with an anti-inflammation drug to discourage biofouling phenomenon, or measurements could be taken in a specific time-line before biofouling takes place. Other challenges relating to the development of a nanobiosensor includes determining effective ways to enhance the signal to noise ratio and to enhance transduction and amplification of the signals. The detection sensitivity, signal stability and reproducibility are also important issues to be considered for the successful fabrication of the nanobiosensor. Future work should address each of the challenges/ issues presented in this section.

8.3. References

[1] Schmidt-Mende L and MacManus-Driscoll J L 2007 ZnO –nanostructures, defects, and devices *Materials Today* **10** 5

[2] Kim J S, Park W I, Lee C and Yi G 2006 ZnO Nanorod Biosensor for Highly Sensitive Detection of Specific Protein Binding *Journal of the Korean Physical Society* **49** 1635

[3] Sheftel V O 2000 Indirect food additives and polymers: migration and toxicology CRC 1114–1116

[4] Huang Y, Duan X, Wei Q, Cui Y, Lauhon L J, Kim K H and Lieber C M 2001 Logic Gates and Computation from Assembled Nanowire Building Blocks *Science* **294** 1313

[5] Huang Y, Duan X, Wei Q and Lieber and C M 2001 Directed Assembly of One-Dimensional Nanostructures into Functional Networks *Science* **291** 630

[6] Duan X, Huang Y, Cui Y, Wang J and Lieber C M 2001 Indium phosphide nanowires as building blocks for nanoscale electronic and optoelectronic devices *Nature* 409 66

[7] Smith P A, Nordquist C D, Jackson T N and Mayer T S 2000 Electric-field assisted assembly and alignment of metallic nanowires *Appl. Phys. Lett.* **77** 1399

[8] Bentley A K, Trethewey J S, Ellis A B and Crone W C 2004 Magnetic Manipulation of Copper–Tin Nanowires Capped with Nickel Ends *Nano Lett.* **4** 487

[9] S.W. Jung, W.I. Park, G.C. Yi, M.Y. Kim 2003 Fabrication and Controlled Magnetic Properties of Ni/ZnO Nanorod Heterostructures *Adv. Mater.* **15** 1358

[10] Lee S W, Jeong M C, Myoung J M, Chae G S and Chung I J 2007 Magnetic alignment of ZnO nanowires for optoelectronic device applications *Appl. Phys. Lett.* **90** 133115

[11] (a) Li C M, Dong H, Cao X, Luong J H, Zhang X 2007 Implantable electrochemical sensors for biomedical and clinical applications: progress, problems, and future possibilities 1: *Curr. Med. Chem.* ***14*** 937

(b) Staples M, Daniel K, Cima M J and Langer R 2006 Application of micro- and nanoelectromechanical devices to drug delivery. *Pharm Res.* ***23*** 847

(c) Wu Y and Meyerhoff M E 2008 Nitric oxide-releasing/generating polymers for the development of implantable chemical sensors with enhanced biocompatibility. *Talanta* ***75*** 642

(d) Chiu N F, Wang J M, Liao C W, Chen C H, Chen H C, Yang L J, Lu S S and Lin C W 2005 An Implantable Multifunctional Needle Type Biosensor with Integrated RF Capability *Proceedings of the 2005 IEEE Engineering in Medicine and Biology 27th Annual Conference*; Shanghai, China, September 1-4, 2005

(e) Gifforda R, Kehoea J J, Barnesa S L, Kornilayev B A, Alterman M A and Wilson G S 2006 Protein interactions with subcutaneously implanted biosensors. *Biomaterials* ***27*** 2587